

MARINA VENDL CRAVEIRO

UPHEAVAL BUCKLING OF PIPELINES TRIGGERED BY THE  
INTERNAL PRESSURE RESULTING FROM THE TRANSPORTATION OF  
OIL AND GAS: THEORETICAL DISCUSSIONS AND GEOMETRICALLY  
NONLINEAR ANALYSIS USING THE FINITE ELEMENT METHOD

São Paulo

2017

MARINA VENDL CRAVEIRO

UPHEAVAL BUCKLING OF PIPELINES TRIGGERED BY THE  
INTERNAL PRESSURE RESULTING FROM THE TRANSPORTATION OF  
OIL AND GAS: THEORETICAL DISCUSSIONS AND GEOMETRICALLY  
NONLINEAR ANALYSIS USING THE FINITE ELEMENT METHOD

Master thesis presented to the Polytechnic  
School at University of São Paulo as a  
requirement for obtaining the Master's degree  
in Science.

São Paulo

2017

MARINA VENDL CRAVEIRO

UPHEAVAL BUCKLING OF PIPELINES TRIGGERED BY THE  
INTERNAL PRESSURE RESULTING FROM THE TRANSPORTATION OF  
OIL AND GAS: THEORETICAL DISCUSSIONS AND GEOMETRICALLY  
NONLINEAR ANALYSIS USING THE FINITE ELEMENT METHOD

Master thesis presented to the Polytechnic  
School at University of São Paulo as a  
requirement for obtaining the Master's degree  
in Science.

Area of Concentration: Engineering of  
Structures

Advisor: Prof. Dr. Alfredo Gay Neto

São Paulo

2017

### Catálogo-na-publicação

Craveiro, Marina Vendl

Upheaval buckling of pipelines triggered by the internal pressure resulting from the transportation of oil and gas: theoretical discussions and geometrically nonlinear analysis using the finite element method / M. V.

Craveiro -- São Paulo, 2017.

169 p.

Dissertação (Mestrado) - Escola Politécnica da Universidade de São Paulo. Departamento de Engenharia de Estruturas e Geotécnica.

1.Buckling of pipelines 2.Finite element method 3.Nonlinear analysis of structures I.Universidade de São Paulo. Escola Politécnica. Departamento de Engenharia de Estruturas e Geotécnica II.t.

This master thesis is dedicated to my parents  
and my sister.

## **ACKNOWLEDGEMENTS**

Foremost, I would like to thank God for the protection and the strength He has given me, guiding my steps in pursuit of my goals. Without faith in Him, nothing would be possible.

I would also like to express my gratitude to Prof. Dr. Alfredo Gay Neto for being a present and patient advisor, always helping, giving ideas and transmitting his knowledge when I needed it.

I would like to thank Prof. Dr. Carlos Eduardo Nigro Mazzilli and Prof. Dr. Clóvis de Arruda Martins for the recommendations given in my Qualifying Examination.

I would like to thank all the other Professors of Polytechnic School with whom I had the opportunity to have classes for the acquired knowledge.

I would also to thank Prof. Ms. Januário Pellegrino Neto and Prof. Dr. Sergio Vicente Denser Pamboukian for, still in college, encouraging me to start the master's program at University of São Paulo.

Lastly, but not less important, I would like to thank my family, especially my parents and my sister, for their support and unconditional love.

If I have seen further, it is by standing upon the  
shoulders of giants.

(Isaac Newton)

## ABSTRACT

The pipelines used to transport oil and gas from the wellheads to the distribution and refining sites can be subjected to high levels of pressure and temperature. Under such conditions, the pipelines tend to expand, but, if the expansion is inhibited, a significant compressive axial force can arise, leading to their buckling, which can occur in the horizontal or vertical plane. In this context, the objective of the present work is to analyze the upheaval buckling of pipelines, considering the internal pressure to which they are subjected during the transportation of oil and gas as its only triggering. Using the concept of effective axial force, it aims at discussing two different approaches for considering the internal pressure in buckling problems: distributed loads dependent on pipeline curvature and equivalent compressive axial forces with follower and non-follower characteristics. It also discusses the influence of using static or dynamic analysis for such approaches. Concerning the upheaval buckling itself, the work intends to analyze and compare the influence of the soil imperfection amplitudes to the influence of the friction between the pipeline and the ground in the critical loads and in the post-buckling configurations of the pipeline. Besides theoretical research, the objectives are achieved through the development of various numerical models, since geometrically-simple models, without the consideration of the interaction between the pipeline and the ground, until more complex models, with the use of contact models to detect the ground and its imperfections. The models are developed in *Giraffe (Generic Interface Readily Accessible for Finite Elements)* using geometrically-exact finite element models of beams, undergoing large displacements and finite rotations. Through the research, it is concluded that there is an equivalence between the application of the internal pressure as a distributed load dependent on pipeline curvature and the application of the internal pressure as a follower compressive axial force. Besides this, it is demonstrated that the type of the analysis (static or dynamic) depends on the nature of the physical system analyzed. With the aid of results presented in terms of internal pressure, classical results about the influence of the imperfection amplitudes and of the friction between the pipeline and the ground in buckling are confirmed. It is also showed that the imperfection amplitudes analyzed play a more important role in the post-buckling configurations of the pipeline than the friction.

Keywords: Buckling. Effective axial force. Internal pressure. Nonlinear analysis. Pipeline.

## RESUMO

Os dutos utilizados para transportar petróleo e gás natural das reservas até os locais de distribuição e refino podem estar submetidos a elevados níveis de pressão e temperatura. Sob tais condições, os dutos tendem a se expandir, porém, se a expansão é inibida, uma força axial de compressão significativa pode surgir nos dutos, ocasionando a flambagem lateral ou vertical dos mesmos. Dentro desse contexto, o objetivo do presente trabalho é analisar a flambagem vertical de dutos, considerando a pressão interna à qual eles estão submetidos durante o transporte de petróleo e gás natural como o único parâmetro desencadeador da flambagem. Usando o conceito de força axial efetiva, o trabalho objetiva discutir duas abordagens diferentes para considerar a pressão interna nos problemas de flambagem: carregamentos distribuídos dependentes da curvatura do duto e forças axiais de compressão equivalentes à pressão com caráter seguidor e não seguidor. O trabalho também discute a influência de usar a análise estática ou dinâmica para analisar essas abordagens de carregamento. Com relação à flambagem vertical propriamente dita, o trabalho pretende analisar e comparar a influência das amplitudes das imperfeições presentes no solo com a influência do atrito entre o duto e o solo nas cargas críticas e nas configuração pós-críticas do duto. Além de pesquisa teórica, os objetivos são atingidos através do desenvolvimento de vários modelos numéricos, desde modelos geometricamente simples, sem a consideração da interação entre o duto e o solo, até modelos mais complexos, com o uso de modelos de contato para detectar o solo e suas imperfeições. Os modelos são desenvolvidos no *Giraffe (Generic Interface Readily Accessible for Finite Elements)* usando elementos finitos geometricamente exatos de viga, sujeitos a grandes deslocamentos e rotações finitas. Através da pesquisa, conclui-se que existe uma equivalência entre a aplicação da pressão interna como um carregamento distribuído dependente da curvatura do duto e a aplicação da pressão interna como uma força axial de compressão seguidora. Além disso, demonstra-se que o tipo de análise (estática e dinâmica) depende da natureza do sistema físico analisado. Com a ajuda de resultados apresentados em termos de pressão interna, os resultados clássicos sobre a influência das amplitudes das imperfeições e do atrito entre o duto e o solo são confirmados. Também é mostrado que as amplitudes das imperfeições analisadas desempenham uma maior influência nas configurações pós-críticas do duto do que o atrito.

Palavras-chave: Análise não linear. Dutos. Flambagem. Força axial efetiva. Pressão interna.

## LIST OF FIGURES

Figure 1	– Global buckling of pipelines. ....	29
Figure 2	– Accident occurred in Guanabara Bay due to the lateral buckling of Petrobras’ pipeline PE-II. ....	30
Figure 3	– Equivalent systems for pipelines subjected to internal and external pressures..	38
Figure 4	– Hobbs’ method for upheaval buckling of pipelines without imperfections – topology and axial force distribution. ....	40
Figure 5	– Hobbs’ method for upheaval buckling of pipelines without imperfections – temperature rise versus buckle length. ....	45
Figure 6	– Hobbs’ method for upheaval buckling of pipelines without imperfections – internal pressure versus buckle length. ....	46
Figure 7	– Lateral buckling modes. ....	46
Figure 8	– Hobbs’ method for lateral buckling (infinite mode) of pipelines without imperfections – temperature rise versus buckle length. ....	49
Figure 9	– Hobbs’ method for lateral buckling (infinite mode) of pipelines without imperfections – internal pressure versus buckle length. ....	50
Figure 10	– Hobbs’ method for lateral buckling (mode 1) of pipelines without imperfections – temperature rise versus buckle length. ....	50
Figure 11	– Hobbs’ method for lateral buckling (mode 1) of pipelines without imperfections – internal pressure versus buckle length. ....	51
Figure 12	– Hobbs’ method for lateral buckling (mode 2) of pipelines without imperfections – temperature rise versus buckle length. ....	51
Figure 13	– Hobbs’ method for lateral buckling (mode 2) of pipelines without imperfections – internal pressure versus buckle length. ....	52
Figure 14	– Hobbs’ method for lateral buckling (mode 3) of pipelines without imperfections – temperature rise versus buckle length. ....	52
Figure 15	– Hobbs’ method for lateral buckling (mode 3) of pipelines without imperfections – internal pressure versus buckle length. ....	53
Figure 16	– Hobbs’ method for lateral buckling (mode 4) of pipelines without imperfections – temperature rise versus buckle length. ....	53
Figure 17	– Hobbs’ method for lateral buckling (mode 4) of pipelines without imperfections – internal pressure versus buckle length. ....	54

Figure 18	– Taylor and Gan’s method for upheaval buckling of pipelines with conformal imperfections – topology and axial force distribution. ....	56
Figure 19	– Taylor and Gan’s method for upheaval buckling of pipelines with conformal imperfections – temperature rise versus buckle length. ....	59
Figure 20	– Taylor and Gan’s method for upheaval buckling of pipelines with conformal imperfections – internal pressure versus buckle length. ....	59
Figure 21	– Taylor and Gan’s method for lateral buckling (mode 1) of pipelines with conformal imperfections – topology and axial force distribution. ....	60
Figure 22	– Taylor and Gan’s method for lateral buckling (mode 1) of pipelines with conformal imperfections – temperature rise versus buckle length. ....	61
Figure 23	– Taylor and Gan’s method for lateral buckling (mode 1) of pipelines with conformal imperfections – internal pressure versus buckle length. ....	62
Figure 24	– Taylor and Gan’s method for lateral buckling (mode 2) of pipelines with conformal imperfections – topology and axial force distribution. ....	62
Figure 25	– Taylor and Gan’s method for lateral buckling (mode 2) of pipelines with conformal imperfections – temperature rise versus buckle length. ....	65
Figure 26	– Taylor and Gan’s method for lateral buckling (mode 2) of pipelines with conformal imperfections – internal pressure versus buckle length. ....	65
Figure 27	– Taylor and Tran’s method for upheaval buckling of pipelines with prop imperfection – datum establishment topology. ....	67
Figure 28	– Taylor and Tran’s method for upheaval buckling of pipelines with prop imperfection – pre-upheaval flexure topology and axial force distribution. ....	68
Figure 29	– Taylor and Tran’s method for upheaval buckling of pipelines with prop imperfection – post-upheaval buckling ( $L < L_i$ ) topology and axial force distribution. ....	72
Figure 30	– Taylor and Tran’s method for upheaval buckling of pipelines with prop imperfection – post-upheaval buckling ( $L > L_i$ ) topology and axial force distribution. ....	73
Figure 31	– Cantilever columns with non-follower and follower loads. ....	86
Figure 32	– Point mass supported by spring. ....	91
Figure 33	– Energy of the mass spring system. ....	92
Figure 34	– Mass spring system under tangential load. ....	94
Figure 35	– Coulomb’s law. ....	94
Figure 36	– Geometrical description of the contact model. ....	100

Figure 37	– Kinematics description used to define the tangential gap function. ....	103
Figure 38	– Scheme of the application of the dynamic load. ....	112
Figure 39	– Boundary conditions of the geometrically-simple models. ....	113
Figure 40	– Configurations obtained from the application of the imperfections – case 1. .	114
Figure 41	– Configurations obtained from the application of the imperfections – case 2. .	114
Figure 42	– Configurations obtained from the application of the imperfections – case 3. .	115
Figure 43	– Post-buckling configurations – static analysis – load type a – case 1.....	115
Figure 44	– Equilibrium paths (midspan) – static analysis – load type a – case 1.....	115
Figure 45	– Post-buckling configurations – static analysis – load type a – case 2.....	116
Figure 46	– Equilibrium paths (midspan) – static analysis – load type a – case 2.....	116
Figure 47	– Post-buckling configurations – static analysis – load type a – case 3.....	116
Figure 48	– Equilibrium paths (midspan) – static analysis – load type a – case 3.....	116
Figure 49	– Post-buckling configurations – static analysis – load types – case 1.....	117
Figure 50	– Equilibrium paths (midspan) – static analysis – load types – case 1.....	118
Figure 51	– Post-buckling configurations – static analysis – load types – case 2.....	118
Figure 52	– Equilibrium paths (midspan) – static analysis – load types – case 2.....	118
Figure 53	– Post-buckling configurations – static analysis – load types – case 3.....	118
Figure 54	– Equilibrium paths (midspan) – static analysis – load types – case 3.....	119
Figure 55	– Eigenvalues – load type a – case 1 with imperfection of 1000 N.....	120
Figure 56	– Eigenvalues – load type a – case 1 without imperfection. ....	120
Figure 57	– Configurations obtained from the application of the imperfections – case 4. .	121
Figure 58	– Post-buckling configurations – static analysis – load type a – case 4.....	121
Figure 59	– Equilibrium paths (free end) – static analysis – load type a – case 4.....	121
Figure 60	– Post-buckling configurations at the time 316 s – dynamic analysis – load type a – case 4.....	123
Figure 61	– Time-series of displacement (free end) – dynamic analysis – load type a – case 4. ....	123
Figure 62	– Post-buckling configurations at the time 316 s – dynamic analysis – load types – case 4.....	123
Figure 63	– Time-series of displacement (free end) – dynamic analysis – load types – case 4. ....	124
Figure 64	– Eigenvalues – load type a – case 4 with imperfection of 1000 N.....	125
Figure 65	– Eigenvalues – load type a – case 4 with imperfection of 1000 N – detail.....	125
Figure 66	– Initial layout of the simplified model – plan view. ....	126

Figure 67	– Comparison between the initial configurations of the pipeline obtained analytically and numerically.....	127
Figure 68	– Comparison between the pipeline configurations resulting from load step 1 and load step 4. ....	128
Figure 69	– Comparison between the pipeline configurations resulting from load step 4 and load step 5. ....	129
Figure 70	– Reaction at the central node of the pipeline.....	129
Figure 71	– Buckle amplitude $y$ versus additional axial force. ....	131
Figure 72	– Post-buckling configuration of the pipeline for a total compressive axial force of 4822343.81 N.....	132
Figure 73	– Post-buckling configurations of the pipeline at the time 1.2 s.....	132
Figure 74	– Location and shape of the isolated imperfection.....	134
Figure 75	– Initial layout of the models with imperfections represented by rigid surfaces – plan view and elevation. ....	135
Figure 76	– Coordinate $y$ of the central node versus the load applied – follower axial force. ....	136
Figure 77	– Coordinate $y$ of the central node versus the load applied – internal pressure..	137
Figure 78	– Coordinate $y$ of the central node versus the load applied – comparison between the application of follower axial forces and internal pressure. ....	137
Figure 79	– Critical load versus imperfection amplitude. ....	138
Figure 80	– Post-buckling configurations for the imperfection 0.05 m/2.5 m. ....	139
Figure 81	– Post-buckling configurations for the imperfection 0.25 m/12.5 m. ....	139
Figure 82	– Post-buckling configurations for the imperfection 0.50 m/25 m. ....	139
Figure 83	– Post-buckling configurations for the imperfection 1.00 m/50 m. ....	140
Figure 84	– Von Mises stress at the central cross section of the pipeline versus internal pressure for the imperfection 0.05 m/2.5 m.....	141
Figure 85	– Von Mises stress at the central cross section of the pipeline versus coordinate $y$ for the imperfection 0.05 m/2.5 m. ....	141
Figure 86	– Von Mises stress at the central cross section of the pipeline versus internal pressure for the imperfection 0.25 m/12.5 m.....	142
Figure 87	– Von Mises stress at the central cross section of the pipeline versus coordinate $y$ for the imperfection 0.25 m/12.5 m. ....	142
Figure 88	– Von Mises stress at the central cross section of the pipeline versus coordinate $y$ for the imperfection 0.25 m/12.5 m – detail of the pre-upheaval stage. ....	143

Figure 89 – Von Mises stress at the central cross section of the pipeline versus internal pressure for the imperfection 0.50 m/25 m.....	143
Figure 90 – Von Mises stress at the central cross section of the pipeline versus coordinate y for the imperfection 0.50 m/25 m. ....	144
Figure 91 – Von Mises stress at the central cross section of the pipeline versus coordinate y for the imperfection 0.50 m/25 m – detail of the pre-upheaval stage. ....	144
Figure 92 – Von Mises stress at the central cross section of the pipeline versus internal pressure for the imperfection 1.00 m/50 m.....	145
Figure 93 – Von Mises stress at the central cross section of the pipeline versus coordinate y for the imperfection 1.00 m/50 m. ....	145
Figure 94 – Von Mises stress at the central cross section of the pipeline versus coordinate y for the imperfection 1.00 m/50 m – detail of the pre-upheaval stage. ....	146
Figure 95 – Prop imperfection.....	148
Figure 96 – Conformal imperfection. ....	148
Figure 97 – Buckling mode of the prop imperfection. ....	149
Figure 98 – Buckling mode of the conformal imperfection. ....	149
Figure 99 – Contact forces for the prop imperfection case at the times 0.0 s, 1.0 s, 1.9 s, 3.0 s, 3.4 s and 3.5 s. ....	150
Figure 100 – Contact forces for the conformal imperfection case at the times 0.0 s, 1.9 s, 3.7 s and 6.3 s. ....	151
Figure 101 – Contact forces for the conformal imperfection case at the time 6.5 s.....	151
Figure 102 – Contact forces for the conformal imperfection case at the time 6.6 s.....	152
Figure 103 – Coordinate y of the central node versus the internal pressure for distinct friction coefficients – imperfection amplitude equal to 0.05 m.....	153
Figure 104 – Coordinate y of the central node versus the internal pressure for distinct friction coefficients – imperfection amplitude equal to 0.05 m – detail.....	153
Figure 105 – Coordinate y of the central node versus the internal pressure for distinct friction coefficients – imperfection amplitude equal to 0.25 m.....	154
Figure 106 – Coordinate y of the central node versus the internal pressure for distinct friction coefficients – imperfection amplitude equal to 0.25 m – detail.....	154
Figure 107 – Coordinate y of the central node versus the internal pressure for distinct friction coefficients – imperfection amplitude equal to 0.50 m.....	155
Figure 108 – Coordinate y of the central node versus the internal pressure for distinct friction coefficients – imperfection amplitude equal to 0.50 m – detail.....	155

Figure 109 – Coordinate y of the central node versus the internal pressure for distinct friction coefficients – imperfection amplitude equal to 1.00 m.....	156
Figure 110 – Coordinate y of the central node versus the internal pressure for distinct friction coefficients – imperfection amplitude equal to 1.00 m – detail.....	156
Figure 111 – Post-buckling configurations for the coefficient of friction equal to 0.1.....	157
Figure 112 – Post-buckling configurations for the coefficient of friction equal to 0.5.....	157
Figure 113 – Post-buckling configurations for the coefficient of friction equal to 0.8.....	157
Figure 114 – Post-buckling configurations for the coefficient of friction equal to 1.0.....	158

## LIST OF TABLES

Table 1 – Numerical example data for the analytical models. ....	44
Table 2 – Constants for lateral buckling modes. ....	48
Table 3 – Classification of physical systems.....	85
Table 4 – Critical loads (Euler’s problems). ....	87
Table 5 – Load data for static analyses.....	114
Table 6 – Load data for dynamic analyses. ....	122
Table 7 – Static load steps used to simulate numerically the stages of the upheaval buckling in the simplified model.....	127
Table 8 – Parameters used to create the prop imperfections – part 1.....	134
Table 9 – Parameters used to create the prop imperfections – part 2.....	134
Table 10 – Static load steps used to simulate the laying process of the pipeline on the ground with a prop imperfection. ....	135

## **LIST OF ABBREVIATIONS**

FEM	Finite element method
HPHT	High pressure and high temperature
VIV	Vortex induced vibration

## LIST OF SYMBOLS

### Greek alphabet

$\alpha$	linear thermal coefficient of the pipeline material
$\alpha_A$	adhesion factor
$\alpha_S^\Delta$	vector that represents the rotations of the center of the spherical surface between configurations $i$ and $i + 1$
$\alpha_S^i$	rotation vector of the center of the spherical surface at configuration $i$
$\beta$	parameter of Newmark's method
$\gamma$	parameter of Newmark's method
$\gamma_s$	submerged weight of soil per unit volume
$\Gamma$	master surface
$\Gamma_\zeta$	direction tangent to the master surface
$\Gamma_\theta$	direction tangent to the master surface
$\delta$	extension of the pipeline generated by the axial force variation
$\delta'$	internal angle of friction between the pipeline and the soil
$\delta\Gamma$	variation of the master surface
$\delta\lambda$	variation of the Lagrange multiplier
$\delta\Pi$	variation of the energy
$\delta\Pi_{f\text{slide}}$	weak form contribution due to friction for the sliding condition
$\delta\Pi_{f\text{stick}}$	weak form contribution due to friction for the stick condition
$\delta\Pi_n$	weak form contribution due to normal contact
$\delta\mathbf{g}_n$	variation of the normal gap function (vector)
$\delta\mathbf{g}_t^{i+1}$	variation of the tangential gap function at configuration $i + 1$ (vector)
$\delta\mathbf{n}$	variation of the contact normal direction
$\delta\mathbf{u}$	virtual displacement
$\delta\mathbf{x}_s$	variation of the position vector of the center of the spherical surface
$\Delta$	index that indicates quantities that relate the configurations $i$ and $i + 1$
$\Delta\lambda$	amount of sliding
$\Delta T$	temperature change
$\varepsilon$	total longitudinal strain of the pipeline

$\epsilon_{\text{end}}$	longitudinal strain induced by difference of longitudinal pressures between the sides of an end cap
$\epsilon_f$	longitudinal strain induced by friction between the pipeline and the soil
$\epsilon_p$	longitudinal strain induced by pressure
$\epsilon_{\text{Poisson}}$	longitudinal strain resulting from Poisson effect
$\epsilon_T$	longitudinal strain induced by temperature change
$\epsilon_n$	normal penalty parameter (normal stiffness)
$\epsilon_t$	tangential penalty parameter (tangential stiffness)
$\zeta$	convective coordinate used to parameterize the master surface
$\bar{\zeta}$	convective coordinate associated with the minimum distance between the center of the spherical surface and the master surface
$\theta$	convective coordinate used to parameterize the master surface
$\bar{\theta}$	convective coordinate associated with the minimum distance between the center of the spherical surface and the master surface
$\kappa(s)$	pipeline curvature at an abscissa $s$
$\lambda$	auxiliary constant or eigenvalue (Section 3); Lagrange multiplier (Section 4)
$\lambda_1$	auxiliary constant (Section 3); wave-length of the oscillatory surface along direction $\zeta$ (Section 4)
$\lambda_2$	auxiliary constant (Section 3); wave-length of the oscillatory surface along direction $\theta$ (Section 4)
$\mu$	mass per unit length
$\nu$	Poisson ratio
$\xi$	generic coordinate $x$
$\Pi$	potential energy
$\Pi_{\text{min}}$	minimum energy
$\Pi_{\text{min}}^c$	minimum energy within the admissible solution space
$\rho_e$	specific mass of the external fluid
$\rho_i$	specific mass of the internal fluid
$\rho_{\text{max}}$	maximum value of negative curvature radius of the conformal imperfection
$\sigma_e$	Von Misses stress
$\sigma_H$	hoop stress
$\sigma_{H,\text{thick}}$	hoop stress for thick-walled pipes
$\sigma_{H,\text{thin}}$	hoop stress for thin-walled pipes

$\sigma_L$	longitudinal stress
$\sigma_{L,thick}$	longitudinal stress for thick-walled pipes
$\sigma_{L,thin}$	longitudinal stress for thin-walled pipes
$\sigma_R$	radial stress
$\sigma_{R,thick}$	radial stress for thick-walled pipes
$\sigma_T$	longitudinal stress induced by temperature change
$\tau_{HR}, \tau_{LH}, \tau_{LR}$	shear stresses
$\phi_1$	phase of the oscillatory surface along direction $\zeta$
$\phi_2$	phase of the oscillatory surface along direction $\theta$
$\phi$	generic friction coefficient
$\phi_A$	fully mobilized axial friction coefficient between the pipeline and the soil
$\phi_L$	lateral friction coefficient between the pipeline and the soil
$\psi$	local geometry of the oscillatory rigid surface
$\omega$	constant or circulatory frequency
$\omega_1$	constant or circulatory frequency
$\omega_3$	constant or circulatory frequency

### Latin alphabet

<b>0</b>	null vector
<b>A</b>	area of the pipeline cross section (Section 2) or vertex of the triangular surface (Section 4)
<b>A<sub>1</sub></b>	auxiliary constant (Section 2) or amplitude of the oscillatory surface in direction $\zeta$ (Section 4)
<b>A<sub>12</sub></b>	amplitude of the oscillatory surface related to directions $\zeta$ and $\theta$ (Section 4)
<b>A<sub>2</sub></b>	auxiliary constant (Section 2) or amplitude of the oscillatory surface in direction $\theta$ (Section 4)
<b>A<sub>e</sub></b>	external area of the pipeline cross section
<b>A<sub>i</sub></b>	internal bore area of the pipeline cross section
<b>B</b>	vertex of the triangular surface
<b>c</b>	constraints in contact problems
<b>c</b>	vector that represents the convective coordinates of the master surface

$\bar{\mathbf{c}}$	vector that represents the convective coordinates corresponding to a specific set of degrees of freedom and associated with the minimum distance between the center of the spherical surface and the master surface
$\mathbf{c}^i$	vector that represents the convective coordinates of the master surface at configuration $i$
$\mathbf{c}^{i+1}$	vector that represents the convective coordinates of the master surface at configuration $i + 1$
$C$	soil cohesion representative of the soil backfill (Section 2) or vertex of the triangular surface (Section 4)
$\mathbf{C}$	damping matrix
$C_1$	auxiliary constant
$C_2$	auxiliary constant
$C_3$	auxiliary constant
$\mathbf{d}$	vector that represents all degrees of freedom that may affect the interaction between the slave and master surfaces
$\bar{\mathbf{d}}$	specific set of degrees of freedom used in the contact formulation
$d\xi$	infinitesimal change of $\xi$
$\mathbf{d}^i$	vector that represents all degrees of freedom that may affect the interaction between the slave and master surfaces at configuration $i$
$\mathbf{d}^{i+1}$	vector that represents all degrees of freedom that may affect the interaction between the slave and master surfaces at configuration $i + 1$
$\mathbf{d}_M$	vector that represents the degrees of freedom necessary to describe the movement of the master surface in space
$d_n$	distance between nodes
$ds$	pipe segment length
$\mathbf{d}_S^\Delta$	vector that represents the six degrees of freedom necessary to describe the evolution of the spherical surface between configurations $i$ and $i + 1$
$dT$	inertial load
$dT_{tw}$	infinitesimal change of $T_{tw}$
$D$	diameter in which hoop stress or radial stress is calculated
$D_e$	external diameter of the pipeline
$D_i$	internal diameter of the pipeline
$e$	eccentricity or Euler's number

$\mathbf{e}_1$	direction of the global coordinate system
$\mathbf{e}_2$	direction of the global coordinate system
$\mathbf{e}_3$	direction of the global coordinate system
$E$	Young's modulus
$f$	deflection at the free end of the cantilever column
$\mathbf{f}$	vector of applied forces
$f(x)$	exponential function
$\bar{\mathbf{f}}(s)$	vector force per unit length that represents the internal pressure load
$f_A$	axial friction parameter corresponding to the real axial displacement of the pipeline
$F$	shear force at the prop imperfection
$F_b$	axial friction force per unit length for buried pipelines
$F_i$	initial shear force at the prop imperfection
$F_{\max}$	maximum friction force possible to occur in the stick state
$F_{\text{try}}$	tentative-force
$F_T$	force tangential to the plane
$g$	gravitational field intensity
$\mathbf{g}$	gravitational field vector
$g_n$	normal gap function (scalar quantify)
$\mathbf{g}_n$	normal gap function (vector)
$\mathbf{g}_t^\Delta$	incremental tangential gap function (vector)
$\mathbf{g}_{t\text{slide}}^\Delta$	sliding tangential gap function (vector)
$\mathbf{g}_t^i$	tangential gap function at configuration $i$ (vector)
$\mathbf{g}_t^{i+1}$	tangential gap function at configuration $i + 1$ (vector)
$\mathbf{G}(s)$	vector that describes the centroid of the pipeline cross section at an abscissa $s$
$G_1$	auxiliary constant
$G_2$	auxiliary constant
$h$	distance between the point mass and the rigid plane
$H$	buried depth of the pipeline centerline
$H_1$	auxiliary constant
$H_2$	auxiliary constant

$i$	imaginary number (Section 3) or configuration obtained previously (Section 4)
$i + 1$	configuration to be obtained
$I$	second moment of area of the pipeline cross section
$\mathbf{I}$	identify matrix
$J$	auxiliary constant
$k$	spring stiffness
$k_1$	constant for lateral buckling modes
$k_2$	constant for lateral buckling modes
$k_3$	constant for lateral buckling modes
$k_4$	constant for lateral buckling modes
$k_5$	constant for lateral buckling modes
$k_{\text{soil}}$	foundation stiffness
$\mathbf{K}$	stiffness matrix
$K_0$	coefficient of pressure at rest
$K_1$	auxiliary constant
$K_2$	auxiliary constant
$l$	column's length
$L$	buckle length of the pipeline
$L_0$	buckle length of the conformal imperfection topology
$L_1$	pipeline arc length after the buckling
$L_i$	initial buckle length of the pipeline caused by the prop imperfection
$L_s$	length of the pipeline that slides in towards the buckle
$L_u$	buckle length for which the pipeline loses its contact with the prop imperfection
$m$	auxiliary parameter equal to $w/EI$ or $\phi_L w/EI$ (Section 2); entire numbers (Section 3); mass of a point (Section 4)
$M$	bending moment on the deflected pipeline
$\mathbf{M}$	mass matrix
$\hat{M}$	maximum bending moment on the deflected pipeline
$M_i$	initial bending moment on the deflected pipeline with prop imperfection
$n$	auxiliary parameter equal to $\sqrt{P/EI}$ (Section 2) or number of degrees of freedom (Section 3)

$\mathbf{n}$	contact normal direction
$\mathbf{n}(s)$	Frenet normal direction
$n_0$	auxiliary parameter equal to $\sqrt{P_{00}/EI}$
$\mathbf{n}^i$	contact normal direction at configuration $i$
$\mathbf{n}^{i+1}$	contact normal direction at configuration $i + 1$
$N$	maximum bending moment at the prop imperfection (Section 2) or number of degrees of freedom necessary to describe the movement of the master surface in space (Section 4)
$N_i$	initial maximum bending moment at the prop imperfection
$O$	origin of the global coordinate system
$p_e$	external pressure
$p_e(\mathbf{G}_s)$	external pressure at $\mathbf{G}_s$
$p_i$	internal pressure
$p_i(\mathbf{G}_s)$	internal pressure at $\mathbf{G}_s$
$p_{icrit}$	critical internal pressure
$P$	axial force at the buckle region (Section 2); axial force (Section 3)
$P_0$	effective axial force
$P_{00}$	axial force at the buckle region for the initial configuration of the pipeline
$P_{0,T}$	axial force induced by temperature change
$P_1$	first critical load
$P_m$	loads for which the column admits nontrivial equilibrium positions
$P_u$	axial force at the buckle region for which the prop force becomes zero
$\mathbf{Q}$	rotation matrix that rules the alignment of the oscillatory surface in space
$\mathbf{Q}^\Delta$	rotation operator necessary to update the direction of the accumulated tangential gap
$\mathbf{Q}_s$	rotation tensor associated with the rotation of the center of the spherical surface
$\mathbf{Q}_S^\Delta$	rotation tensor associated with the rotation of the center of the spherical surface between configurations $i$ and $i + 1$
$r$	radius of the spherical surface
$\mathbf{r}$	orthogonality relations
$r_e$	external radius of the pipeline
$r_i$	internal radius of the pipeline

$\mathbf{r}^i$	position vector, with origin at the center of the spherical surface, that locates the pointwise contact on the spherical surface at configuration $i$
$\mathbf{r}^{i+1}$	position vector, with origin at the center of the spherical surface, that locates the pointwise contact on the spherical surface at configuration $i + 1$
$R_1$	auxiliary constant
$R_2$	auxiliary constant
$R_N$	normal reaction force
$R_T$	tangential reaction force
$s$	axial displacement that occurs at the lift-off points of the pipeline (Section 2) or curvilinear abscissa that describes positions along the pipeline length (Section 5)
$S$	center of the spherical surface
$t$	thickness of the pipeline cross section (Section 2) or time (Section 3)
$\mathbf{t}(s)$	Frenet tangential direction
$\mathbf{t}^{i+1}$	direction of the sliding at configuration $i + 1$
$\mathbf{t}_M^\Delta$	vector that represents the local change, from configuration $i$ to configuration $i + 1$ , in the material points where the contact is established on the master surface
$\mathbf{t}_S^\Delta$	vector that represents the local change, from configuration $i$ to configuration $i + 1$ , in the material points where the contact is established on the spherical surface
$T_{tw}$	true axial force in the pipeline wall
$u$	real axial displacement of the pipeline (Section 2); displacement of the point mass (Section 4)
$u'$	first derivative of the real axial displacement of the pipeline with respect to the coordinate $x$
$u''$	second derivative of the real axial displacement of the pipeline with respect to the coordinate $x$
$u_\phi$	axial displacement of the pipeline corresponding to the fully mobilized axial friction coefficient
$\mathbf{u}_S^\Delta$	vector that represents the displacements of the center of the spherical surface between configurations $i$ and $i + 1$
$u_T$	relative tangential displacement between the point mass and the rigid plane

$v$	deflection in y-direction
$\mathbf{v}$	vector of displacements
$v'$	first derivative of the deflection with respect to the coordinate $x$
$v''$	second derivative of the deflection with respect to the coordinate $x$
$v'''$	third derivative of the deflection with respect to the coordinate $x$
$v''''$	fourth derivative of the deflection with respect to the coordinate $x$
$\dot{\mathbf{v}}$	vector of velocities
$\ddot{v}$	second derivative of the deflection with respect to time
$\ddot{\mathbf{v}}$	vector of accelerations
$\hat{v}$	maximum amplitude of the buckle of the pipeline
$\hat{v}'$	maximum slope of the pipeline
$v_0$	vertical deflection of the conformal imperfection topology
$v_0'$	first derivative of the vertical deflection of the conformal imperfection topology with respect to the coordinate $x$
$v_0''$	second derivative of the vertical deflection of the conformal imperfection topology with respect to the coordinate $x$
$\hat{v}_0$	maximum vertical amplitude of the conformal imperfection topology
$v_h$	solution of the homogeneous differential equation
$v_i$	initial deflection of the pipeline laid on the prop imperfection
$v_i'$	first derivative of the initial deflection of the pipeline laid on the prop imperfection with respect to coordinate $x$
$v_i''$	second derivative of the initial deflection of the pipeline laid on the prop imperfection with respect to coordinate $x$
$\hat{v}_i$	maximum vertical amplitude of the prop imperfection topology
$v_l$	deflection at the free end of the cantilever column
$v_l'$	slope at the free end of the cantilever column
$\hat{v}_m$	mode of the structure
$v_p$	particular solution of the differential equation
$w$	pipeline self-weight per unit length
$x$	longitudinal coordinate with origin at the midspan of the buckle length of the pipeline
$x'$	longitudinal coordinate with origin at the end of the pipeline
$\mathbf{x}_A$	position vector of the vertex A of the triangular surface

$\mathbf{x}_B$	position vector of the vertex B of the triangular surface
$\mathbf{x}_C$	position vector of the vertex C of the triangular surface
$\mathbf{x}_P$	position vector of the pilot node of the oscillatory surface
$\mathbf{x}_S^i$	position vector of the center of the spherical surface at configuration i
$y$	coordinate in the direction perpendicular to the pipeline axis in the buckling plane
$\mathbf{y}_1$	vector of displacements used to transform the second order differential equations of motion into first order differential equations of motion
$\dot{\mathbf{y}}_1$	first derivative of $\mathbf{y}_1$ with respect to time
$\mathbf{y}_2$	vector equal to $\dot{\mathbf{y}}_1$
$\dot{\mathbf{y}}_2$	first derivative of $\mathbf{y}_2$ with respect to time

## CONTENTS

<b>1</b>	<b>INTRODUCTION</b> .....	28
1.1	OBJECTIVES .....	30
1.2	METHODOLOGY .....	31
1.3	STRUCTURE OF THE WORK.....	32
<b>2</b>	<b>LITERATURE REVIEW</b> .....	33
2.1	STRAINS AND STRESSES .....	33
<b>2.1.1</b>	<b>Pipe strains</b> .....	33
<b>2.1.2</b>	<b>Pipe stresses</b> .....	35
2.2	EFFECTIVE AXIAL FORCE.....	37
2.3	BUCKLING OF PIPELINES .....	39
<b>2.3.1</b>	<b>Analytical analyses</b> .....	39
2.3.1.1	Pipelines without imperfections .....	39
2.3.1.2	Pipelines with imperfections.....	54
<b>2.3.2</b>	<b>Numerical analyses</b> .....	76
<b>2.3.3</b>	<b>Contextualization of objectives and methodology</b> .....	79
<b>3</b>	<b>STABILITY OF STRUCTURES</b> .....	82
<b>4</b>	<b>CONTACT MODELS</b> .....	91
4.1	GENERAL DESCRIPTION OF THE CONTACT PROBLEM .....	91
4.2	BRIEF EXPOSITION OF THE LINES OF RESEARCH ON CONTACT MECHANICS.....	97
4.3	CONTACT MODEL USED IN NUMERICAL SIMULATIONS.....	99
<b>5</b>	<b>NUMERICAL ANALYSES</b> .....	108
5.1	GENERAL DESCRIPTION OF THE NUMERICAL SIMULATIONS .....	108
<b>5.1.1</b>	<b>Material and geometric data</b> .....	109
<b>5.1.2</b>	<b>Geometry modeling</b> .....	109
<b>5.1.3</b>	<b>Load modeling</b> .....	110
5.2	GEOMETRICALLY-SIMPLE MODELS .....	112
5.3	ADVANCED MODELS .....	125
<b>5.3.1</b>	<b>Models with imperfections imposed as concentrated forces</b> .....	126
<b>5.3.2</b>	<b>Models with imperfections represented by rigid surfaces</b> .....	133
5.3.2.1	Approaches for applying the internal pressure and influence of the imperfection amplitude in upheaval buckling.....	133

5.3.2.2	Pointwise contact versus conformal contact between the pipeline and the imperfection.....	146
5.3.2.3	Influence of the friction between the pipeline and the soil in upheaval buckling .....	152
<b>6</b>	<b>DISCUSSIONS.....</b>	<b>159</b>
<b>7</b>	<b>CONCLUSIONS.....</b>	<b>164</b>
	<b>REFERENCES .....</b>	<b>166</b>

## 1 INTRODUCTION

The production of oil and gas has increased in Brazil in the recent years. According to data from National Agency of Petroleum, Natural Gas and Biofuels<sup>1</sup> (2015), the production of oil increased from 1.65 million barrels per day in 2005 to 2.30 million barrels per day in 2014 and the production of natural gas increased from 17.10 billion cubic meters per year in 2005 to 31.90 billion cubic meters per year in 2014. Despite the high production values, the amount of existing proved reservoirs is even larger: at the end of 2014 there were 16.20 billion barrels of oil and 471.10 billion cubic meters of natural gas. Most of such reservoirs, about 95% and 85%, respectively, are in the sea and many of them in deep waters, such as the pre-salt reservoirs. These conditions require constant development of new technologies of oil and gas exploitation by industry.

In the productive chain of oil and gas, providing from onshore and offshore fields, once performed the extraction, it is necessary to transport the fluid to the distribution and refining sites. Such transportation is made predominantly by pipelines. For example, specifically in the case of subsea pipelines, according to Bai and Bai (2014), the term of subsea flowlines is used to describe subsea pipelines that transport oil and gas from the wellhead to the riser base. The riser, in its turn, is connected to the processing facilities. Finally, the transportation from there to shore is performed by export pipelines.

Since the oil and gas fields have high pressure and high temperature (HPHT), the fluids usually leave the reservoirs still keeping such thermodynamic state during the transportation. If it changes, wax and hydrate may be formed as the fluid cools along the pipeline, which is not desired. Therefore, in order to make the transportation more efficient, it is necessary that the pipelines operate at high pressure and temperature conditions. These conditions are becoming more and more severe since the oil and gas industries are advancing and discovering new reservoirs, especially in deep water regions. According to Bai and Bai (2014), there are three different levels of HPHT operation. The first level corresponds to reservoirs that have pressures up to 103 MPa and temperatures up to 177 °C. The second level, in its turn, is defined as “extreme” operations with pressures up to 138 MPa and temperatures up to 204 °C. Finally, the third level corresponds to “ultra” operations with pressures up to 207 MPa and temperatures up to 260 °C. In Brazil, the pipelines operated by Transpetro (2017), for example, are subjected to pressures not larger than 20 MPa. So, their operation can be included

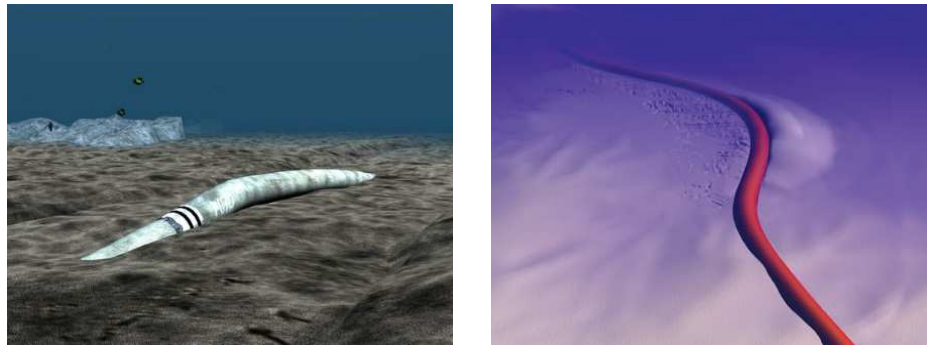
---

<sup>1</sup> Agência Nacional do Petróleo, Gás Natural e Biocombustíveis

in the first level described by Bai and Bai (2014).

Among other implications of HPHT operation in pipelines, the tendency of longitudinal expansion can be cited. In practice, the expansion movement can be restricted, both by constraints at the pipeline ends and by the soil-pipeline interaction, generating a compressive axial force that, combined, for example, with the soil imperfections and the laying deviations, can cause the buckling of the pipeline. When the compressive axial force reaches a certain critical level of magnitude, the pipeline can experience two types of buckling: upheaval buckling and lateral buckling (Figure 1). The first type, which, as its name suggests, occurs in the vertical plane, is more common in buried pipelines and the second type, which occurs in the horizontal plane, is more common in exposed pipelines, since the lateral resistance in the first type is larger than in the second type.

Figure 1 – Global buckling of pipelines.



(a) upheaval buckling

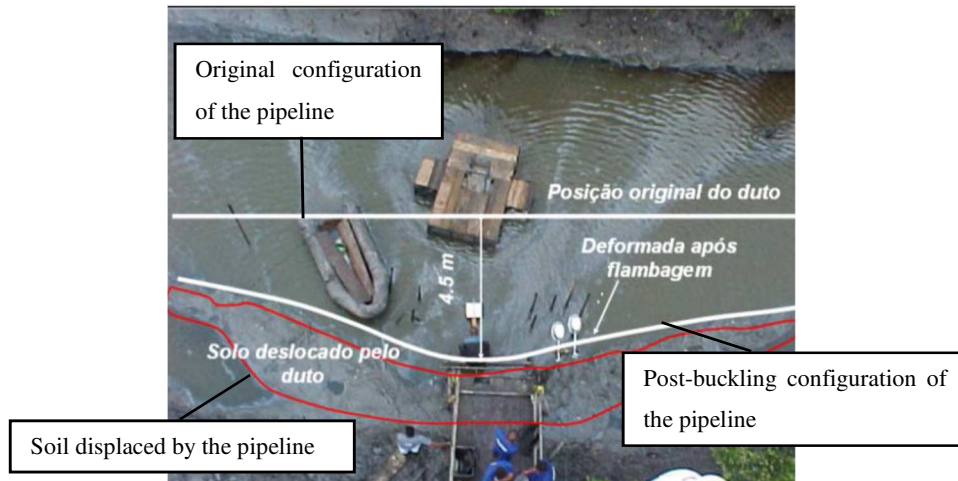
(b) lateral buckling

Source: (a) Nordnes (2015) and (b) E&P Magazine (2015).

The aforementioned two types of buckling consist in global phenomena and, by themselves, do not correspond to failure modes, but only to load responses. However, according to the recommended practice DNV-RP-F110 of Det Norske Veritas (2007), the buckling of pipelines can propitiate, due to excessive bending, the occurrence of failures like local buckling, fracture and fatigue. The local buckling occurs due to the combination of longitudinal forces, pressure and bending. It can occur by yielding of the cross section or buckling on the compressive side of the pipe. The fracture is caused by excessive tensile strains and can include brittle fracture and plastic collapse. Finally, fatigue can occur due to cyclic loads such as vortex induced vibration (VIV), pressures, thermal and hydrodynamic loads (FAN, 2013). Such failure modes may cause serious accidents since the fluid that is transported may leak and contaminate the environment. In 2000, for example, in Guanabara Bay, Brazil, the lateral buckling caused local buckling and fracture of the wall of the Petrobras' pipeline PE-II, leaking 1300 cubic

meters of oil. This accident, illustrated in Figure 2, occurred due to the increase of the operational pressure and temperature of the pipeline (CARDOSO, 2005).

Figure 2 – Accident occurred in Guanabara Bay due to the lateral buckling of Petrobras' pipeline PE-II.



Source: adapted from Cardoso (2005).

In this context, studies related to buckling of pipelines are justified, because this phenomenon may lead to structural damages that may cause accidents. Accidents have disastrous consequences for the economy, both as regards the loss of production and the reconstruction of damaged structures, and for the environment. Thus, their probability of occurrence must be minimized.

## 1.1 OBJECTIVES

The general objective of the present work is to analyze the upheaval instability of pipelines (flowlines) triggered by the internal pressure to which they are subjected during the transportation of oil and gas from wellheads, experiencing different load approaches, boundary conditions and soil imperfections.

More specifically, the objectives can be divided into two groups. The first, concerning the procedures for modelling and analyzing the buckling phenomenon, aims at verifying and discussing the equivalence between different approaches for considering the internal pressure: distributed loads dependent on pipeline curvature and equivalent compressive axial forces with follower and non-follower characteristics. It also discusses the influence of using static or dynamic analysis for such approaches. The second group of objectives,

concerning the buckling phenomenon properly speaking, aims at analyzing relatively two main parameters that can influence the buckling of pipelines regarding the critical load and the post-buckling configuration: the isolated imperfections existing on the ground on which the pipeline is laid and the soil friction coefficients.

## 1.2 METHODOLOGY

The objectives proposed for the present work will be achieved through literature review and numerical simulations. Concerning the theoretical part of this work, the topics addressed are: effective axial force, buckling of pipelines, stability of structures and contact models. The numerical simulations, in their turn, involve the development of models using finite element software for nonlinear analysis *Giraffe (Generic Interface Readily Accessible for Finite Elements)*, under continuous development at University of São Paulo. Such geometrically nonlinear finite element models allow the consideration of large displacements and finite rotations, which can be especially important for the study of the pipeline post-buckling configurations, which can, in their turn, play a fundamental role in the study of possible failure modes resulting from the buckling of pipelines. It is worth mentioning, however, that the study of such failure modes by itself is not in the scope of the present work.

In a first step, geometrically-simple pipeline models are simulated using Timoshenko beam elements, without the consideration of the contact between the pipeline and the ground. The objective of such step is to understand the phenomenon of buckling due to internal pressure for several simple cases, real or hypothetical, experiencing different boundary conditions and imperfection magnitudes. It also aims at discussing the equivalence between approaches that involve the application of the internal pressure as a distributed load dependent on pipeline curvature and as an equivalent compression with follower and non-follower characteristics, besides discussing the influence of using static or dynamic analysis for such approaches.

In a second step, more complex models are simulated, which involve, besides the pipeline itself, the ground and the contact between the pipeline and ground. Varying parameters such as imperfection amplitudes and soil friction coefficients, the objective of the models is to determine the influence of these parameters in the buckling of pipelines, discussing relatively how they modify the critical load and the post-buckling configuration of the pipeline.

For the two steps of numerical simulations, whenever possible, the results obtained numerically are compared to results obtained from existing analytical models.

### 1.3 STRUCTURE OF THE WORK

The present work is structured into seven sections.

Section 1 presents an introduction to buckling of pipelines, with the general description of the subject. It also includes the justification, the objectives and the methodology of the research.

Section 2 presents a bibliographic review about the following topics: pipe strains, pipe stresses, effective axial force and buckling of pipelines. Through this section, the work seeks, in addition to contextualizing the objectives and the methodology of the work, to provide a theoretical basis for discussions presented in later sections.

Section 3 presents some aspects of stability of structures that are important to understand the numerical simulations performed by the present work. This section presents discussions about the existing methods to analyze stability problems and when each method should be used. For that, a classification of forces that can act on a physical system is shown.

Section 4 presents general concepts about contact models, besides some lines of researches that have been developed in the area and the contact formulation used in the numerical models presented later in the work.

Section 5 describes the finite element models used to analyze the buckling of pipelines and achieve the objectives proposed by the work, as well as presents the results obtained from the numerical simulations.

Section 6 presents discussions about the results obtained from the numerical simulations, often resorting to works presented in Section 2 and Section 3 to support them.

Section 7 presents the conclusions of the work and indicates some recommendations for future researches.

## 2 LITERATURE REVIEW

This section presents an overview of buckling of pipelines. Firstly, some basic concepts about pipe strains and stresses are highlighted for a better understanding of the influence of temperature and pressure in the pipe structure. Then, the main lines of research related to buckling of pipelines are summarized in order to contextualize the objectives of the present work. Among them, including both analytical and numerical analyses, one may cite those concerning the effective axial force, those concerning the buckling description and those concerning the parameters that can influence the buckling of pipelines.

### 2.1 STRAINS AND STRESSES

#### 2.1.1 Pipe strains

As mentioned in the introduction of the present work, HPHT pipelines tend to expand longitudinally. This movement can be prevented partially or totally by the friction that arises between the pipeline and the soil and by the end restraints. According to Bai and Bai (2014), the effects of temperature, pressure and friction can be discussed in terms of strains. As assumed by Bai and Bai (2014), the present work will also assume that the material of the pipeline is elastic-linear.

The longitudinal strain  $\varepsilon_T$  induced by a temperature change  $\Delta T$ , if there is no restriction to the pipeline movement, is given by Eq. (1). The parameter  $\alpha$  is the linear thermal coefficient of the pipeline material. It is worth mentioning that positive strains and stresses are taken as being of tension.

$$\varepsilon_T = \alpha \Delta T \quad (1)$$

The longitudinal strain  $\varepsilon_P$  induced by pressure, in its turn, has two components. The first component consists in the strain  $\varepsilon_{\text{end}}$  caused by the difference of longitudinal pressures between the sides of an end cap, if it exists in the pipeline. Considering the Hooke's law, such strain can be determined through Eq. (2), in which  $p_e$  is the external pressure,  $p_i$  is the internal pressure,  $A_e$  is the external area of the pipeline cross section,  $A_i$  is the internal bore area of the pipeline cross section,  $A$  is the area of the pipeline cross section and  $E$  is the Young's modulus.

$$\varepsilon_{\text{end}} = \frac{p_i A_i - p_e A_e}{EA} \quad (2)$$

The second component  $\varepsilon_{\text{Poisson}}$  of the longitudinal strain induced by pressure results from Poisson effect and it is proportional to the hoop and radial strains. Such strain is given by Eq. (3), in which  $\nu$  is the Poisson ratio.

$$\varepsilon_{\text{Poisson}} = -\frac{2\nu}{E} \left( \frac{p_i A_i - p_e A_e}{A} \right) \quad (3)$$

It can be noted that the strain caused by the end cap effect and the strain caused by the Poisson effect are opposed and  $\varepsilon_p$  can be given by Eq. (4).

$$\varepsilon_p = \frac{(1 - 2\nu)}{E} \left( \frac{p_i A_i - p_e A_e}{A} \right) \quad (4)$$

The friction resistance developed between the pipeline and the soil consists in a passive effect, that is, it is activated only if the pipeline moves or tends to move, and tries to avoid the strains caused by temperature and pressure.

For a pipeline that is not buried and does not have longitudinal movement restriction at its ends, the strain  $\varepsilon_f$  induced by friction is given by Eq. (5), which  $\phi_A$  is the axial friction coefficient between the pipeline and the soil,  $R_N$  is the normal force of contact per unit length of pipeline and  $x'$  is the longitudinal coordinate with origin at the end of the pipeline.

$$\varepsilon_f = -\frac{\phi_A R_N x'}{EA} \quad (5)$$

If the pipeline is buried, the existing resistance to its movement is larger, since there is the action of the soil around the whole pipeline cross section. One of the ways to estimate the axial friction force per unit length  $F_b$  can be found in the recommended practice DNV-RP-F110 of Det Norske Veritas (2007) and in the guideline of American Society of Civil Engineers (2001). This force is shown in Eq. (6), which uses the following notation:  $D_e$  is external diameter of the pipeline,  $\alpha_A$  is the adhesion factor,  $C$  is the soil cohesion representative of the soil backfill,  $H$  is the buried depth of the pipeline centerline,  $\gamma_s$  is the submerged weight of soil per unit volume,  $K_0$  is the coefficient of pressure at rest and  $\delta'$  is the internal angle of

friction between the pipeline and the soil.

$$F_b = \pi D_e \alpha_A C + \pi D_e H \gamma_s (1 + K_0) \tan(\delta') / 2 \quad (6)$$

With such friction force, the strain  $\varepsilon_f$  induced by friction for buried pipelines is given by Eq. (7).

$$\varepsilon_f = -\frac{F_b x'}{EA} \quad (7)$$

Finally, the total longitudinal strain  $\varepsilon$  of the pipeline, considering the effects of temperature, pressure and friction, is given by Eq. (8).

$$\varepsilon = \varepsilon_T + \varepsilon_P + \varepsilon_f \quad (8)$$

### 2.1.2 Pipe stresses

Once the strains are partially or totally restrained in practice, axial stresses arise in the pipeline. For example, when a pipeline is completely restrained in the longitudinal direction, the stress  $\sigma_T$  induced by temperature change is given by Eq. (9). In terms of the force in the pipe wall, the temperature change  $\Delta T$  generates an axial force  $P_{0,T}$  given by Eq. (10).

$$\sigma_T = -E\alpha\Delta T \quad (9)$$

$$P_{0,T} = -EA\alpha\Delta T \quad (10)$$

Concerning the pressure effects in the pipeline, three components of stress can be generated, even without restriction to movement: hoop stress ( $\sigma_H$ ), radial stress ( $\sigma_R$ ) and longitudinal stress ( $\sigma_L$ ). Such stresses correspond to principal stresses if there are no shear stresses in directions of the cylindrical coordinate system.

For a thin-walled pipe, the radial stress is negligible and the longitudinal and hoop stresses are given by Eq. (11) and Eq. (12), respectively, in which  $t$  is the thickness of the pipeline cross section and  $D_i$  is the internal diameter of the pipeline. Two assumptions are made: there are end caps and the pipeline is free to expand. Adaptations can be made in such expressions to address other situations.

$$\sigma_{L,\text{thin}} = \frac{(p_i D_i - p_e D_e)}{4t} \quad (11)$$

$$\sigma_{H,\text{thin}} = \frac{(p_i D_i - p_e D_e)}{2t} \quad (12)$$

Finally, for a thick-walled pipe, the radial, longitudinal and hoop stresses are given by Eq. (13), Eq. (14) and Eq. (15), respectively. The assumptions made for the thin-walled pipe are still valid for the following equations and  $D$  is the diameter in which hoop stress or radial stress is calculated (YOUNG; BUDYNAS; SADEGH, 2011).

$$\sigma_{R,\text{thick}} = \frac{p_i D_i^2 - p_e D_e^2}{D_e^2 - D_i^2} - \frac{D_i^2 D_e^2}{D^2 (D_e^2 - D_i^2)} (p_i - p_e) \quad (13)$$

$$\sigma_{L,\text{thick}} = \frac{p_i D_i^2 - p_e D_e^2}{D_e^2 - D_i^2} \quad (14)$$

$$\sigma_{H,\text{thick}} = \frac{p_i D_i^2 - p_e D_e^2}{D_e^2 - D_i^2} + \frac{D_i^2 D_e^2}{D^2 (D_e^2 - D_i^2)} (p_i - p_e) \quad (15)$$

In order to verify if the pipe subjected to the previous stresses is yielding, the Von Misses criterion can be used. Through such criterion, based on the distortion-energy theory, the general form of the Von Misses stress ( $\sigma_e$ ), given by Eq. (16), has to be compared to the yielding strength of the pipe material.  $\tau_{LH}$ ,  $\tau_{LR}$  and  $\tau_{HR}$  are shear stresses.

$$\sigma_e = \sqrt{\frac{1}{2} [(\sigma_L - \sigma_H)^2 + (\sigma_H - \sigma_R)^2 + (\sigma_R - \sigma_L)^2 + 6(\tau_{LH}^2 + \tau_{LR}^2 + \tau_{HR}^2)]} \quad (16)$$

For thin-walled pipes, Eq. (16) can be simplified, since  $\sigma_R$ ,  $\tau_{LH}$  and  $\tau_{LR}$  are approximately zero. Such simplification generates Eq. (17).

$$\sigma_e = \sqrt{\sigma_L^2 + \sigma_H^2 - \sigma_L \sigma_H + 3\tau_{HR}^2} \quad (17)$$

## 2.2 EFFECTIVE AXIAL FORCE

To analyze the global buckling of pipelines (lateral and upheaval buckling), the concept of effective axial force must be introduced. The reason for such need is in the fact that the axial force governing parameter, responsible for buckling, when pressure is present, is not the integration of the longitudinal stresses, detailed in Section 2.1.2, on the pipeline cross section. The axial force resulting from such integration is important to analyze local phenomena, such as local buckling, but not global phenomena.

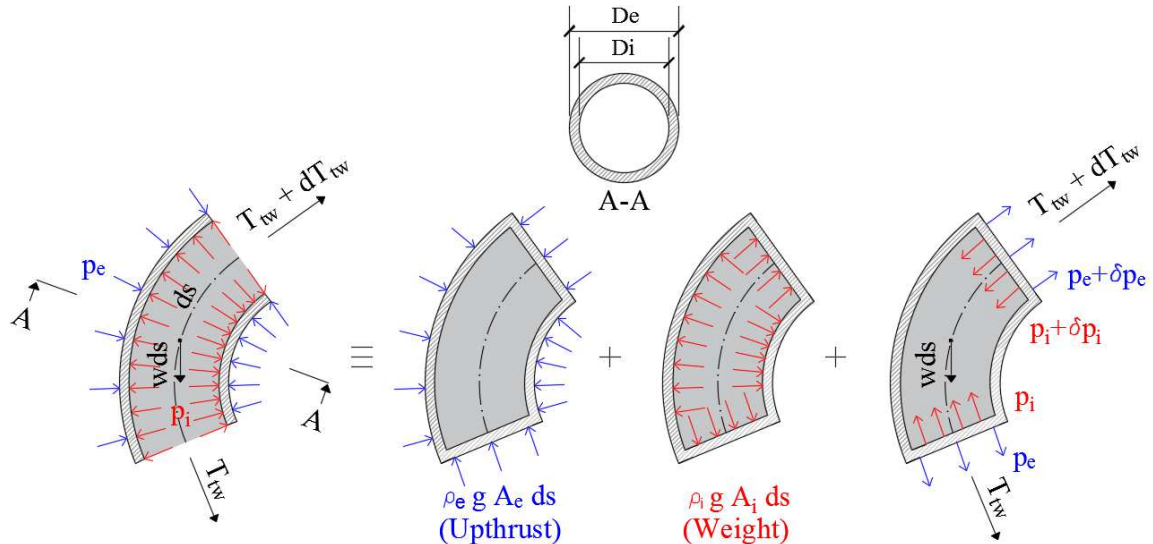
It is important to have in mind that, for a global analysis, the effects of internal and external pressures can be analyzed by their integration on the internal and external wall areas of the pipeline, respectively. However, this procedure requires a lot of algebraic work depending on pipe geometry, such as dealing with curved pipe configurations. Gay Neto, Pimenta and Martins (2017) and therein referenced works discuss the topic, proposing, by the way, a formulation to apply the pressures as equivalent distributed loads that are dependent on pipe curvature. Such formulation will be commented with more details later in the present work.

Another way for considering the pressure effects in the buckling of pipelines is analyzing an equivalent force in the pipeline axial direction related to pressure loads. This approach, although easier, has to be used with caution since its physical interpretation is non-direct. For example, pipelines without end caps and only subjected to internal pressure have the tendency of contraction in the axial direction. It happens because the existing tensile hoop stress generates, by Poisson effect, a compressive strain in the axial direction, if there is no restriction in the pipe. However, when the axial movement of the pipeline is restricted in practical situations, a tensile stress arises in the pipeline. In this way, sometimes it is difficult to understand why pipelines buckle due to internal pressure. Actually, as aforementioned, the force that governs the buckling of pipelines is not the real force given by the integration of the stresses on the cross section. This phenomenon is governed by the called effective axial force, which becomes compressive due to internal pressure. Therefore, there are other pressure effects in the pipeline axial direction besides the contribution of the Poisson effect.

Sparks (1984) is one of the main authors who deal with the effective axial force. Fyrileiv and Collberg (2005), in their turn, summarize the knowledge about the topic. For the next discussions, based on the studies of the previous authors, consider the pipe segment shown in Figure 3 and the following additional notation:  $ds$  is the pipe segment length,  $T_{tw}$  is the true axial force in the pipe wall (as a result of the integration of the stresses on the pipe cross section),  $dT_{tw}$  is an infinitesimal change of  $T_{tw}$ ,  $w$  is the pipe self-weight per unit length,  $\rho_i$  is the specific

mass of the internal fluid,  $\rho_e$  is the specific mass of the external fluid and  $g$  is the gravitational field intensity.

Figure 3 – Equivalent systems for pipelines subjected to internal and external pressures.



Source: adapted from Sparks (1984).

A pipe segment without end caps and subjected to internal and external pressures is not a closed pressure field. Therefore, the Archimedes' principle cannot be applied. To apply such principle is necessary to transform the original pipe physical system into an equivalent sum of three different pipe physical systems. The first of the three physical systems is a closed pipe on which acts the external pressure. By the Archimedes' principle, the action of the external pressure is equivalent to an upward-directed force. The magnitude of this force is the weight of the external fluid displaced by the pipe segment (buoyancy of the pipe). The second system is a closed pipe on which acts the internal pressure. The action of the internal pressure is equivalent to a downward-directed force. The magnitude of this force is the weight of the internal fluid. Finally, the last physical system is a closed pipe on which act, besides the pipe self-weight and the true axial force, pressures at the pipe ends. These pressures have the opposite signs to those applied in the first and in the second physical systems, compensating the additional terms included in those systems. Gay Neto, Pimenta and Martins (2017) discuss the three systems performing the integration of the pressures on the internal and external wall areas of the pipeline.

The effective axial force ( $P_0$ ) is the resultant axial force at the pipe segment ends, with positive values for tension and negative values for compression, given by Eq. (18).

$$P_0 = T_{tw} + p_e A_e - p_i A_i \quad (18)$$

With respect to Eq. (18), the term called true axial force  $T_{tw}$  can be composed, for example, by the contributions of the axial effect of temperature, the axial effect of soil friction and the axial effect of pressure (the Poisson effect and the end cap effect – if there are end caps in the pipe indeed). Besides this, it is worth emphasizing that the present work has the objective to analyze only the internal pressure effect as a constant value (and even without considering the internal hydrostatic pressure characterization). Thus, the term  $p_e A_e$  will be disregarded in all analyses.

## 2.3 BUCKLING OF PIPELINES

Once understood the concept of effective axial force, it is necessary to know when such force causes buckling. Studies related to this subject are presented in the following sections, which deal with analytical and numerical analyses separately.

### 2.3.1 Analytical analyses

There are analytical studies about buckling of pipelines with and without imperfections. These studies are discussed below and consider positive axial forces as being of compression.

#### 2.3.1.1 Pipelines without imperfections

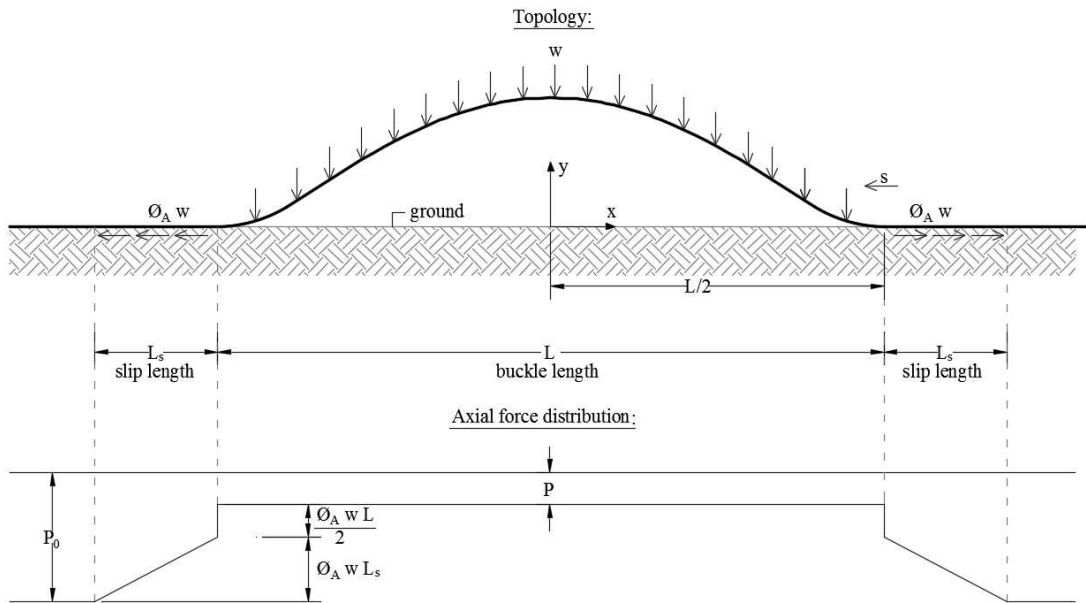
Hobbs (1984) was one of the first researchers to deal with buckling specifically in pipelines. His work involves studies about upheaval buckling and lateral buckling without imperfections.

For the upheaval buckling, Hobbs (1984) summarizes the existing method and results for railway tracks, since the same idea can be applied for pipelines. The analysis of upheaval buckling involves basically two regions: the deformed region of the pipeline (buckle region) and the slip region. For the buckle region, Hobbs (1984) assumes the pipeline as a Bernoulli-Euler beam that is subjected to an axial force  $P$  and to its self-weight and considers that the problem is elastic-linear with small slopes. Besides this, Hobbs (1984) considers that the soil is rigid and that the friction is fully mobilized. The analysis consists in solving the

differential equation for the deflected pipeline. It is assumed that the shape of the buckle is one half-wave and that the bending moment at the lift-off point is zero. Figure 4 illustrates the described model with the following notation:  $w$  is the pipeline self-weight per unit length (if the pipeline is buried, the overburden is also included);  $L$  is the buckle length;  $\phi_A$  is the axial friction coefficient between the pipeline and the soil,  $L_s$  is the length of the pipeline that slides in towards the buckle and  $s$  is the axial displacement that occurs at the lift-off point.

From the assumptions made, the pipeline deflection  $v$  in  $y$ -direction can be obtained from the solution of Eq. (19), in which  $I$  is the second moment of area of the cross section,  $v''$  is the second derivative of the deflection with respect to the coordinate  $x$  and  $M$  is the bending moment on the deflected pipeline.  $M$  can be obtained by Eq. (20) considering the parameters shown in Figure 4.

Figure 4 – Hobbs' method for upheaval buckling of pipelines without imperfections – topology and axial force distribution.



Source: adapted from Hobbs (1984).

$$M = EIv'' \quad (19)$$

$$M = -Pv - \frac{w}{8}(-L^2 + 4x^2) \quad (20)$$

Substituting Eq. (20) into Eq. (19), Eq. (21) is obtained, in which the parameters  $m$  and  $n^2$  are, respectively,  $w/EI$  and  $P/EI$ .

$$v'' + n^2v + \frac{m}{8}(-L^2 + 4x^2) = 0 \quad (21)$$

The solution of Eq. (21) is the sum of the solution  $v_h$  of the equivalent homogeneous differential equation with the particular solution  $v_p$ . The solution of the equivalent homogeneous differential equation is given by Eq. (22), in which the constants  $A_1$  and  $A_2$  still need to be determined.

$$v_h = A_1 \cos(nx) + A_2 \sin(nx) \quad (22)$$

The particular solution, in its turn, is given by Eq. (23).

$$v_p = -\frac{m}{2n^2}x^2 + \frac{m}{8n^2}L^2 + \frac{m}{n^4} \quad (23)$$

Therefore, the expression for the pipeline deflection  $v$  can be obtained by Eq. (24). The pipeline slope  $v'$ , which is the first derivative of  $v$  with respect to the coordinate  $x$ , can also be determined. Eq. (25) provides the expression for the slope.

$$v = A_1 \cos(nx) + A_2 \sin(nx) - \frac{m}{2n^2}x^2 + \frac{m}{8n^2}L^2 + \frac{m}{n^4} \quad (24)$$

$$v' = -A_1 \sin(nx) n + A_2 \cos(nx) n - \frac{m}{n^2}x \quad (25)$$

The deflection at the buckle ends and the slope at the midspan are zero. With such boundary conditions, the constants  $A_1$  and  $A_2$  can be obtained and Eq. (24) and Eq. (25) can be rewritten. Eq. (26) and Eq. (27) are the final expressions for the deflection and for the slope, respectively.

$$v = \frac{m}{n^4} \left[ -\frac{\cos(nx)}{\cos\left(n\frac{L}{2}\right)} - \frac{n^2x^2}{2} + \frac{n^2L^2}{8} + 1 \right] \quad (26)$$

$$v' = \frac{m}{n^4 \cos\left(n\frac{L}{2}\right)} n \sin(nx) - \frac{m}{n^2}x \quad (27)$$

According to Hobbs (1984), the relation between the axial force  $P$  and the buckle length  $L$  can be obtained considering that the slope at the buckle ends also should be zero (rigid soil). From such assumption,  $nL = 8.9868$  is obtained. Therefore, the relation between  $P$  and  $L$  is given by Eq. (28).

$$P = 80.76 \frac{EI}{L^2} \quad (28)$$

Since the real length of the pipeline becomes larger than  $L$  after the buckling (there is a stress relief), the axial force  $P$  at the buckle is smaller than the axial force  $P_0$  away from the buckle. Figure 4 presents the axial force distribution along the buckle: the non-uniform axial force distributions correspond to the axial force distributions at the slip regions and the discontinuities correspond to the axial forces generated by the friction that arises from the vertical reactions  $wL/2$  at the lift-off points.

The relation between  $P$  and  $P_0$  can be obtained from a compatibility equation for axial displacements. As the buckling occurs, the buckle length increases. Obviously, the buckle length differs from the pipeline arc length after the buckling, as previously mentioned. The difference between the pipeline arc length after the buckling ( $L_1$ ) and the buckle length ( $L$ ) is given by Eq. (29).

$$L_1 - L = \int_0^{L/2} (v')^2 dx \quad (29)$$

To maintain the equilibrium,  $L_1 - L$  has to be equal to the sum of the extension  $\delta$  of the pipeline generated by the axial force variation with the inward displacement  $s$  that occurs at the slip length, which is not lifted off from the ground. The axial displacement  $s$  appears when the difference between  $P_0$  and  $P$  exceeds the friction force  $\phi_A w L/2$  available at the lift-off points.

The extension of the pipeline generated by the axial force variation can be obtained by Eq. (30).

$$\delta = \frac{(P_0 - P)L}{EA} \quad (30)$$

With respect to the axial displacement that occurs at the slip length, it is

necessary to first obtain the slip length. From Figure 4, Eq. (31) and Eq. (32) can be obtained. It is worth remembering that the friction is assumed fully mobilized.

$$P_0 - \phi_A w L_s - \phi_A \frac{wL}{2} = P \quad (31)$$

$$L_s = \frac{(P_0 - P)}{\phi_A w} - 0.5L \quad (32)$$

Then, the displacement  $s$  that occurs at the slip length can be found from Eq. (33) and Eq. (34):

$$s = \frac{\phi_A w L_s L_s}{EA} \quad (33)$$

$$s = \frac{[(P_0 - P) - 0.5L\phi_A w]^2}{EA\phi_A w} \quad (34)$$

The compatibility equation for axial displacements is expressed by Eq. (35).

$$\delta + s = L_1 - L \quad (35)$$

Performing the substitutions, the relation between  $P_0$  and  $P$  is given by Eq. (36).

$$P_0 = P + \frac{wL}{EI} [0.00001597EA\phi_A w L^5 - 0.25(\phi_A EI)^2]^{1/2} \quad (36)$$

Other parameters can also be found, as the maximum amplitude of the buckle  $\hat{v}$ , the maximum bending moment  $\hat{M}$  and the maximum slope  $\hat{v}'$  ( $\leq 0,1$  for the assumption of small slopes). These parameters are shown, respectively, in Eq. (37), Eq. (38) and Eq. (39).

$$\hat{v} = 0.002408 \frac{wL^4}{EI} \quad (37)$$

$$\hat{M} = 0.06938wL^2 \quad (38)$$

$$\hat{v}' = 0.008657 \frac{wL^3}{EI} \quad (39)$$

When the coefficient of friction between the pipeline and the soil is very large, there is no slip length. Therefore, for such case, the new compatibility equation and the new relation between  $P$  and  $P_0$  are given, respectively, by Eq. (40) and Eq. (41).

$$\delta = L_1 - L \quad (40)$$

$$P_0 = P + 0.00001597 \frac{w^2 EAL^6}{(EI)^2} \quad (41)$$

As shown, the load  $P$  and the buckle length  $L$  are dependent. In the Euler's column buckling theory, since the position and the types of support are well defined, the buckle length is known. However, this fact does not happen in the case of pipelines, which are in contact with the soil. Once the buckle length is unknown, it is difficult to predict analytically the load for which the pipeline buckles. Therefore, it is common to adopt certain values for the buckle length and, then, obtain the loads  $P$  and  $P_0$ . The results can be summarized, for example, by graphs that relate the temperature rise (it can be obtained by Eq. (10) using  $P_0$ ) or the pressure variation (it can be obtained by Eq. (18) using  $P_0$ ) and the buckle length or the buckle amplitude.

To illustrate the formulation proposed by Hobbs (1984) for the upheaval buckling, an example is shown below. The data are presented in Table 1. It is important to highlight that Hobbs (1984) presents the results only in terms of temperature rise. As the present work focuses on the internal pressure effect, besides the graph of temperature rise versus buckle length (Figure 5), the graph of internal pressure versus buckle length is also presented in Figure 6, for several coefficients of friction. As the external pressure is not considered, the pressure variation is equal to the internal pressure. At this point of the work, the only concern is the presentation of the results obtained by Hobbs (1984). The best way to apply the internal pressure, as well as the verification of equivalence between the various possible load approaches, will be discussed in the numerical analyses presented later in this work.

Table 1 – Numerical example data for the analytical models.

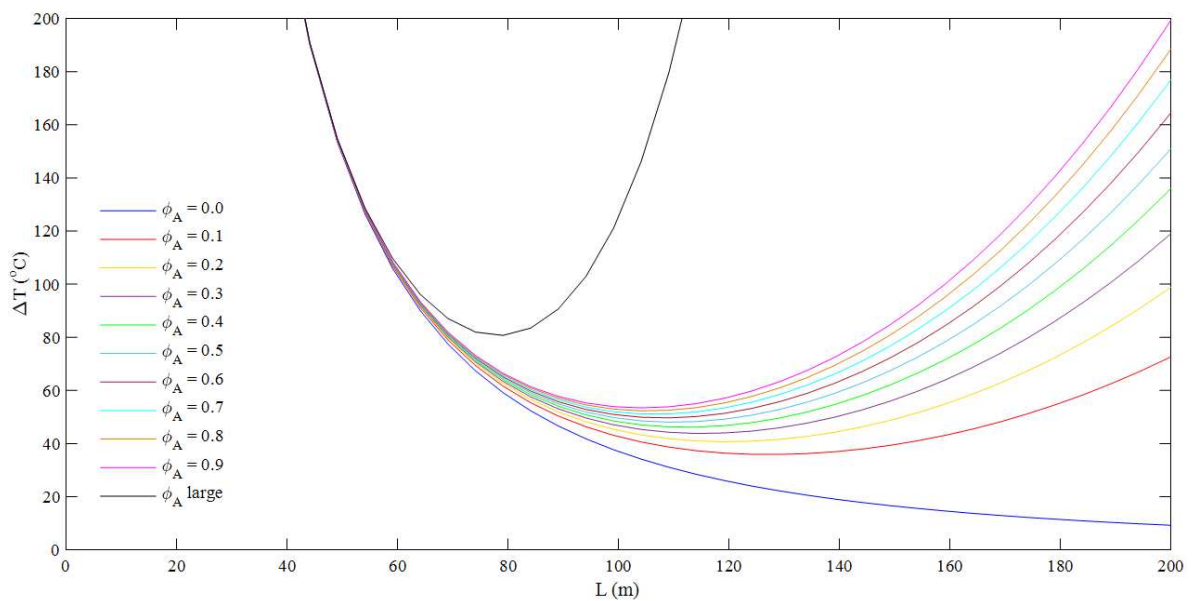
$D_e$ (m)	$t$ (m)	$A$ (m <sup>2</sup> )	$I$ (m <sup>4</sup> )	$w$ (kN/m)	$E$ (GPa)	$\alpha$ (°C <sup>-1</sup> )
0.650	0.015	0.029924	0.001509	2.349	200	0.000011

Source: prepared by the author.

From Figure 5 and Figure 6, it can be noted that the critical loads for buckling (the minimum points of the curves) are smaller when the friction coefficients are smaller than when the friction coefficients are larger, which is a result consistent with the expectations.

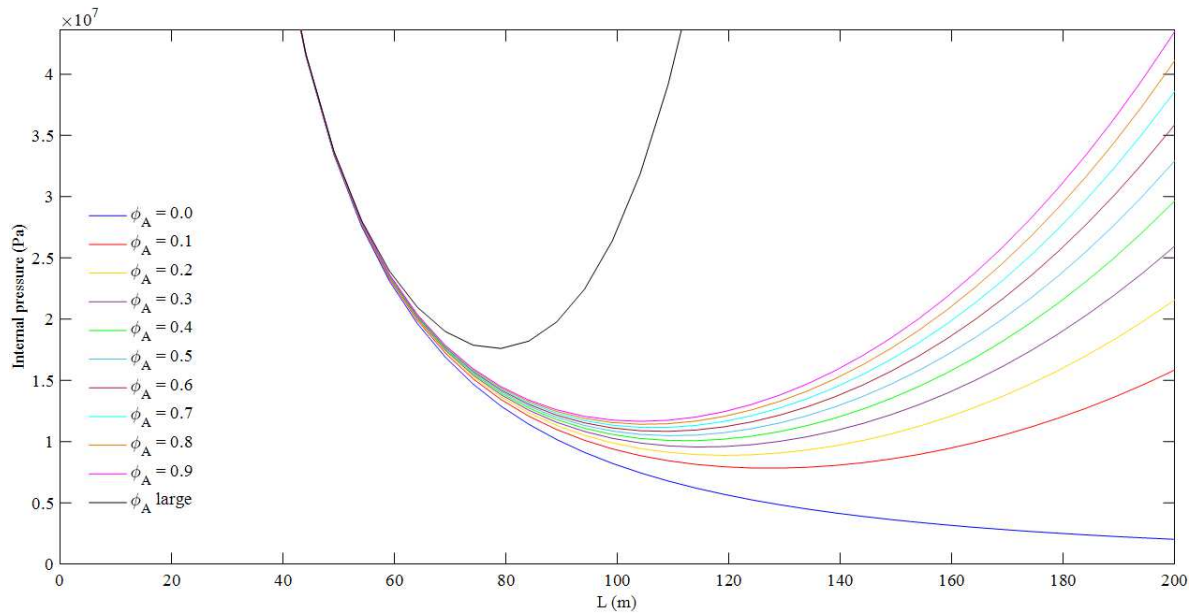
Hobbs (1984) also applies the procedure previously described for the lateral buckling and the same kind of results is obtained. The possible lateral buckling modes are represented in Figure 7. It is worth mentioning that, in the lateral buckling, the deflection  $v$  does not belong to the vertical plane, but to the horizontal plane, in which the buckling occurs. Therefore, to generalize, the present work considers that the deflection  $v$  occurs in the direction perpendicular to the pipeline axis in the buckling plane (horizontal plane for lateral buckling, for example).

Figure 5 – Hobbs' method for upheaval buckling of pipelines without imperfections – temperature rise versus buckle length.



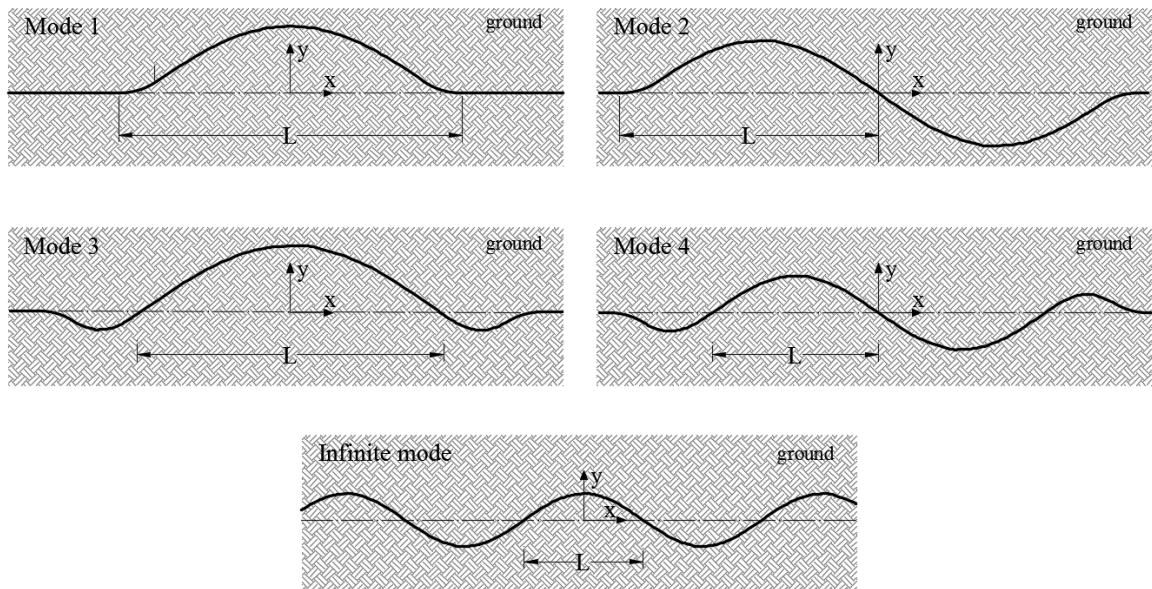
Source: prepared by the author.

Figure 6 – Hobbs’ method for upheaval buckling of pipelines without imperfections – internal pressure versus buckle length.



Source: prepared by the author.

Figure 7 – Lateral buckling modes.



Source: adapted from Hobbs (1984).

The author, to simplify the study, adopts initially a buckling mode with infinite series of half-waves to derive the expressions for lateral buckling, since the soil cannot be considered rigid in this type of buckling and the assumption of concentrated reactions at the ends of the buckle would not be true.

The analysis of the infinite buckling mode does not cause many modifications

in the differential equation that governs the buckle, Eq. (21), except that the parameter  $m$  becomes  $\phi_L w/EI$ , in which  $\phi_L$  is the lateral friction coefficient between the pipeline and the soil. Besides this, there is a modification in the boundary condition used to determine the relation between  $P$  and  $L$ . Hobbs (1984) imposes that the shear force at  $x = \pm L/2$  is equal to zero. Although this condition seems to be incoherent, the formulation proposed by Hobbs (1984) will be shown and, then, relevant discussions will be performed. From the condition,  $nL = 2\pi$  is obtained. Therefore, the relation between  $P$  and  $L$  is given by Eq. (42).

$$P = 4\pi^2 \frac{EI}{L^2} \quad (42)$$

In the infinite buckling mode, there is no slip length. Therefore, the compatibility equation is given by Eq. (40) and the relation between  $P$  and  $P_0$  can be obtained by Eq. (43).

$$P_0 = P + 0.00004705 \frac{\phi_L^2 w^2 EAL^6}{(EI)^2} \quad (43)$$

Other parameters can also be found, as the maximum amplitude of the buckle  $\hat{v}$ , the maximum bending moment  $\hat{M}$  and the maximum slope  $\hat{v}'$  ( $\leq 0,1$  for the assumption of small slopes). These parameters are shown, respectively, in Eq. (44), Eq. (45) and Eq. (46).

$$\hat{v} = 0.0044495 \frac{\phi_L w L^4}{EI} \quad (44)$$

$$\hat{M} = 0.05066 \phi_L w L^2 \quad (45)$$

$$\hat{v}' = 0.01267 \frac{\phi_L w L^3}{EI} \quad (46)$$

As commented in advance, the imposition of null shear forces at  $x = \pm L/2$  for the infinite mode seems to be incoherent, since the problem is antisymmetric. And, in fact, the points  $x = \pm L/2$  consist in points of inflection, in which the bending moments are zero, but the shear forces are not. More recently, Peek (2009) also detects such problem and proposes a formulation without the assumption of Hobbs (1984). Without going into too much details, his formulation is described below. Peek (2009) does not establish an explicit equation that relates

P and L. For the determination of the critical load  $P_0$ , the author determines L for which the ratio between  $L_1 - L$  and L is minimum. With L, Peek (2009) determines P for which  $P_0$  is minimum through expressions which provide from the compatibility condition. The author concludes that results are not much different from those obtained by Hobbs (1984). For a specific numerical example, the author shows that the critical force obtained by Hobbs (1984) is only 1.4% larger than that obtained using the new conditions. So, the boundary conditions do not seem to change the results very much.

Hobbs (1984) also summarizes the work of Kerr (1978), who addresses the lateral buckling that occurs in railway tracks using the principle of virtual displacements and the variational calculus, and Martinet (1936 *apud* HOBBS, 1984, p. 181) to detail the buckling modes 1, 2, 3 and 4. Considering that L is the half-wavelength of the most significant part of the buckle and using the constants shown in Table 2, the expressions for the lateral buckling are given by Eq. (47), Eq. (48), Eq. (49) and Eq. (50). It is worth mentioning that, for Hobbs (1984), there is no difference between lateral and axial friction coefficients. However, as some authors consider such difference in later works, the following expressions incorporate separately the lateral friction coefficient and the axial friction coefficient.

$$P = k_1 \frac{EI}{L^2} \quad (47)$$

$$P_0 = P + k_3 \phi_A w L \left\{ \left[ 1 + k_2 \frac{EA \phi_L^2 w L^5}{\phi_A (EI)^2} \right]^{0.5} - 1 \right\} \quad (48)$$

$$\hat{v} = k_4 \frac{\phi_L w L^4}{EI} \quad (49)$$

$$\hat{M} = k_5 \phi_L w L^2 \quad (50)$$

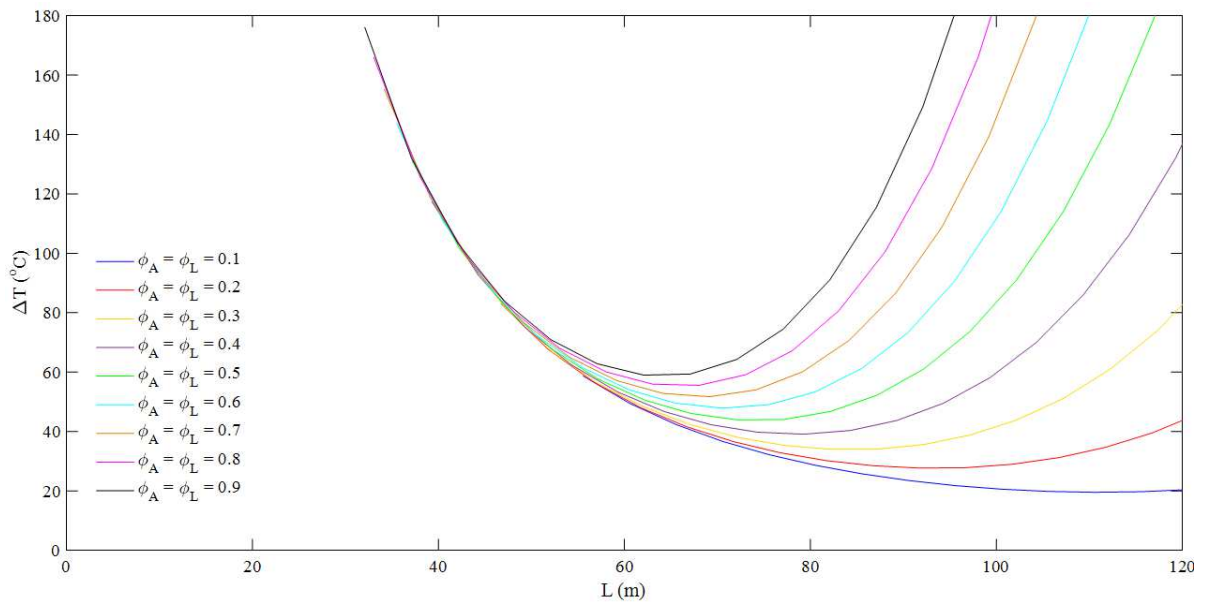
Table 2 – Constants for lateral buckling modes.

Mode	$k_1$	$k_2$	$k_3$	$k_4$	$k_5$
1	80.76	0.00006391	0.500	0.002407	0.06938
2	$4\pi^2$	0.00017430	1.000	0.005532	0.10880
3	34.06	0.00016680	1.294	0.010320	0.14340
4	28.20	0.00021440	1.608	0.010470	0.14830

Source: Hobbs (1984).

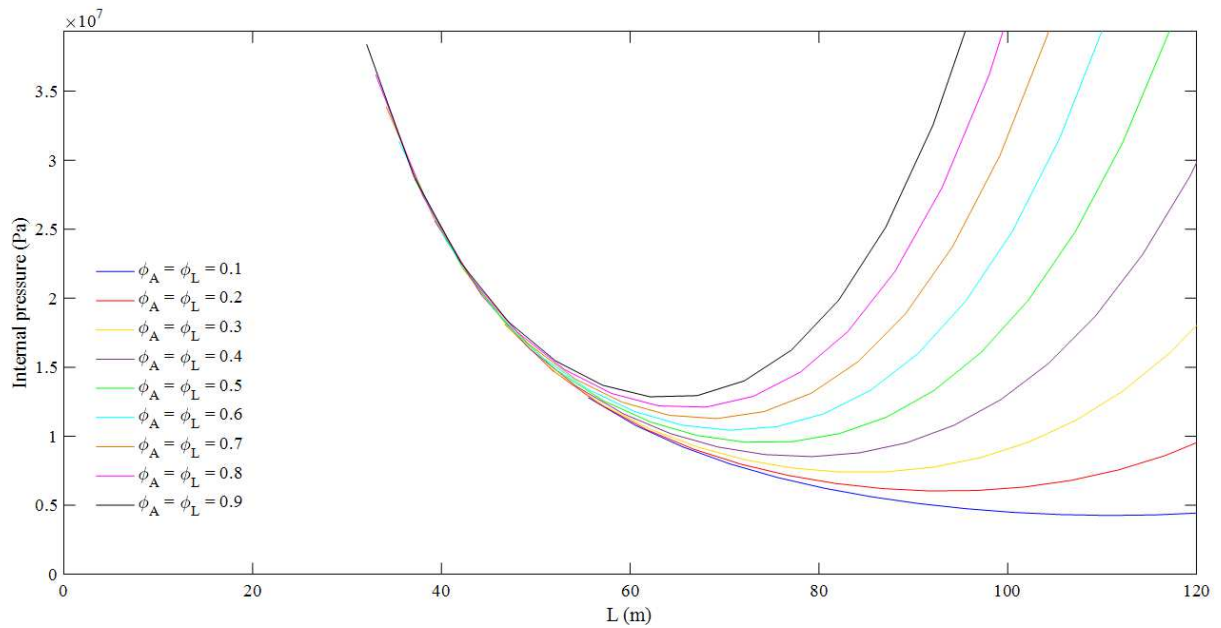
To illustrate the formulation proposed by Hobbs (1984) for the lateral buckling, an example is shown below. The data are the same as those presented in Table 1 and the graphs of temperature rise versus buckle length obtained for several coefficients of friction (lateral and axial coefficients of friction were considered equal) are shown in Figure 8, Figure 10, Figure 12, Figure 14 and Figure 16 for the five buckling modes. The graphs of internal pressure versus buckle length, in their turns, are shown in Figure 9, Figure 11, Figure 13, Figure 15 and Figure 17.

Figure 8 – Hobbs' method for lateral buckling (infinite mode) of pipelines without imperfections – temperature rise versus buckle length.



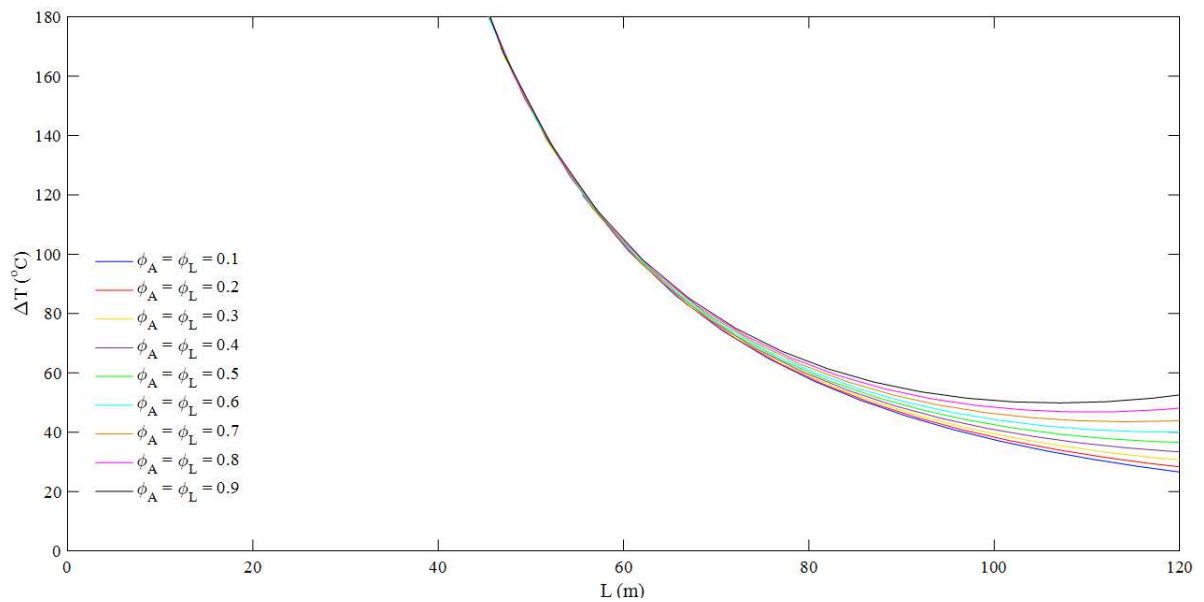
Source: prepared by the author.

Figure 9 – Hobbs’ method for lateral buckling (infinite mode) of pipelines without imperfections – internal pressure versus buckle length.



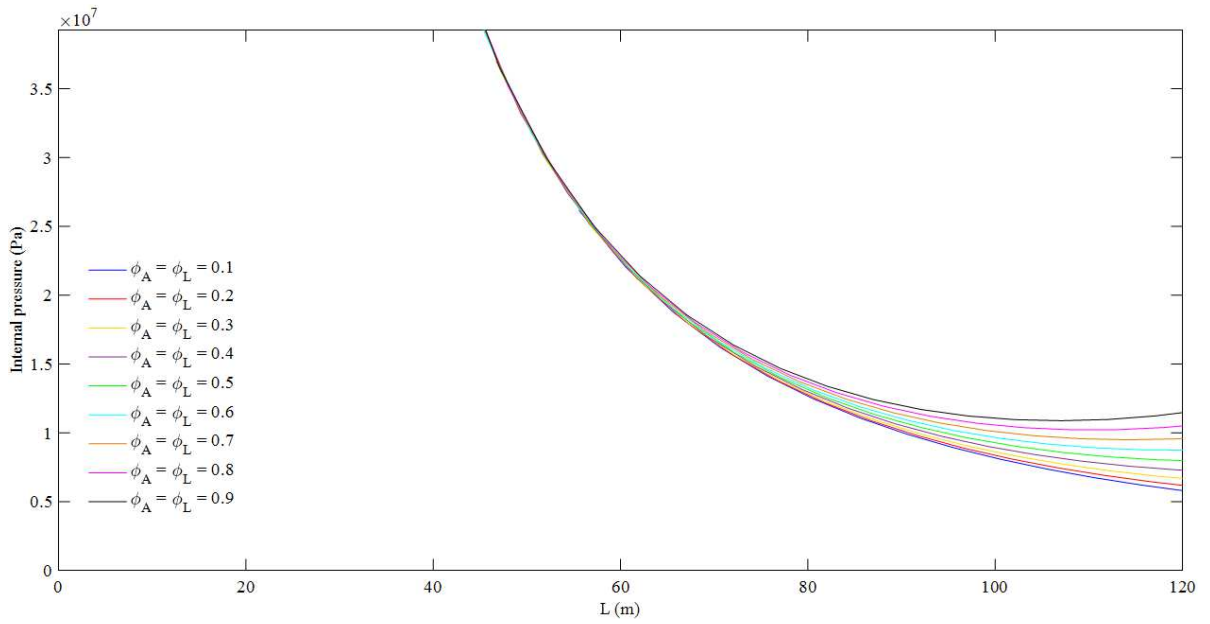
Source: prepared by the author.

Figure 10 – Hobbs’ method for lateral buckling (mode 1) of pipelines without imperfections – temperature rise versus buckle length.



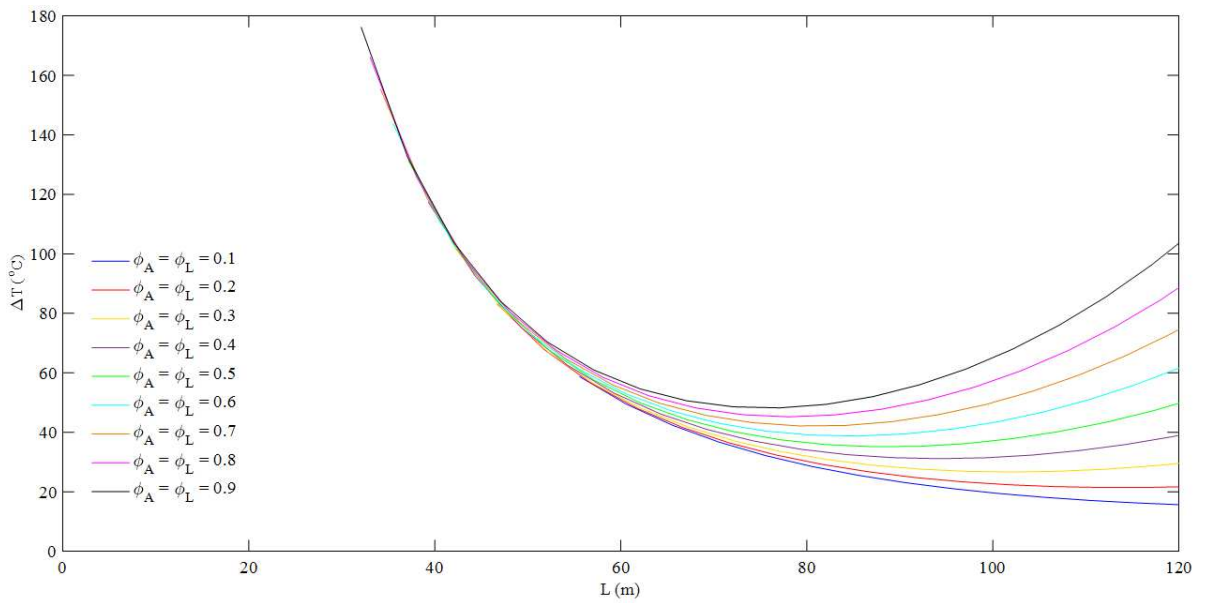
Source: prepared by the author.

Figure 11 – Hobbs’ method for lateral buckling (mode 1) of pipelines without imperfections – internal pressure versus buckle length.



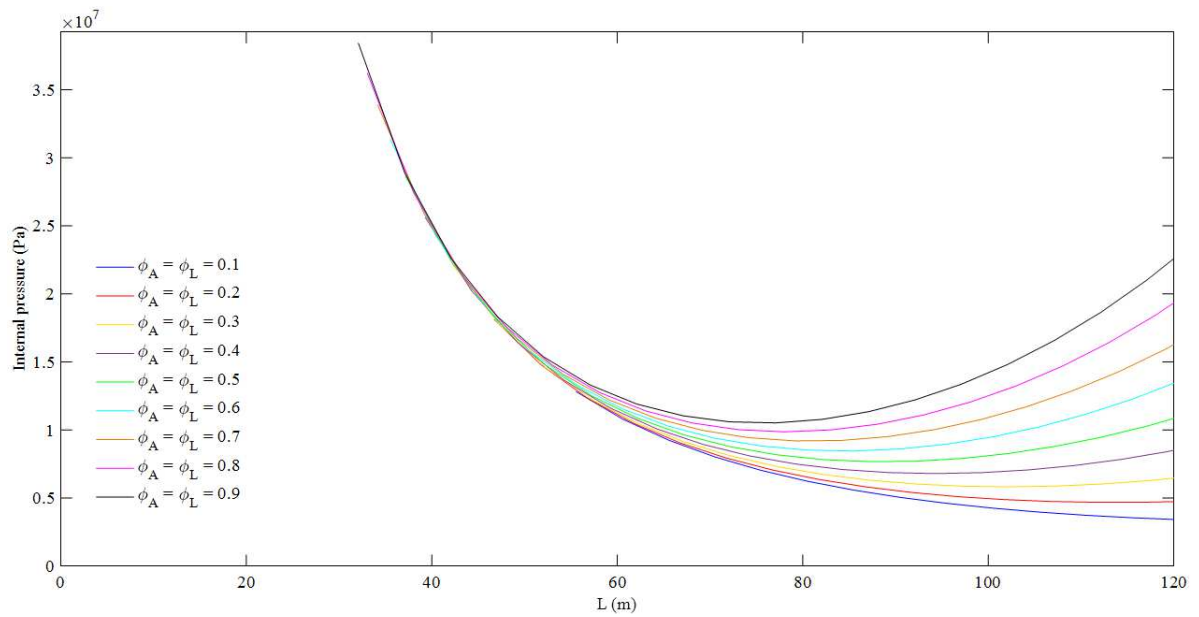
Source: prepared by the author.

Figure 12 – Hobbs’ method for lateral buckling (mode 2) of pipelines without imperfections – temperature rise versus buckle length.



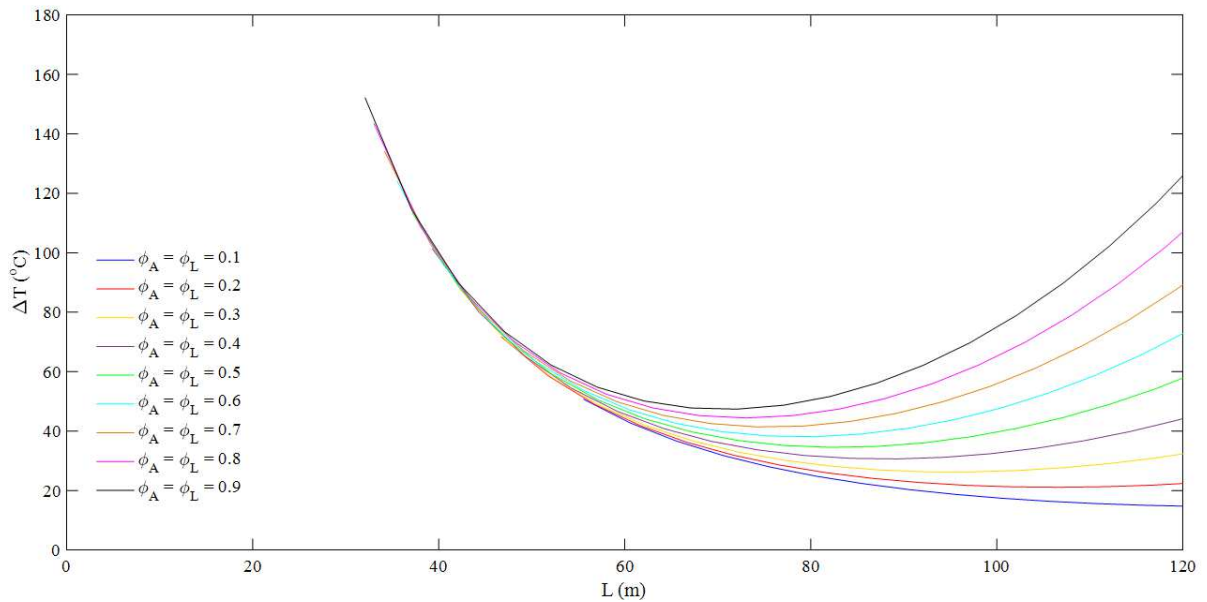
Source: prepared by the author.

Figure 13 – Hobbs' method for lateral buckling (mode 2) of pipelines without imperfections – internal pressure versus buckle length.



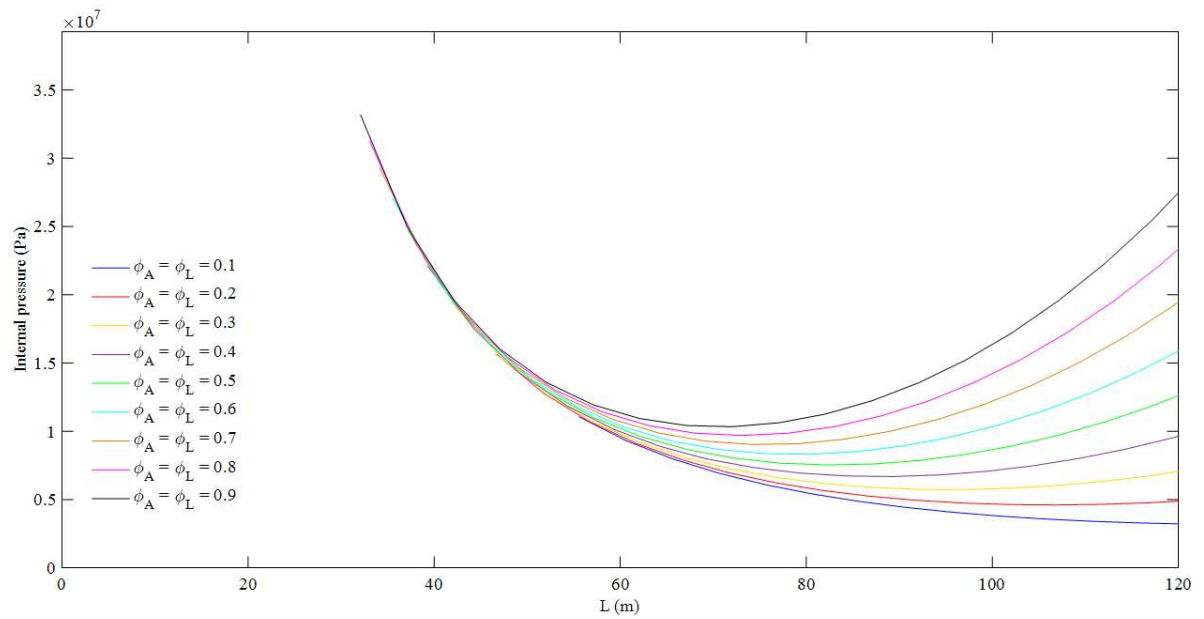
Source: prepared by the author.

Figure 14 – Hobbs' method for lateral buckling (mode 3) of pipelines without imperfections – temperature rise versus buckle length.



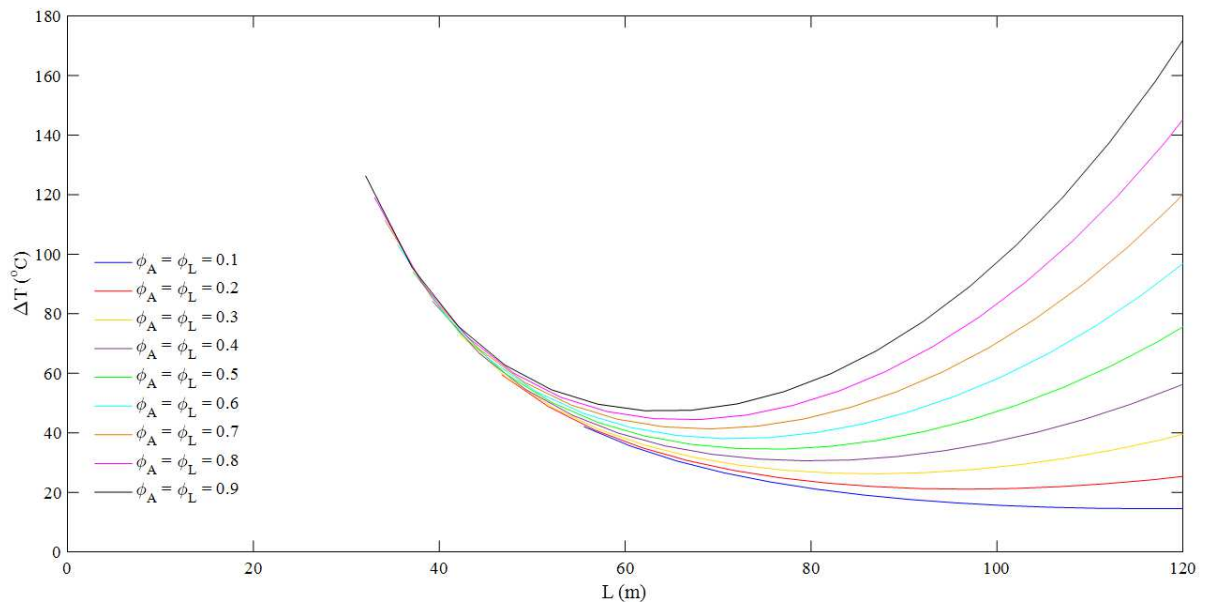
Source: prepared by the author.

Figure 15 – Hobbs' method for lateral buckling (mode 3) of pipelines without imperfections – internal pressure versus buckle length.



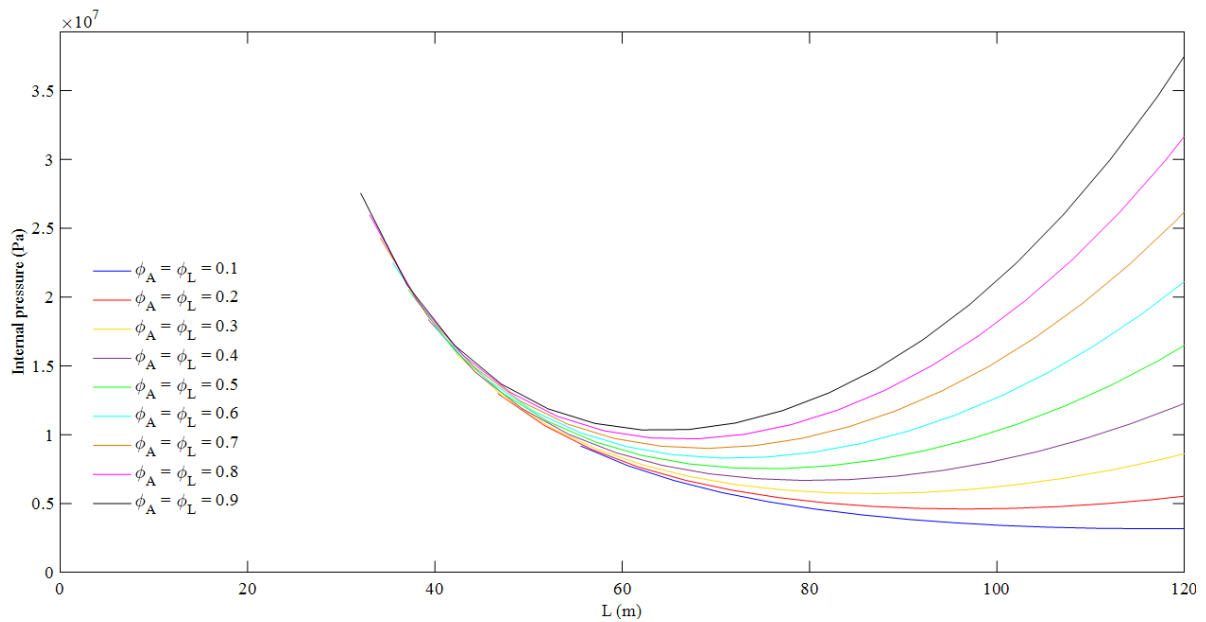
Source: prepared by the author.

Figure 16 – Hobbs' method for lateral buckling (mode 4) of pipelines without imperfections – temperature rise versus buckle length.



Source: prepared by the author.

Figure 17 – Hobbs’ method for lateral buckling (mode 4) of pipelines without imperfections – internal pressure versus buckle length.



Source: prepared by the author.

Hobbs (1984) concludes that lateral buckling occurs with smaller compressive forces than upheaval buckling. According to the author, these results are not true if the pipeline is buried, since the lateral resistance becomes larger and does not allow the pipeline to buckle in the horizontal plane. Considering that the pipeline is not buried, the axial force for which the pipeline buckles is smaller for the buckling modes 2, 3 and 4 than for the buckling modes 1 and infinite.

It is worth reinforcing that Hobbs (1984) does not consider imperfections in his models, although the author highlights its importance since perfect pipelines do not buckle and real pipelines have imperfections. These imperfections can be, for example, irregularities of the ground and initial out-of-straightness due to the laying operations.

### 2.3.1.2 Pipelines with imperfections

Considering the need for new researches in the field pointed by Hobbs (1984), Taylor and Gan (1986) perform similar analyses to the work of the previous author. They study both upheaval buckling and lateral buckling (modes 1 and 2) and assume small deflections and elastic-linear behavior of the pipe material. In their work, however, there is the consideration

of structural imperfections. Beyond the consideration of such imperfections, the authors consider a deformation-dependent axial friction, that is, the friction is not fully mobilized.

Concerning the axial friction model assumed by Taylor and Gan (1986), it is given by Eq. (51), in which  $\phi_A$  is the fully mobilized axial friction coefficient,  $u_\phi$  is the axial displacement corresponding to  $\phi_A$ ,  $u$  is the real axial displacement of the pipeline at the slip region and  $f_A$  is the axial friction parameter corresponding to  $u$ . It is worth highlighting that the convention used in the expression considers that the friction force that arises at the slip region and the displacement have the same orientation. If this convention is not used, the exponent of Eq. (51) has to become negative.

$$\frac{f_A}{\phi_A} = 1 - e^{\frac{25u}{u_\phi}} \quad (51)$$

Using the previous axial friction model, the authors study first the upheaval buckling. The same notation used to explain the work of Hobbs (1984) will be used here to present the formulation proposed by Taylor and Gan (1986). However, some new parameters have to be introduced:  $v_0$  is the vertical deflection of the conformal imperfection topology,  $\hat{v}_0$  is the maximum vertical amplitude of the conformal imperfection topology,  $L_0$  is the buckle length of the conformal imperfection topology,  $n_0$  is equal to  $\sqrt{P_{00}/EI}$  and  $P_{00}$  is the axial force at the buckle region for the initial configuration. The model is represented in Figure 18.

With Eq. (26) and Eq. (37), proposed by Hobbs (1984), Taylor and Gan (1986) obtain Eq. (52) for the pipeline deflection, which is dependent on the maximum buckle amplitude. The parameter  $K_1$  used in Eq. (52) is 15.698465.

$$v = \frac{\hat{v}}{K_1} \left[ -\frac{\cos(nx)}{\cos\left(n\frac{L}{2}\right)} - \frac{n^2x^2}{2} + \frac{n^2L^2}{8} + 1 \right] \quad (52)$$

It can be noted from Figure 18 that the pipeline is totally in contact with the imperfection in the initial configuration. It can be interpreted as a vertical deviation from the idealized lay proposed by Hobbs (1984). The authors, however, consider the problem as stress-free-when-initially-deformed. The imperfection is idealized to have the same shape of the final configuration of the pipeline, but in a smaller scale. Therefore, the shape of the imperfection



$$\begin{aligned} \Pi = & \int_0^{L_0/2} \frac{EI}{2} (v'' - v_0'')^2 dx + \int_{L_0/2}^{L/2} \frac{EI}{2} (v'' - v_0'')^2 dx + \int_0^{L_0/2} w(v - v_0) dx + \\ & \int_{L_0/2}^{L/2} w(v - v_0) dx - \int_0^{L_0/2} \frac{P}{2} [(v')^2 - (v_0')^2] dx - \int_{L_0/2}^{L/2} \frac{P}{2} [(v')^2 - (v_0')^2] dx = 0 \end{aligned} \quad (55)$$

Imposing the equilibrium state – Eq. (56), Taylor and Gan (1986) determine the relation between the axial force that acts at the buckle and the buckle length. This relation is given by Eq. (57), in which  $R_1$  is given by Eq. (58).

$$\frac{d\Pi}{d\hat{v}} = 0 \quad (56)$$

$$P = 80.76 \frac{EI}{L^2} \left[ 1 - \frac{R_1}{75.60} \left( \frac{L_0}{L} \right)^2 \right] \quad (57)$$

$$\begin{aligned} R_1 = & 4.60314 \left\{ \sin \left( 4.4934 \frac{L_0}{L} \right) + \right. \\ & \left. 2.30157 \left[ \frac{\sin \left[ 4.4934 \left( 1 + \frac{L_0}{L} \right) \right]}{\left( \frac{L}{L_0} + 1 \right)} + \frac{\sin \left[ 4.4934 \left( 1 - \frac{L_0}{L} \right) \right]}{\left( \frac{L}{L_0} - 1 \right)} \right] \right\} \end{aligned} \quad (58)$$

Once analyzed the buckle region, Taylor and Gan (1986) study the slip region to determine the relation between the axial force  $P_0$  away from the buckle and the axial force  $P$  at the buckle. The slip length field equation is given by Eq. (59). The corresponding boundary conditions are given by Eq. (60), Eq. (61) and Eq. (62).

$$EAu'' = -f_A w \quad \frac{L}{2} \leq x \leq \frac{L}{2} + L_s \quad (59)$$

$$\lim_{x \rightarrow \infty} [u, u'] = 0 \quad (60)$$

$$\frac{du}{dx}(L/2) = \frac{(P_0 - P) - \phi_A(1 - e^{\frac{25u}{u_0}})w \frac{L}{2}}{EA} \quad (61)$$

$$u(L/2) = s \quad (62)$$

Making the necessary substitutions and simplifications in Eq. (59), Eq. (63) is obtained.

$$(P_0 - P) = \left[ 2\phi_A wEA \left( \frac{e^{\frac{25s}{u_0}} - 1}{5} - s \right) \right]^{0.5} + \phi_A w \frac{L}{2} \left( 1 - e^{\frac{25s}{u_0}} \right) \quad (63)$$

The compatibility equation at the interface of the slip and buckle regions, considering the orientations indicated in Figure 18, can be expressed by Eq. (64), which yields to Eq. (65).

$$s = \frac{(P_0 - P)L}{2EA} - 0.5 \left[ \int_0^{L/2} (v')^2 dx - \int_0^{L_0/2} (v_0')^2 dx \right] \quad (64)$$

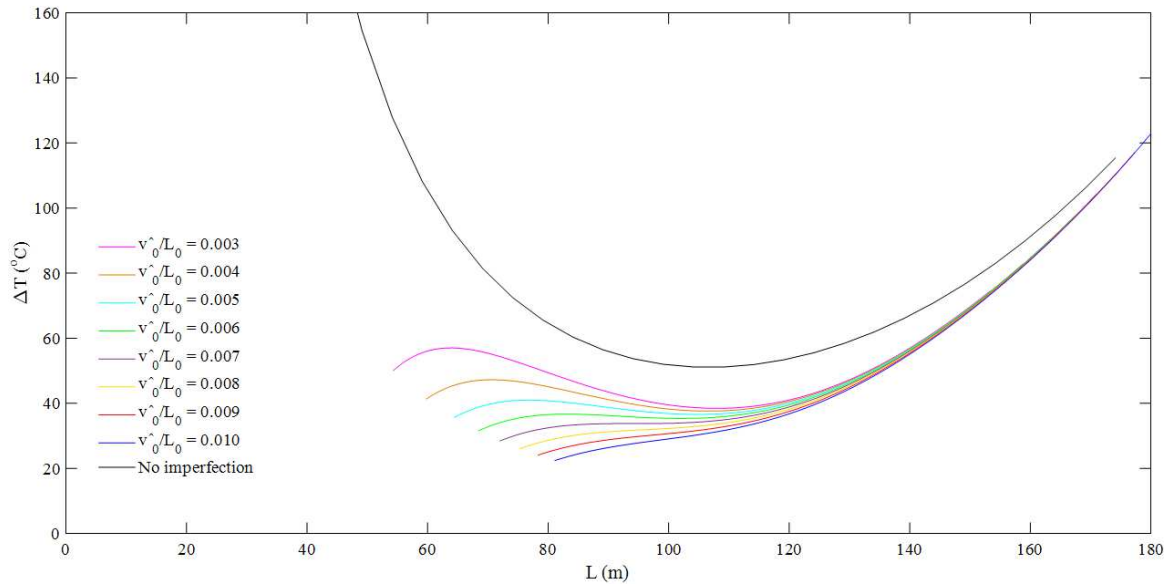
$$s = \frac{(P_0 - P)L}{2EA} - 7.9883 \cdot 10^{-6} \left( \frac{W}{EI} \right)^2 (L^7 - L_0^7) \quad (65)$$

From Eq. (64) and Eq. (65), one can see that  $P_0 - P$  depends on  $s$  and  $s$  depends on  $P_0 - P$ . To solve the problem, for a known parameter  $\hat{v}_0/L_0$  and several arbitrary values of  $L$  from  $L_0$ , it is necessary to employ a nonlinear iterative algorithm, for example, Newton-Raphson method. Using this method,  $P_0 - P$  and  $s$  can be found. Besides this, through Eq. (57),  $P$  and, consequently,  $P_0$  can be determined. As it was already reported by Hobbs (1984), the results can be summarized, for example, by graphs that relate the temperature rise or the pressure variation and the buckle length or the buckle amplitude.

Based on the data presented in Table 1, numerical results are presented below using the formulation proposed by Taylor and Gan (1986). The analyses are made with values of  $\hat{v}_0/L_0$  between 0.003 and 0.010. Besides this, the fully mobilized axial friction coefficient was adopted equal to 0.7 and the corresponding axial displacement was adopted equal to 5 mm. The results are summarized and compared to those obtained from the formulation of Hobbs

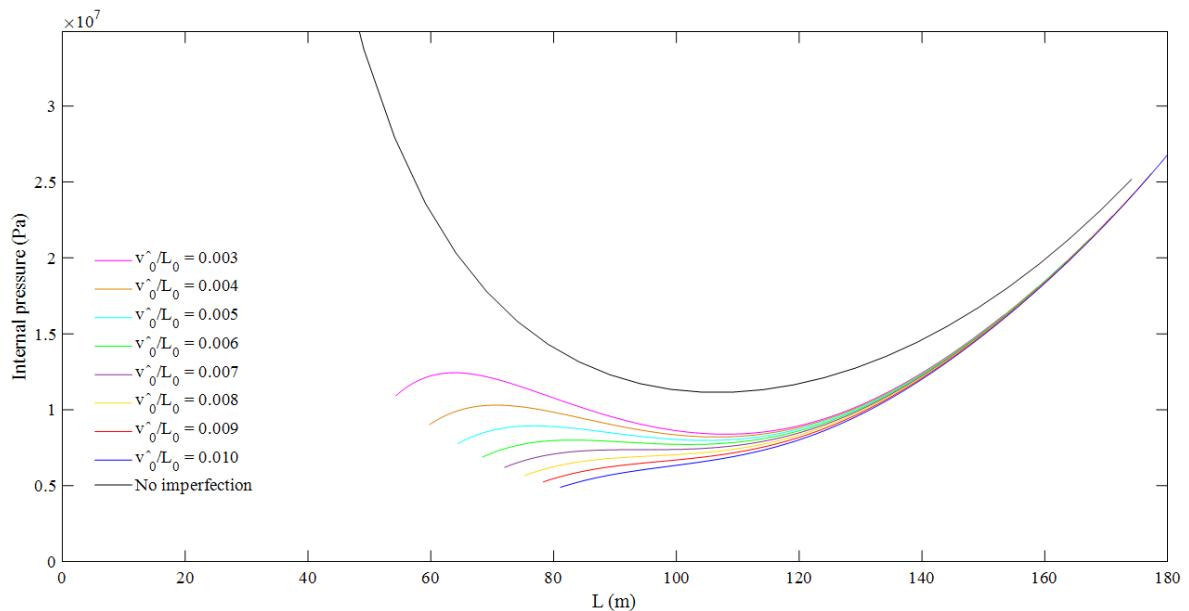
(1984) in Figure 19 and Figure 20.

Figure 19 – Taylor and Gan’s method for upheaval buckling of pipelines with conformal imperfections – temperature rise versus buckle length.



Source: prepared by the author.

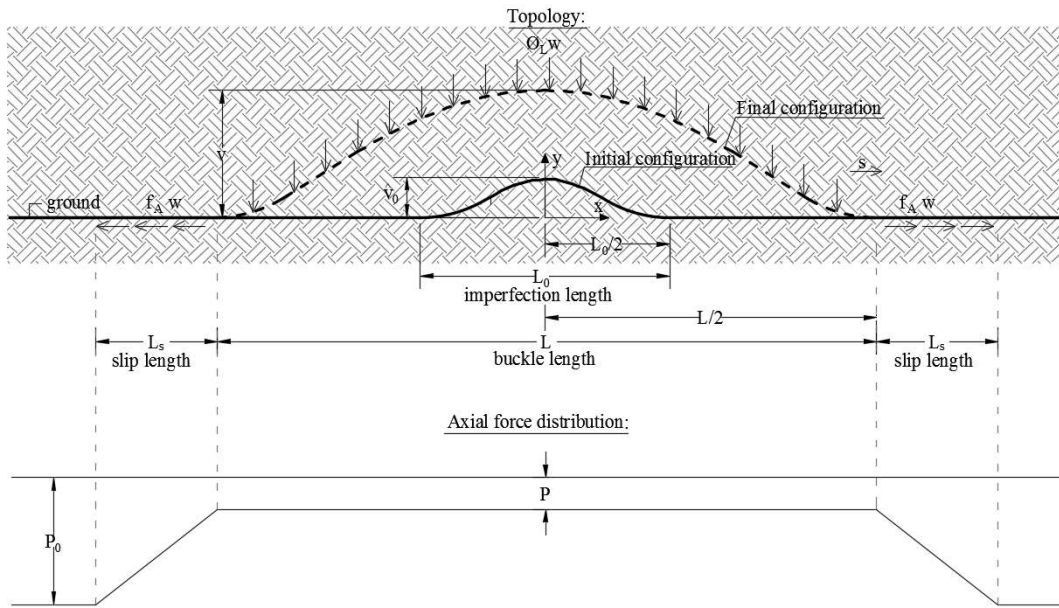
Figure 20 – Taylor and Gan’s method for upheaval buckling of pipelines with conformal imperfections – internal pressure versus buckle length.



Source: prepared by the author.

Taylor and Gan (1986) also analyze the lateral buckling. Concerning the lateral buckling mode 1, its features are represented in Figure 21.

Figure 21 – Taylor and Gan’s method for lateral buckling (mode 1) of pipelines with conformal imperfections – topology and axial force distribution.



Source: adapted from Taylor and Gan (1986).

The analysis of the buckle region can be done in the same way as it is done in upheaval buckling. The difference is in the substitution of  $w$  by  $\phi_L w$  in Eq. (54) and Eq. (55), since the lateral friction is considered fully mobilized. Therefore, Eq. (52), Eq. (53), Eq. (56), Eq. (57) and Eq. (58) remain the same. The analysis of the slip region, in its turn, requires modifications in the boundary conditions of Eq. (59). More specifically, Eq. (61) has to be modified since there are no vertical concentrated forces at the lift-off points. The new expression is given by Eq. (66).

$$\frac{du}{dx}(L/2) = \frac{(P_0 - P)}{EA} \quad (66)$$

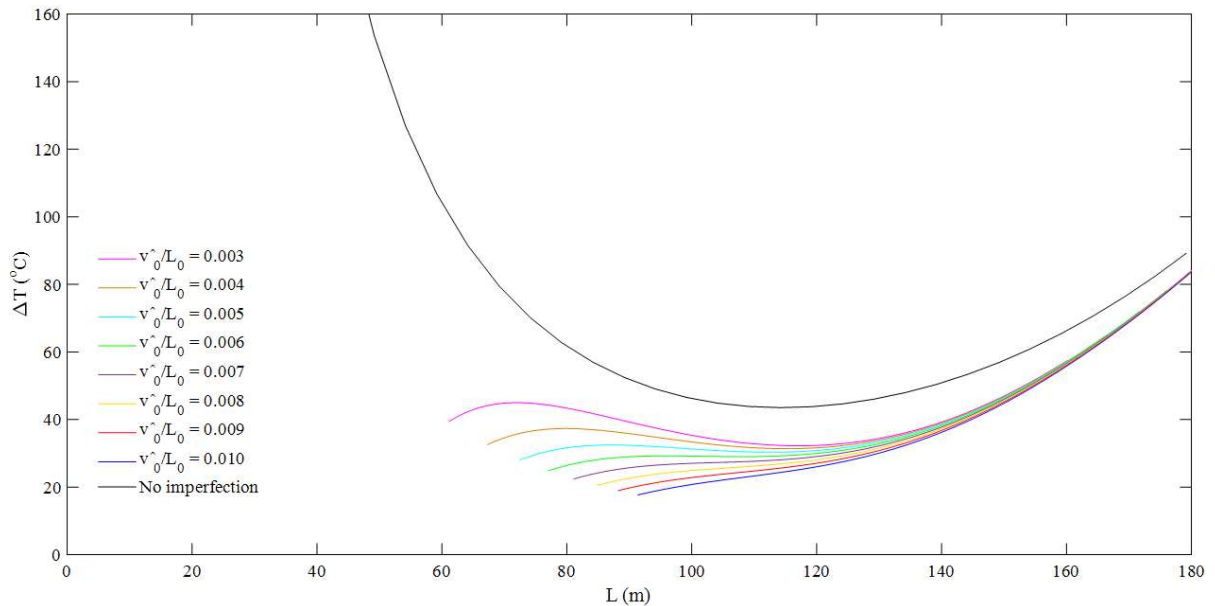
With the previous modification in the boundary condition, Eq. (63) and Eq. (65) also change. The new expressions are indicated in Eq. (67) and Eq. (68).

$$(P_0 - P) = \left[ 2\phi_A wEA \left( \frac{e^{25\frac{s}{u_0}} - 1}{5} - s \right) \right]^{0.5} \quad (67)$$

$$s = \frac{(P_0 - P)L}{2EA} - 7.9883 \cdot 10^{-6} \left( \frac{\phi_L W}{EI} \right)^2 (L^7 - L_0^7) \quad (68)$$

The same example presented for the upheaval buckling is presented below considering the formulation of the lateral buckling mode 1 proposed by Taylor and Gan (1986). The graph that relates the temperature rise and the buckle length is shown in Figure 22. The graph that relates the internal pressure and the buckle length, in its turn, is shown in Figure 23.

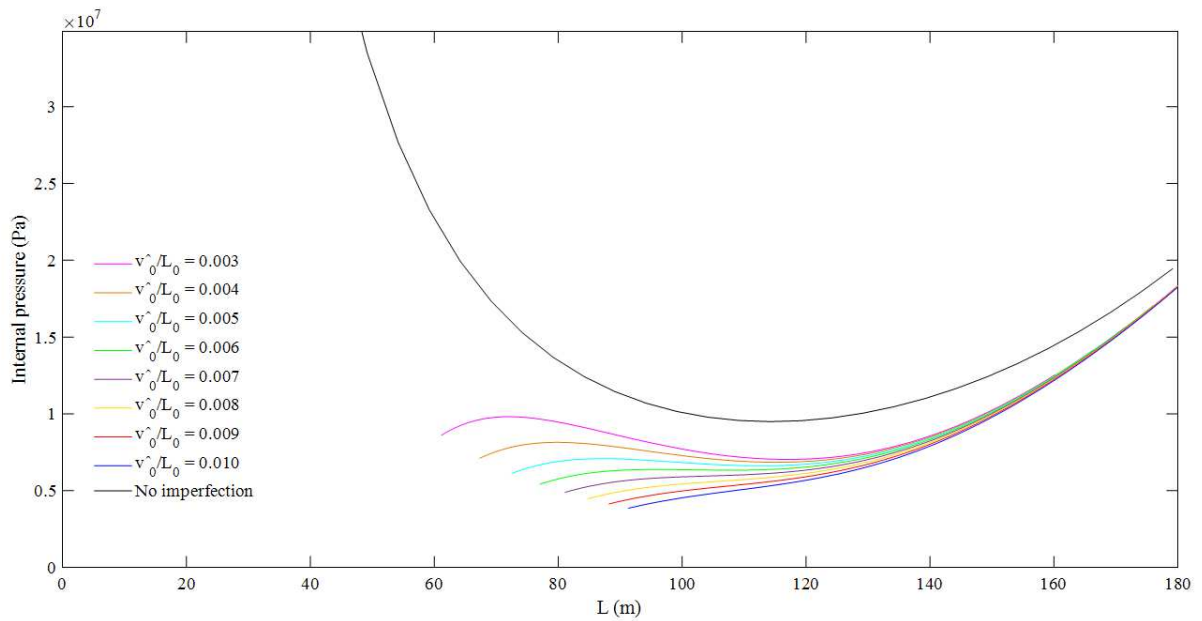
Figure 22 – Taylor and Gan’s method for lateral buckling (mode 1) of pipelines with conformal imperfections – temperature rise versus buckle length.



Source: prepared by the author.

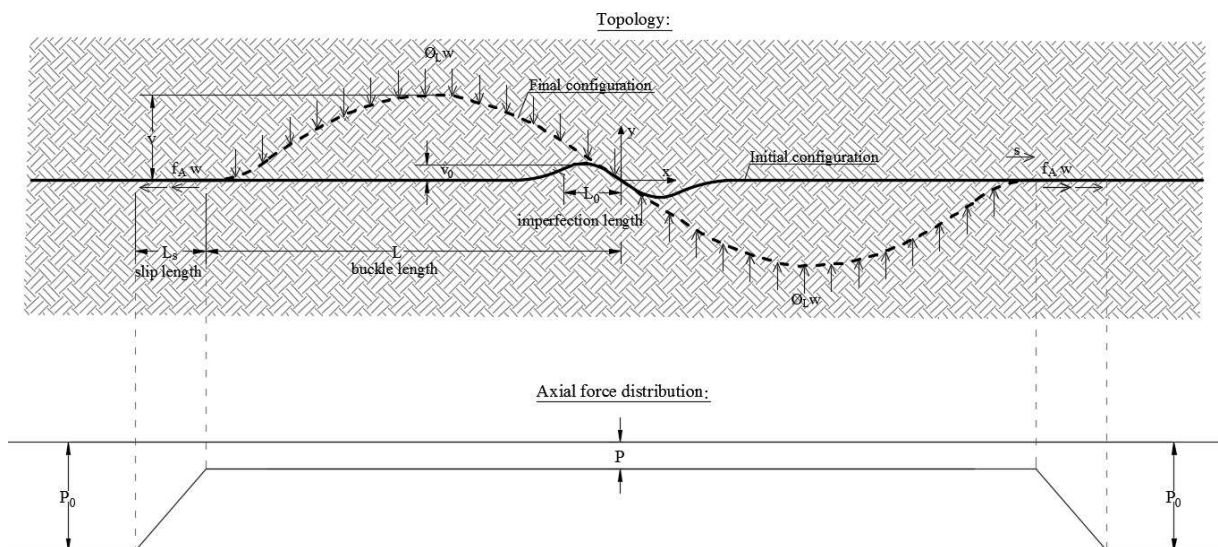
Concerning the lateral buckling mode 2, the features proposed by Taylor and Gan (1986) are represented in Figure 24.

Figure 23 – Taylor and Gan’s method for lateral buckling (mode 1) of pipelines with conformal imperfections – internal pressure versus buckle length.



Source: prepared by the author.

Figure 24 – Taylor and Gan’s method for lateral buckling (mode 2) of pipelines with conformal imperfections – topology and axial force distribution.



Source: adapted from Taylor and Gan (1986).

Since the deflection equation changes, the buckle region of the lateral buckling mode 2 is analyzed in a different way from the previous modes. For this case, the deflection equation is given by Eq. (69). The maximum buckle amplitude, in its turn, is given by Eq. (70) and it occurs at  $x = 0.3464L$ .

$$v = \frac{\phi_L w L^4}{16\pi^4 EI} \left[ 1 - \cos\left(\frac{2\pi x}{L}\right) + \pi \sin\left(\frac{2\pi x}{L}\right) + \frac{2\pi^2 x}{L} \left(1 - \frac{x}{L}\right) \right] \quad (69)$$

$$\hat{v} = 0.005532 \frac{\phi_L w L^4}{EI} \quad (70)$$

Using Eq. (69) and Eq. (70), Taylor and Gan (1986) obtain an expression for the pipeline deflection that is dependent on the maximum buckle amplitude. This expression is given by Eq. (71). The parameter  $K_2$  used in Eq. (71) is 8.6211496.

$$v = \frac{\hat{v}}{K_2} \left[ 1 - \cos\left(\frac{2\pi x}{L}\right) + \pi \sin\left(\frac{2\pi x}{L}\right) + \frac{2\pi^2 x}{L} \left(1 - \frac{x}{L}\right) \right] \quad (71)$$

As occurred in the upheaval buckling, the pipeline is totally in contact with the imperfection in the initial configuration and the shape of the imperfection can be obtained by Eq. (71) substituting the buckle parameters by the imperfection parameters. Such substitution results in Eq. (72) and Eq. (73).

$$v_0 = \frac{\hat{v}_0}{K_2} \left[ 1 - \cos\left(\frac{2\pi x}{L_0}\right) + \pi \sin\left(\frac{2\pi x}{L_0}\right) + \frac{2\pi^2 x}{L_0} \left(1 - \frac{x}{L_0}\right) \right] \quad 0 \leq x \leq L_0 \quad (72)$$

$$v_0 = 0.005532 \frac{\phi_L w L_0^4}{EI} \quad (73)$$

Concerning the total potential energy related to the final configuration, Eq. (55) can be used with  $L/2$  and  $L_0/2$  being replaced by  $L$  and  $L_0$ , respectively, since the regions under consideration for the deflected pipeline and for the imperfection are  $0 \leq x \leq L$  and  $0 \leq x \leq L_0$ , respectively. Besides this,  $w$  must be replaced by  $\phi_L w$ .

Imposing the equilibrium state – Eq. (56), Taylor and Gan (1986) also determine the relation between the axial force that acts at the buckle and the buckle length for the lateral buckling mode 2. This relation is given by Eq. (74), in which  $R_2$  is given by Eq. (75).

$$P = 4\pi^2 \frac{EI}{L^2} \left[ 1 - \frac{3}{5} \left( \frac{R_2}{3\pi + \pi^3} \right) \left( \frac{L_0}{L} \right)^2 \right] \quad (74)$$

$$R_2 = \sin\left(2\pi\frac{L_0}{L}\right) \left[ \frac{\left(\frac{L}{L_0}\right)\left(\pi^2 + \frac{L}{L_0}\right)}{1 - \left(\frac{L}{L_0}\right)^2} \right] + 2\pi\frac{L_0}{L} + \pi \left[ 1 - \cos\left(2\pi\frac{L_0}{L}\right) \right] \left(\frac{L}{L + L_0}\right) \quad (75)$$

The slip region can be analyzed in the same way as the lateral buckling mode 1 is analyzed, but the parameters  $L/2$  and  $L_0/2$  also have to be replaced by, respectively,  $L$  and  $L_0$ . Therefore, Eq. (60) and Eq. (67) remain the same and Eq. (62), Eq. (64), Eq. (65) and Eq. (66) have to be substituted by Eq. (76), Eq. (77), Eq. (78) and Eq. (79).

$$\frac{du}{dx}(L) = \frac{(P_0 - P)}{EA} \quad (76)$$

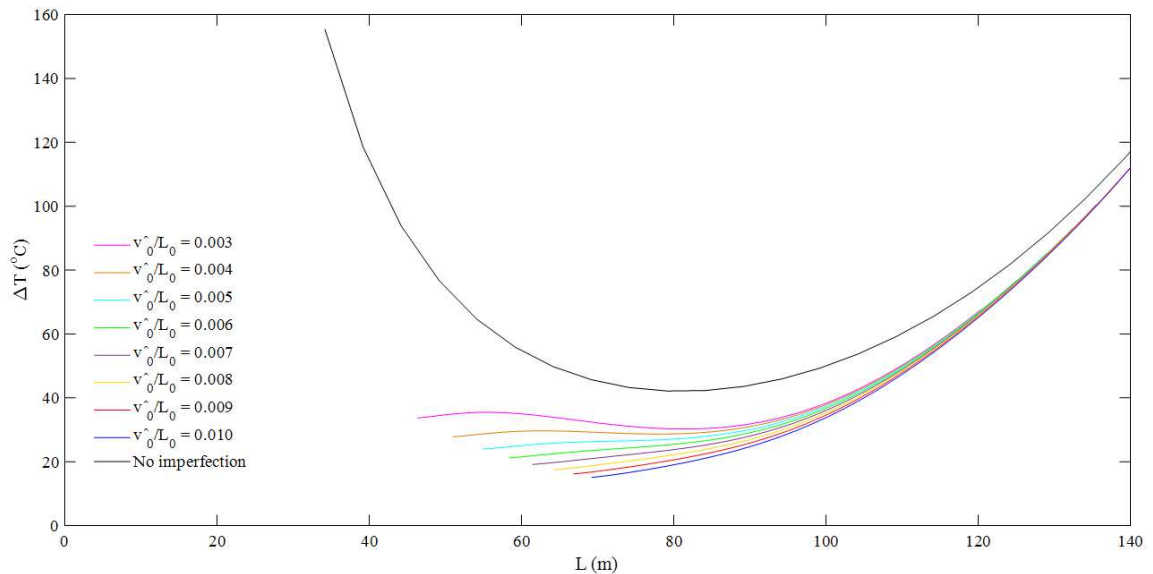
$$u(L) = s \quad (77)$$

$$s = \frac{(P_0 - P)L}{EA} - 0.5 \left[ \int_0^L (v')^2 dx - \int_0^{L_0} (v_0')^2 dx \right] \quad (78)$$

$$s = \frac{(P_0 - P)L}{EA} - 0.00008715 \left(\frac{\phi_L w}{EI}\right)^2 (L^7 - L_0^7) \quad (79)$$

The example previously performed for the upheaval buckling and for the lateral buckling mode 1 is presented below considering the formulation of the lateral buckling mode 2 proposed by Taylor and Gan (1986). The graph that relates the temperature rise and the buckle length is shown in Figure 25. The graph that relates the internal pressure and the buckle length, in its turn, is shown in Figure 26.

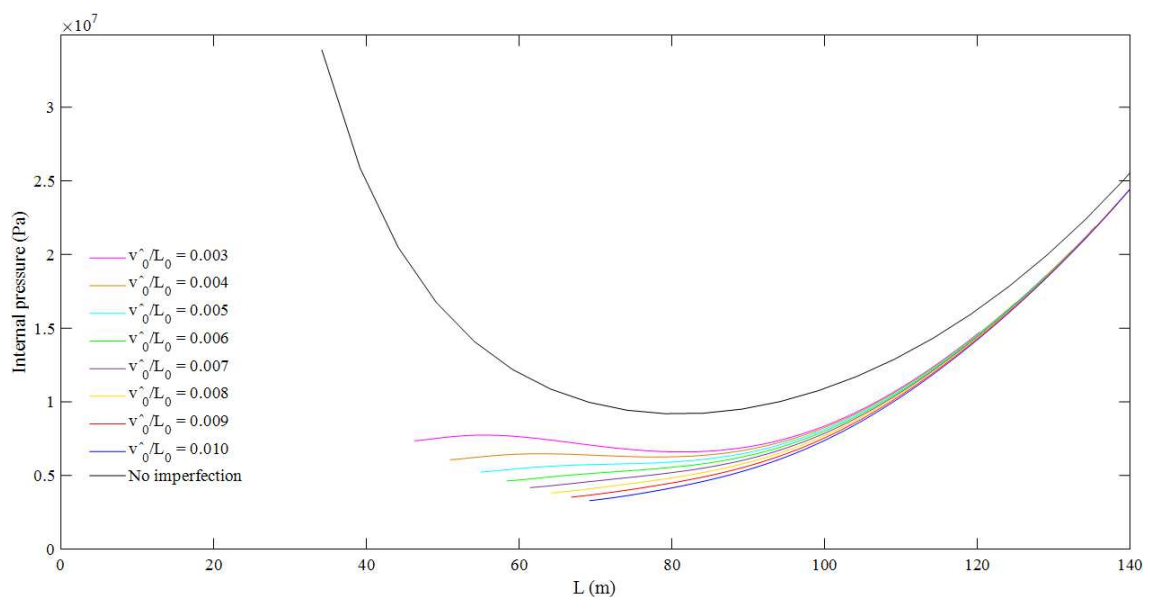
Figure 25 – Taylor and Gan’s method for lateral buckling (mode 2) of pipelines with conformal imperfections – temperature rise versus buckle length.



Source: prepared by the author.

The work of Taylor and Gan (1986) concludes that the cases with small imperfections have larger critical loads than the cases with large imperfections, but small imperfections cause abrupt displacements when the critical load is reached. In Figure 19, for example, small imperfections cause the snap-through phenomenon. As the imperfection amplitudes increase, the critical loads decrease.

Figure 26 – Taylor and Gan’s method for lateral buckling (mode 2) of pipelines with conformal imperfections – internal pressure versus buckle length.



Source: prepared by the author.

The amount of existing analytical studies related to buckling of pipelines with imperfections is quite large since the imperfections can assume many shapes. However, in general, the same kind of qualitative conclusions obtained by Taylor and Gan (1986) are obtained by other authors. In order not to make the work so extensive, only one more study is summarized in order to illustrate another mechanism of buckling of pipelines caused by a different type of imperfection. The work chosen to be discussed, Taylor and Tran (1996), is reference in the literature, being cited by many other authors. Besides this, it will be the basis of comparison for the numerical results of the present work.

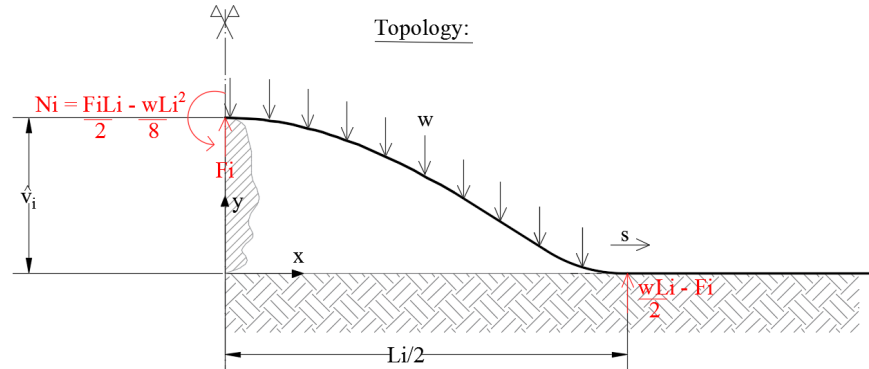
Taylor and Tran (1996) discuss imperfections focusing on the upheaval buckling. The authors divide the isolated imperfections that can occur in the vertical plane into three different types. The first imperfection is that in which the pipeline is totally in contact with the ground, as proposed by Taylor and Gan (1986). The second type, on the other hand, is an imperfection that is not totally in contact with the ground. Thus, there are voids between the pipeline and the ground. Finally, the third type consists in the second type of imperfection, but, in this case, the voids become filled by sand or other materials. The third case can be understood as a particular case of the first case. Taylor and Tran (1996) focus on the second type of imperfection, called prop imperfection, presenting a mathematical formulation that considers the following assumptions: the imperfections are symmetrical, the soil is rigid, the deflections are small, the material is elastic-linear and the friction is fully mobilized.

A prop imperfection is generated by irregularities of the ground, which can be provided from natural conditions as, for example, the presence of rocks, or from the undercrossing of nonparallel pipelines. Basically, according to Taylor and Tran (1996), the upheaval buckling in pipelines that are laid on such prop imperfections has four stages, which the authors call: datum establishment, pre-upheaval flexure, upheaval and post-upheaval buckling. Each of these stages are summarized below.

The stage called datum establishment consists in the determination of the initial configuration assumed by the pipeline after the laying operations, considering that there is a deviation from the idealized lay caused by the prop imperfection. The authors consider that such deflected configuration is stress free. In this stage, there is no axial force, since the pipeline is still empty. So, the pipeline is only subject to its self-weight and to the force of the prop imperfection, which can be understood as an existing reaction at the point where the pipeline rests on the imperfection. The topology assumed by the authors is presented in Figure 27, in which  $L_i$  is the initial buckle length of the pipeline caused by the prop imperfection,  $F_i$  is the initial shear force at the prop imperfection, which is half of the total prop force, and  $N_i$  is the

initial maximum bending moment at the prop imperfection.

Figure 27 – Taylor and Tran’s method for upheaval buckling of pipelines with prop imperfection – datum establishment topology.



Source: adapted from Taylor and Tran (1996).

The bending moment  $M_i$  on the pipeline, for the datum state, can be obtained by Eq. (80).

$$M_i = -\frac{F_i L_i}{2} + \frac{w L_i^2}{8} + F_i x - \frac{w x^2}{2} \quad (80)$$

From Eq. (19), the differential equation of the deflected pipeline is given by Eq. (81), in which  $v_i$  is the deflection of the pipeline laid on the prop imperfection and  $v_i''$  is the second derivative of  $v_i$  with respect to  $x$ .

$$v_i'' = \frac{1}{EI} \left( -\frac{F_i L_i}{2} + \frac{w L_i^2}{8} + F_i x - \frac{w x^2}{2} \right) \quad (81)$$

Considering that the deflection, the slope and the curvature are zero at the lift-off points of the pipeline and that the slope is zero at the midspan, the initial deflection of the pipeline is given by Eq. (82).

$$v_i = \frac{w}{72EI} \left[ 2L_i \left( \frac{L_i}{2} - x \right)^3 - 3 \left( \frac{L_i}{2} - x \right)^4 \right] \quad (82)$$

The relation between  $L_i$  and the maximum vertical amplitude  $\hat{v}_i$  of the prop

imperfection is given by Eq. (83). The force of the prop imperfection  $2F_i$ , in its turn, is given by Eq. (84).

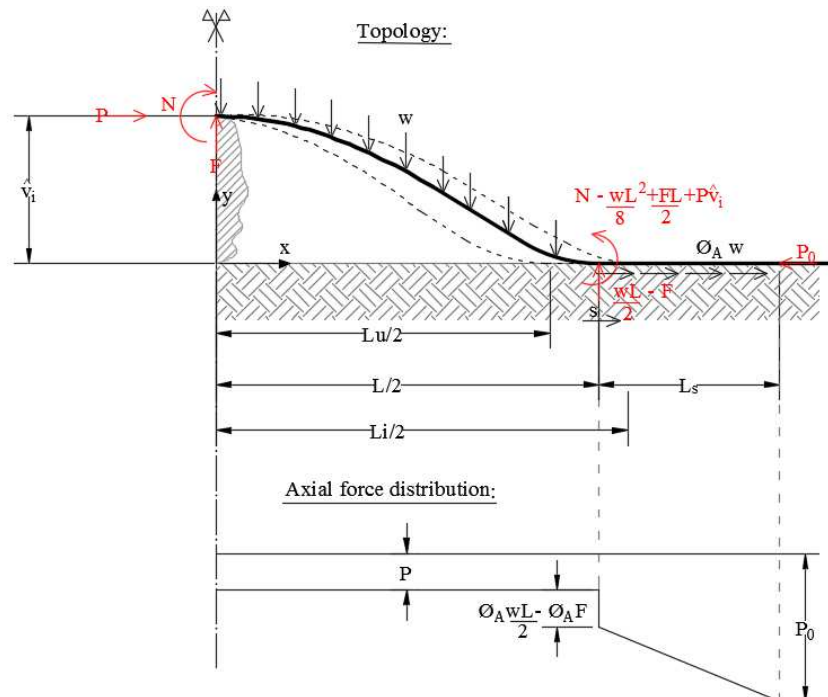
$$L_i = 5.8259 \left( \frac{\hat{v}_i EI}{w} \right)^{0.25} \tag{83}$$

$$2F_i = \frac{2w \left[ 5.8259 \left( \frac{\hat{v}_i EI}{w} \right)^{0.25} \right]}{3} \tag{84}$$

When the pipeline is filled with oil or gas, a compressive axial force  $P$  arises in the pipeline and, initially, there is a reduction of  $L_i$  as such force increases. This reduction happens until  $L_i$  reaches a specific value  $L_u$ , for which the pipeline loses its contact with the prop imperfection, that is, the prop force becomes zero. The described stage corresponds to the called pre-upheaval flexure. Figure 28 illustrates the topology and the axial force distribution of this stage, in which  $N$  is the maximum bending moment at the prop imperfection.

The relation between the bending moment  $M$  and the curvature of the deflected pipeline with prop imperfection can be obtained by Eq. (85).

Figure 28 – Taylor and Tran’s method for upheaval buckling of pipelines with prop imperfection – pre-upheaval flexure topology and axial force distribution.



Source: adapted from Taylor and Tran (1996).

$$\frac{M}{EI} = v'' - v_i'' \quad (85)$$

The boundary conditions of the Eq. (85) are given by Eq. (86) and Eq. (87).

$$v\left(\frac{L}{2}\right) = v'\left(\frac{L}{2}\right) = v''\left(\frac{L}{2}\right) = v'(0) = 0 \quad (86)$$

$$v(0) = \hat{v}_i \quad (87)$$

It can be noted that, although the curvature at the lift-off point of the deflected pipeline is required to be zero, the bending moment at this point is not zero due to the stress-free-when-initially-deformed pipeline assumption, which subtracts the product  $EIv_i''$  from the product  $EIv''$  at the lift-off point for obtaining the final bending moment. It can be understood by Eq. (88), derived from Eq. (85).

$$M\left(\frac{L}{2}\right) = EIv''\left(\frac{L}{2}\right) - EIv_i''\left(\frac{L}{2}\right) = -EIv_i''\left(\frac{L}{2}\right) \quad (88)$$

The bending moment  $M$  can be obtained by Eq. (89), in which  $F$  is the shear force at the prop imperfection.

$$M = P(\hat{v}_i - v) + N + Fx - \frac{wx^2}{2} \quad (89)$$

Performing manipulations of Eq. (85) with Eq. (82), Eq. (83), Eq. (86), Eq. (87) and Eq. (89), the relation between  $L_i/L$  and  $nL$  is obtained by Eq. (90).

$$\frac{L_i}{L} = \frac{5.8259}{nL} \left[ \frac{\left(4 - \frac{(nL)^2}{4}\right) \cos\left(\frac{nL}{2}\right) + 2nL \sin\left(\frac{nL}{2}\right) - 4 - \frac{(nL)^2}{4}}{\cos\left(\frac{nL}{2}\right) - 1} \right]^{1/4} \quad (90)$$

The deflection of the pipeline, in its turn, is given by Eq. (91), in which  $C_1$ ,  $C_2$ , and  $C_3$  are given, respectively, by Eq. (92), Eq. (93) and Eq. (94).

$$v = \frac{w}{n^4 EI} \left\{ -2 \cos \left[ n \left( \frac{L}{2} - x \right) \right] + C_1 \sin \left[ n \left( \frac{L}{2} - x \right) \right] - n^2 x^2 + C_2 n x + C_3 \right\} \quad (91)$$

$$C_1 = \frac{nL}{3} \left( \frac{L_i}{L} - 3 \right) + \frac{nF}{w} \quad (92)$$

$$C_2 = C_1 + nL \quad (93)$$

$$C_3 = \frac{(nL_i)^4}{1152} + 2 \cos \left( \frac{nL}{2} \right) - C_1 \sin \left( \frac{nL}{2} \right) \quad (94)$$

Finally, the shear force  $F$  at the prop imperfection is given by Eq. (95).

$$F = \frac{w}{n \left[ 1 - \cos \left( \frac{nL}{2} \right) \right]} \left[ 2 \sin \left( \frac{nL}{2} \right) + \left( \frac{nL_i}{3} - nL \right) \cos \left( \frac{nL}{2} \right) - \frac{nL_i}{3} \right] \quad (95)$$

The slip region also has to be analyzed to establish the relation between  $P$  and  $P_0$ . This region can be analyzed in the same way as it is done for the upheaval buckling case of the study of Taylor and Gan (1986). The difference is that Taylor and Tran (1996) do not consider a deformation-dependent axial friction. With such assumption, Eq. (63) becomes Eq. (96). Eq. (64) is still valid.

$$(P_0 - P) = [2\phi_A w EA(-s)]^{0.5} + \phi_A \left( w \frac{L}{2} - F \right) \quad (96)$$

For a specific imperfection length  $L_i$ , the solution for the pre-upheaval flexure can be obtained from the determination of the axial displacement  $s$  at the lift-off point from Eq. (64) and Eq. (96) using a nonlinear iterative algorithm for several values of  $L$  from  $L_i$  to  $L_u$ .  $L_u$  is the buckle length which occurs when  $F = 0$ . With  $s$ ,  $P_0$  can be determined.

The next stage called upheaval by Taylor and Tran (1996) corresponds to the instant when the prop force becomes zero, that is, the pipeline loses its contact with the imperfection. It can be demonstrated that such stage occurs when  $nL = 6.857667$  and  $L_i/L = 1.3421$ , if the pipeline is considered stress-free-when-initially-deformed. Therefore, the relation between  $P_u$ , the axial force at the buckle region when  $F$  becomes zero, and  $L_u$  is given

by Eq. (97). If the pipeline is not considered stress-free-when-initially-deformed, the relation between  $P_u$  and  $L_u$  is given by Eq. (98).

$$P_u = 42.027 \frac{EI}{(0.7451L_i)^2} \quad (97)$$

$$P_u = 80.76 \frac{EI}{(0.775L_i)^2} \quad (98)$$

It can be noted that, when the pipeline is considered stress-free-when-initially-deformed, the axial force necessary to cause upheaval buckling of a pipeline laid on a prop imperfection is 63% of the axial force necessary to cause upheaval buckling of an idealized pipeline, which is given by Eq. (28). So, as expected, the idealized model is not on the security side.

From the upheaval stage, with the continuous increase of the axial force  $P$  by temperature and internal pressure, the buckle length starts to increase from  $L_u$ . This movement is called post-upheaval buckling by the authors and can be subdivided into two stages. The first corresponds to the stage in which  $L < L_i$  and the second corresponds to the stage in which  $L > L_i$ . For the first case, Figure 29 illustrates the topology and the axial force distribution.

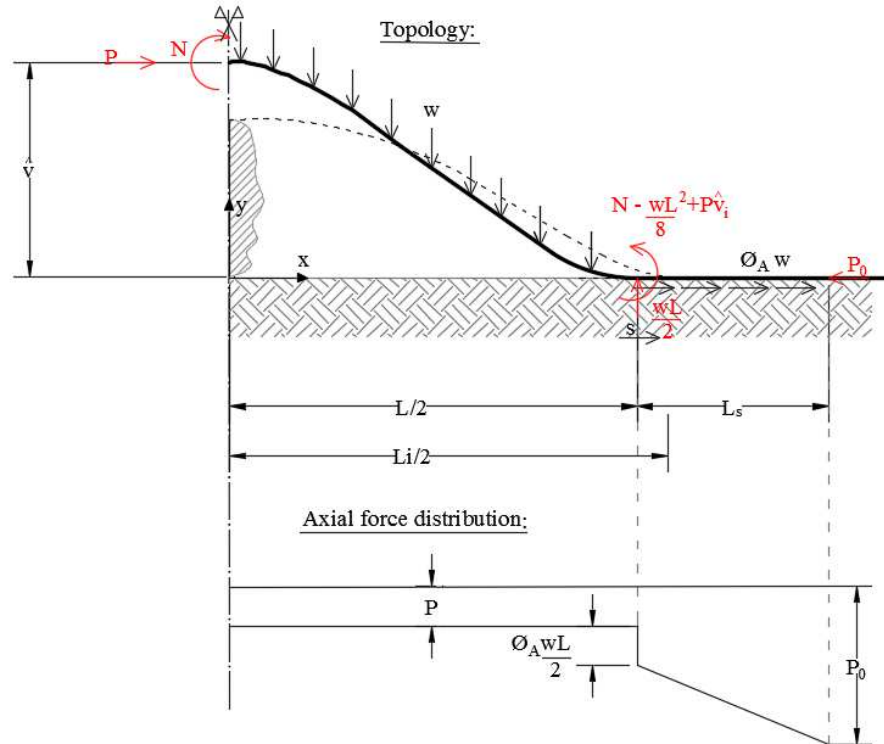
The relation between the bending moment  $M$  and the curvature of the deflected pipeline with prop imperfection can be obtained again by Eq. (85) as well as the boundary conditions of the Eq. (85) can be obtained by Eq. (86) and Eq. (99).

$$v(0) = \hat{v} \quad (99)$$

The bending moment  $M$  can be obtained by Eq. (100).

$$M = P(\hat{v} - v) + N - \frac{wx^2}{2} \quad (100)$$

Figure 29 – Taylor and Tran’s method for upheaval buckling of pipelines with prop imperfection – post-upheaval buckling ( $L < L_i$ ) topology and axial force distribution.



Source: adapted from Taylor and Tran (1996).

Performing manipulations of Eq. (85) with Eq. (86), Eq. (99) and Eq. (100), the characteristic equation is obtained by Eq. (101).

$$2\sin\left(\frac{nL}{2}\right) + \left(\frac{nL_i}{3} - nL\right)\cos\left(\frac{nL}{2}\right) - \frac{nL_i}{3} = 0 \quad (101)$$

The deflection of the pipeline, in its turn, is given by Eq. (102).

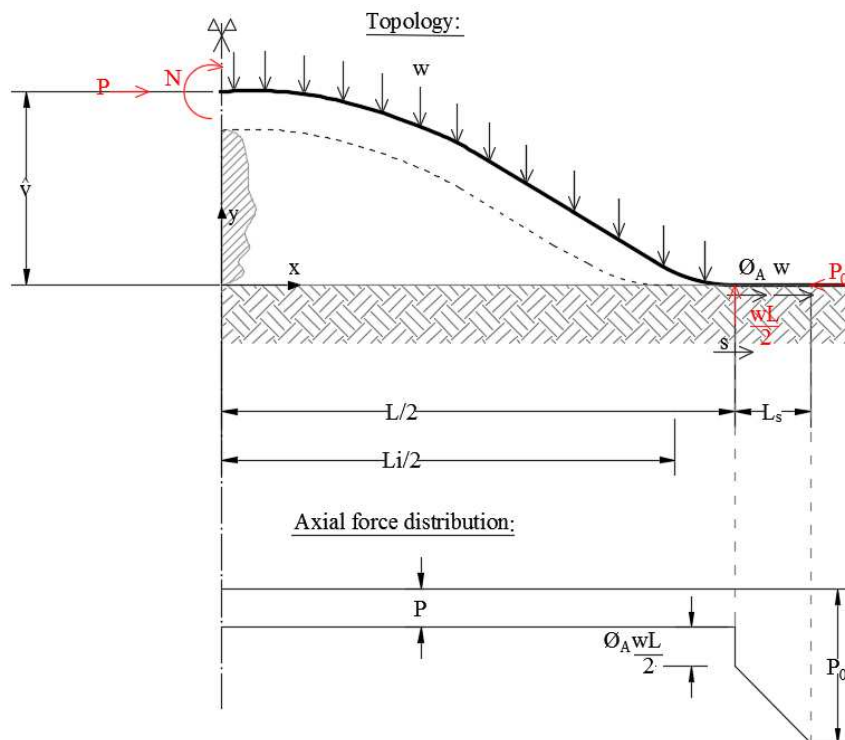
$$v = \frac{w}{n^4 EI} \left\{ -2\cos\left[n\left(\frac{L}{2} - x\right)\right] + \left(\frac{nL_i}{3} - nL\right)\sin\left[n\left(\frac{L}{2} - x\right)\right] + 2 - \frac{(nL)^2}{12} \left(2\frac{L_i}{L} - 3\right) + \frac{n^2 L_i x}{3} - n^2 x^2 \right\} \quad (102)$$

To establish the relation between  $P$  and  $P_0$ , the slip length can be analyzed in the same way as it is done for the pre-upheaval stage using  $F = 0$  in Eq. (96). Eq. (64) remains the

same. For a specific imperfection length  $L_i$ , the solution for the post-upheaval buckling stage can be obtained in the same way as it is obtained for the pre-upheaval stage using values of  $L$  from  $L_u$ .

Finally, the last stage that occurs in the upheaval buckling is the post-upheaval buckling with  $L > L_i$ . Figure 30 illustrates the topology and the axial force distribution.

Figure 30 – Taylor and Tran’s method for upheaval buckling of pipelines with prop imperfection – post-upheaval buckling ( $L > L_i$ ) topology and axial force distribution.



Source: adapted from Taylor and Tran (1996).

There are two equilibrium conditions. The first is related to the region where  $0 \leq x \leq L_i/2$ . The bending moment for such condition is given by Eq. (103) with the boundary conditions given by Eq. (104).

$$M = EI(v'' - v_i'') = P(\hat{v} - v) + N - \frac{wx^2}{2} \quad (103)$$

$$v'(0) = 0 \text{ and } v(0) = \hat{v} \quad (104)$$

The second equilibrium condition is related to the region where  $L_i/2 \leq x \leq L/2$ .

The bending moment for such condition is given by Eq.(105) with the boundary conditions given by Eq. (106).

$$M = EIv'' = P(\hat{v} - v) + N - \frac{wx^2}{2} \quad (105)$$

$$v\left(\frac{L}{2}\right) = v'\left(\frac{L}{2}\right) = v''\left(\frac{L}{2}\right) = 0 \quad (106)$$

Performing some manipulations, the previous equations provide the characteristic equation presented in Eq. (107).

$$\sin\left(\frac{nL}{2}\right) - \frac{nL}{2} \cos\left(\frac{nL}{2}\right) + \sin\left(\frac{nL_i}{2}\right) - \frac{nL_i}{6} \cos\left(\frac{nL_i}{2}\right) - \frac{nL_i}{3} = 0 \quad (107)$$

The equations of the deflected curve are given by Eq. (108) and Eq. (109), for  $0 \leq x \leq L_i/2$  and  $L_i/2 \leq x \leq L/2$ , respectively.

$$v = \frac{w}{EIn^4} \left\{ \left[ -\frac{nL}{2} \sin\left(\frac{nL}{2}\right) - \cos\left(\frac{nL}{2}\right) - \frac{nL_i}{6} \cos\left(\frac{nL_i}{2}\right) - \cos\left(\frac{nL_i}{2}\right) \right] \cos(nx) - \frac{nL_i}{3} \sin(nx) + 2 + \frac{(nL)^2}{8} - \frac{(nL_i)^2}{24} + \frac{n^2 L_i x}{3} - n^2 x^2 \right\} \quad (108)$$

$$v = \frac{w}{EIn^4} \left\{ \left[ -\frac{nL}{2} \sin\left(\frac{nL}{2}\right) - \cos\left(\frac{nL}{2}\right) \right] \cos(nx) + \left[ \frac{nL}{2} \cos\left(\frac{nL}{2}\right) - \sin\left(\frac{nL}{2}\right) \right] \sin(nx) + 1 + \frac{(nL)^2}{8} - \frac{n^2 x^2}{2} \right\} \quad (109)$$

Concerning the slip region, Eq. (64) has to be rewritten to include the regions  $0 \leq x \leq L_i/2$  and  $L_i/2 \leq x \leq L/2$  separately. Therefore, Eq. (64) becomes Eq. (110). Eq. (96) remains the same. For a specific imperfection length  $L_i$ , the solution for the post-upheaval buckling stage can be obtained in the same way as it is obtained for the pre-upheaval stage using values of  $L$  from  $L_i$ .

$$s = \frac{(P_0 - P)L}{2EA} - 0.5 \left[ \int_0^{L_i/2} (v')^2 dx + \int_{L_i/2}^{L/2} (v')^2 dx - \int_0^{L_i/2} (v_i')^2 dx \right] \quad (110)$$

According to Taylor and Tran (1996), who have also performed numerical case studies, the results are similar to existing experimental data and, as proposed by Taylor and Gan (1986), the imperfections have great influence in the critical load, making it smaller.

All previous formulations deal with symmetrical buckling. However, the existing studies are not restricted to this case. Ballet and Hobbs (1992), for example, propose a formulation for the pre-upheaval stage of buckling of pipelines laid on prop imperfections which considers that the configuration of the pipeline after the laying process is not symmetric with respect to the prop. Although the authors do not show a complete formulation, through graphs of temperature rise versus buckle amplitude for a numerical example, Ballet and Hobbs (1992) point out that the asymmetrical buckling is possible and that the critical load is smaller in the asymmetrical case than in the symmetrical case. Hunt and Blackmore (1997) also study the asymmetrical buckling dealing with an imperfection that has the shape of a step. According to the authors, this type of imperfection has a greater destabilizing effect than the prop imperfection.

As a result of various existing analytical models for buckling of pipelines with imperfection, an interesting aspect to be discussed is how the standards deal with such subject. The recommended practice DNV-RP-F110 of Det Norske Veritas (2007), for example, proposes three possible global buckling scenarios: exposed pipelines on even ground, exposed pipelines on uneven ground and buried pipelines. The first scenario does not imply that imperfections are not considered. The imperfections exist, but only in the horizontal plane, in which, by the way, the buckling occurs. In the second scenario, besides the possibility of occurrence of lateral imperfections, there are also vertical imperfections. Thus, the global deformation occurs first in the vertical plane and, then, in the horizontal plane. Finally, the third case is related to buried pipelines which can be subjected to upheaval buckling.

An important aspect is that the recommended practice does not consider the occurrence of buckling as an impediment for the design of pipelines, that is, buckling can occur as long as the integrity of the post-buckling configuration is ensured. Such integrity is verified through design criteria related to failure modes such as local buckling, fracture and fatigue. For the specific case of the recommended practice DNV-RP-F110 of Det Norske Veritas (2007), exposed pipelines are designed to buckle in a controlled manner and buried pipelines are

designed not to buckle. Besides this, as information, since the topic does not belong to the scope of the research, the recommended practice DNV-RP-F110 of Det Norske Veritas (2007) deals only with local buckling. Other failure modes can be found in the offshore standard DNV-OS-F101 of Det Norske Veritas (2013).

To verify the susceptibility of global buckling, the recommended practice DNV-RP-F110 of Det Norske Veritas (2007) establishes that for the first and the third scenarios there is the possibility of using the analytical models, as those reviewed in this work. The recommended practice also proposes some simplified procedures. However, it recommends that analytical procedures are used only at the conceptual design phase, because they have so many limitations, such as: elastic-linear material behavior, simplified axial and lateral soil-pipeline interaction, small rotation theory and imposed shape of initial and post-buckling configurations according to assumed buckling mode, that is, the critical load is related to an assumed buckling mode that may differ from the real pipeline as-laid configuration. Therefore, the finite element method (FEM) should be used to perform the analyses. It allows, among other things, to model nonlinear material behavior, to use large deflection theory and to model soil profiles more realistically. The next section describes some researches that have been carried out using numerical analyses with FEM.

### **2.3.2 Numerical analyses**

Recent studies, besides analytical analysis, propose numerical analysis. Through numerical analysis using FEM, for example, it is possible to simulate more complex and more realistic models of pipelines that could not be solved by analytical methods. As mentioned, the contact between the pipeline and the soil, for example, can be simulated using arbitrary soil profiles. Furthermore, it is possible to simulate nonlinear material properties and use large deflection theory (physical and geometrical nonlinearities, respectively).

Liu *et al.* (2014), for example, use four numerical simulation methods in finite element software ABAQUS to analyze the lateral buckling of pipelines under high temperatures. These four methods are separated into two main groups. The first group is related to 2D models. These models represent the pipeline through beam elements and the ground through a rigid flat surface. Contact elements are created between the pipeline and the ground, representing their normal and tangential contacts. The second group, in its turn, is related to 3D models. In these models, both the pipeline and the ground are represented by solid elements. The contact between the pipeline and the ground occurs in three directions and the constitutive

model for the soil is the Mohr-Coulomb model. Unlike 2D models, 3D models can simulate the penetration of the pipeline into the ground, capturing the resulting increase of lateral resistance. It is also worth mentioning that both 2D and 3D models use elastic-linear materials and that the sequence of load application is the same: first there is the introduction of the initial curved configuration of the pipeline to simulate the initial lateral imperfection, then the pipe self-weight is applied and, finally, the temperature rise is also introduced.

Each of the previous two groups are simulated using two types of analysis, totalizing the four numerical simulation methods used by the authors. The first analysis “[...] controls the stable structure displacement and addresses the static equilibrium of the unstable response segment in implicit analysis [...]” (LIU *et al.*, 2014, p. 64). The second analysis is “[...] the acceleration control method in which inertia controls acceleration and addresses the steady structure displacement in explicit analysis [...]” (LIU *et al.*, 2014, p. 64).

With the results obtained from the four simulations, such as the pipeline global buckling shapes, the buckle amplitudes and the critical temperature rise, for a specific case study, Liu *et al.* (2014) compare them to each other. Besides this, the authors compare the results of the 2D implicit model to the results obtained from the analytical model proposed by Taylor and Gan (1986). The authors conclude that there are some differences between 2D models and 3D models. According to the authors, such differences occur because the 3D models incorporate the increase of lateral resistance providing from the penetration of the pipeline into the soil. With the increase of the lateral resistance, the critical temperatures are larger and the buckle amplitudes are smaller than those that occur in 2D models. Comparing the results obtained from the implicit and explicit analyses, the results also differ. According to Liu *et al.* (2014), although the critical loads are similar, the explicit analysis considers the influence of speed in the buckling phenomenon and part of the work generated by internal forces is converted into kinetic energy. In other words, more axial stress is required to attain the same deformation amplitude as that attained by the implicit analysis. Finally, concerning the comparison between the results of the 2D implicit model and the results obtained from the analytical model proposed by Taylor and Gan (1986), some differences occur because the analytical model assumes that the final buckled configuration of the pipeline has the same shape of the imperfect initial configuration. In the numerical analysis, it can be noted that it does not happen. The resulting differences are: the buckle amplitudes are on the security side in the analytical model, but the critical temperature, contrary, is not.

It is clearly shown by the previous work that, depending on the assumptions made and on the type analysis chosen, the results may change completely. Thus, the process of

modeling in numerical analysis must be done carefully and in a consistent way with the conditions that exist in practice. In general, the representation of pipelines by means of beam elements brings significant reduction in the computational cost, when compared to shell/solid models. Besides this, depending on the type of analysis required, with more or less details, this assumption provides suitable results for the global phenomenon of buckling of pipelines, being used by many authors. For local phenomena, however, more complex models can be desirable.

Continuing in the context of the FEM, for the upheaval case proposed by Taylor and Gan (1986), for example, Liu, Wang and Yan (2013), besides analytical formulation, develop an elastoplastic analysis for buckling of pipelines using finite element software ABAQUS<sup>TM</sup>. The authors apply such methods in a practical case in China. The study is made based on temperature rises that play the role of temperature and pressure increases, jointly. The conclusions of the work are similar to those reached by other researches: the critical load depends on the imperfection amplitude. Furthermore, for the same imperfection amplitudes, the critical load is larger when the covered depth and the soil strength are larger.

The work of Zeng, Duan and Che (2014), in its turn, simulates, using ABAQUS<sup>TM</sup>, the upheaval buckling of pipelines caused by high temperature for three different groups of rigid conformal imperfections. To define the groups, the research considers parameters as the imperfection amplitude, the imperfection length and the imperfection shape. Based on comparisons between the three groups of imperfection, the authors conclude that when the ratio between the imperfection amplitude and the imperfection length increases, buckling occurs with smaller critical loads and less abruptly. The same occurs for compacted imperfections. The authors also propose approximated formulas, based on the results obtained from the numerical analyses, to determine the critical loads for the analyzed imperfections, which depend on the ratio between the imperfection amplitude and the imperfection length.

Zhang and Duan (2015) employ the FEM to study the upheaval buckling and to perform similar analysis to Zeng, Duan and Che (2014). The objective of the authors is to determine an expression for the critical load, which depends on the ratio between the imperfection amplitude and the imperfection length and on the ratio between the curvature of the imperfection and the imperfection length. Unlike the formulas proposed by Zeng, Duan and Che (2014), which are specific for each of the three imperfection groups analyzed, the formula proposed by Zhang and Duan (2015) intends to be universal. Such formula is presented in Eq. (111), in which  $\rho_{\max}$  is the maximum value of negative curvature radius of the conformal imperfection.

$$P = \left( 0.032 \frac{L_0}{\hat{v}_0} - 2.003 \frac{\rho_{\max}}{L_0} + 1.404 \right) (w^2 EI)^{\frac{1}{3}} \quad (111)$$

For achieving that, the authors simulate pipelines in software ABAQUS<sup>TM</sup> with eight different conformal imperfection types. For each imperfection type, in its turn, the authors simulate pipelines with ten different ratios between the imperfection amplitude and the imperfection length. Based on the results and using linear regression, the authors determine Eq. (111) for the critical load. Zhang and Duan (2015) concludes that, for the same ratio between the curvature of the imperfection and the imperfection length, when the ratio between the imperfection amplitude and the imperfection length increases, the critical load decreases. Besides this, for the same ratio between the imperfection amplitude and the imperfection length, when the ratio between the curvature of the imperfection and the imperfection length increases, the critical load decreases.

Besides studies about the influence of imperfections in the buckling of pipelines, there are studies that simulate practical cases of pipelines, applying both temperature and pressure loads and modeling the soil profile. In such cases, the objective is usually to know if certain pipelines are or not likely to buckle. Isaac (2013), for example, analyzes a specific case study with soil-pipeline contact and temperature and pressure loads. The objective is to know if the pipeline buckles and what is the best lay configuration that would allow controlling the buckling of the pipeline. The author concludes that the snake lay is an option to control the lateral buckling. The snake lay triggers buckles at pre-determined locations along the pipeline, controlling the global buckling. For the case study, the author determines the best number of snakes to share the expansion under thermal and pressure loads.

With the few studies discussed in the present section, it is possible to exemplify the advances provided by the use of FEM. These advances are not only restricted to a more realistic modeling of pipelines. The FEM is also a tool that helps to analyze which are the parameters, such as the imperfections, in large or small scale, that can influence the global buckling of pipelines. The tool also helps in the derivation of practical formulas that can be used by the designers.

### 2.3.3 Contextualization of objectives and methodology

As mentioned in Section 1.1, the general objective of the present work is to

analyze the upheaval instability of pipelines triggered by internal pressure. First of all, it is important to say that, given the large number of possible studies on buckling of pipelines, it was decided to study only the upheaval case. With respect to the triggering load, in its turn, an aspect that is worth to be discussed is that all works exposed previously, both those related to analytical and numerical analysis, do not analyze specifically the effects of internal pressure. Although they have comments about pressure, Hobbs (1984), Taylor and Gan (1986), Taylor and Tran (1996), Ballet and Hobbs (1992), Liu, Wang and Yan (2013), and Zeng, Duan and Che (2014), for example, analyze the critical load only in terms of critical temperature rise. Liu, Wang and Yan (2013), by the way, consider that part of the temperature rise refers to pressure. It is clear that the objective of the works is to determine the magnitude of the critical load generically, regardless of the cause of the axial force. The use of the temperature is just a way to have some kind of practical measure for the critical load. Pressure could be used, making it possible to interpret the order of magnitude of the critical loads in terms of internal pressure. Other researches, in their turn, simulate practical cases of pipelines, applying both temperature and pressure load. In such cases, the objective is usually to know if certain pipelines are or not likely to buckle. So, the focus is not on the triggering load. The work of Isaac (2013) can be cited in this context.

Works that are really concerned with the role of the internal pressure in the buckling of pipelines are few. Dvorkin and Toscano (2001), for example, analyze, using the finite difference method to determine the pressure load, the global buckling in pipelines that are subjected to internal and external pressures, besides compressive axial forces (they can be associated with temperature, for example). According to Dvorkin and Toscano (2001), imperfect pipelines have a resultant force providing from pressure loads that has a tendency to modify the pipe curvature. When internal pressure is larger than external pressure, it results in a destabilizing load pointing from the center of curvature and the critical load is smaller than the critical load in perfect pipelines. The inverse situation, in its turn, generates a stabilizing load and the critical load is larger than the critical load in perfect pipelines. Other qualitative conclusion, similar to that obtained by other authors, is that smaller imperfections cause critical loads closer to critical loads of perfect pipelines than larger imperfections.

Given the limited amount of discussion about the internal pressure in the context of buckling of pipelines, the general objective of the present work is justified. Using different approaches for considering the internal pressure, the simple and advanced numerical simulations of the present work allow to discuss the works of Sparks (1984) and Fyrileiv and Collberg (2005), which deal with the concept of effective axial force, as well as the work of

Gay Neto, Pimenta and Martins (2017), which deals with a specific formulation for applying the internal pressure as a distributed load dependent on pipe curvature. Such formulation, which constitutes an advance of the formulation proposed by Dvorkin and Toscano (2001) in the scope of finite elements, by the way, will be tested through the practical numerical simulations of the present work.

The influence of the isolated imperfections existing on the ground and of the soil friction coefficients in the buckling of pipelines is widely discussed in literature, as presented, but not using internal pressure loads. The present work, additionally, also intends to perform a relative study about the influence of these two parameters. Such study is benefited by the use of geometrically-exact 3D Timoshenko beam elements to represent the pipeline, especially with respect to the post-buckling configurations of the pipeline, since large displacements and finite rotations are possible. Contact models also contribute to enhance the numerical results. The suitable prediction of post-buckling configurations can be important, for example, to study possible failure modes resulting from the buckling of pipelines.

Through the scenario described, it is possible to infer that the objectives of the present work are valid and will contribute to the knowledge in the area.

### 3 STABILITY OF STRUCTURES

As detailed in Section 2, once determined the internal pressure or the equivalent axial force acting on the pipeline, it is necessary to know if the pipeline buckles when subjected to these loads. Moreover, if the pipe buckles, it is necessary to know what is the magnitude of its displacements after the buckling. Clearly, this scenario consists in a stability problem, because the focus is on the load for which the pipeline loses the stability of its initial configuration and tries to find another stable configuration. For this reason, some aspects of stability of structures will be presented in this section. The intention, however, is not to discuss stability of structures deeply, but to discuss simple ideas that will be the basis of comparison between analytical and numerical solutions in Section 5. Basically, the present work is concerned with critical loads and post-buckling configurations.

Before discussing the topics of structural stability that are of interest to the present work, it is appropriate to briefly present the historical development of the basic stability theory. Such historical development is presented below, being based on Thompson (1982) and Godoy (1999).

Although there are indications that, for example, the Greeks, between 400 b. C. and 200 b. C., carried out investigations on stability of structures, the first significant theoretical studies in the area began to arise only in the seventeenth century. In 1686, Isaac Newton (1642-1727) detailed experimental studies of the motions of a simple pendulum in both air and water. This system, with damped oscillations, is an example of an asymptotically stable system. James Bernoulli (1654-1705) and Daniel Bernoulli (1700-1782), in their turn, may have induced Leonard Euler (1707-1783) to study structural stability. This is because, James Bernoulli studied the deflection of an elastic rod in bending, concluding that its resistance was provided by the extension and the contraction of the longitudinal fibers and that there was a relationship between the bending moment and the curvature of the deflected rod. Although James Bernoulli and Daniel Bernoulli did not work with stability, the last one suggested to Leonard Euler to develop the differential equation of the rod. And it was in this process that, in addition to obtaining such differential equation, Leonard Euler, in 1744, with the aid of the variational calculus, determined the equilibrium configurations of a compressed elastic column. The study of Leonard Euler is considered the first to deal with a bifurcation problem. However, his study did not have practical application for a century, because stability was not a problem for the rock and timber structures built at that time. Lagrange (1736-1813) also addressed stability of structures, developing the analytical energy approach to mechanics, which generated the

fundamental energy theorem that proposes that a minimum of the total potential energy is a sufficient condition for stability. The general bifurcation theory arose, then, in the nineteenth century, being developed by Henri Poincaré (1854-1912), who also created the global qualitative dynamics in which there is also much of stability theory. Lyapunov (1857-1918), in his turn, presented, in 1892, a rigorous mathematical definition for stability, besides introducing his generalized energy functions.

According to Thompson (1982), with the advance of science and applied mechanics, the original classical development of stability has been fragmented and diversified, not being restricted to elastic stability theory. The most recent researches in the area use, among others, theoretical, experimental, computational and behavioral approaches to study, for example, both critical loads and post-buckling configurations. The subject is quite broad, but as already commented, the present work will not present it deeply, since only some basic aspects of elastic stability will be necessary herein. Once contextualized the stability of structures, such basic aspects will be useful to understand the discussions proposed in Section 5.

Based on the general concept of stability, a nonperturbed solution of a structure (equilibrium or movement) is stable if the distances between it and perturbed solutions remain within the established limits for all time and perturbation. Many stability definitions come from such concept and may be used to quantify the stability. Although this concept is in a dynamic context, the existing methods for analyzing stability problems are not restricted to dynamic methods. Ziegler (1968), for instance, discusses four methods to deal with such problems. The first method is called imperfection method and consists in analyzing the behavior of imperfect structures. The main idea of this method is to determine the load for which the static displacements become excessive or infinite (in the linear case). The equilibrium method, the second of the four methods discussed by Ziegler (1968), consists in analyzing the equilibrium of perfect structures. When the trivial equilibrium position loses its stability, a nontrivial equilibrium position appears. With this in mind, the equilibrium method looks for the loads for which such perfect structures admit nontrivial equilibrium configurations. The third method, in its turn, is based on the potential energy of the system and originated from Lagrange's studies. The transition from stability to instability may occur when the potential energy ceases to be positive definite (or ceases to be a point of minimum). According to Bazant and Cedolin (2010), the second method represents a part of the third method, however, the second method does not answer the question of stability: it gives only equilibrium states, which may be stable or not. It is also worth mentioning that all previous methods have the objective of analyzing a static nature for the structure base-state. The last method presented by Ziegler (1968), however, is

kinetic and meets the stability concept presented. The called vibration method establishes that, in stable systems, small perturbations result in bounded motions in the vicinity of the equilibrium position. Thus, the idea of this method is to find the load for which such motions become unbounded (here one may also interpret such criterion by Lyapunov's point of view).

Ziegler (1968) also shows that both static and dynamic methods provide the same critical loads for the Euler's column buckling problems. However, this conclusion cannot be generalized for all systems. A question that arises is when the static and dynamic methods should be used. Besides Ziegler (1968), Thompson (1982), Bazant and Cedolin (2010) and Gay Neto and Martins (2013) also address the question. To understand the topic, it is fundamental to list what types of force can be present in a physical system. In general, the forces can be divided into active forces (loads) and reactive forces (reactions). The reactions, in systems whose constraints do not depend explicitly on time, can be either nonworking or dissipative. The loads, in their turn, can be divided into non-stationary loads, which vary over time, and stationary loads, which do not vary over time. The stationary loads can be subdivided into loads that depend on velocity and loads that depend on displacement. The loads that depend on velocity correspond to dissipative, gyroscopic and impressive loads. Dissipative loads do negative work on the system, gyroscopic loads do not do work on the system and impressive loads do positive work on the system. The loads which depend on displacement, in their turn, correspond to non-circulatory loads (elastic and conservative loads) and circulatory loads. Besides the loads that depend on velocity and on displacement, it is also possible to identify the inertial effects (resulting from mathematical manipulations given by the D'Alembert's principle and depending on acceleration) and the nonlinearities that can depend on acceleration, velocity and displacement.

Based on such classification of forces and on the works cited previously, it is possible to classify the systems and to outline the situations in which static and dynamic analyses are valid. Systems with non-stationary loads have to be analyzed by dynamic methods. With relation to stationary systems, first of all, it is important to mention that all of them are assumed to have inertial effects and dissipative and elastic loads. Therefore, in conservative systems, besides the previous loads, there are only conservative loads. In gyroscopic systems, there are, besides conservative loads, gyroscopic loads. Impressive systems, in their turn, can have impressive and conservative loads. Circulatory systems can have conservative and circulatory loads and, finally, gyroscopic circulatory systems can have gyroscopic, conservative and circulatory loads. Table 3 shows the classification of physical systems.

Table 3 – Classification of physical systems.

Loads/ Systems	Dependent on velocity		Dependent on displacement		Examples	Can static analysis be used?
	Gyroscopic	Impressive	Conservative	Circulatory		
Conservative			X		Buckling of Euler's columns	Yes
Gyroscopic	X		X		Divergence of a pin-ended pipe	Yes
Impressive		X	X		Galloping of a bluff structure	No
Circulatory			X	X	Flutter of an aircraft panel	No
Gyroscopic circulatory	X		X	X	Flutter of a cantilever pipe	No

Note: all systems are assumed to have inertial, dissipative and elastic forces.

Source: adapted from Thompson (1982).

It is possible to say that conservative and gyroscopic systems can be analyzed by both static and dynamic methods and that impressive, circulatory and gyroscopic circulatory systems cannot be analyzed by static methods. Bazant and Cedolin (2010) state that the dynamic analysis consists in the fundamental test of stability, but the static analysis can bring useful simplifications when it can be used.

To illustrate the aforementioned discussions, two examples, based on Ziegler (1968), are discussed in this section (Figure 31). They consist in prismatic cantilever columns with flexural rigidity  $EI$  and elastic-linear material behavior. There is also an assumption of small strains and small deflections. The first example has a non-follower load  $P$  at the free end and will be discussed by equilibrium method. The second example has a follower load  $P$  at the free end and will be discussed by equilibrium and vibration methods. As considered in the previous section, the notation  $(\dots)'$  stands for the derivative with respect to coordinate  $x$ .



The same procedure can be done for other boundary conditions in the first example. The results are summarized in Table 4.

Table 4 – Critical loads (Euler's problems).

Case	Boundary conditions		First critical load ( $m=1$ )
	First end	Second end	
1	pinned	roller	$P_1 = \pi^2 EI/l^2$
2	fixed	fixed	$P_1 = \pi^2 EI/(0.5l)^2$
3	fixed	roller	$P_1 = \pi^2 EI/(0.7l)^2$
4	fixed	free	$P_1 = \pi^2 EI/4l^2$

Source: adapted from Ziegler (1968).

Using the equilibrium method for the second example, the linearized equation of the deflection curve and the boundary conditions are given, respectively, by Eq. (117) and Eq. (118).

$$EIv'' = P(v_1 - v) - Pv_1'(l - x) \quad (117)$$

$$v(0) = v'(0) = 0; v(l) = v_1; v'(l) = v_1' \quad (118)$$

The general solution of Eq. (117) can be obtained by Eq. (119).

$$v = G_1 \cos \left[ \left( \frac{P}{EI} \right)^{0.5} x \right] + G_2 \sin \left[ \left( \frac{P}{EI} \right)^{0.5} x \right] - v_1'(l - x) + v_1. \quad (119)$$

The boundary conditions can be used together with Eq. (119), generating a linear and homogeneous system that yields to the nontrivial condition given Eq. (120).

$$\left( \frac{P}{EI} \right)^{0.5} \left\{ \cos^2 \left[ \left( \frac{P}{EI} \right)^{0.5} l \right] + \sin^2 \left[ \left( \frac{P}{EI} \right)^{0.5} l \right] \right\} = \left( \frac{P}{EI} \right)^{0.5} = 0 \quad (120)$$

Eq. (120) indicates that do not exist nontrivial equilibrium configurations when  $P$  is nonzero and, therefore, the column should not buckle. Of course, it is an unexpected (and non-coherent) result. It occurs because the system analyzed is neither conservative nor gyroscopic. It is a circulatory system in which the direction of the force depends on the column deflection. The column cannot be analyzed by static methods, thus the vibration method has to be used.

According to Ziegler (1968), in the kinetic approach, the flexural oscillations of the column are investigated. Considering that the inertial load  $dT$  is given by Eq. (121) and that  $\mu$  is the mass per unit length and  $\xi$  is a generic coordinate  $x$ , the differential equation of the deflection curve can be given by Eq. (122). The notation  $(\dot{\dots})$  stands for the derivative with respect to time and  $d\xi$  is an infinitesimal change of  $\xi$ .

$$dT = \mu \ddot{v}(\xi, t) d\xi \quad (121)$$

$$EIv''(x, t) = P[v(l, t) - v(x, t)] - Pv'(l, t)(l - x) - \mu \int_x^l \ddot{v}(\xi, t)(\xi - x) d\xi \quad (122)$$

Differentiating Eq. (122) twice with respect to  $x$ , it leads to Eq. (123), whose boundary conditions are given by Eq. (124).

$$EIv'''' + Pv'' + \mu \ddot{v} = 0 \quad (123)$$

$$v(0, t) = v'(0, t) = 0; \quad v''(l, t) = v'''(l, t) = 0 \quad (124)$$

A solution can be given by the Eq. (125) and Eq. (126).

$$v(x, t) = f(x)(H_1 \cos \lambda t + H_2 \sin \lambda t) \quad (125)$$

$$f(x) = J e^{i\omega x} \quad (126)$$

Substituting Eq. (125) into Eq. (123), the characteristic equation results in Eq. (127) and, with the roots of Eq. (127), Eq. (126) can be rewritten, resulting in Eq. (128).

$$EI\omega^4 - P\omega^2 - \mu\lambda^2 = 0 \quad (127)$$

$$f(x) = \sum_{k=1}^4 J_k e^{i\omega_k x} \quad (128)$$

Substituting Eq. (128) into the boundary conditions of Eq. (123), a second characteristic equation is found ( $\lambda$  is the unknown constant) and it is given by Eq. (129).

$$\begin{aligned}
g[\lambda^2, (P/EI)] = & \\
[2 (\mu/EI)\lambda^2 + (P/EI)^2] + 2 (\mu/EI) \lambda^2 \cosh(\omega_1 l) \cos(\omega_3 l) + & \quad (129) \\
i(P/EI) \sqrt{(\mu/EI)\lambda^2} \sinh(\omega_1 l) \sin(\omega_3 l) = 0 &
\end{aligned}$$

Eq. (129) can be represented by a curve in a  $[(\mu/EI)\lambda^2, (P/EI)l^2]$ -plane and consists in an infinity of branches. If  $P$  increases, the curve can stop to intersect the first branch and  $\lambda_1^2$  and  $\lambda_2^2$  become complex, implying in crescent oscillation amplitudes. It can be demonstrated that it occurs when the critical load  $P_1$  is approximately eight times the Euler's load for the case 4 of the Table 4, given by Eq. (130).

$$P_1 = 2.031 \frac{\pi^2 EI}{l^2} \quad (130)$$

The two examples were discussed using the assumption of small deflections. The Section 5, however, will present numerical examples of pipelines using software *Giraffe*, which performs analyses with geometrical nonlinearities, and the results will be compared.

Concerning more complex structures, beyond columns, they can be discretized with  $n$  degrees of freedom to be analyzed. With such discretization, the Lyapunov's first method can also be used to study the kinetic stability of structures, determining when the structure loses the stability and which is the instability type, for example, divergence or flutter. The idea of the Lyapunov's first method coincides with that presented for the vibration method: the structure loses stability when small perturbations result in unbounded motions in the vicinity of the equilibrium position. It is the general concept of stability and the Lyapunov's first method is a way to quantify such concept.

The differential equations of motion for a system with  $n$  degrees of freedom are given by Eq. (131) in which  $\mathbf{M}$  is the mass matrix,  $\mathbf{C}$  is the damping matrix,  $\mathbf{K}$  is the stiffness matrix,  $\mathbf{v}$  is the vector of displacements,  $\dot{\mathbf{v}}$  is the vector of velocities,  $\ddot{\mathbf{v}}$  is the vector of accelerations and  $\mathbf{f}$  is the vector of applied forces.

$$\mathbf{M}\ddot{\mathbf{v}} + \mathbf{C}\dot{\mathbf{v}} + \mathbf{K}\mathbf{v} = \mathbf{f} \quad (131)$$

For a system without damping and under free vibrations, the differential equations of motion can be simplified, being given by Eq. (132).

$$\mathbf{M}\ddot{\mathbf{v}} + \mathbf{K}\mathbf{v} = \mathbf{0} \quad (132)$$

It is also possible to transform the second order differential equations of motion into first order differential equations. For this, it is necessary to introduce the new variables  $\mathbf{y}_1$  and  $\mathbf{y}_2$ . The variable  $\mathbf{y}_1$  is equal to  $\mathbf{v}$  and  $\mathbf{y}_2$  is the first derivative of  $\mathbf{y}_1$  with respect to time ( $\dot{\mathbf{y}}_1$ ). It results in Eq. (133), in which  $\dot{\mathbf{y}}_2$  is the first derivative of  $\mathbf{y}_2$  with respect to time. For a system without damping and under free vibrations, Eq. (134) can be used.

$$\mathbf{M}\dot{\mathbf{y}}_2 + \mathbf{C}\mathbf{y}_2 + \mathbf{K}\mathbf{y}_1 = \mathbf{f} \quad \mathbf{y}_2 = \dot{\mathbf{y}}_1 \quad (133)$$

$$\mathbf{M}\dot{\mathbf{y}}_2 + \mathbf{K}\mathbf{y}_1 = \mathbf{0} \quad \mathbf{y}_2 = \dot{\mathbf{y}}_1 \quad (134)$$

In the present work, only the second order differential equations of motion will be considered. So, the form of the solution of Eq. (132) can be given by Eq. (135), in which  $\hat{\mathbf{v}}_m$  is the mode of the structure,  $t$  is the time,  $\omega$  is the circulatory frequency and  $i$  is the imaginary number.

$$\mathbf{v} = e^{i\omega t} \hat{\mathbf{v}}_m \quad (135)$$

Substituting Eq. (135) and its second derivative with respect to time into the Eq. (132), it results in Eq. (136), which represents an eigenvalue problem with  $\lambda = \omega^2$  being the eigenvalue.

$$\mathbf{M}^{-1}\mathbf{K}\hat{\mathbf{v}}_m = \omega^2 \hat{\mathbf{v}}_m \quad (136)$$

Therefore, to study the stability of structures and to apply the Lyapunov's first method, it is necessary to evaluate and analyze the eigenvalues  $\lambda$  during the loading process. Based on Bazant and Cedolin (2010), in a simplified form, when a real positive value of  $\lambda$  decreases, reaches the zero and becomes negative, the instability is characterized by divergence, since the exponent of Eq. (135) becomes real, generating unbounded, but not oscillatory, motions. When two real positive neighboring values of  $\lambda$  become equal and imaginary values of  $\lambda$  arise, the instability is characterized by crescent oscillations, which is called flutter.

With the previous rules, the Lyapunov's first method will also be useful in Section 5.

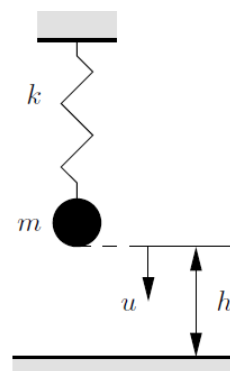
## 4 CONTACT MODELS

The onshore and offshore pipelines used to transport oil and gas from the wellheads are laid on the ground. So, the soil-pipeline interaction plays a fundamental role in the analysis of pipelines under operation. Such interaction can be simulated by means of contact models. So, since the buckling of pipelines is a phenomenon that has to consider the soil-pipeline interaction, it is important to present some considerations about contact models in the present work. The objective of this section is to describe the contact problem and the basic methodologies to obtain its solutions, present some lines of research that have been developed in the area and present the formulation used to perform the numerical simulations described in Section 5.

### 4.1 GENERAL DESCRIPTION OF THE CONTACT PROBLEM

The contact mechanics is quite complex and a good way to understand its characteristics and methodologies is to consider a very simple example extracted from Wriggers (2006), in which a point with mass  $m$  is supported by a linear spring with stiffness  $k$ . The displacement  $u$  of the point mass can be restricted by a rigid plane that is at a distance  $h$  from it (Figure 32). It is worth highlighting that however simple the practical problem may be – even for elastic-linear problems with small strains in the context of continuum mechanics – the contact problem will always be nonlinear.

Figure 32 – Point mass supported by spring.



Source: Wriggers (2006).

The energy  $\Pi$  of the system presented in Figure 32 can be written as a function of the displacement  $u$  of the point mass, as shown in Eq. (137).

$$\Pi = \frac{1}{2}ku^2 - mgu \quad (137)$$

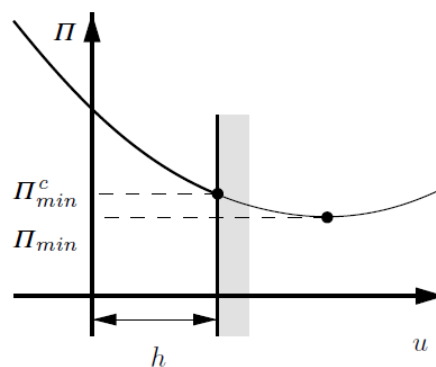
In order not to allow penetrations of the point mass into the rigid plane, a restriction to its movement has to be imposed by the inequality shown in Eq. (138), which establishes that or there is a gap between the point mass and the rigid plane or such gap is closed. This is the general idea of contact models: imposition of constraints to avoid penetrations of a body inside another.

$$c = h - u \geq 0 \quad (138)$$

If there was no restriction to the displacement  $u$ , the energy would have a minimum value  $\Pi_{\min}$  at  $u = mg/k$ , computed through the variation given by Eq. (139). However, due to Eq. (138), the solution of Eq. (137) is not at the minimum point associated with  $\Pi_{\min}$ , but at the minimum point associated with  $\Pi_{\min}^c$ , which is the minimum energy within the admissible solution space. See Figure 33, extracted from Wriggers (2006), for a better understanding.

$$\delta\Pi = ku\delta u - mg\delta u = 0 \quad (139)$$

Figure 33 – Energy of the mass spring system.



Source: Wriggers (2006).

By variation of Eq. (138), one can restrict the virtual displacement  $\delta u$  at the contact constraint, obtaining Eq. (140), which states that  $\delta u$  can only point in the upward direction.

$$\delta u \leq 0 \quad (140)$$

Since  $mg$  is larger than  $ku$  in the case of contact, and using Eq. (140) in Eq. (139), it yields to the variational inequality given by Eq. (141).

$$ku\delta u - mg\delta u \geq 0 \quad (141)$$

Once the contact between the point mass and the rigid plane is established, a reaction force  $R_N$  arises and has to obey the restriction given by Eq. (142) in order to indicate only compressive states or inactive reaction forces.

$$R_N \leq 0 \quad (142)$$

The nonlinearity of the contact problem is in the fact that there are two possible situations that generate a load-displacement curve that has non-differentiable points. The first situation is that in which the spring stiffness is large enough not to allow contact between the point mass and the rigid plane. This is represented by the conditions given by Eq. (143). The second situation is that in which there is contact between the point mass and the rigid plane and it is represented by the conditions given by Eq. (144). Eq. (143) and Eq. (144) can be combined in the statement given by Eq. (145), which are known as Hertz–Signorini–Moreau conditions in contact mechanics.

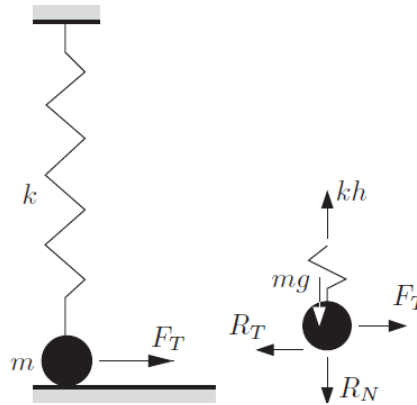
$$R_N = 0 \text{ and } c > 0 \quad (143)$$

$$R_N < 0 \text{ and } c = 0 \quad (144)$$

$$R_N \leq 0, c \geq 0 \text{ and } R_N c = 0 \quad (145)$$

It is also possible to include friction in the contact between the point mass and the rigid plane. For that, consider the system illustrated in Figure 34, in which the point mass is in contact with the rigid plane ( $R_N \leq 0$ ) and there is a force  $F_T$  tangential to the plane.  $\phi$  is the friction coefficient.

Figure 34 – Mass spring system under tangential load.



Source: Wriggers (2006).

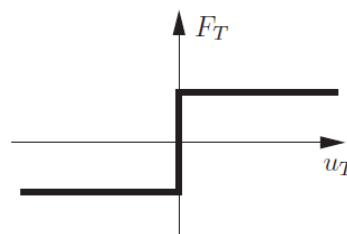
Assuming static equilibrium, the vertical and horizontal equilibrium equations are given by Eq. (146) and Eq. (147), respectively, in which  $R_T$  is the tangential reaction force.

$$R_N + mg - kh = 0 \quad (146)$$

$$R_T = F_T \quad (147)$$

There are several constitutive relations to represent the friction between the point mass and the rigid plane. The simplest constitutive relation is the Coulomb's law, illustrated in Figure 35. It establishes two states: the stick state and the sliding state. The stick state is characterized by no relative tangential movement between the point mass and the plane. In the sliding state, on the other hand, there is a relative displacement  $u_T$  between them.

Figure 35 – Coulomb's law.



Source: Wriggers (2006).

The Coulomb's law provides the inequality given by Eq. (148), which depends on the normal and tangential reaction forces. The stick state is given by Eq. (149) and the sliding

state is given by Eq. (150). Again, the conditions can be combined in only one statement, given by Eq. (151).

$$f(R_N, R_T) = |R_T| + \emptyset R_N \leq 0 \quad (148)$$

$$|R_T| < -\emptyset R_N \text{ and } u_T = 0 \quad (149)$$

$$|R_T| = -\emptyset R_N \text{ and } u_T \neq 0 \quad (150)$$

$$|u_T| \geq 0, f \leq 0 \text{ and } |u_T|f = 0 \quad (151)$$

Both normal and tangential inequalities cannot be applied directly to solve the contact problem and special methods have to be used to obtain its solution, such as the Lagrange multiplier method and the penalty method. Using the normal contact between the point mass and the rigid plane as example, these two methods are explained below.

The idea of the Lagrange multiplier method is to assume that the constraint to the displacement of the point mass is active, that is, the conditions given by Eq. (144) are satisfied. So, this method adds a term related to the constraint to the energy of the system, generating Eq. (152), in which  $\lambda$  is the Lagrange multiplier. From Eq. (145), it is possible to deduce that the Lagrange multiplier is equivalent to the reaction force  $R_N$ .

$$\Pi = \frac{1}{2}ku^2 - mgu + \lambda c \quad (152)$$

The variation of Eq. (152) with respect to  $u$  and  $\lambda$  leads to Eq. (153) and Eq. (154), respectively. The first expression represents the equilibrium of the point mass, which includes the reaction force that appears due to its contact with the rigid plane. The second expression, in its turn, states that Eq. (138) is satisfied with  $u = h$ .

$$ku\delta u - mg\delta u - \lambda\delta u = 0 \quad (153)$$

$$c\delta\lambda = 0 \quad (154)$$

The variation is no longer restricted and it is possible to find  $\lambda$  or  $R_N$  through Eq.

(155). Eq. (142) also has to be checked in order to discard possible adhesion cases. If the condition is not satisfied, it means that the constraint is inactive and, hence,  $\lambda$  is zero and the correct solution for the problem is that corresponding to  $\Pi_{\min}$ .

$$\lambda = kh - mg \quad (155)$$

With respect to the penalty method, unlike the Lagrange multiplier method, for an active constraint, it introduces a penalty term into Eq. (137), as shown in Eq. (156). The structure of the penalty term is the same as the potential energy of a spring. So, the normal penalty parameter  $\epsilon_n$  can be understood as a spring stiffness in the contact between the point mass and the rigid plane.

$$\Pi = \frac{1}{2}ku^2 - mgu + \frac{1}{2}\epsilon_n c^2 \quad \epsilon_n > 0 \quad (156)$$

The variation of Eq. (156) yields to Eq. (157). Using Eq. (138), the solution of Eq. (157) can be given by Eq. (158) and the constraint equation  $c$ , in its turn, can be given by Eq. (159).

$$ku\delta u - mg\delta u - \epsilon_n c\delta u = 0 \quad (157)$$

$$u = \frac{mg + \epsilon_n h}{k + \epsilon_n} \quad (158)$$

$$c = \frac{kh - mg}{k + \epsilon_n} \quad (159)$$

Since  $mg \geq kh$  when the contact is present, it is possible to say that Eq. (159) gives the penetration of the point mass into the rigid plane, that is, the compression of the spring that represents the contact. Such penetration depends on the spring stiffness. So, to impose the constraint given by Eq. (138),  $\epsilon_n$  has to tend to infinite. Again, it is possible to distinguish two limiting situations. In the first limiting situation, as mentioned,  $\epsilon_n$  tends to infinite and, therefore, the penetration is very small, which is coherent for active constraints. In the second limiting situation,  $\epsilon_n$  tends to zero, being only valid for inactive constraints. So, a small penalty

parameter for active constraints implies in large penetration into the plane.

To finalize, the reaction force  $R_N$  can be found using Eq. (160), which comes from Eq. (157). It is possible to see that for values of  $\epsilon_n$  tending to infinite, Eq. (160) approaches to that obtained using the Lagrange multiplier method.

$$R_N = \epsilon_n c = \epsilon_n \frac{kh - mg}{k + \epsilon_n} \quad (160)$$

According to Wriggers (2006) both methods have advantages and disadvantages. The Lagrange multiplier method, for example, fulfills the constraint equation exactly, but requires additional variables. The penalty method, on the other hand, does not require additional variables, but implies in non-physical penetrations. For the simple example presented, the use of one or another method does not make so much difference. But, for more complex situations, it does. So, the choice of the best method to be used depends on the application and on the contact model employed.

It is important to emphasize that the previous examples were important to show the general characteristics of the contact problems. The same ideas can be applied, though not so easily, to more practical problems, which involve the continuum mechanics and more complex constitutive relations for the contact bodies. For that, one can obtain, using virtual displacements, the weak form of the problem and the variational inequality due to possible contacts. The best strategy to model the contact and obtain the solution, again, depends on the specific situation, and there is no consensus on which procedure is the best, as it will be commented in Section 4.2.

## 4.2 BRIEF EXPOSITION OF THE LINES OF RESEARCH ON CONTACT MECHANICS

As mentioned, the example of Section 4.1, although simple, provides the basic characteristics of contact mechanics. Obviously, the real contact problems are more complex, not involving only point masses, but complex geometries, which can require, for example, an in-depth knowledge of continuum mechanics. And the difficulties in dealing with contact problems, which are essentially nonlinear, are not only related to geometry and its implications. Although, in some cases, it is possible to consider linear elasticity with small strains, as, for example, in the design of bearings and gears, in many other cases, there is a need to consider that the contact bodies undergo large displacements and finite rotations and that their

constitutive equations are inelastic, as for example, in car impact simulations. The dynamic effects and the consideration of multiple contact surfaces including self-contact are other obstacles in the analysis of contact problems (WRIGGERS, 2006). Due to the complexity of contact problems, for most applications, computational numerical methods have been employed to study them. Nevertheless, it is worth mentioning that even the more modern technologies cannot encompass all contact problems, making the contact mechanics an area with several possible lines of research. It is possible to say that there is still no best contact model to be used in practice for all kind of bodies.

According to Wriggers (2006), it is possible to distinguish some areas in computational contact mechanics, which analyze different contact problems. One of them is the finite element method (FEM), which can be applied both for problems with small and large deformations and both for problems in the elastic and inelastic range. There are also discrete element methods (DEM) that are used to study contact problems in which particles come into contact. Multibody systems have also been used to study small systems in which it is possible to describe the bodies as if they were rigid.

Concerning the FEM, tool used by the present work to perform the numerical simulations of the pipeline, it is possible to appoint some techniques for modelling contact problems. According to Gay Neto, Pimenta and Wriggers (2016), such techniques can be grouped into: node to node formulations, node to surface formulations, surface to surface formulations and contact involving beam elements. The node to node formulations, as the name suggests, establish the contact between nodes. The basis of these formulations can be found in the works of Francavilla and Zienkiewicz (1975) and Stadter and Weiss (1979). A gap function that measures the distance between the nodes is defined. This function plays the same role of the Eq. (138) shown in the previous section. If the penetration is detected, the terms related to the contact between the nodes can be included in the weak form of the model. The limitation of the node to node formulations is that the nodes that are candidates to come into contact have to be pre-established. If these nodes change during the simulation, especially in problems with large deformations, such change will not be captured by the formulations.

With respect to the node to surface formulations, they define a slave point and a master surface, assuming a pointwise contact. The point of contact in the master surface can be found by a minimum distance optimization problem, being possible to change the point of contact in problems with large deformations. According to Gay Neto, Pimenta and Wriggers (2016), the limitation of the node to surface formulations is the necessity of solving several contact problems, one for each slave point used to represent the surface that was not chosen as

master. The master surface, in its turn, has to be “[...] parameterized using convective coordinates, related to material points on the surface, where contact may take place [...]” (GAY NETO; PIMENTA; WRIGGERS, 2017, p. 2). The works of Bathe and Chaudhary (1985) and Bandeira, Wriggers and Pimenta (2003) can be cited in the context of node to surface formulations.

Unlike the node to surface formulations, which impose the contact constraint directly in points, the surface to surface formulations impose the constraint in the weak form through, for example, Lagrange multipliers, being more elaborated than the previous. The weak form is then integrated on the contact interface area. The inclusion of the contact constraint in the weak form is made after the verification of minimum distances between the integration points of a surface and another. In this context, the Mortar method can be mentioned as an interesting alternative to enforce the contact condition in a weak sense. Puso (2003) and Fischer and Wriggers (2005) are examples of researchers that deal with surface to surface formulations.

Finally, there are specific formulations to address the contact between beam elements. The following works deal with the topic: Wriggers and Zavarise (1997) describe a frictionless pointwise contact between circular beams without master-slave distinctions; Zavarise and Wriggers (2000) generalize the previous for frictional pointwise contacts; Gay Neto, Martins and Pimenta (2013) and Gay Neto, Pimenta and Wriggers (2014), in their turn, apply the beam to beam formulation in self-contact scenarios with large twisting.

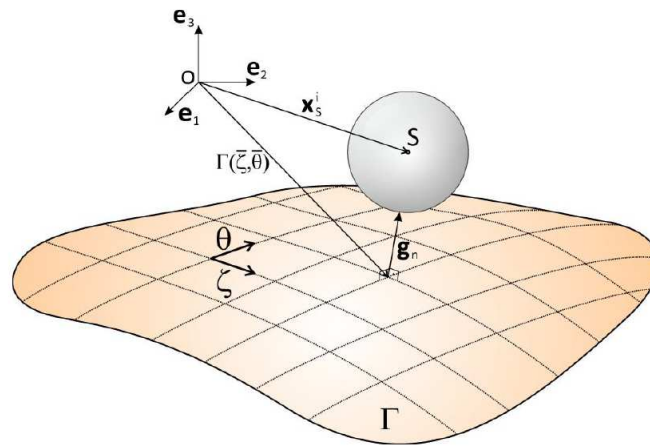
The contact model used by the present work to perform the numerical simulations of the pipeline is described in Gay Neto, Pimenta and Wriggers (2013) and Gay Neto, Pimenta and Wriggers (2017), consisting in a node to surface formulation. The first reference deals specifically with the contact between spheres and rigid and flat surfaces and the second generalizes the previous for any nature of surfaces, which is important to simulate the contact between the pipeline and the soil imperfections. The next section presents the main ideas of such contact model. For the detailed formulation, Gay Neto, Pimenta and Wriggers (2017) can be consulted.

#### 4.3 CONTACT MODEL USED IN NUMERICAL SIMULATIONS

The contact model proposed by Gay Neto, Pimenta and Wriggers (2013) and Gay Neto, Pimenta and Wriggers (2017), in the context of finite elements, uses a particular node-surface description, in which nodes are the center of spherical surfaces, whose kinematics allows to obtain the normal and tangential gaps. Figure 36 presents the geometrical description

of the contact model. As proposed by Gay Neto, Pimenta and Wriggers (2017), the upper-right index  $i$  refers to a configuration obtained previously. For next configurations to be obtained, the upper-right index  $i + 1$  is used. The upper-right index  $\Delta$ , in its turn, indicates quantities that relate the configurations  $i$  and  $i + 1$ . The lower-right index refers to the material point to which a certain quantify is referred. For example,  $\mathbf{x}_S^i$  refers to the position vector of the material point  $S$  at configuration  $i$ . The global coordinate system is  $(O, \mathbf{e}_1, \mathbf{e}_2, \mathbf{e}_3)$ .

Figure 36 – Geometrical description of the contact model.



Source: Gay Neto, Pimenta and Wriggers (2017).

From Figure 36, the spherical surface with center  $S$  is called slave. This can come into contact with another general surface  $\Gamma$ , called master. For the present work, for example, the centers of the spherical surfaces are rigidly attached to the nodes of the beam finite elements used to discretize the pipeline and the radii  $r$  of these spherical surfaces are equal to the external radius of the pipeline cross section.

To describe the spherical surface at a certain configuration  $i$ , it is necessary to find the position of its center  $\mathbf{x}_S^i$  and the orientation of the surface, given by the rotation tensor  $\mathbf{Q}_S$ , which is associated with the rotation vector  $\boldsymbol{\alpha}_S^i$  of the center of the spherical surface.  $\mathbf{Q}_S$  can be evaluated using Rodrigues' rotation parameters. More details can be found in Gay Neto, Pimenta and Wriggers (2017).

Six degrees of freedom are necessary to describe the evolution of the spherical surface between configurations  $i$  and  $i + 1$ . They are represented by the vector  $\mathbf{d}_S^\Delta$  given by Eq. (161), in which  $\mathbf{u}_S^\Delta$  is the vector of displacements of  $S$  between configurations  $i$  and  $i + 1$  and  $\boldsymbol{\alpha}_S^\Delta$  is the vector that represents the rotations of  $S$  between configurations  $i$  and  $i + 1$ .

$$\mathbf{d}_S^\Delta = \begin{bmatrix} \mathbf{u}_S^\Delta \\ \boldsymbol{\alpha}_S^\Delta \end{bmatrix} \quad (161)$$

The master surface  $\Gamma$ , which is candidate to come into contact with the spherical surface, is parameterized using the convective coordinates  $\zeta$  and  $\theta$ . Such coordinates can be represented by the vector  $\mathbf{c} = [\zeta \ \theta]^T$ . The master surface is also dependent on a N-dimensional vector  $\mathbf{d}_M$  that contains N values of generalized coordinates, which correspond to the degrees of freedom necessary to describe the movement of the master surface in space. Eq. (162) gives the parameters on which the master surface is dependent.

$$\Gamma = \hat{\Gamma}(\mathbf{c}, \mathbf{d}_M) \quad (162)$$

In order to encompass all degrees of freedom that may affect the interaction between the slave and master surfaces, Eq. (161) can be complemented, generating  $\mathbf{d} = [\mathbf{d}_S^T \ \mathbf{d}_M^T]^T$ .

For a specific set of degrees of freedom  $\bar{\mathbf{d}}$ , it is possible to seek for the corresponding convective coordinates  $\bar{\mathbf{c}}$  associated with the minimum distance between S and  $\Gamma$ . Considering that the master surface is smooth, the tangent directions  $\Gamma_\theta$  and  $\Gamma_\zeta$  can always be defined and the minimum distance can be found by the orthogonality relations shown in Eq. (163).

$$\mathbf{r} = \begin{cases} \Gamma_\zeta \cdot (\mathbf{x}_S - \Gamma) = 0 \\ \Gamma_\theta \cdot (\mathbf{x}_S - \Gamma) = 0 \end{cases} \quad (163)$$

In order to find  $\bar{\mathbf{c}} = [\bar{\zeta} \ \bar{\theta}]^T$ , Eq. (163) can be solved using the Newton-Raphson method, which is detailed in Gay Neto, Pimenta and Wriggers (2017). Once found the convective coordinates that provide the minimum distance between S and  $\Gamma$ , the contact normal direction  $\mathbf{n}$  can be found by Eq. (164). The normal gap function  $\mathbf{g}_n$  given by Eq. (165), in the vector form, can be tested along time-evolution in order to detect penetrations of the slave surface into the master surface. It is also possible to define a scalar quantify  $g_n$  to measure the gap, which is given by Eq. (166).

$$\mathbf{n} = \left( \frac{\Gamma_\zeta \times \Gamma_\theta}{\|\Gamma_\zeta \times \Gamma_\theta\|} \right)_{\bar{c}} \quad (164)$$

$$\mathbf{g}_n = (\mathbf{x}_S - \Gamma) - r\mathbf{n} \quad (165)$$

$$g_n = (\mathbf{x}_S - \Gamma) \cdot \mathbf{n} - r \quad (166)$$

In the model proposed by Gay Neto, Pimenta and Wriggers (2017), the contact inequalities are enforced by the penalty method. So, in case of penetration, the constraint is included in the weak form of the model. Based on Section 4.1, it is possible to define the potential energy  $\Pi$  through Eq. (167). It leads to the weak form contribution  $\delta\Pi_n$  due to normal contact, given by Eq. (168).

$$\Pi = \frac{1}{2} \epsilon_n \mathbf{g}_n \cdot \mathbf{g}_n \quad (167)$$

$$\delta\Pi_n = \epsilon_n \mathbf{g}_n \cdot \delta\mathbf{g}_n \quad (168)$$

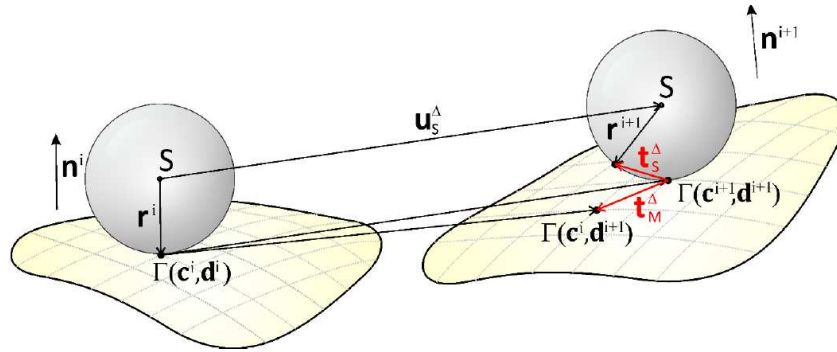
The variation of Eq. (165) leads to Eq. (169).

$$\delta\mathbf{g}_n = (\delta\mathbf{x}_S - \delta\Gamma) - r\delta\mathbf{n} \quad (169)$$

From the previous expressions, Gay Neto, Pimenta and Wriggers (2017) develop mathematically the terms due to normal contact to be included in the whole system's weak form, for nonlinear models. In this context, the authors also develop the expression for the tangent operator. The final expressions can be included in a nonlinear finite element solver to find the nonlinear solution of the problem.

Once the normal contact between the slave and master surfaces is established, the contact model is also able to evaluate the tangential contact effects. For that, the tangential gap function is determined from the kinematics description of the slave and master surfaces. The kinematics description is illustrated in Figure 37.

Figure 37 – Kinematics description used to define the tangential gap function.



Source: Gay Neto, Pimenta and Wriggers (2017).

From Figure 37, it is possible to see two configurations of the system composed by the slave surface and the master surface. The first configuration  $i$  corresponds to the beginning of the contact between the two bodies, in which there is a pointwise contact at  $\Gamma(\mathbf{c}^i, \mathbf{d}^i)$ . As already presented,  $\mathbf{c}^i$  stands for values of convective coordinates and  $\mathbf{d}^i$  stands for the degrees of freedom of the system, both at configuration  $i$ . On the spherical surface, such pointwise contact may be located by the position vector  $\mathbf{r}^i$ , with origin at the center  $S$  of the spherical surface. The contact normal direction, in its turn, is given by the vector  $\mathbf{n}^i$ .

When the configuration changes from  $i$  to  $i + 1$ , the tendency of sliding can be quantified by a vector that connects the current and previous material points where the contact between the slave surface and the master surface is established. These points can be obtained by the projection of  $S$  on the master surface. With respect to the master surface, the material point at  $\Gamma(\mathbf{c}^i, \mathbf{d}^i)$  in the configuration  $i$  becomes  $\Gamma(\mathbf{c}^i, \mathbf{d}^{i+1})$  in the new configuration  $i + 1$ . It is clear that the convective coordinates of the previous contact point does not change because the point remains the same, but the degrees of freedom of the system change. When sliding occurs, the new position of the contact point is given by  $\Gamma(\mathbf{c}^{i+1}, \mathbf{d}^{i+1})$ . Since the contact point changes, both the convective coordinates and the degrees of freedom of the system change in the configuration  $i + 1$ . With respect to the spherical surface, the center point  $S$  moves  $\mathbf{u}_S^\Delta$  and the vector  $\mathbf{r}^i$  rotates  $\mathbf{Q}_S^\Delta$ . The vector  $\mathbf{t}_S^\Delta$  represents the local change in the material points where the contact is established on the spherical surface and the vector  $\mathbf{t}_M^\Delta$  represents the local change in the material points where the contact is established on the master surface.

Based on the previous discussions, Eq. (170), Eq. (171) and Eq. (172) can be written:

$$\mathbf{t}_S^\Delta = -\mathbf{r}^i + \mathbf{u}_S^\Delta + \mathbf{r}^{i+1} - [\Gamma(\mathbf{c}^{i+1}, \mathbf{d}^{i+1}) - \Gamma(\mathbf{c}^i, \mathbf{d}^i)] \quad (170)$$

$$\mathbf{t}_M^\Delta = \Gamma(\mathbf{c}^i, \mathbf{d}^{i+1}) - \Gamma(\mathbf{c}^{i+1}, \mathbf{d}^{i+1}) \quad (171)$$

$$\mathbf{t}_S^\Delta - \mathbf{t}_M^\Delta = -\mathbf{r}^i + \mathbf{u}_S^\Delta + \mathbf{r}^{i+1} + \Gamma(\mathbf{c}^i, \mathbf{d}^i) - \Gamma(\mathbf{c}^i, \mathbf{d}^{i+1}) \quad (172)$$

The rotation motion, in its turn, is given by Eq. (173). Besides this, with Eq. (174), Eq. (175) can be written.

$$\mathbf{r}^{i+1} = \mathbf{Q}_S^\Delta \mathbf{r}^i \quad (173)$$

$$\mathbf{r}^i = -r \mathbf{n}^i \quad (174)$$

$$\mathbf{r}^{i+1} - \mathbf{r}^i = (\mathbf{Q}_S^\Delta - \mathbf{I}) \mathbf{r}^i = r(\mathbf{I} - \mathbf{Q}_S^\Delta) \mathbf{n}^i \quad (175)$$

Substituting Eq. (175) into Eq. (172), it yields to Eq. (176).

$$\mathbf{t}_S^\Delta - \mathbf{t}_M^\Delta = r(\mathbf{I} - \mathbf{Q}_S^\Delta) \mathbf{n}^i + \mathbf{u}_S^\Delta + \Gamma(\mathbf{c}^i, \mathbf{d}^i) - \Gamma(\mathbf{c}^i, \mathbf{d}^{i+1}) \quad (176)$$

The incremental tangential gap, from configuration  $i$  to configuration  $i + 1$ , is defined by Gay Neto, Pimenta and Wriggers (2017) as the difference between  $\mathbf{t}_S^\Delta$  and  $\mathbf{t}_M^\Delta$ , projected in the contact tangent plane at configuration  $i + 1$ . It can be defined mathematically by Eq. (177), in which  $\mathbf{n}^{i+1}$  is the contact normal direction at configuration  $i + 1$ .

$$\mathbf{g}_t^\Delta = (\mathbf{t}_S^\Delta - \mathbf{t}_M^\Delta) - (\mathbf{t}_S^\Delta - \mathbf{t}_M^\Delta) \cdot \mathbf{n}^{i+1} \mathbf{n}^{i+1} \quad (177)$$

To propagate the information of the tangential gap of the configuration  $i$  to the next configuration  $i + 1$ , Eq. (178) can be used. It represents the tendency of sliding for a given contact pair. The rotation operator  $\mathbf{Q}^\Delta$  is necessary to update the direction of the accumulated tangential gap, from a global perspective, when both slave and master surfaces experience same rigid body motions. More details about  $\mathbf{Q}^\Delta$  can be found in Gay Neto, Pimenta and Wriggers (2017) and therein references.

$$\mathbf{g}_t^{i+1} = \mathbf{g}_t^\Delta + \mathbf{Q}^\Delta \mathbf{g}_t^i \quad (178)$$

The constitutive relation used by Gay Neto, Pimenta and Wriggers (2017) to represent the contact tangential behavior is the Coulomb's law. As shown in Section 4.1, through Coulomb's law, two states may occur: the stick state and the sliding state. So, it is necessary to define the maximum friction force possible to occur in the stick state, which is given by  $F_{\max} = \phi R_N$ . In the context of the present model,  $R_N$  can be given by  $R_N = |\epsilon_n \mathbf{g}_n|$ . Once determined  $F_{\max}$ , it is necessary to compute the friction force that acts on the interface between the surfaces indeed and compare it to  $F_{\max}$ , determining which state is valid: the stick state or the sliding state. For that, Gay Neto, Pimenta and Wriggers (2017) use the tangential penalty approach, adopting a tangential stiffness  $\epsilon_t$  for the stick state and, thus, controlling the amount of sliding.

Using the penalty method, the tentative-force  $F_{\text{try}}$  given by Eq. (179) has to be evaluated along the time-evolution. This is the force that is compared to  $F_{\max}$  in order to verify if sliding occurs.

$$F_{\text{try}} = \epsilon_t \|\mathbf{g}_t^{i+1}\| \quad (179)$$

If sliding occurs, the evaluation of its amount  $\Delta\lambda$  and its direction  $\mathbf{t}^{i+1}$  becomes necessary. With respect to the amount of sliding, it can be computed by Eq. (180)

$$\begin{aligned} \text{if } F_{\text{try}} > F_{\max} \quad \Delta\lambda &= \frac{F_{\text{try}} - F_{\max}}{\epsilon_t} \\ \text{if } F_{\text{try}} < F_{\max} \quad \Delta\lambda &= 0 \end{aligned} \quad (180)$$

The sliding tangential gap  $\mathbf{g}_{\text{t slide}}^\Delta$  is given by Eq. (181) and the direction of sliding  $\mathbf{t}^{i+1}$  can be obtained by Eq. (182), which uses the current tangential gap direction.

$$\mathbf{g}_{\text{t slide}}^\Delta = \Delta\lambda \mathbf{t}^{i+1} \quad (181)$$

$$\mathbf{t}^{i+1} = \frac{\mathbf{g}_t^{i+1}}{\|\mathbf{g}_t^{i+1}\|} \quad (182)$$

The weak form contributions due to friction are given by Eq. (183) and Eq. (184), for the stick and sliding conditions, respectively.

$$\delta\Pi_{f_{\text{stick}}} = \epsilon_t \mathbf{g}_t^{i+1} \cdot \delta\mathbf{g}_t^{i+1} \quad (183)$$

$$\delta\Pi_{f_{\text{slide}}} = (\phi_{\epsilon_n} \|\mathbf{g}_n^{i+1}\| \mathbf{t}^{i+1}) \cdot \delta\mathbf{g}_t^{i+1} \quad (184)$$

As it was done for the normal contact, from the previous expressions, Gay Neto, Pimenta and Wriggers (2017) develop the contributions due to tangential contact to be included in the whole system's weak form, besides the tangent operator.

With the contact model proposed by Gay Neto, Pimenta and Wriggers (2017), it is also possible to consider contact dissipation effects. They will not be considered in the simulations of the pipeline, therefore they will not be described herein. More details are available in Gay Neto, Pimenta and Wriggers (2017).

As mentioned, the node to surface formulation proposed by Gay Neto, Pimenta and Wriggers (2017) can be used with any nature of surface. Two types of surface are described below. They are used in the numerical simulations of Section 5.

The first type of surface corresponds to a triangular rigid surface. In the simulations of the pipeline, it is used to represent the flat portion of the ground on which the pipeline is laid. With A, B, C being the vertices of the triangular surface and  $\mathbf{x}_A$ ,  $\mathbf{x}_B$  and  $\mathbf{x}_C$  being the position vectors of such vertices, the surface can be parameterized using Eq. (185).

$$\Gamma(\zeta, \theta) = \begin{bmatrix} -\frac{1}{2}(\zeta + \theta) & \frac{1}{2}(1 + \zeta) & \frac{1}{2}(1 + \theta) \end{bmatrix} \begin{bmatrix} \mathbf{x}_A \\ \mathbf{x}_B \\ \mathbf{x}_C \end{bmatrix} \quad (185)$$

The triangular surface is rigidly attached to a node, called pilot node, which rules its movement (translation and rotation). To define the triangular surface in the initial configuration is necessary to define the global coordinates of its vertices and of the pilot node.

Another surface used in the simulations of the pipeline is the oscillatory rigid surface, which allows to define wave patterns on a surface, in one or in two directions. It is employed to represent the isolated imperfections of the ground.

The oscillatory rigid surface can be parameterized using Eq. (186), in which  $\mathbf{x}_p$  is the position vector of the pilot node that describes the surface movement (it is also the origin

of the surface herein),  $\mathbf{Q}$  is a rotation matrix that rules the alignment of the surface in space and  $\psi(\zeta, \theta)$ , given by Eq. (187), describes the local geometry of the oscillatory rigid surface. More details about the rotation matrix can be found in Gay Neto, Pimenta and Wriggers (2017) and Gay Neto (2017).

$$\Gamma(\zeta, \theta) = \mathbf{x}_p + \mathbf{Q} \begin{bmatrix} \zeta \\ \theta \\ \psi(\zeta, \theta) \end{bmatrix} \quad (186)$$

$$\psi(\zeta, \theta) = A_1 \sin\left(\frac{2\pi\zeta}{\lambda_1} + \phi_1\right) + A_2 \sin\left(\frac{2\pi\theta}{\lambda_2} + \phi_2\right) + A_{12} \sin\left(\frac{2\pi\zeta}{\lambda_1} + \phi_1\right) \sin\left(\frac{2\pi\theta}{\lambda_2} + \phi_2\right) \quad (187)$$

Finally, the parameters  $A_1$ ,  $A_2$  and  $A_{12}$  are amplitudes, the parameters  $\lambda_1$  and  $\lambda_2$  are wave-lengths and the parameters  $\phi_1$  and  $\phi_2$  are phases. All these parameters have to be adjusted to create the geometry of the imperfection desired. The initial directions of  $\zeta$  and  $\theta$  and the coordinates of the pilot node also have to be initially defined.

## 5 NUMERICAL ANALYSES

The present work aims at analyzing the upheaval buckling of pipelines due to internal pressure through computational numerical simulations. For that, software *Giraffe* was chosen to perform the simulations.

The numerical simulations are divided into two main groups. The first group is composed by geometrically-simple models that do not have the commitment to faithfully represent the practical problems involving buckling of pipelines. The idea is to discuss possible approaches for applying the internal pressure load in the pipeline, besides discussing the influence of using static or dynamic analysis to obtain the structural response to these loads. These are more theoretical discussions than practical ones. So, these simple models only represent the pipeline with pre-established boundary conditions at its ends. The contact between the pipeline and the ground is not considered and the imperfections necessary to trigger the buckling are applied as concentrated forces. Section 5.2 deals with the first group of numerical simulations.

The second group of numerical simulations, in its turn, besides the pipeline, also includes the ground on which the pipeline is laid, considering the contact between them. As a first study, the pipeline is laid on a flat ground and the imperfections are imposed as concentrated forces. The idea is to have a model comparable to the model of Taylor and Tran (1996) in order to verify the one proposed by the present work, having as reference an existing analytical model. In the sequence, more sophisticated simulations are performed, using contact models to detect soil imperfections modeled with rigid surfaces. The objective of such simulations is to, besides verifying the results obtained from the previous simulations in more practical cases, analyze the influence of the soil imperfections and the soil friction coefficients in the critical load and in the post-buckling configuration of the pipeline. Section 5.3 deals with the second group of numerical simulations.

Before describing the particularities and the results obtained by each group, Section 5.1 presents the data and the characteristics common to all simulations.

### 5.1 GENERAL DESCRIPTION OF THE NUMERICAL SIMULATIONS

This section presents the general data and assumptions adopted to perform the numerical simulations.

### 5.1.1 Material and geometric data

The material and the geometric data of the pipeline are the same in all simulations. So, their influence in the buckling of pipelines will not be investigated by the present work.

Regarding the material data, the pipe material is the carbon steel API 5L X80 specified by American Petroleum Institute (2012), which has yielding strength equal to 552 MPa, Young's modulus equal to 200 GPa and specific mass equal to 7850 kg/m<sup>3</sup>. It was assumed that the constitutive equation of the steel follows the Hooke's law, disregarding any nonlinear/plasticity effects.

With respect to the dimensions of the pipeline cross section, they were chosen in such a way that they were compatible with the values found in real pipelines. In practice, in order to meet the transport capacity requirement, the initial estimative of the diameter of the pipeline cross section depends on hydraulic analyses. Once this capacity is not an information readily available, the present work opted to randomly select a diameter used in practice, considering that it meets the demand required by a generic reservoir. The standard NBR 15280-1 (BRAZILIAN ASSOCIATION OF TECHNICAL STANDARDS<sup>2</sup>, 2009) presents nominal diameters ranging from 0.0127 m (0.5 inch) to 1.6256 m (64 inches). The nominal diameters of the pipelines operated by Transpetro (2017) in Brazil, in its turn, range from 0.0762 m (3 inches) to 1.1684 m (46 inches). In this context, the external diameter of the pipeline chosen to be simulated in this work is 0.65 m, which is approximately equivalent to the 26-inch nominal diameter. The thickness of the pipeline wall, in its turn, can be estimated through the nominal diameter of the pipeline, the design internal pressure, the admissible stress of the pipe material and the installation conditions (BRAZILIAN ASSOCIATION OF TECHNICAL STANDARDS, 2009). The minimum thickness required for the 26-inch nominal diameter is 0.00710 m. In order to consider a gap for this value, the thickness of the pipeline was adopted equal to 0.015 m. This value, by the way, is in the range of thicknesses of the pipelines operated by Transpetro (2017): 0.0052 m (0.203 inch) to 0.0369 m (1.452 inch).

### 5.1.2 Geometry modeling

The x-direction of the models corresponds to the pipeline longitudinal axis, the

---

<sup>2</sup> Associação Brasileira de Normas Técnicas (ABNT)

y-direction corresponds to the vertical direction and the z-direction corresponds to the horizontal direction transverse to the pipeline longitudinal axis.

Concerning the pipeline, it is modeled as a straight line composed by 3-node beam elements. *Giraffe* employs a geometrically-exact 3D Timoshenko beam theory that allows the consideration of large displacements and finite rotations. The most important kinematic assumption that is made considers that the cross sections are rigid. Details about the formulation used in static analyses can be found in Gay Neto, Martins and Pimenta (2013). For the details about the formulation used in dynamic analyses, in its turn, the references Gay Neto, Pimenta and Wriggers (2014) and Gay Neto (2016) can be consulted.

With respect to the boundary conditions, Section 5.2 addresses pipelines with very simple supports at their ends (Table 4), without the consideration of the contact between them and the ground. Section 5.3, on the other hand, uses the contact model described in Section 4.3 to consider the interaction between the pipeline and the ground (with its imperfection), modeled with rigid surfaces.

### 5.1.3 Load modeling

Besides the pipeline self-weight, only the effect of the internal pressure is addressed in the numerical simulations, as the only triggering for buckling. It is considered two-way. The first approach consists in the application of equivalent compressive axial forces at the ends of the pipeline that generate the same effect of the internal pressure, that is, that generate the same effective axial force. The relation between both is given by Eq. (18). As the present work has the objective to analyze only the internal pressure effects in the buckling of pipelines, the term  $p_e A_e$  of such equation can be disregarded. Furthermore, 3D Timoshenko beam elements are used to represent the pipelines. These beam elements have the assumption that the cross sections are rigid and the Poisson effect is not considered for the pressure load. Besides this, the considered pipelines do not have end caps. Therefore, the term  $T_{tw}$  could appear only due to the action of other external loads, such as axial external forces, which would generate non-null true wall force in the pipeline. With such assumptions, Eq. (18) can be simplified, generating Eq. (188). Here, a guess of critical compressive force is evaluated by analytical models, and always a larger magnitude of loading is set in numerical models, thus leading not only to predict buckling, but also post-buckling behavior. Throughout the numerical simulations, such axial forces can be applied with follower and non-follower characteristics, as it will be shown later.

$$P_0 = T_{tw} - p_i A_i \quad (188)$$

The second approach, distinctly, consists in considering the pressure as a force per unit length  $\bar{\mathbf{f}}(s)$  given by the vector expression (GAY NETO; PIMENTA; MARTINS, 2017)

$$\begin{aligned} \bar{\mathbf{f}}(s) = \lim_{ds \rightarrow 0} \frac{d\mathbf{f}}{ds} = & (\rho_i \pi r_i^2 - \rho_e \pi r_e^2) \mathbf{g} - (\rho_i \pi r_i^2 - \rho_e \pi r_e^2) \mathbf{g} \cdot \mathbf{t}(s) \mathbf{t}(s) + \\ & [\pi r_e^2 p_e(\mathbf{G}_s) - \pi r_i^2 p_i(\mathbf{G}_s)] \kappa(s) \mathbf{n}(s), \end{aligned} \quad (189)$$

in which  $s$  is the curvilinear abscissa that describes positions along the pipeline length,  $r_i$  is the internal radius of the pipeline,  $r_e$  is the external radius of the pipeline,  $\mathbf{g}$  is the gravitational field vector,  $\mathbf{G}(s)$  is the vector that describes the centroid of the pipeline cross section at an abscissa  $s$ ,  $\kappa(s)$  is the curvature at such abscissa and  $\mathbf{t}(s)$  and  $\mathbf{n}(s)$  are Frenet tangential and normal directions, respectively, used to describe the pipeline axis spatial curve. The values  $p_e(\mathbf{G}_s)$  and  $p_i(\mathbf{G}_s)$  represent, respectively, external and internal pressurizations.

As the effect of the external/internal hydrostatic pressure will not be taken into account in present numerical models, neither external pressurization, but only the internal pressurization, most of terms of the Eq. (189) can be disregarded, simplifying it to Eq. (190).

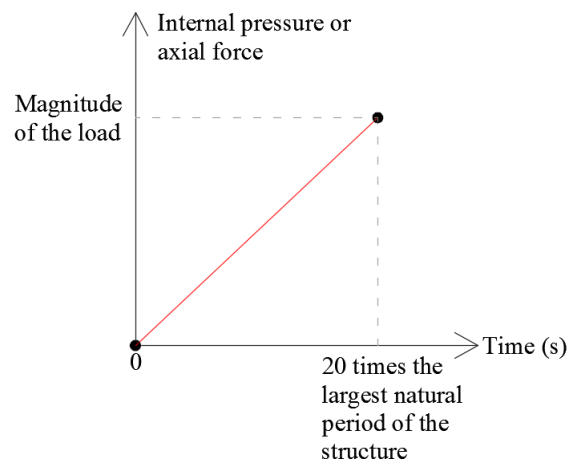
$$\bar{\mathbf{f}}(s) = -\pi r_i^2 p_i(\mathbf{G}_s) \kappa(s) \mathbf{n}(s) \quad (190)$$

Analyzing Eq. (190), one may see that it represents a load in direction  $\mathbf{n}(s)$  – characterized by the direction connecting each point at abscissa  $s$  to its center of curvature – but pointing to the opposite sense from the center of curvature, consisting, therefore, in a destabilizing load, which tries to increase the curvature level. Such directions are updated with the deformation of the pipeline under loading, characterizing the follower behavior of the internal pressure. Eq. (190) is also curvature-dependent, as it can be noted by the presence of the parameter  $\kappa(s)$ , which, again, depends on the pipeline deformation. It is worth mentioning that the formula was derived for Bernoulli-Euler assumptions and the structural model of the present work permits first order shear deformations on beams. However, the properties of the pipeline ensure compatibility of formulations, since shear strains are negligible. More in-depth discussions can be found in Gay Neto, Pimenta and Martins (2017).

The numerical simulations can involve both static and dynamic analyses to

investigate the pipeline response to internal pressure, as it will be detailed later. Specifically in relation to the dynamic analysis, for the cases in which it is used, in order to avoid exciting any natural vibration mode of the structure and to represent a quasi-static behavior of the simulation (prior to instability occurrence), the internal pressure or axial force magnitudes are applied linearly from zero, at the initial time, to the time that is approximately twenty times the largest natural period of the structure (estimate adopted). The scheme of the application of the dynamic load can be seen in Figure 38. Damping is not considered and the method used to integrate the equations of motion over time is the Newmark's implicit method, with a time step of 0.01 s and parameters  $\beta$  and  $\gamma$  equal to 0.3 and 0.5, respectively, chosen to minimize the numerical damping. More details about the implemented version of the Newmark's method can be found in Gay Neto (2016).

Figure 38 – Scheme of the application of the dynamic load.



Source: prepared by the author.

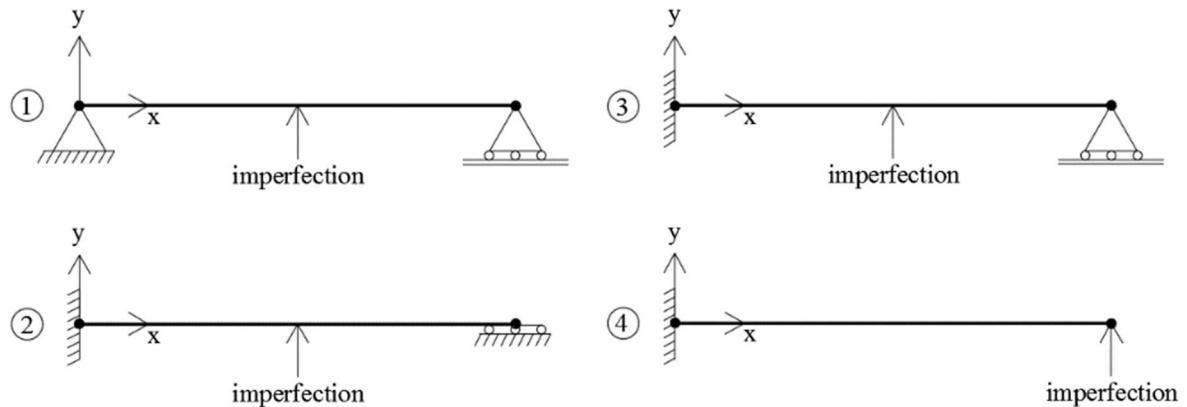
Once the general aspects of the numerical models have been described, the next sections deal with their peculiar characteristics, purposes and results.

## 5.2 GEOMETRICALLY-SIMPLE MODELS

In this section, pipelines with the boundary conditions shown in Table 4, which are also illustrated in Figure 39, are simulated using *Giraffe*. The length of the pipelines is 100 m and, as commented, the pipelines are represented in the models by a straight line composed by a set of 3-node beam elements. The pipelines are discretized with 101 equidistant nodes, totaling 50 beam elements, and the boundary conditions are imposed at the first and last nodes

of the straight line.

Figure 39 – Boundary conditions of the geometrically-simple models.



Source: prepared by the author.

In the first stage of the numerical analysis, pipelines with the first three boundary conditions shown in Figure 39 are simulated statically. The internal pressure load is applied three-way, in different simulations. The first approach, named load type a, consists in the application of the internal pressure as the distributed load proposed by Gay Neto, Pimenta and Martins (2017). For that, it is necessary to specify the value of internal pressure in *Giraffe* so that it performs the distribution of the load along the pipeline. The second approach, named load type b, consists in the application of a follower compressive axial force at the second end of the pipeline. The third approach, in its turn, named load type c, consists in the previous axial force, but with a non-follower behavior. The relation between the load type a and the load types b and c is given by Eq. (188).

The magnitudes of the loads are chosen to be larger than the critical magnitudes derived in Section 3, with the objective of capturing the buckling phenomenon and the post-buckling configuration. Besides this, four different imperfection magnitudes are applied as concentrated forces at the pipeline midspan to induce the instability: 100 N, 500 N, 1000 N and 5000 N. These imperfections act in the vertical direction ( $y$ -direction) perpendicular to the element axis ( $x$ -direction), as illustrated in Figure 39. The displacement in  $z$ -direction of all pipeline nodes is restricted in order to induce the upheaval buckling.

The load data for the first three cases of boundary conditions are shown in Table 5.

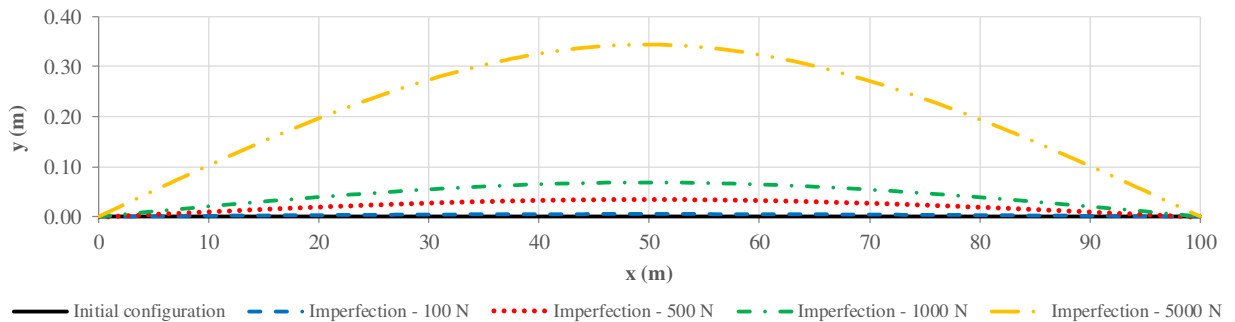
Table 5 – Load data for static analyses.

Case	First critical load $P_1$ (N)	Critical internal pressure $p_{icrit}$ (Pa)	Applied loads		
			Load type a	Load type b	Load type c
			(Pa)	(N)	(N)
	Table 4	Eq. (188) with $T_{tw} = 0$ and $P_0 = P_1$	Adopted	Eq. (188)	Eq. (188)
1	-297882	986668	$1.20 \times 10^6$	-362288	-362288
2	-1191528	3946672	$3.95 \times 10^6$	-1192533	-1192533
3	-607923	2013608	$2.05 \times 10^6$	-618909	-618909

Source: prepared by the author.

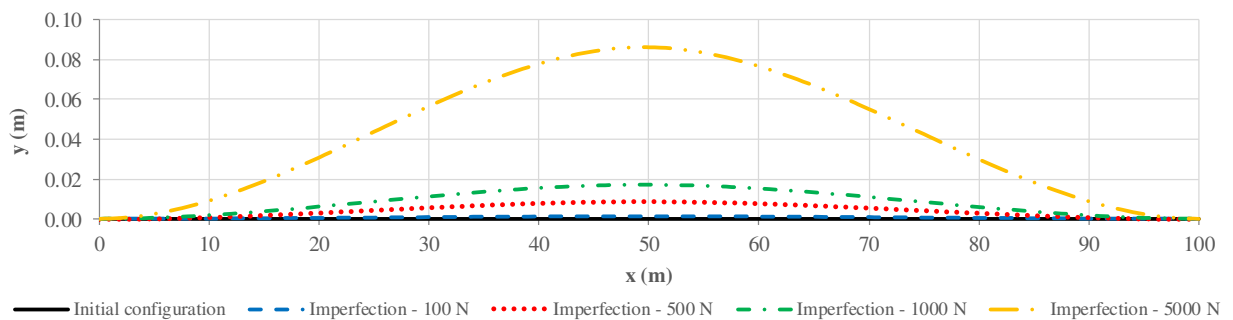
Figure 40 to Figure 42 present the pipeline configurations obtained from the application of the imperfections for the first three cases of boundary conditions.

Figure 40 – Configurations obtained from the application of the imperfections – case 1.



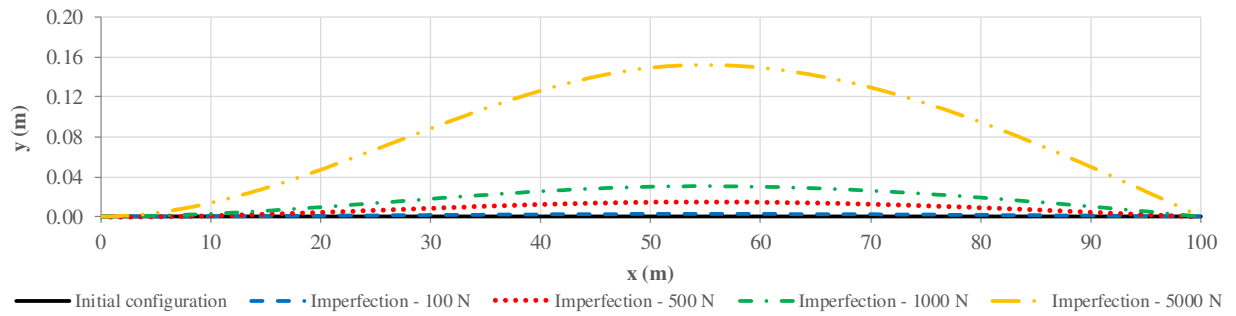
Source: prepared by the author.

Figure 41 – Configurations obtained from the application of the imperfections – case 2.



Source: prepared by the author.

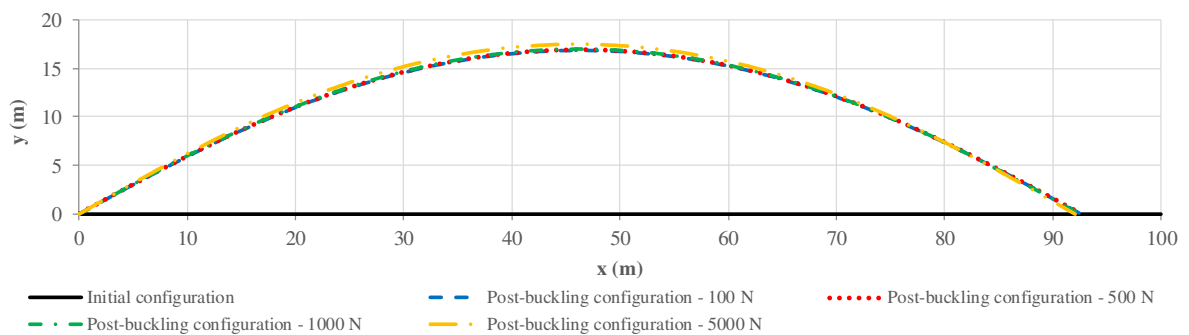
Figure 42 – Configurations obtained from the application of the imperfections – case 3.



Source: prepared by the author.

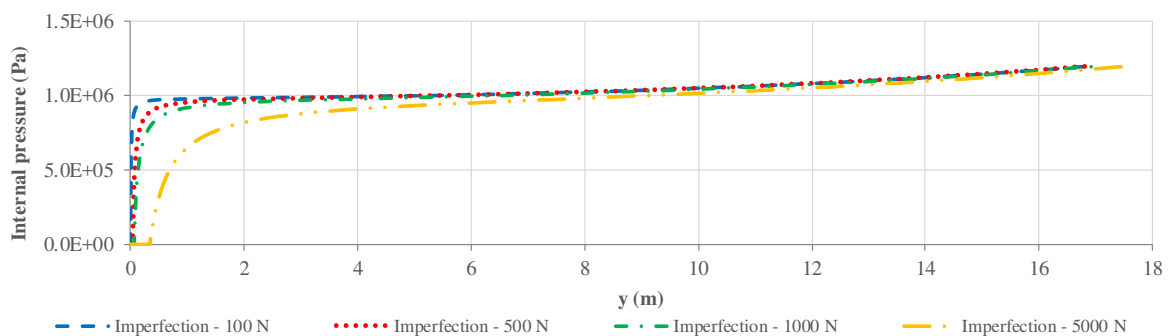
The results obtained from the static application of the load type a in the pipelines for the various cases of boundary conditions and imperfections are shown in Figure 43, Figure 44, Figure 45, Figure 46, Figure 47 and Figure 48.

Figure 43 – Post-buckling configurations – static analysis – load type a – case 1.



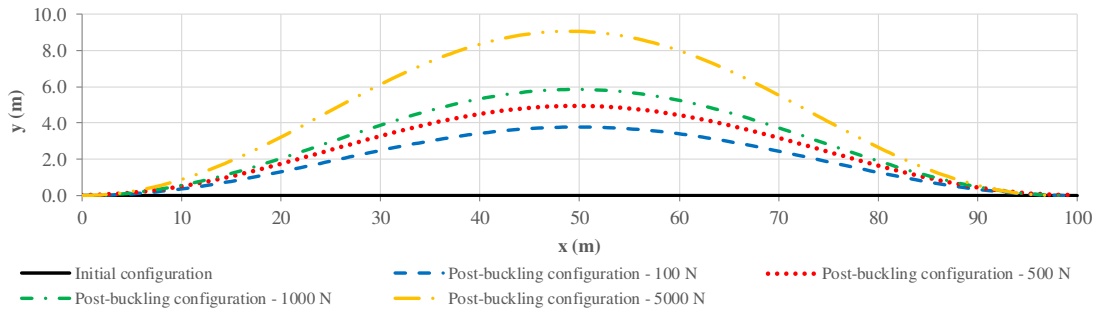
Source: prepared by the author.

Figure 44 – Equilibrium paths (midspan) – static analysis – load type a – case 1.



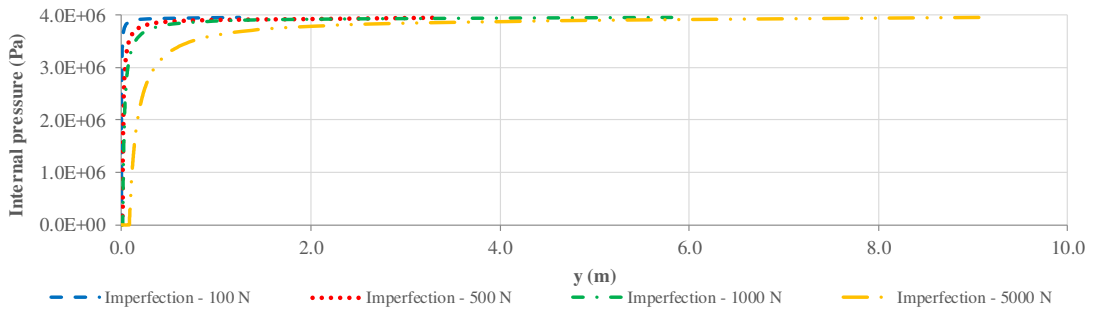
Source: prepared by the author.

Figure 45 – Post-buckling configurations – static analysis – load type a – case 2.



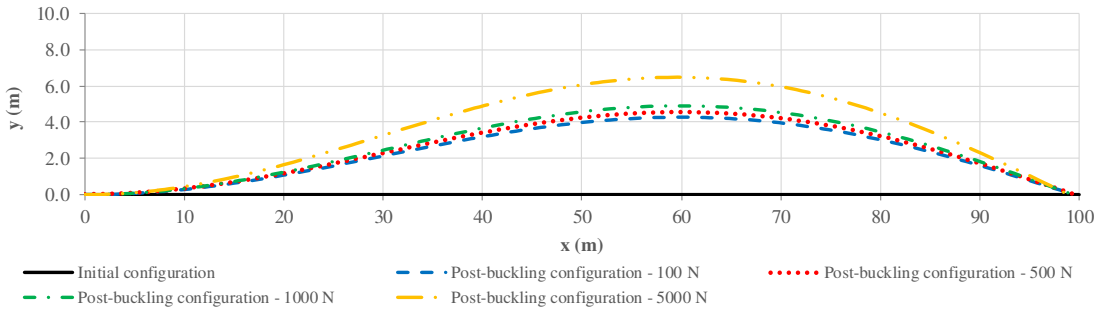
Source: prepared by the author.

Figure 46 – Equilibrium paths (midspan) – static analysis – load type a – case 2.



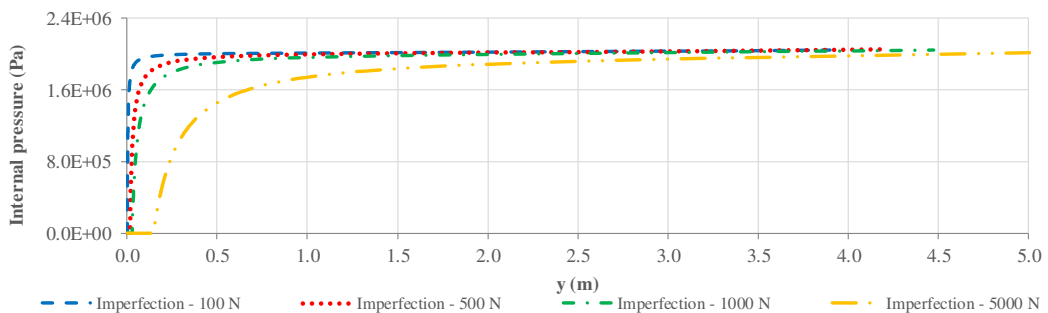
Source: prepared by the author.

Figure 47 – Post-buckling configurations – static analysis – load type a – case 3.



Source: prepared by the author.

Figure 48 – Equilibrium paths (midspan) – static analysis – load type a – case 3.



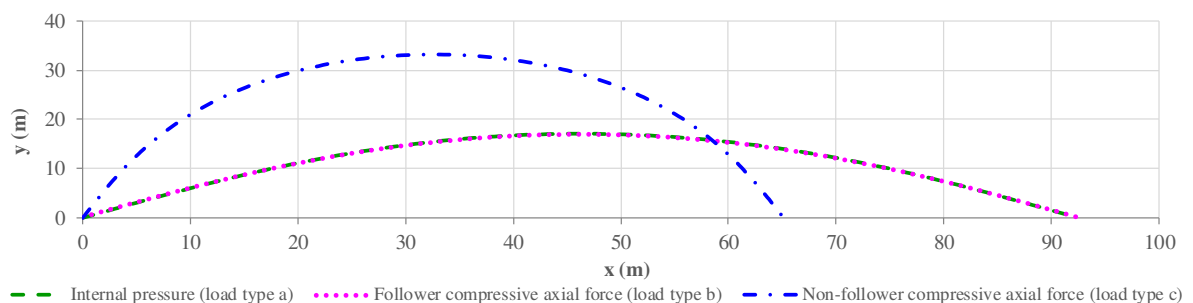
Source: prepared by the author.

Comparing the post-buckling configurations for the various imperfections (Figure 43, Figure 45 and Figure 47), it can be implied that, for the cases 1 and 3, the post-buckling configuration does not change significantly with the increase of the magnitude of the imperfections. The difference starts to appear only for the imperfection of 5000 N in both post-buckling configurations and equilibrium paths. In the case 2, however, the post-buckling configuration changes with the imperfections. In this case, for instance, the difference between the midspan displacements for the imperfections of 1000 N and 5000 N almost reaches the value of 100%. It can also be verified from Figure 43, Figure 45 and Figure 47 the necessity of nonlinear analyses to determine the correct final shapes of the deflected pipelines, since the displacements and rotations are not small. It is possible to visualize, for instance, the longitudinal displacements when these degrees of freedom are free.

Analyzing the equilibrium paths (Figure 44, Figure 46 and Figure 48), it is important to say that the horizontal levels that exist when the internal pressure is zero represent the deflections caused by the initial imperfections. Also from the equilibrium paths, the results obtained by the authors described in Section 2.3.1 can be visualized qualitatively in terms of internal pressure. For small imperfections, the critical internal pressures tend to the critical internal pressures obtained for perfect pipelines using the small deflection theory (Table 4). If the imperfections increase, the critical internal pressures decrease. The equilibrium paths, however, present a smoother stiffness change during the load application and the displacements do not change so abruptly.

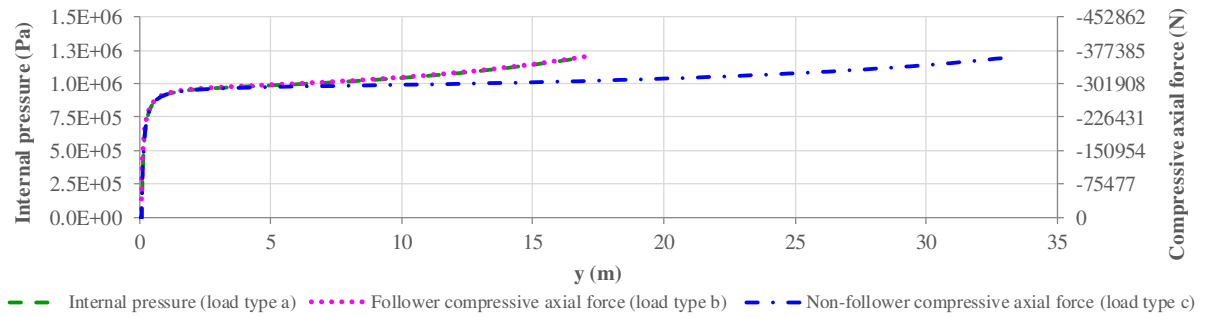
The next stage of the numerical analysis consists in applying compressive axial forces in the pipelines corresponding to the internal pressures of the previous stage (Table 5). These forces are applied as follower and non-follower loads (load type b and load type c, respectively). The results are obtained for the imperfection of 1000 N and compared to the results obtained from the application of the load type a.

Figure 49 – Post-buckling configurations – static analysis – load types – case 1.



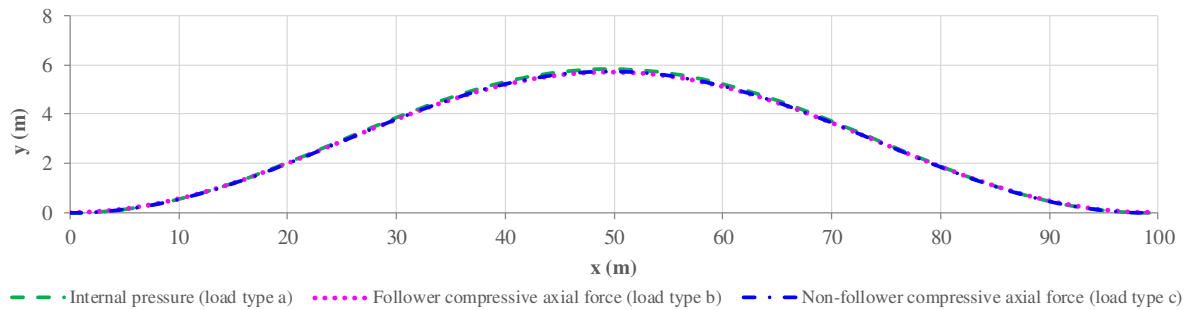
Source: prepared by the author.

Figure 50 – Equilibrium paths (midspan) – static analysis – load types – case 1.



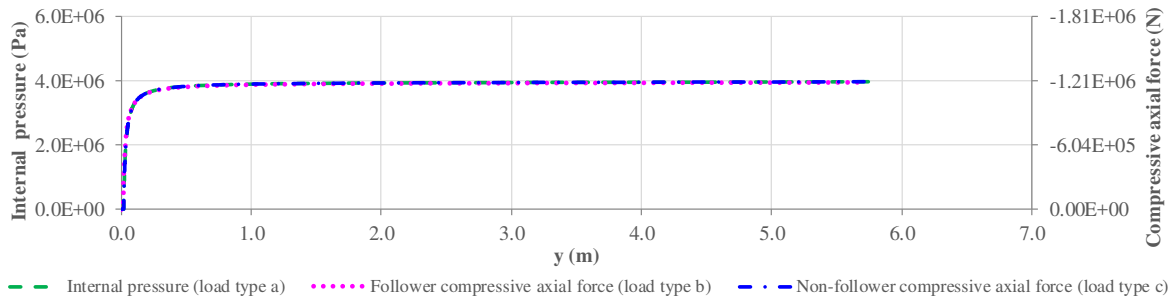
Source: prepared by the author.

Figure 51 – Post-buckling configurations – static analysis – load types – case 2.



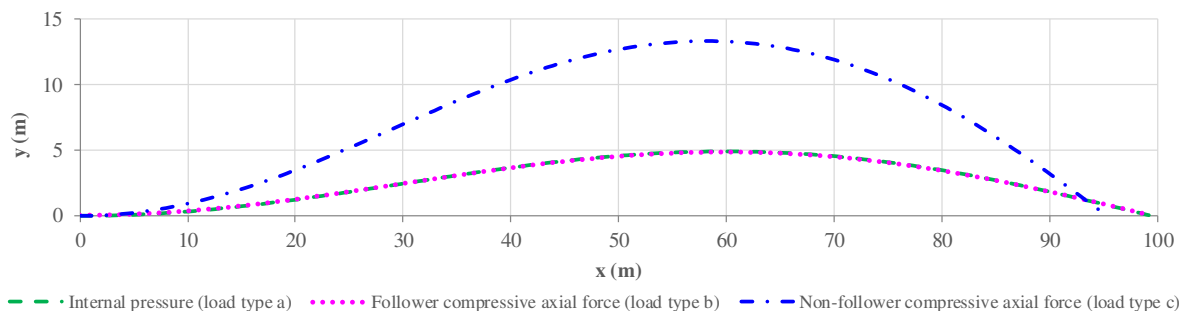
Source: prepared by the author.

Figure 52 – Equilibrium paths (midspan) – static analysis – load types – case 2.



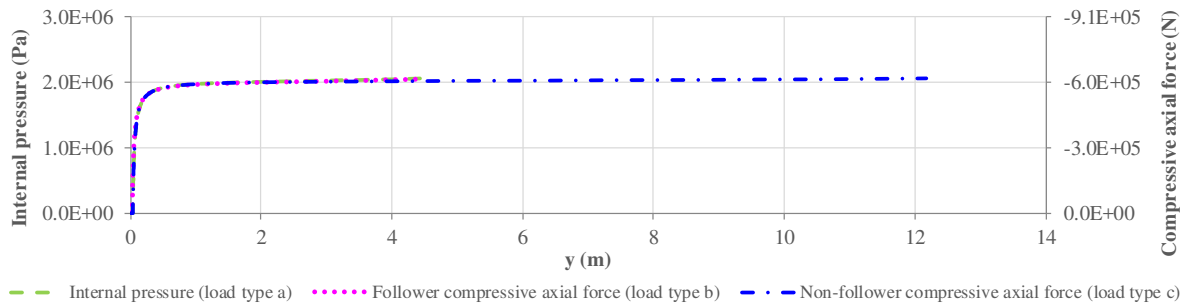
Source: prepared by the author.

Figure 53 – Post-buckling configurations – static analysis – load types – case 3.



Source: prepared by the author.

Figure 54 – Equilibrium paths (midspan) – static analysis – load types – case 3.

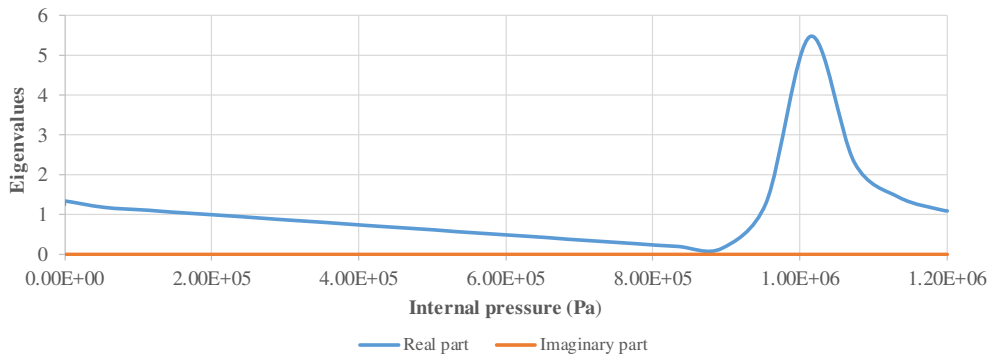


Source: prepared by the author.

From Figure 49 to Figure 54, it is possible to see that the three load approaches provide equivalent critical loads. However, the post-buckling configurations do not coincide for all approaches. Only the analyses with load type a and load type b result in the same post-buckling configurations and equilibrium paths. It happens because the internal pressure has a follower behavior, depending on the deflections of the pipeline. The deflections and the rotations are not small for the post-buckling deformed configurations. Therefore, the direction of the equivalent compressive axial force has to be updated as the pipe deflects to provide the same results obtained using the load type a. The only exception is the second case in which the three load approaches coincide. It occurs because both pipe ends are unable to rotate. Thus, the follower load does not change its direction.

Once determined and analyzed the equilibrium paths of the three cases of boundary conditions, it is interesting to use the Lyapunov's first method to analyze the stability of the pipeline during the load application. For that, it is necessary to determine the eigenvalues of the system's state variable matrix, analyzing their values and signs. As the results of the three cases generate similar discussions, only the results of the case 1, with load type a and imperfection magnitude of 1000 N, are presented. Figure 55 shows the evolution of the lowest eigenvalue during the load application.

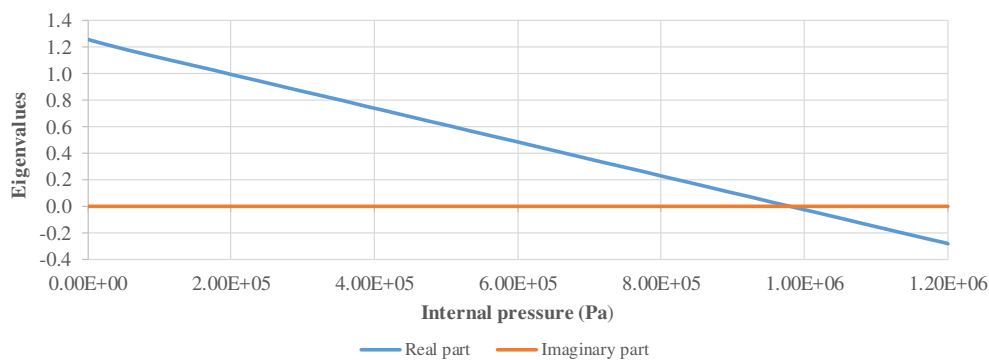
Figure 55 – Eigenvalues – load type a – case 1 with imperfection of 1000 N.



Source: prepared by the author.

From Figure 55, it is possible to see that the whole time-series of the eigenvalue is real positive. Therefore, during the application of the load, all equilibrium configurations are stable. It does not mean that the buckling does not occur, but that the pipeline, even after the buckling occurrence, can find a different equilibrium configuration that is stable. Once there is a new equilibrium configuration, the trivial straight configuration loses its stability. So, if it is necessary to estimate the load magnitude for which the buckling occurs, one can simulate the same problem without imperfections. The results are shown in Figure 56. It can be noted that the real positive eigenvalue decreases until zero and becomes negative, featuring the instability called divergence (BAZANT; CEDOLIN, 2010). The load for which this transition occurs is the critical load for a perfect pipeline, which coincides with the critical internal pressure obtained from Figure 44. In other words, the straight configuration, although it is an equilibrium configuration since there is no imperfection and the buckling does not occur, becomes unstable. If an imperfection is imposed, as presented in Figure 55, the pipeline naturally seeks for another equilibrium configuration, which is, in the present case, stable.

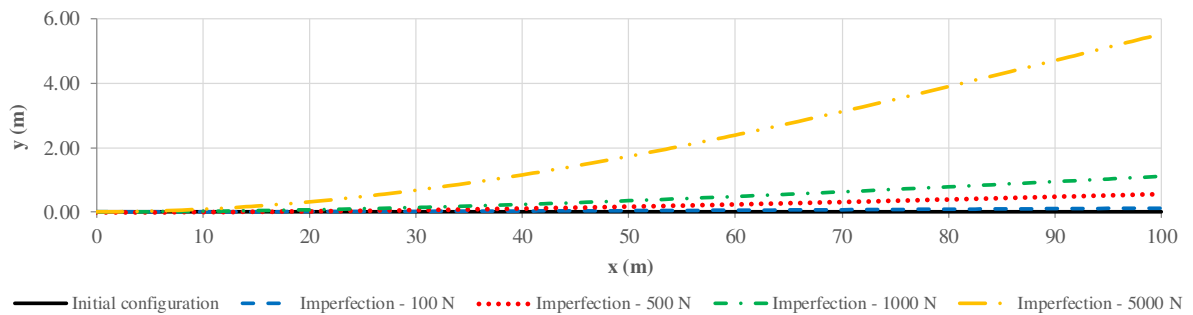
Figure 56 – Eigenvalues – load type a – case 1 without imperfection.



Source: prepared by the author.

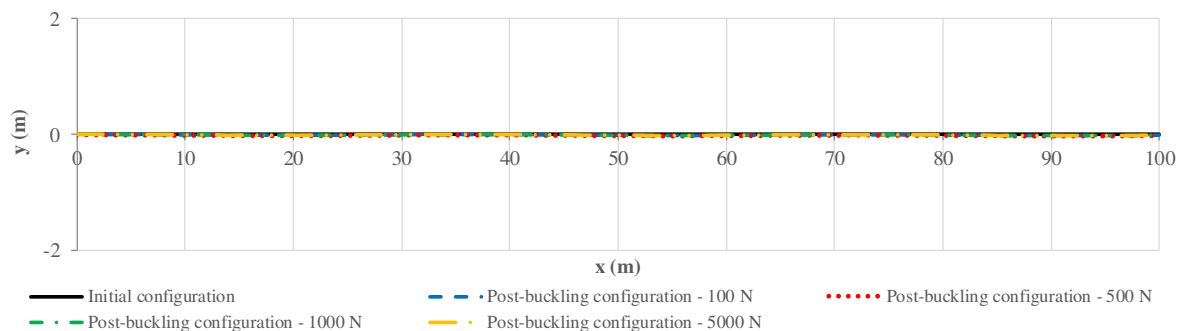
The case 4 of Table 4 has not been commented yet. Figure 57 presents the pipeline configurations obtained from the application of the four imperfections: 100 N, 500 N, 1000 N and 5000 N. Besides this, trying to capture the buckling, an internal pressure of 30 MPa is applied. This pressure is equivalent to approximately one hundred and twenty times the critical load indicated in Table 4. Performing the static analysis, the results obtained are shown in Figure 58 and Figure 59.

Figure 57 – Configurations obtained from the application of the imperfections – case 4.



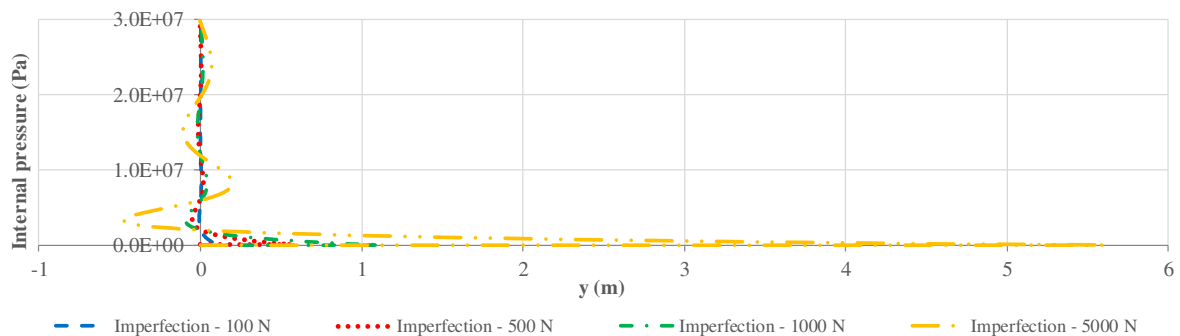
Source: prepared by the author.

Figure 58 – Post-buckling configurations – static analysis – load type a – case 4.



Source: prepared by the author.

Figure 59 – Equilibrium paths (free end) – static analysis – load type a – case 4.



Source: prepared by the author.

Analyzing the results, it is possible to see that, initially, the internal pressure has an effect that is opposite to the imperfection one. It is coherent since the load nature (follower), the boundary conditions and the deflected pipeline generate a resultant that acts in the opposite sense of imperfection. It occurs until the pipe curvature reverses, when the deflections change their sense. This process should occur cyclically (and dynamically). It can be observed from Figure 58 and Figure 59 that if the static analysis is used to perform the simulations, the critical internal pressure corresponding to the critical load indicated in Table 4 is not identified. Although the applied internal pressure is much larger than the critical internal pressure obtained for a perfect pipeline using the small deflection theory, the pipeline does not buckle. It occurs because the method of analysis is not compatible with the system proposed. The system analyzed is not conservative, but circulatory. Thus, the discussions presented in Section 3 can be applied in this case. The correct way to analyze the problem is to use a dynamic approach, once the simplification given by the static analysis leads to erroneous results, as previously predicted by Ziegler (1968). Therefore, the critical load is not that obtained by the Euler's problem (Table 4) but that obtained by Eq. (130).

To perform the dynamic analysis, the load is also applied three-way at the free end of the pipeline. Load types a, b and c remain the same as those described for the cases 1, 2 and 3. In order to represent a quasi-static behavior, without relevant excitation to any natural vibration mode of the structure, such loads are applied linearly from zero, at the initial time, to the values indicated in Table 6, at the time 316 s.

Table 6 – Load data for dynamic analyses.

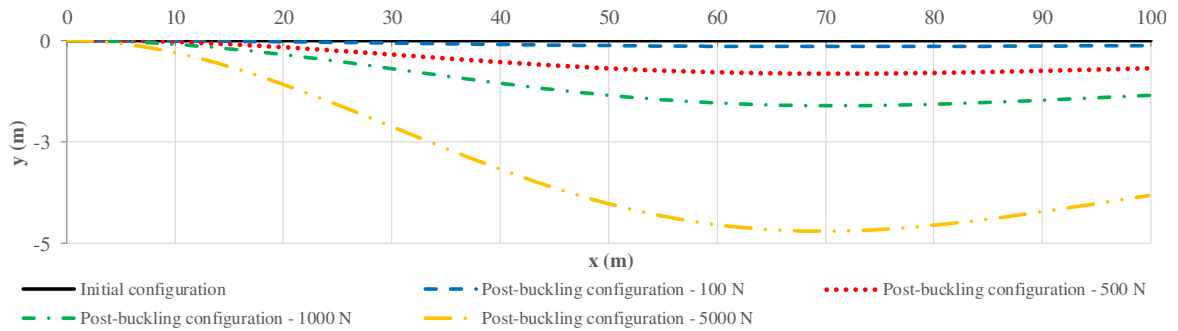
Case	First critical load $P_1$ (N)	Critical internal pressure $P_{icrit}$ (Pa)	Applied loads		
			Load type a	Load type b	Load type c
			(Pa)	(N)	(N)
	Eq. (130)	Eq. (188) with $T_{tw} = 0$ and $P_0 = P_1$	Adopted	Eq. (188)	Eq. (188)
4	-604998	2003923	$2.20 \times 10^6$	-664196	-664196

Source: prepared by the author.

Performing the same simulations that were made for the first three cases, the results obtained from the dynamic analysis are shown below for the three load types. It is important to explain that Figure 63 has two axes of ordinates in order to separate the results

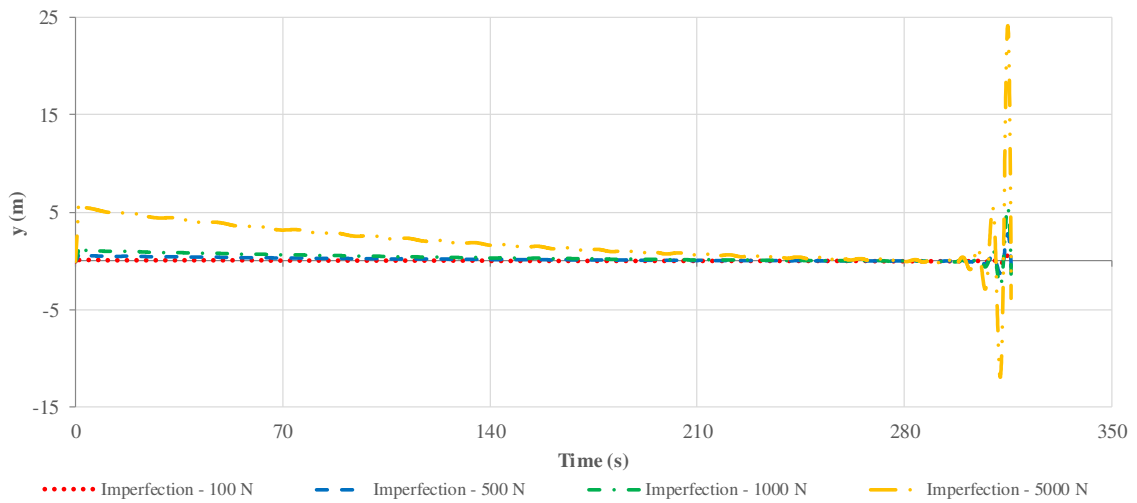
obtained from the application of the load types a and b from the results obtained from the application of the load type c.

Figure 60 – Post-buckling configurations at the time 316 s – dynamic analysis – load type a – case 4.



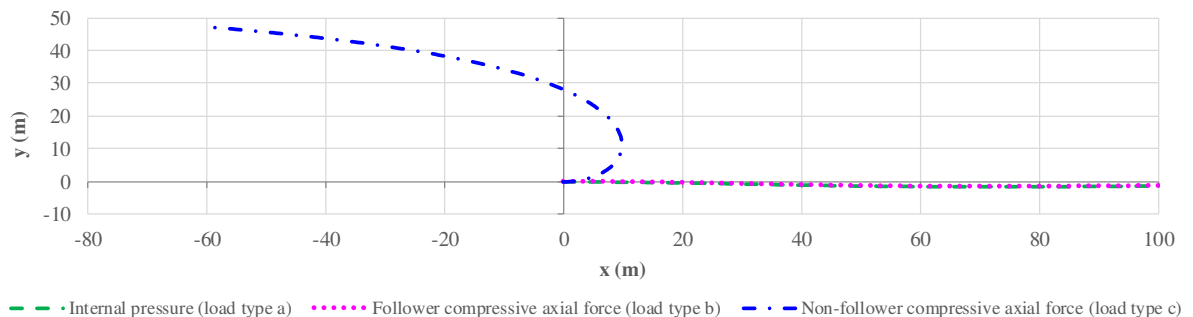
Source: prepared by the author.

Figure 61 – Time-series of displacement (free end) – dynamic analysis – load type a – case 4.



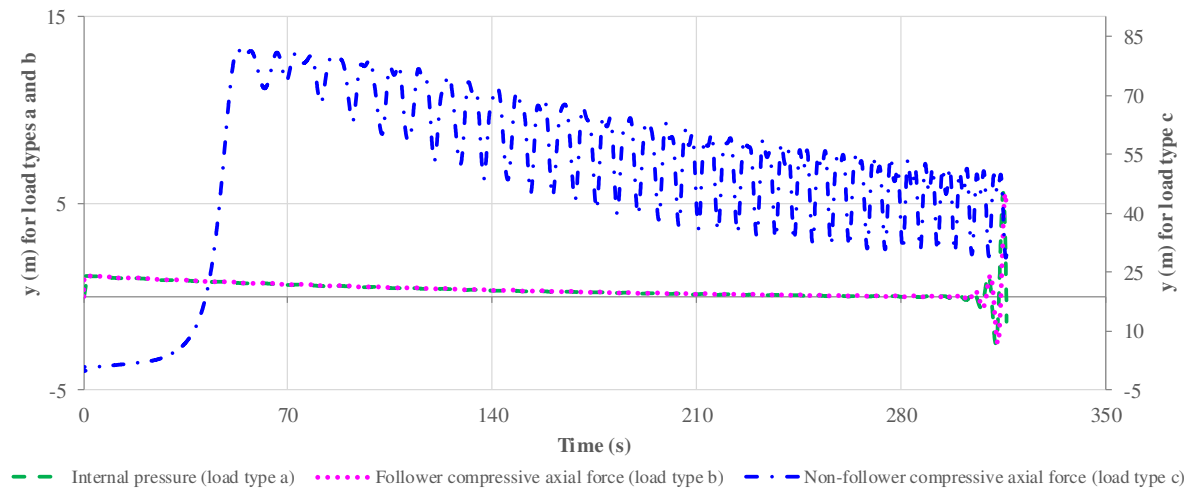
Source: prepared by the author.

Figure 62 – Post-buckling configurations at the time 316 s – dynamic analysis – load types – case 4.



Source: prepared by the author.

Figure 63 – Time-series of displacement (free end) – dynamic analysis – load types – case 4.



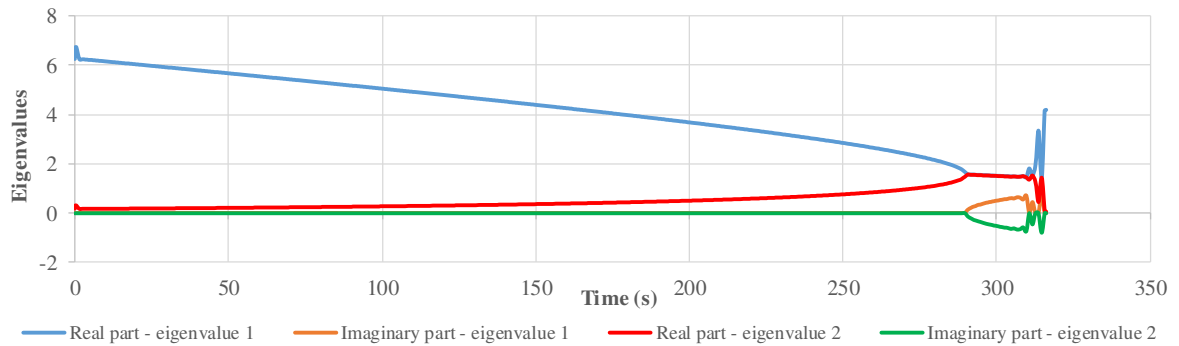
Source: prepared by the author.

It is possible to observe from Figure 60 that the post-buckling configurations present significant differences for the various imperfections. The same analysis that was made for cases 1, 2 and 3 may be made again for case 4: the critical load (obtained from the equivalent critical time of Figure 61) for pipelines with small imperfections tends to the critical load for perfect pipelines – Eq. (130). Besides this, from Figure 61, it can be noted that the instability of the system is characterized by crescent oscillation amplitudes (flutter).

From Figure 62 and Figure 63, it is observed again an equivalence between the analyses performed with internal pressure and follower compressive axial force. The problem with non-follower compressive axial force presents results totally different since it represents another phenomenon (conservative) that does not characterize the internal pressure effects and could be analyzed statically.

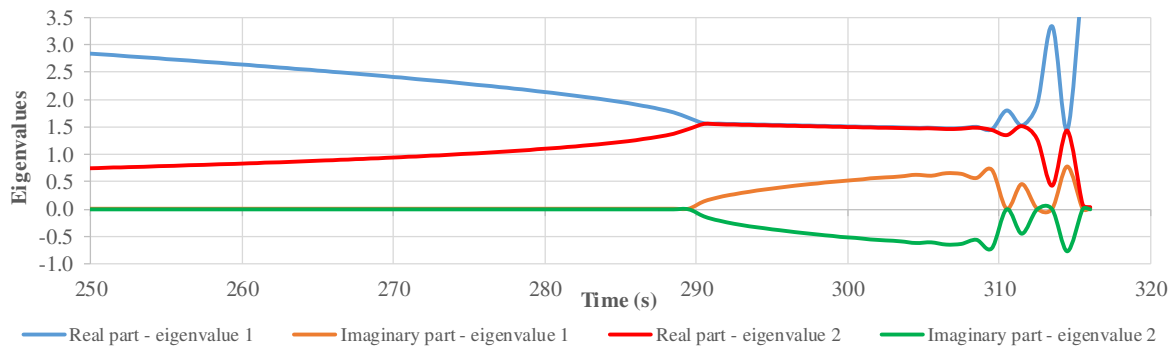
One aspect that differentiates the case 4 from the other cases is the instability type. In the cases 1, 2 and 3, the instability is characterized by the divergence whereas the instability of case 4 is characterized by the flutter (BAZANT; CEDOLIN, 2010). So, to finalize the analyses of the geometrically-simple models, a more accurate analysis of this difference can be done by the extraction of the eigenvalues of the system's state variable matrix and by the Lyapunov's first method. Figure 64 shows the evolution of the two lowest eigenvalues during the load application for the case 4, with load type a and imperfection magnitude of 1000 N. It is possible to see that the time for which the two real positive eigenvalues become equal and imaginary parts appear coincides with the time for which the flutter starts (Figure 65 and Figure 63, respectively).

Figure 64 – Eigenvalues – load type a – case 4 with imperfection of 1000 N.



Source: prepared by the author.

Figure 65 – Eigenvalues – load type a – case 4 with imperfection of 1000 N – detail.



Source: prepared by the author.

### 5.3 ADVANCED MODELS

This section presents the description and the results of the set of simulations that use contact models to represent the interaction between the pipeline and the ground on which it is laid. It is intended that the boundary conditions of the models in this section result mainly from such interaction and that the end supports are of less relevance for the study of the buckling of pipelines. So, here, the length of the pipelines is 1000 m. It is larger than the length of the pipelines of the previous simulations in order to distance the buckle region (central region of the pipeline) from the pipeline ends and, thus, to avoid possible interferences of them in the buckling. The pipelines are discretized with 1001 equidistant nodes, totaling 500 beam elements.

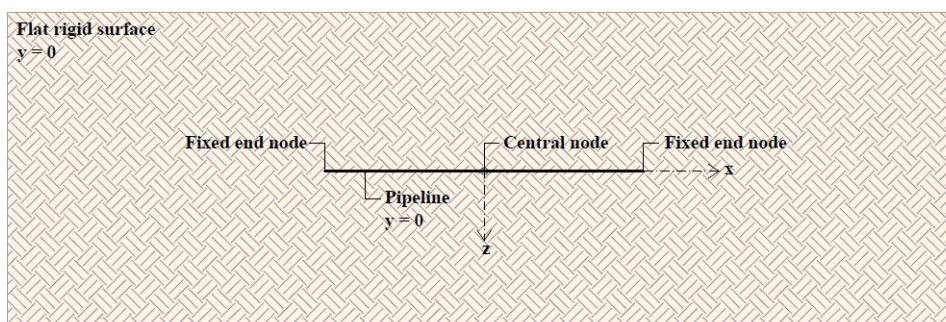
Section 5.3.1 shows a simplified buckling scenario in which, although the pipeline is in contact with the soil, the imperfection is imposed as a concentrated force. The aim of this section is to perform initial verifications and analyses of the numerical model, having as reference the model presented by Taylor and Tran (1996). In the sequence, in Section 5.3.2, the

effects of the imperfections and the friction between the pipeline and the soil are analyzed with the aid of more sophisticated simulations, using contact models to also detect isolated imperfections present on the ground and modeled with rigid surfaces. The models of Section 5.3.2 also consolidate the discussions about the approaches for applying the internal pressure promoted in Section 5.2.

### 5.3.1 Models with imperfections imposed as concentrated forces

To simulate the upheaval buckling process proposed by Taylor and Tran (1996), the pipeline is disposed straightly at the level of a rigid surface that represents the soil (Figure 66). Such rigid surface is modeled with the triangular rigid surfaces described in Section 4.3. No friction between the pipeline and the soil is considered. The displacement in z-direction of all pipeline nodes is restricted in order to induce the upheaval buckling. Besides this, the pipeline end nodes are initially fixed to avoid rigid body movements that may occur prior to the establishment of the contact between the pipeline and the soil. The pipeline under these conditions is then subjected to a sequence of static load steps that represent partially the stages of the upheaval buckling proposed by Taylor and Tran (1996) for an imperfection amplitude of 0.50 m. These load steps are described in Table 7.

Figure 66 – Initial layout of the simplified model – plan view.



Source: prepared by the author.

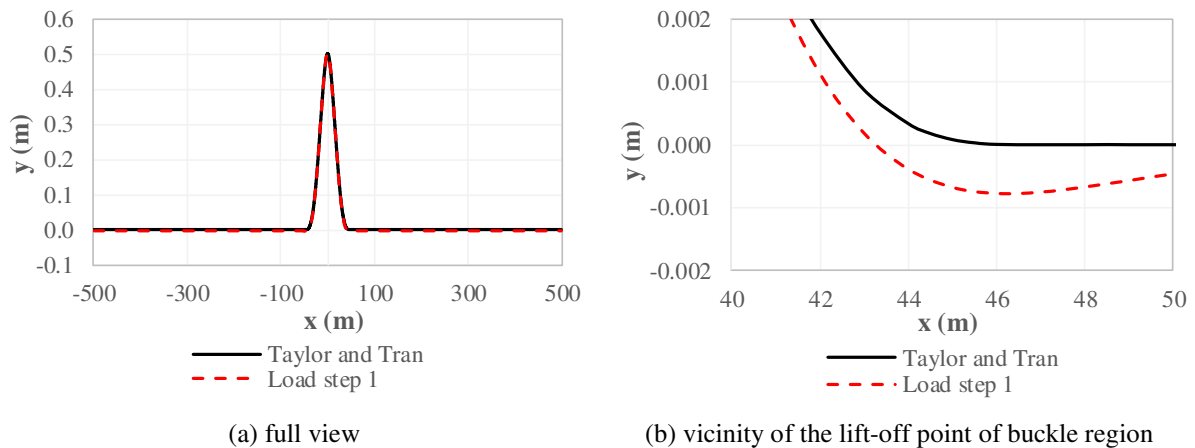
From an idealized straight configuration of the pipeline, the load step 1 of the static analysis, through the pipeline self-weight and the upward-directed force calculated from Eq. (84), establishes the imperfect initial configuration of the pipeline. Assuming that the ground is at the level  $y = 0$ , Figure 67 presents a comparison between the initial configurations obtained analytically and numerically. It is possible to see that the two configurations are almost the same. Only some differences near the lift-off points of the buckle region can be noted.

Table 7 – Static load steps used to simulate numerically the stages of the upheaval buckling in the simplified model.

Load steps	Description
1	Application of the pipeline self-weight and of a concentrated upward-directed force at the central node of the pipeline, whose magnitude is 143175.82 N, calculated from Eq. (84), and that represents the reaction at the point of the imperfection in contact with the pipeline.
2	Release of the displacement in x-direction of the end nodes of the pipeline.
3	Restriction of the displacement in y-direction of the central node and the elimination of the upward-directed force applied in load step 1.
4	Static application of a pair of auto-equilibrated compressive forces in x-direction at the pipeline end nodes, whose magnitude is 4672343.81 N, calculated from Eq. (98).
5	Release of the displacement in y-direction of the central node of the pipeline.

Source: prepared by the author.

Figure 67 – Comparison between the initial configurations of the pipeline obtained analytically and numerically.



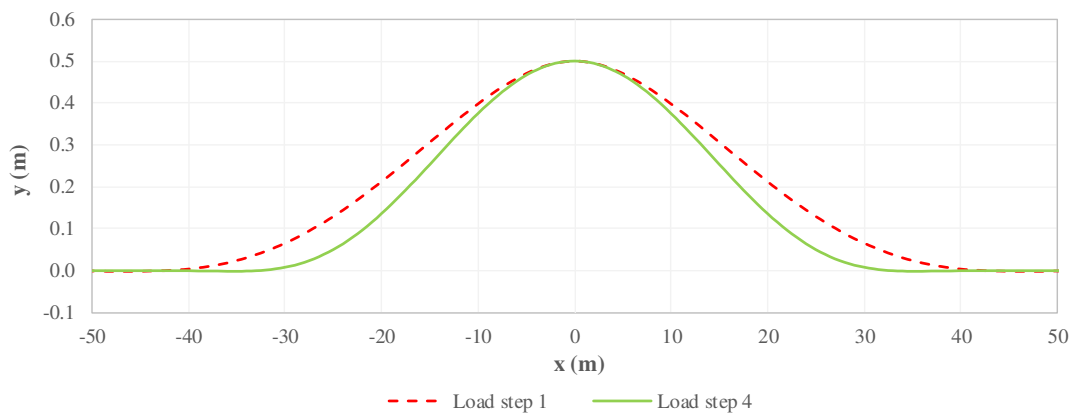
Source: prepared by the author.

The load step 2 releases the displacement in x-direction of the pipeline end nodes for the application of axial loads. The load step 3, in its turn, fixes the position of the central node of the pipeline, transforming the force applied in load step 1 into a reaction arising from the restriction to the displacement in y-direction of this node.

The pre-upheaval flexure described by Taylor and Tran (1996) is simulated

through the load step 4. It is worth mentioning that the initial configuration of the pipeline laid on the prop imperfection is not stress free in the numerical simulation. Therefore, the best expression to estimate the axial force for which the pipeline loses its contact with the imperfection is Eq. (98). Under such force, the length of the pipeline that is not in contact with the ground is reduced. The comparison between the pipeline configuration resulting from load step 1 and the pipeline configuration resulting from load step 4 is shown in Figure 68.

Figure 68 – Comparison between the pipeline configurations resulting from load step 1 and load step 4.

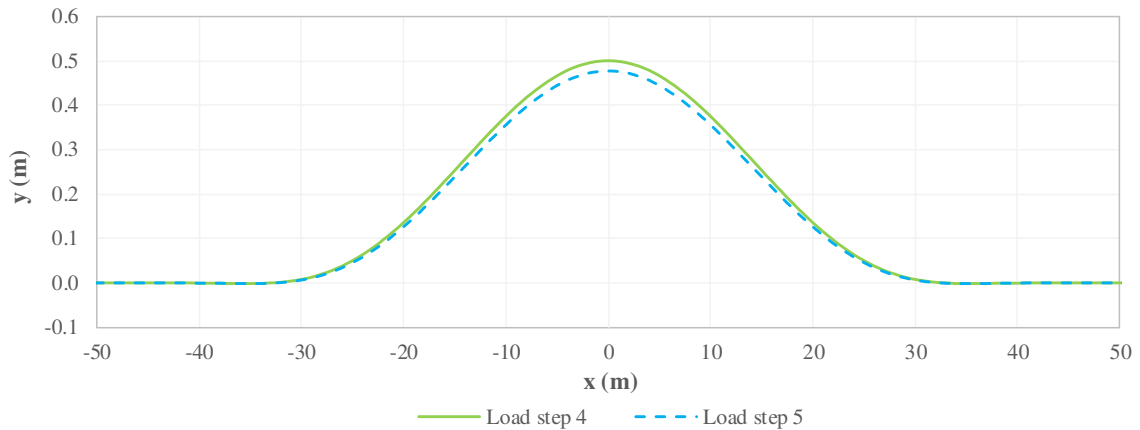


Source: prepared by the author.

It is expected that, by releasing the displacement in y-direction of the central node in load step 5, the pipeline configuration remains the same as the one obtained in load step 4, because the force calculated from Eq. (98), according to Taylor and Tran (1996), cancels the reaction at the point of contact between the pipeline and the imperfection. In other words, by releasing the displacement in y-direction of the central node, the tendency of the pipeline to move down caused by its self-weight should be compensated by the tendency of the pipeline to move up caused by the axial forces applied in load step 4. However, the central node moved about 0.02 m down relative to the configuration obtained in load step 4 (Figure 69). This difference occurred because the reaction at the central node did not become exactly zero in load step 4. That is, the forces applied in load step 4 are slightly larger than those required to cancel the force of the prop imperfection, as it can be seen in Figure 70, which shows that the reaction, although very close to zero, becomes negative in load step 4. One could expect that eliminating such negative reaction, by releasing the displacement in y-direction of the central node, it would increase the amplitude y in load step 5, but the opposite occurs (Figure 69). The explanation may be found in the interpretation of Eq. (98): with EI fixed, an axial force larger than the

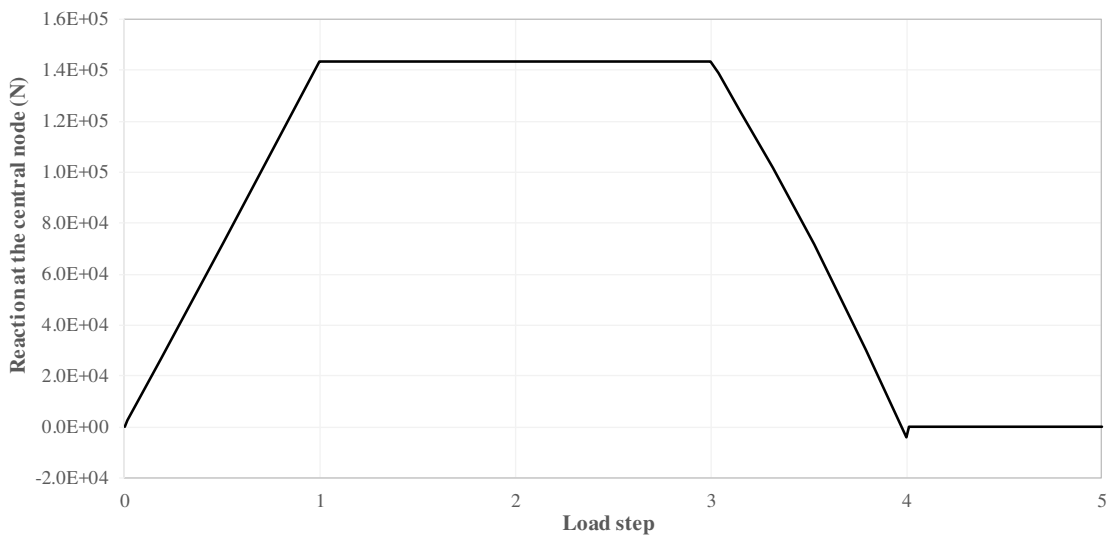
necessary implies in obtaining a smaller buckle length. This is geometrically related to a smaller buckle amplitude. This is why the pipeline moves down with the release of the displacement in y-direction of the central node of the pipeline: to lead to a smaller buckle length.

Figure 69 – Comparison between the pipeline configurations resulting from load step 4 and load step 5.



Source: prepared by the author.

Figure 70 – Reaction at the central node of the pipeline.



Source: prepared by the author.

At this point, it is already possible to see slightly differences between the analytical and numerical approaches. These occur due to both mathematical simplifications and differences in the assumptions adopted for the structural analysis. It is important to remember that, in general, the analytical models assume many simplifications such as: totally rigid soil and linear analysis with small rotations and displacements. The results of the present numerical

model, however, are obtained from geometrically nonlinear analysis and, although the soil is represented by a theoretical rigid surface, the penalty assumed for contact enforcement always allows some flexibility to the soil, implying small penetrations of the pipeline into it that modify the initial configuration of the pipeline if it is compared to the initial configuration obtained using the analytical model (Figure 67b). The foundation stiffness  $k_{\text{soil}}$  can be estimated with the aid of the normal penalty parameter  $\epsilon_n$  per node used in the model (1.00 GN/m) and the area of influence of the node, given by the multiplication of the distance between nodes  $d_n$  by the pipeline external diameter  $D_e$ . Using Eq. (191), the  $k_{\text{soil}}$  results in 1.54 GN/m<sup>3</sup> for the present model, representing a soil with high stiffness. Based on Béton-Kalender (1962 *apud* MORAES, 1976, p. 15), such level of stiffness can already be considered representative of rocks.

$$k_{\text{soil}} = \frac{\epsilon_n}{d_n D_e} \quad (191)$$

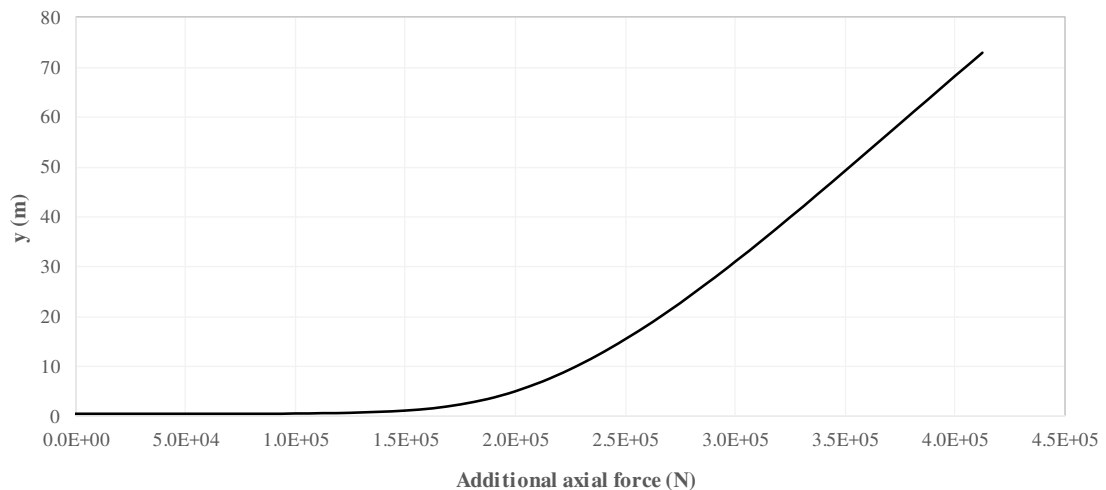
Once the imminence of loss of contact was achieved by the static load steps described in Table 7, additional compressive axial forces are applied dynamically at the pipeline end nodes in order to obtain post-critical configurations. The dynamic analysis was chosen because, mainly due to the boundary conditions, it is difficult to predict if the systems are conservative or not in the advanced models of the present work. So, since the dynamic analysis is the fundamental test of stability, it eliminates conceptual doubts regarding the system nature and the best type of analysis to be employed. The additional forces have magnitude equal to 2000000 N and are applied in 16 s to generate a quasi-static simulation, as already mentioned. Figure 71 relates the axial forces applied to the buckle amplitudes resulting from the application of these forces. The graph includes only the load range considered relevant, as well as other graphs shown later in this work.

In order to compare the results of post-buckling configurations obtained from the analytical model proposed by Taylor and Tran (1996) and from the numerical model, the present work takes as reference the post-buckling configuration at the time 1.2 s (Figure 72), which refers to a total compressive axial force of 4822343.81 N (force applied statically plus force applied dynamically at the time 1.2 s).

From Figure 72, it is determined that the buckle length at the time 1.2 s is approximately 72 m. With this information and using the post-upheaval buckling formulation of Taylor and Tran (1996), described with details in Section 2.3.1.2, to determine the

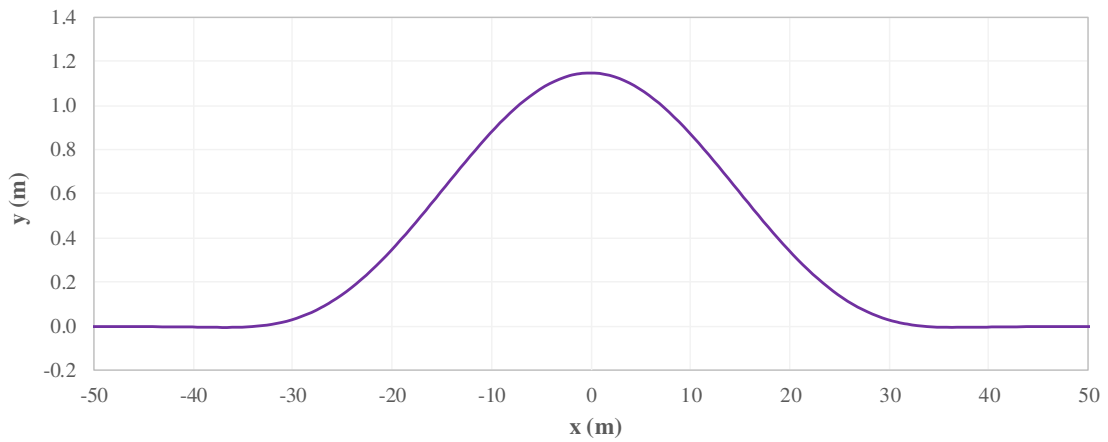
compressive axial force that corresponds to the specific pipeline configuration shown in Figure 72, the magnitude 2842042.51 N is reached. Apparently, the value obtained is quite different from the value applied in the numerical model. However, the formulation proposed by Taylor and Tran (1996) assumes that the initial configuration of the pipeline is stress free. Such condition is not the same in the present numerical model. So, in order to compare compatible values, it is possible to think that the difference between the upheaval axial forces obtained by Eq. (97) and Eq. (98) can be considered as an additional axial force due to the pre-stress effect, reaching 4883879.73 N. Comparing this result to the compressive axial force applied in numerical model, it can be observed a difference of approximately 1.26%, which is quite acceptable, given all the differences between the models. It is possible to say that, for this load level, the assumption of small displacements and rotations still provides good results. With the increase of the load, the differences become larger, since this assumption is no longer valid.

Figure 71 – Buckle amplitude  $y$  versus additional axial force.



Source: prepared by the author.

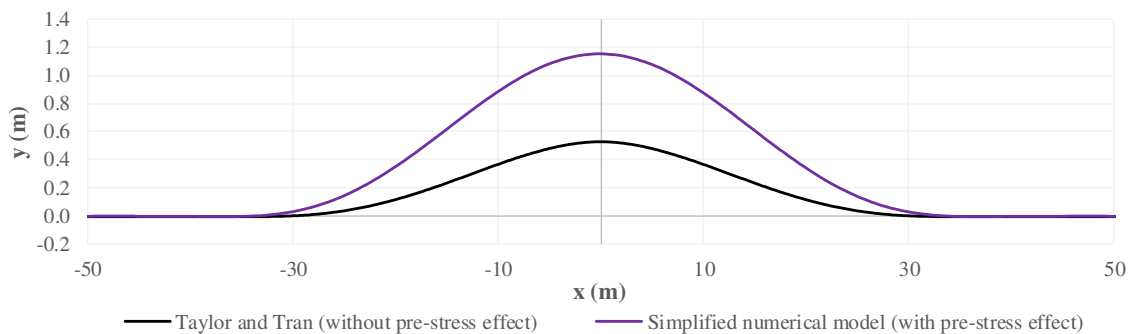
Figure 72 – Post-buckling configuration of the pipeline for a total compressive axial force of 4822343.81 N.



Source: prepared by the author.

Comparisons between the pipeline post-buckling configurations obtained using Taylor and Tran (1996) and the simplified numerical model presented in this section cannot be made directly since the analytical model was described only for stress free initial configurations. Unlike the critical load that could be estimated considering the pre-stress effect, modifications in the post-upheaval buckling formulation are not straightforward, not being scope of the present work. Nevertheless, with the readily available data, it is possible to observe from Figure 73 that the inclusion or not of the pre-stress interferes considerably not only in the critical load but also in the post-buckling configuration of the pipeline, making important its consideration when the post-buckling analysis is necessary, as, for example, in the study of failure modes resulting from buckling of pipelines.

Figure 73 – Post-buckling configurations of the pipeline at the time 1.2 s.



Source: prepared by the author.

### 5.3.2 Models with imperfections represented by rigid surfaces

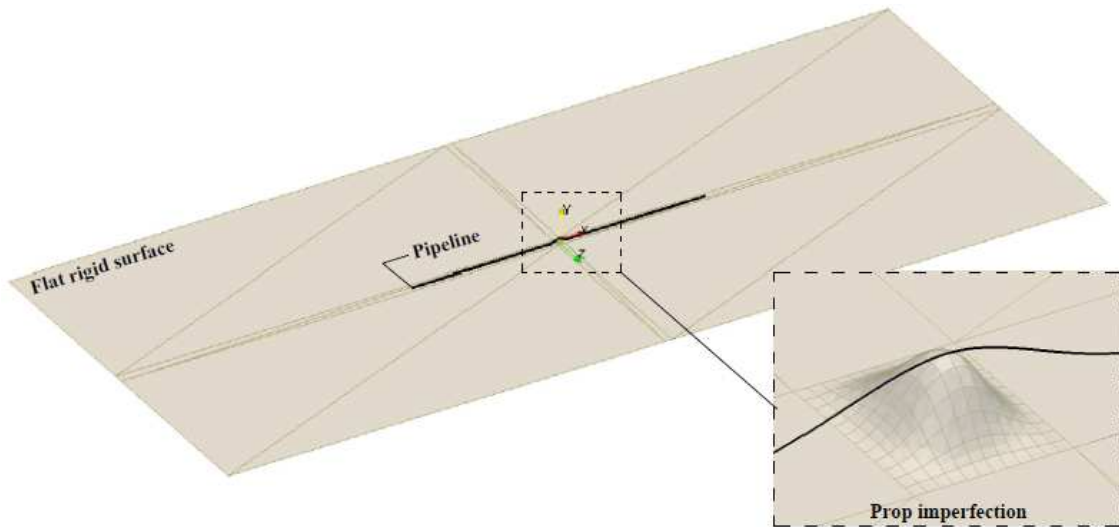
Once a more simplified version of the present numerical model has been verified and compared to an existing analytical model, this section presents advances in the numerical model in order to verify the discussions about the approaches for applying the internal pressure and to study the influence of the imperfection amplitude and of the friction between the pipeline and the soil in upheaval buckling.

#### 5.3.2.1 Approaches for applying the internal pressure and influence of the imperfection amplitude in upheaval buckling

To verify the approaches for applying the internal pressure and to discuss the influence of the imperfection amplitude in upheaval buckling, numerical simulations are employed, in which the isolated imperfection is represented by a rigid surface inserted in the middle of a flat rigid surface and under the center of the pipeline. So, the imperfection can be detected by the contact model as a region of the soil. The imposition of the imperfection in such a way represents a step forward in relation to the model presented in Section 5.3.1, making the simulations closer to the mechanisms that occur in reality. This is because, in the simulation of Section 5.3.1, the loss of contact between the pipe and the imperfection was imposed manually by eliminating the restriction to the displacement in  $y$ -direction of the central node when  $P_u$  is reached, which is a procedure based on the analytical formulation proposed by Taylor and Tran (1996). That is, it was not possible to “disconnect” the numerical models from the analytical models, which is not convenient in practice.

For modeling the isolated imperfection, it is used the oscillatory rigid surface described in Section 4.3. Four imperfection amplitudes are used to perform the simulations: 0.05 m, 0.25 m, 0.50 m and 1.00 m. These imperfections are modeled with one wave in each direction (Figure 74). Besides this, the wave-lengths in each direction are chosen in such a way that the pipeline, when released from the level of the imperfection and under the action of its self-weight, establishes only one point of contact with the top of the imperfection. It originates the afore called prop imperfection and, to obey this condition, the resulting imperfection wave-lengths are, respectively: 2.5 m, 12.5 m, 25 m and 50 m. The parameters of Eq. (187) assumed to create the imperfections are described in Table 8 and Table 9.

Figure 74 – Location and shape of the isolated imperfection.



Source: prepared by the author.

Table 8 – Parameters used to create the prop imperfections – part 1.

Imp. N <sup>o</sup>	Amplitude (m)	Wave-length (m)	A <sub>1</sub> (m)	A <sub>2</sub> (m)	A <sub>12</sub> (m)
1	0.05	2.5	-0.0125	0.0125	-0.0125
2	0.25	12.5	-0.0625	0.0625	-0.0625
3	0.50	25.0	-0.1250	0.1250	-0.1250
4	1.00	50.0	-0.2500	0.2500	-0.2500

Source: prepared by the author.

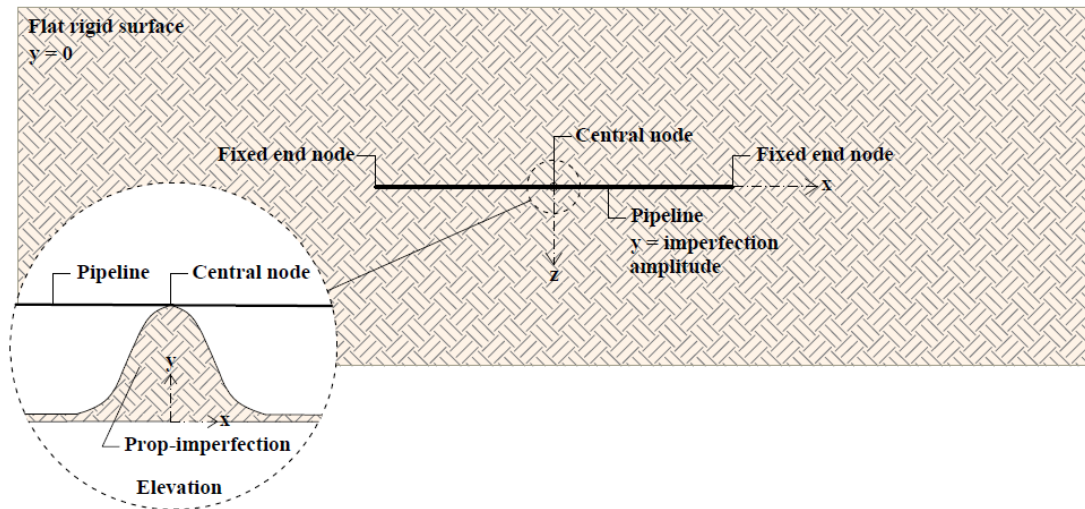
Table 9 – Parameters used to create the prop imperfections – part 2.

Imp. N <sup>o</sup>	$\lambda_1$ (m)	$\lambda_2$ (m)	$\phi_1$ (rad)	$\phi_2$ (rad)
1	2.5	2.5	$-\pi/2$	$\pi/2$
2	12.5	12.5	$-\pi/2$	$\pi/2$
3	25.0	25.0	$-\pi/2$	$\pi/2$
4	50.0	50.0	$-\pi/2$	$\pi/2$

Source: prepared by the author.

At the beginning of the simulation, unlike the simplified model in which the pipeline is initially at the ground level, the pipeline is disposed straightly at the level of the top of the imperfection. For the first simulations, friction is still not considered and, again, the displacement in z-direction of all nodes is restricted and the end nodes are fixed. Figure 75 illustrates the initial layout of the pipeline.

Figure 75 – Initial layout of the models with imperfections represented by rigid surfaces – plan view and elevation.



Source: prepared by the author.

For establishing the imperfect initial configuration of the pipeline from the initial layout, it is necessary to simulate the process of laying the pipeline on the prop imperfection. This stage is developed statically through four load steps, which seek to eliminate possible numerical problems due to rigid body movement during the laying process. The four load steps are described in Table 10.

Table 10 – Static load steps used to simulate the laying process of the pipeline on the ground with a prop imperfection.

Load steps	Description
1	Application of the pipeline self-weight.
2	Restriction of all degrees of freedom of the central node of the pipeline.
3	Release of all degrees of freedom, with the exception of the displacement in z-direction, of the end nodes of the pipeline.
4	Release of all degrees of freedom, with the exception of the displacement in z-direction, of the central node of the pipeline.

Source: prepared by the author.

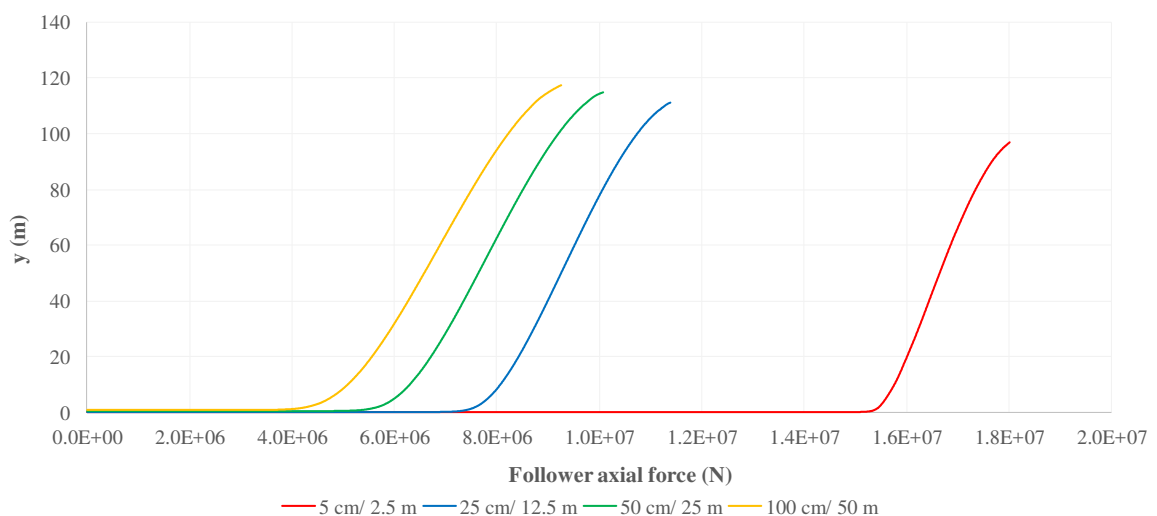
At the end of the laying process, the imperfect initial configuration of the pipeline is established with a reaction at the central node that represents the contact between the pipeline and the soil. It is possible to use this reaction as a parameter of comparison between

the present model and the analytical model proposed by Taylor and Tran (1996). For example, for the case with imperfection amplitude equal to 0.50 m, the contact force that appears at the central node is 143130 N, which differs only in 0.032% from the force applied in load step 1 of the model of Section 5.3.1.

Once the imperfect initial configuration of the pipeline has been established, it is subjected dynamically to the internal pressure load. The analysis of the influence of the imperfection amplitude in upheaval buckling is made firstly from the results obtained through the application of follower compressive axial forces equivalent to the internal pressure at the pipeline end nodes. Then, the same type of results is obtained through the application of the internal pressure properly speaking, by Eq. (190). As already mentioned, the follower compressive axial force was estimated by analytical prediction – Eq. (98), but taking a larger value to also capture post-buckling configurations. So, the magnitude chosen is 25000000 N. Using Eq. (188), the corresponding internal pressure is approximately 82806942 Pa.

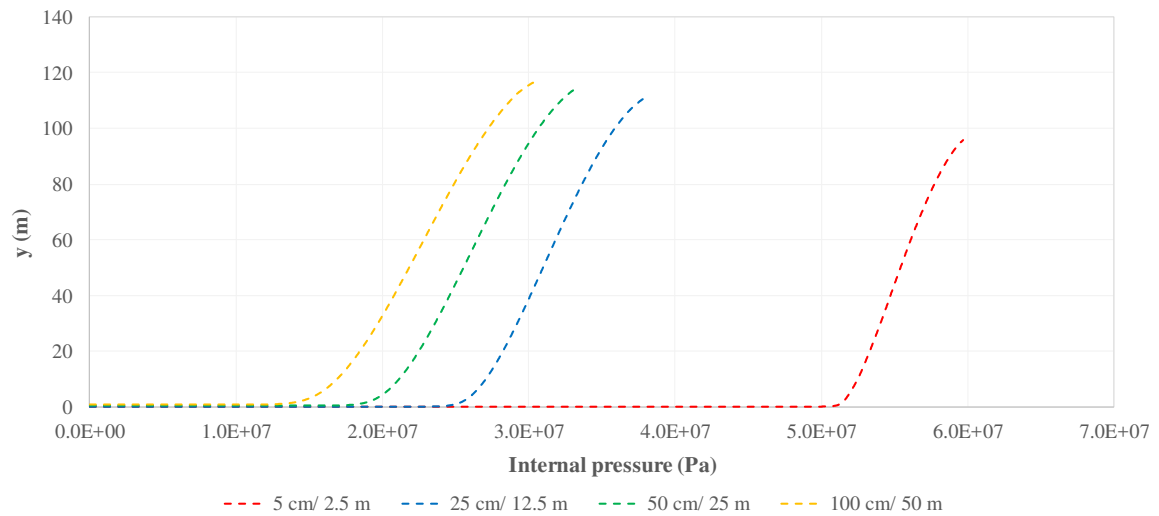
The graph of the coordinate  $y$  of the central node of the pipeline versus the follower compressive axial force is shown in Figure 76 for the four ratios between the imperfection amplitude and the imperfection wave-length analyzed. The graph presented in Figure 77, in its turn, shows the coordinate  $y$  of the central node of the pipeline versus the internal pressure for the same imperfections. Finally, Figure 78 presents a comparison between Figure 76 and Figure 77 in terms of the time of load application, which can be obtained using Figure 38.

Figure 76 – Coordinate  $y$  of the central node versus the load applied – follower axial force.



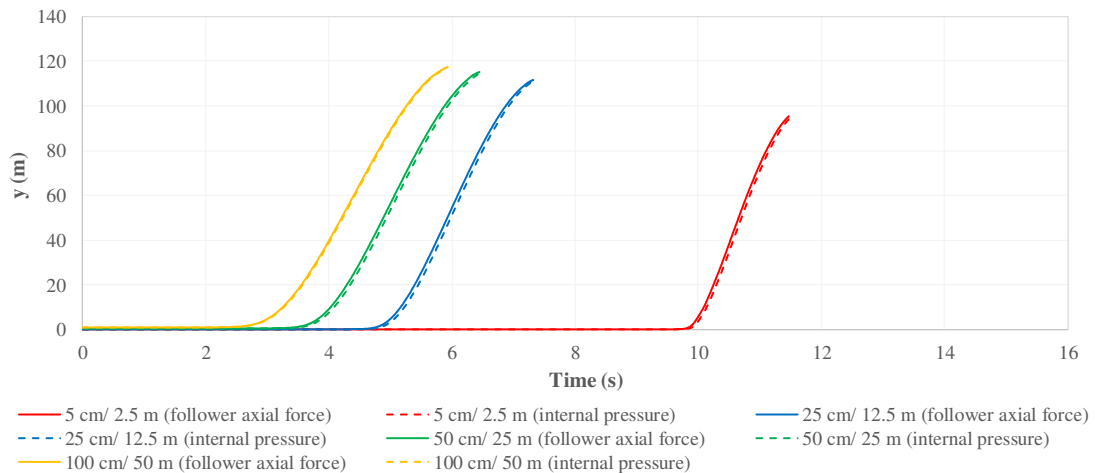
Source: prepared by the author.

Figure 77 – Coordinate  $y$  of the central node versus the load applied – internal pressure.



Source: prepared by the author.

Figure 78 – Coordinate  $y$  of the central node versus the load applied – comparison between the application of follower axial forces and internal pressure.

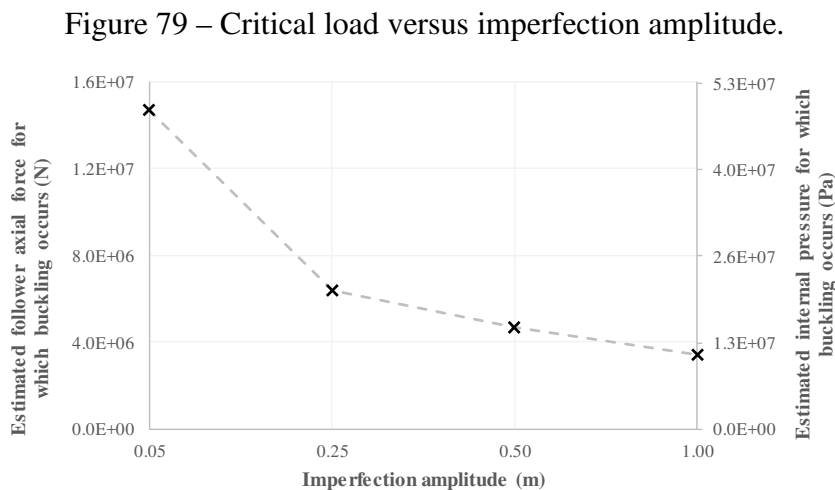


Source: prepared by the author.

Through Figure 78, it is possible to observe the equivalence between the application of the compressive axial forces and the application of the internal pressure by Eq. (190), since Eq. (188) is obeyed. The two approaches provide approximately the same graphs of the coordinate  $y$  of the pipeline central node versus the load applied. It is important to mention that the compressive axial forces have the same follower behavior as the internal pressure, in which the direction of the forces depends on the pipeline deflections. For the cases shown in the present section, however, in which the buckle region is limited to the central region of the pipeline, the follower behavior of the axial forces is not an essential factor for the

coincidence of the results of the two load approaches. It occurs because the axial loads are applied at the pipeline ends, so their directions do not change significantly. If the buckle region extended over the entire length of the pipeline, the axial force behavior would play a more important role for the coincidence of the results.

Another topic that can be analyzed from Figure 76, Figure 77 and Figure 78 is the influence of the imperfection amplitude in the buckling critical load. It is possible to observe that larger imperfection amplitudes lead to smaller buckling critical loads, which coincides with the previous results of several authors mentioned in Section 2.3. Another aspect that can be commented is that the buckling critical load does not change in the same ratio of the imperfection amplitude. Besides this, the ratio between the variation of critical load and of imperfection amplitude is dependent on the imperfection amplitude. Figure 79 demonstrates the nonlinear relationship between the critical loads and the imperfection amplitudes.

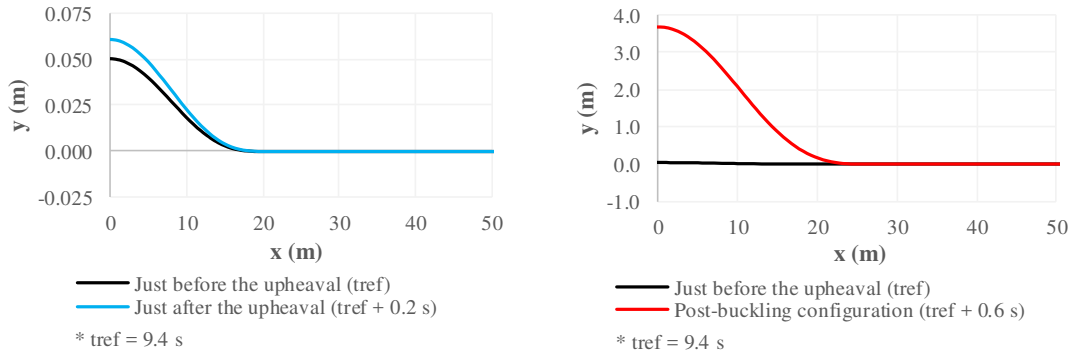


Source: prepared by the author.

Besides the comparisons between the critical loads for different imperfections, it is important to present comparisons in terms of post-buckling configurations. It is worth mentioning that, although there are analytical studies that present expressions for the deformed configuration of the pipeline, comparisons of the shapes of these configurations are not so common in those studies. They are necessary to understand how is the pipeline behavior after the buckling begins. Figure 80 to Figure 83 present the post-buckling configurations for the four imperfections analyzed. Since such configurations are symmetrical, only half of the pipeline is presented. It can be observed that, for the same load increase from the buckling critical loads, the smallest imperfection amplitude leads to the largest displacements in y-direction and as the amplitude increases, such displacements tend to stabilize with smaller

values. It occurs because, for smaller imperfections, the buckling occurs with larger loads and, thus, more energy is accumulated, resulting in larger and more abrupt displacements.

Figure 80 – Post-buckling configurations for the imperfection 0.05 m/2.5 m.

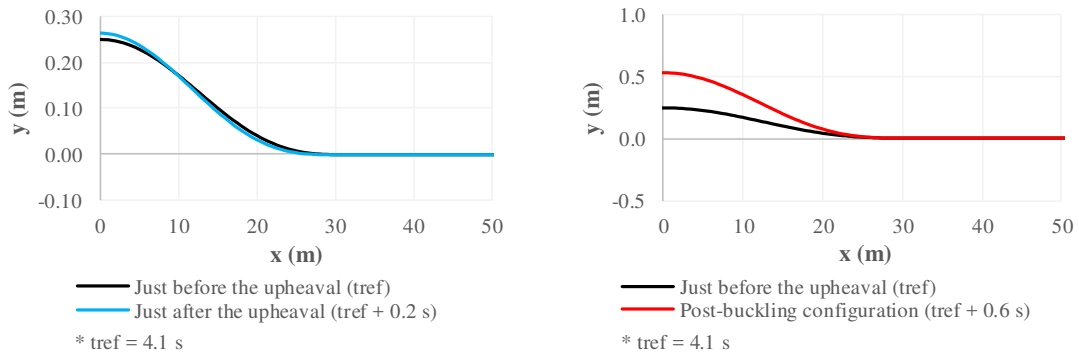


(a) at the times 9.4 s and 9.6 s

(b) at the times 9.4 s and 10.0 s

Source: prepared by the author.

Figure 81 – Post-buckling configurations for the imperfection 0.25 m/12.5 m.

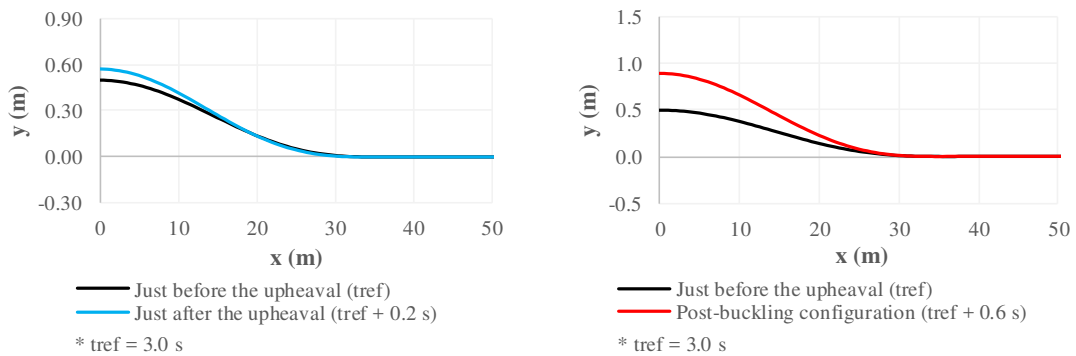


(a) at the times 4.1 s and 4.3 s

(b) at the times 4.1 s and 4.7 s

Source: prepared by the author.

Figure 82 – Post-buckling configurations for the imperfection 0.50 m/25 m.

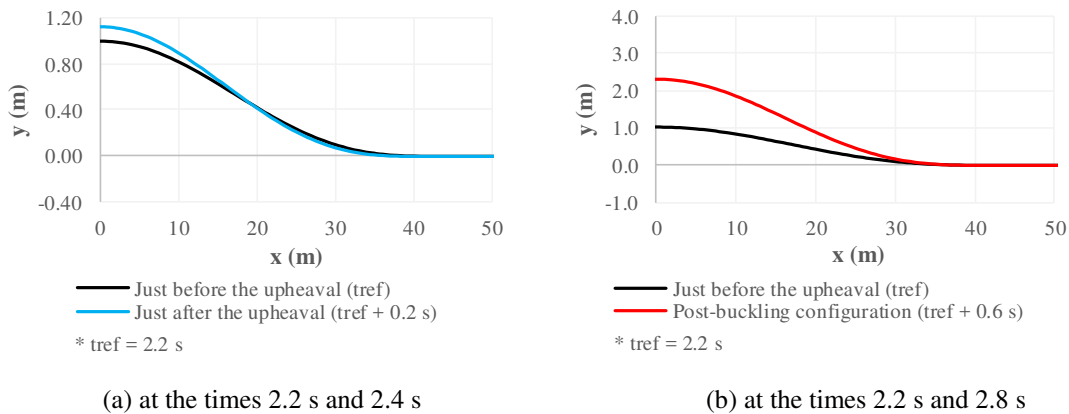


(a) at the times 3.0 s and 3.2 s

(b) at the times 3.0 s and 3.6 s

Source: prepared by the author.

Figure 83 – Post-buckling configurations for the imperfection 1.00 m/50 m.

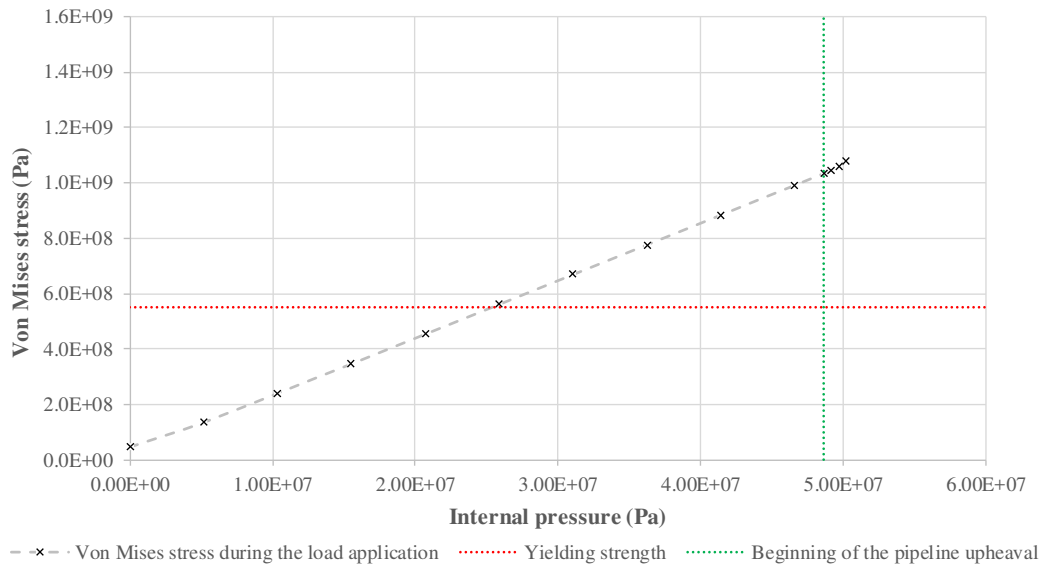


Source: prepared by the author.

In Section 5.1.1, it was commented that the numerical simulations of the present work assume that the constitutive equation of the steel follows the Hooke's law. This is a limitation of the numerical model since, obviously, this is not always valid in practice, depending on the level of stress to which the pipeline is subjected and on the material strength. Although the intention of the work is not to address the plastic deformation range of the steel, it is important to verify, for the cases studied, even if simplistically, for which level of loading the elastic-linear assumption remains valid using the steel API 5L X80. For that, the Von Mises criterion is used.

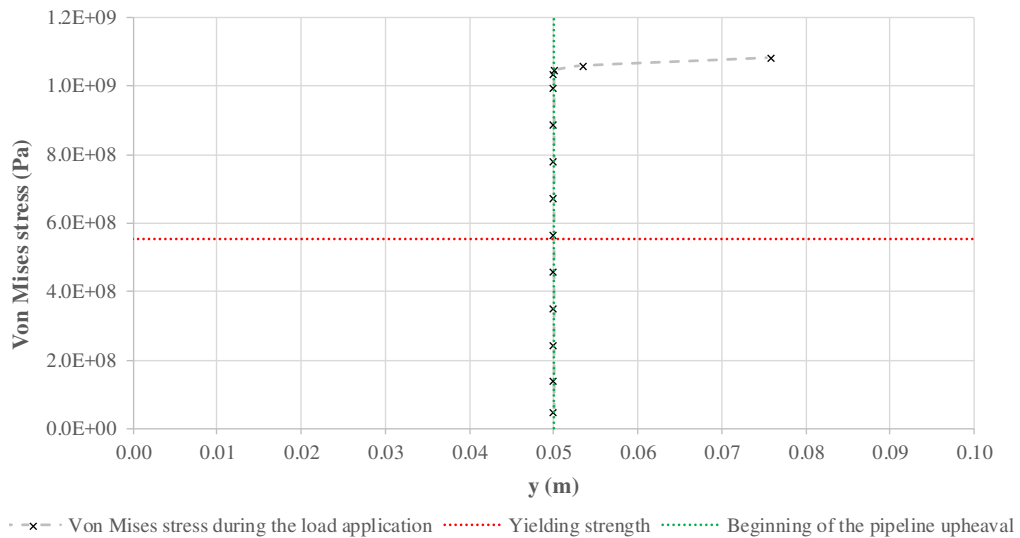
Figure 84 shows the evolution of the Von Mises stress at the central cross section of the pipeline during the application of the internal pressure for the imperfection amplitude equal to 0.05 m. For the evaluation of the Von Mises stress by Eq. (17), only the longitudinal and hoop stresses (determined from the internal loads of the structure and from Eq. (12), respectively) are considered, that is, it is assumed that the pipeline is a thin-walled pipe. It is also worth mentioning that always the worst combination of stresses (unfavorable for safety) was considered to determine the Von Mises stress. Figure 85, for a visual understanding of the limit of the elastic-linear assumption, shows the relationship between the normal stress at the central cross section of the pipeline and the coordinate  $y$  of its axis. It is possible to see that, before the beginning of the pipeline upheaval, the stress exceeds the yielding strength of the steel API 5L X80 and, therefore, the elastic-linear assumption is not valid and the pipeline starts to have plastic strains.

Figure 84 – Von Mises stress at the central cross section of the pipeline versus internal pressure for the imperfection 0.05 m/2.5 m.



Source: prepared by the author.

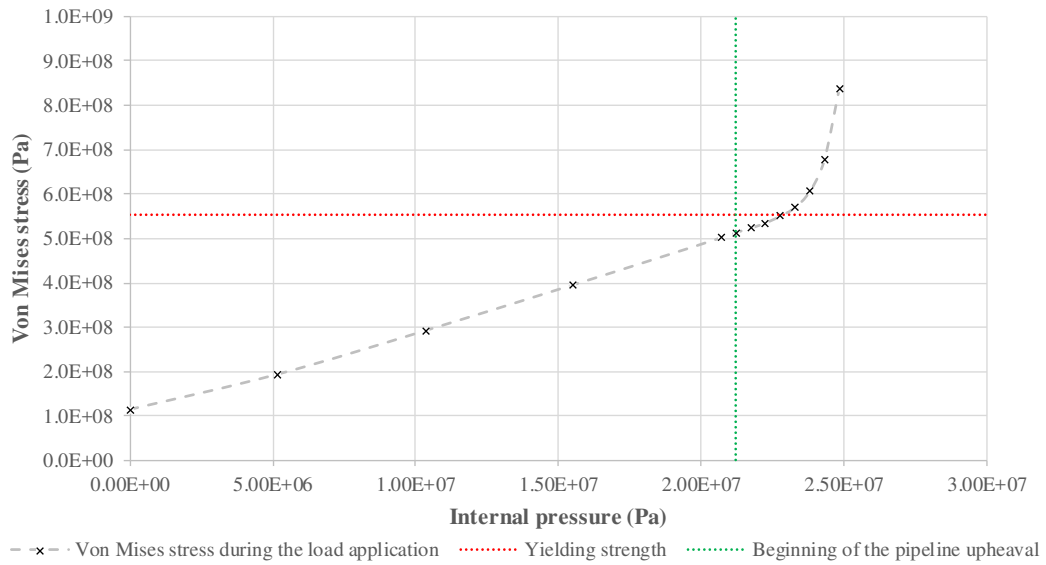
Figure 85 – Von Mises stress at the central cross section of the pipeline versus coordinate y for the imperfection 0.05 m/2.5 m.



Source: prepared by the author.

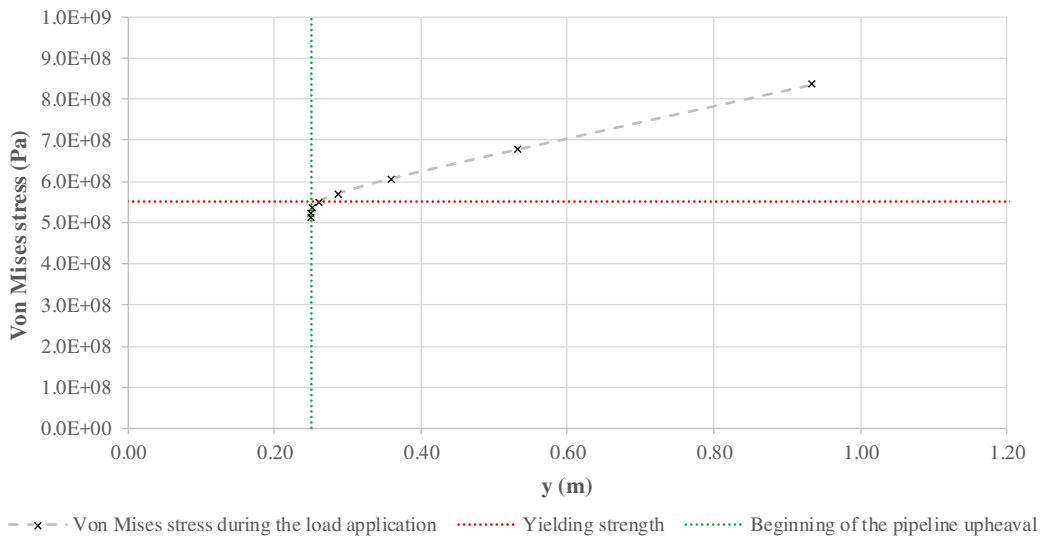
The same analysis can be done for the other three imperfections. Figure 86 to Figure 88 present the results for the imperfection amplitude equal to 0.25 m. It is possible to see that the Von Mises stress exceeds the yielding strength of the steel API 5L X80 after the pipeline upheaval. For this case, to ensure elastic strains, the internal pressure cannot exceed 22816573 Pa, which corresponds to the coordinate y of the central cross section of the pipeline equal to 0.263 m.

Figure 86 – Von Mises stress at the central cross section of the pipeline versus internal pressure for the imperfection 0.25 m/12.5 m.



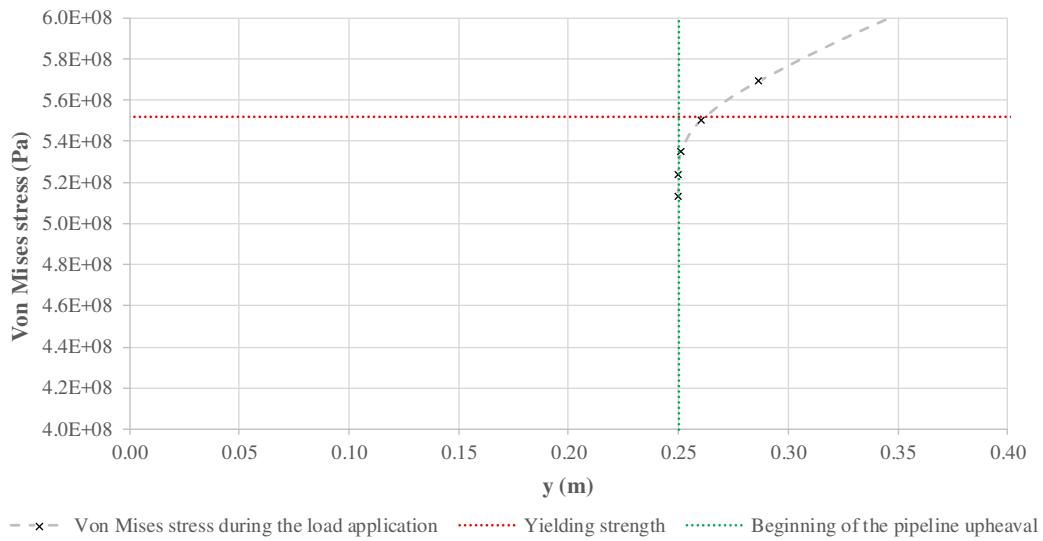
Source: prepared by the author.

Figure 87 – Von Mises stress at the central cross section of the pipeline versus coordinate y for the imperfection 0.25 m/12.5 m.



Source: prepared by the author.

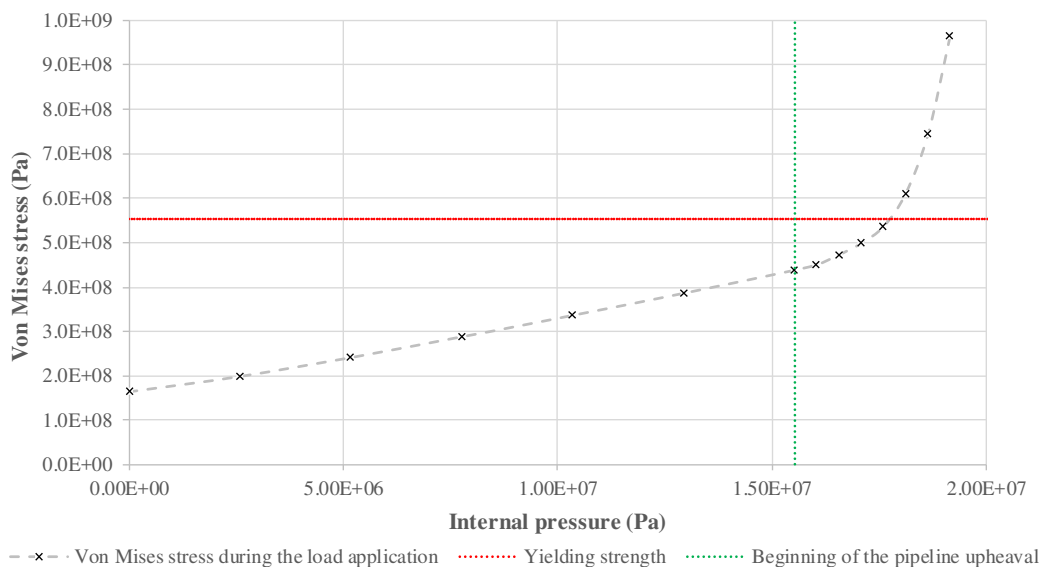
Figure 88 – Von Mises stress at the central cross section of the pipeline versus coordinate y for the imperfection 0.25 m/12.5 m – detail of the pre-upheaval stage.



Source: prepared by the author.

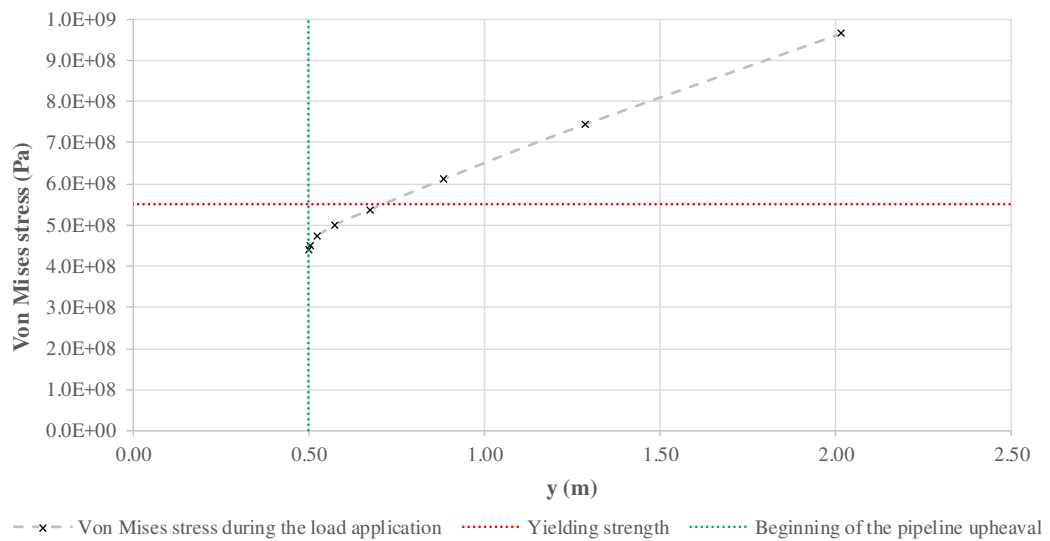
Figure 89 to Figure 91 present the results for the imperfection amplitude equal to 0.50 m. To belong to the elastic range (again the Von Mises stress exceeds the yielding strength after the pipeline upheaval), the analysis has to be performed with the internal pressure not larger than 17702631 Pa, which corresponds to the coordinate y of the central cross section of the pipeline equal to 0.718 m.

Figure 89 – Von Mises stress at the central cross section of the pipeline versus internal pressure for the imperfection 0.50 m/25 m.



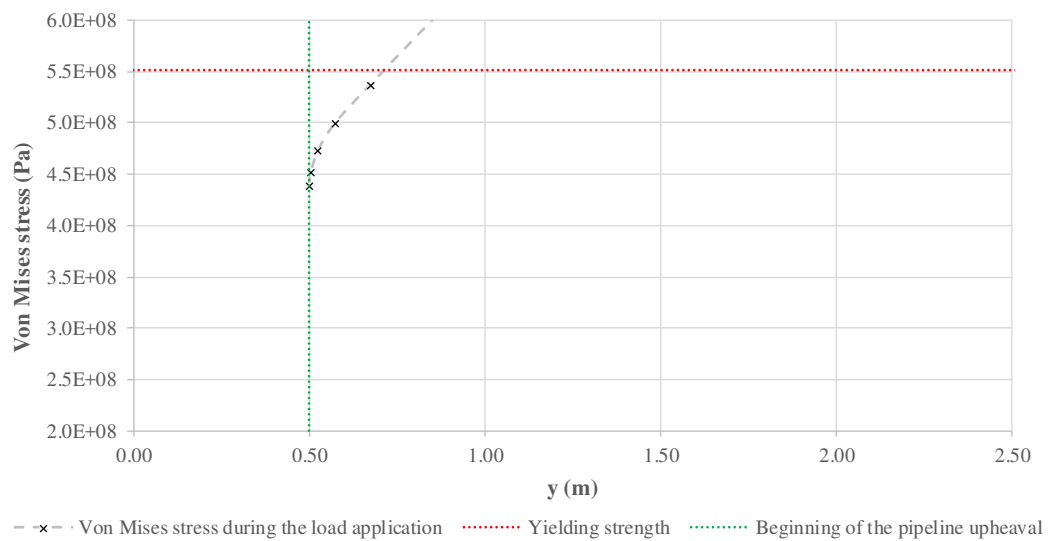
Source: prepared by the author.

Figure 90 – Von Mises stress at the central cross section of the pipeline versus coordinate y for the imperfection 0.50 m/25 m.



Source: prepared by the author.

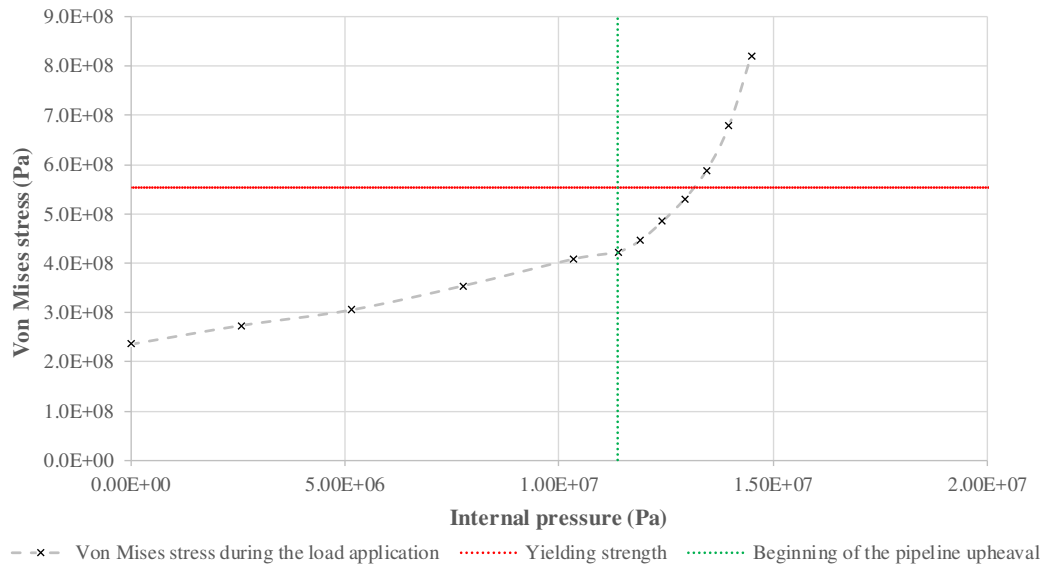
Figure 91 – Von Mises stress at the central cross section of the pipeline versus coordinate y for the imperfection 0.50 m/25 m – detail of the pre-upheaval stage.



Source: prepared by the author.

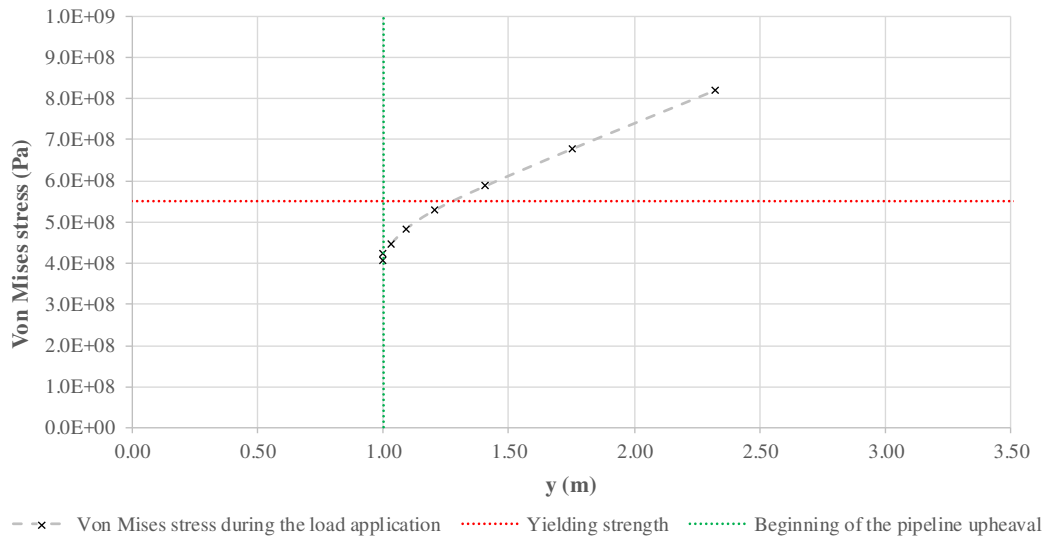
Finally, Figure 92 to Figure 94 present the results for the imperfection amplitude equal to 1.00 m. For the analysis be compatible with the constitutive relation assumed, the internal pressure has to be limited to 13136257 Pa, which corresponds to the coordinate y of the central cross section of the pipeline equal to 1.284 m.

Figure 92 – Von Mises stress at the central cross section of the pipeline versus internal pressure for the imperfection 1.00 m/50 m.



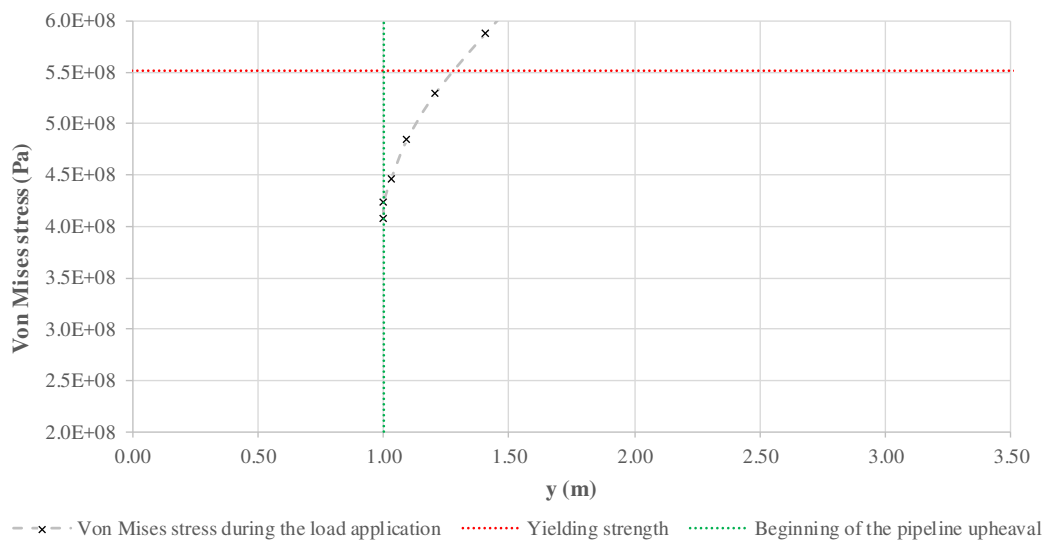
Source: prepared by the author.

Figure 93 – Von Mises stress at the central cross section of the pipeline versus coordinate y for the imperfection 1.00 m/50 m.



Source: prepared by the author.

Figure 94 – Von Mises stress at the central cross section of the pipeline versus coordinate  $y$  for the imperfection 1.00 m/50 m – detail of the pre-upheaval stage.



Source: prepared by the author.

Through the stress analysis, it is possible to observe that, depending on the case, the yielding strength of the steel API 5L X80 can be reached before or after the pipeline upheaval. For the cases of imperfection of the present work, only the imperfection of 0.05 m led to the yielding of the steel before the pipeline upheaval. One explanation for this is in the fact that the pipeline with the smallest imperfection buckles with the largest load, generating more stress due to the increase of internal pressure, in addition to generating more accentuated displacements when the buckling occurs. At the current stage of the research, it is not possible to predict if the consideration of the plasticity implies in significant changes in the results of the present model. As commented, it does not belong to the scope of the present work, but it can be part of a future continuation of it.

### 5.3.2.2 Pointwise contact versus conformal contact between the pipeline and the imperfection

As mentioned, the shape of the imperfections adopted to perform the simulations was chosen in such a way that the imperfect initial configuration of the pipeline had only one point of contact with the top of the imperfection, which characterizes the prop imperfection. It is worth mentioning that, besides this type of imperfection with a pointwise contact with the pipeline, a type of imperfection with a conformal contact also was studied. The results, however, were not relevant for the context of this work and, therefore, they will not be presented with the same details as it is done for the prop imperfection. Only some considerations and

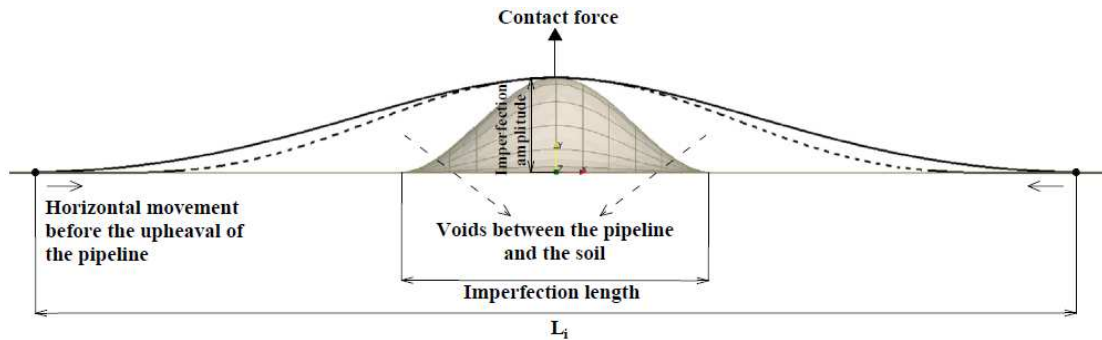
comparisons are interesting to be made.

The amplitudes chosen for the study of the conformal imperfections are the same as those chosen for the study of the prop imperfections: 0.05 m, 0.25 m, 0.50 m and 1.00 m. To transform the prop imperfections into the corresponding conformal imperfections, it is necessary to increase the wave-lengths to 280 m, 620 m, 820 m and 990 m, respectively, in such a way that the pipeline, after the laying process, is totally in contact with the imperfection. Analytical models, as that presented by Taylor and Gan (1986), propose that the shape of the imperfect initial configuration of the pipeline, which coincides with the imperfection shape, results from a vertical deviation from the idealized straight lay of the pipeline. In present numerical models, however, it is not possible to create an imperfection that has the shape of the elastic line of the deformed pipeline, because the imperfection follows the shape of the oscillatory rigid surface, which requires larger wave-lengths than those presented in the analytical models to generate conformal imperfections.

Comparing the buckling critical loads of the pipelines laid on prop imperfections and on conformal imperfections, it can be verified that the last cases have critical loads much larger than the first cases. The model with imperfection amplitude of 0.50 m can be used to exemplify the order of magnitude of the results obtained. In the case of the pipeline laid on the prop imperfection, the buckling critical load, in terms of equivalent compressive axial force, is approximately 5.00 MN. In the case of the pipeline laid on the conformal imperfection, in its turn, the buckling critical load is approximately 165 MN (400 MN were applied in 16 s in order to capture the buckling). It can be noted that the increase of critical load is quite significant, in the order of 3200%.

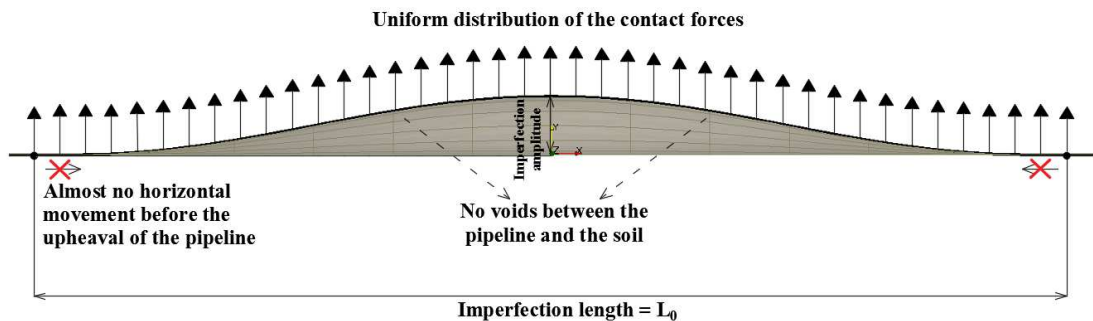
The explanation for the difference of critical loads can be associated with the existing voids between the pipeline and the soil in the case of the prop imperfection and to the absence of such voids in the case of the conformal imperfection. The presence of voids allows the pipeline inward movement, using energy for the pre-upheaval flexure. In the case of the conformal imperfection, however, there is no space for the shortening of the initial wave-length  $L_0$ , that is, there is no pre-upheaval flexure. With such condition, the pipeline accumulates energy when it tries to compress the imperfection, increasing the buckling critical load. The descriptions of the pipeline pre-upheaval stages are presented schematically in Figure 95 and Figure 96 for the prop imperfection and for the conformal imperfection, respectively.

Figure 95 – Prop imperfection.



Source: prepared by the author.

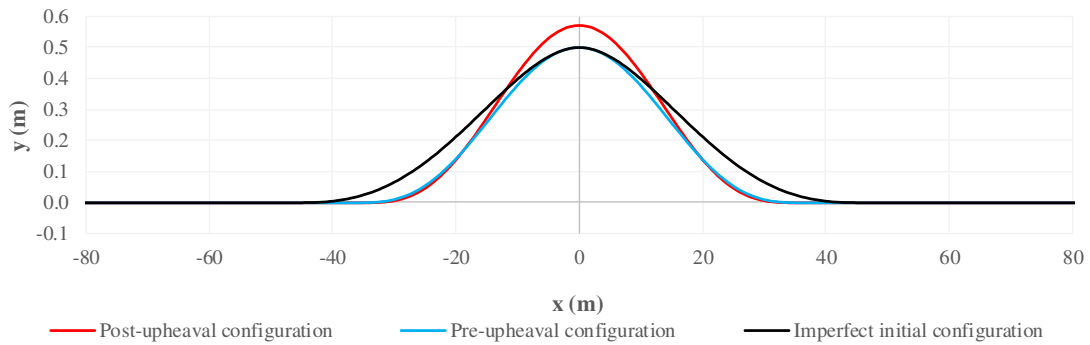
Figure 96 – Conformal imperfection.



Source: prepared by the author.

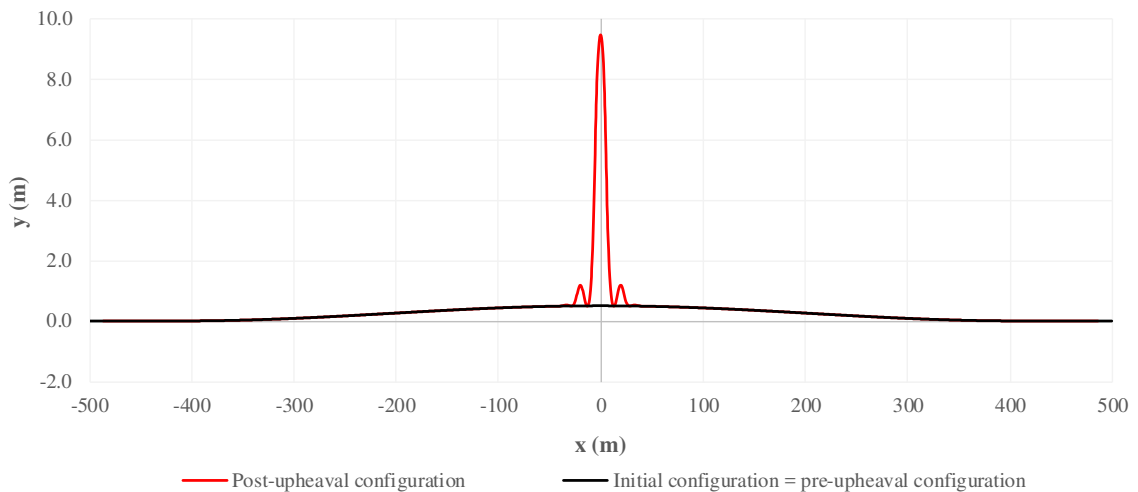
Besides the difference between the critical loads, the prop imperfection and the conformal imperfection analyzed induce different buckling modes in the pipeline. The buckling mode that arises in the prop imperfection case is the first buckling mode characterized by a half-wave and that requires the smallest critical load. The arising of this buckling mode starts to be outlined in the pre-upheaval flexure that occurs due to the existing voids. The conformal imperfection, unlike the previous, has an approximately initial uniform distribution of the contact forces due to the continuous contact between the pipeline and the soil. It hinders the pre-upheaval flexure of the pipeline, accumulating more energy in the pipeline with the increase of the load applied. So, when the buckling occurs, it occurs with a larger critical load and the pipeline assumes a higher buckling mode with multiple waves. The difference of buckling modes between the two types of imperfection analyzed can be seen schematically in Figure 97 and Figure 98.

Figure 97 – Buckling mode of the prop imperfection.



Source: prepared by the author.

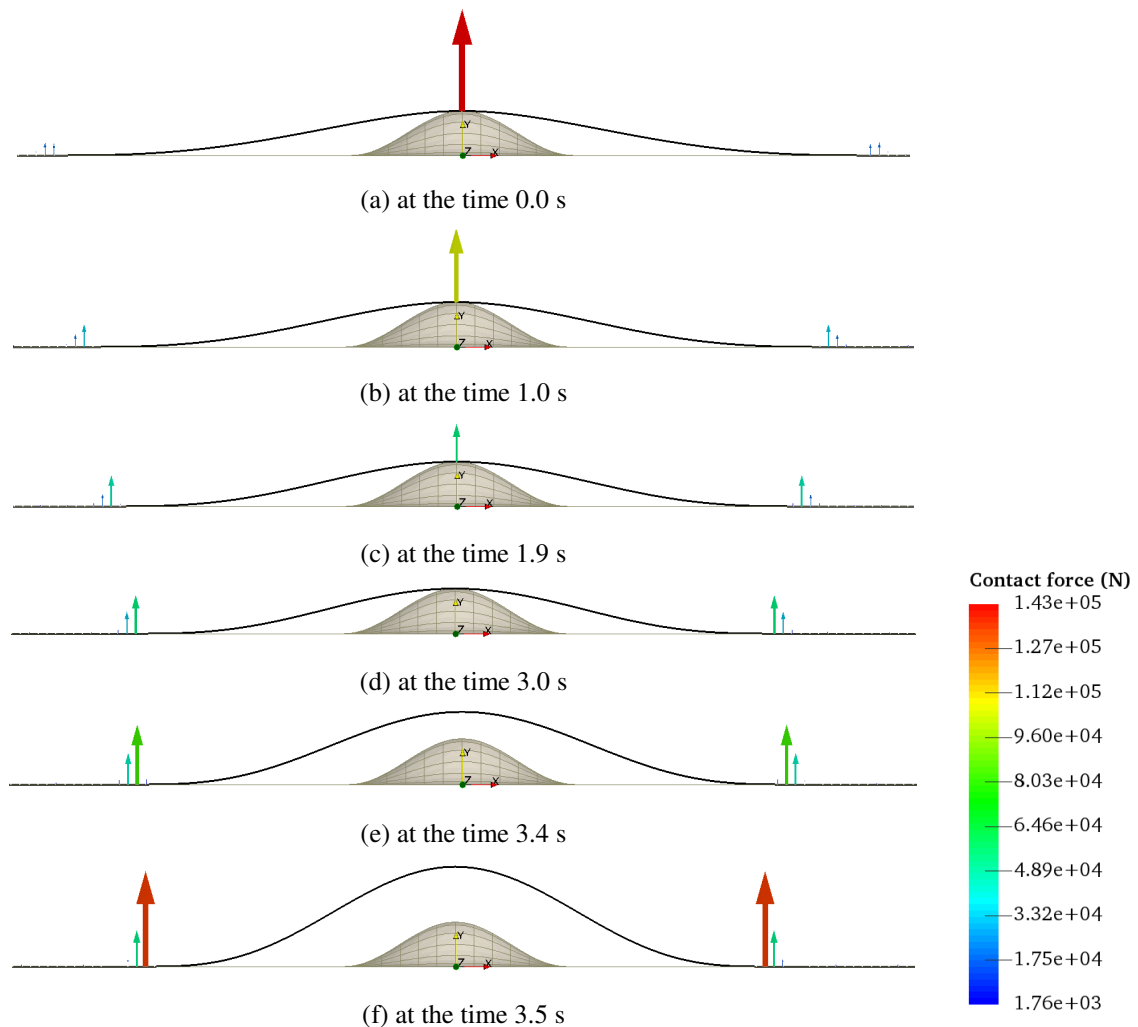
Figure 98 – Buckling mode of the conformal imperfection.



Source: prepared by the author.

For the prop imperfection case, Figure 99 shows the evolution of the contact forces during the application of the dynamic load. It is possible to note that, with the increase of the load, there is a decrease of the contact force at the pipeline central node, that is, on the top of the imperfection. This decrease is accompanied by the increase of the contact forces at the ends of the buckle length. These, by the way, have an inward movement that demonstrates the decrease of the buckle length that occurs in pre-upheaval flexure. From the instant that the contact force at the central node becomes zero (Figure 99d), the pipeline upheaval starts. It is important to emphasize that there are also contact forces in the regions external to the buckle length, but these forces have smaller magnitudes than those in the buckle region, not being visible in the scale presented in Figure 99.

Figure 99 – Contact forces for the prop imperfection case at the times 0.0 s, 1.0 s, 1.9 s, 3.0 s, 3.4 s and 3.5 s.



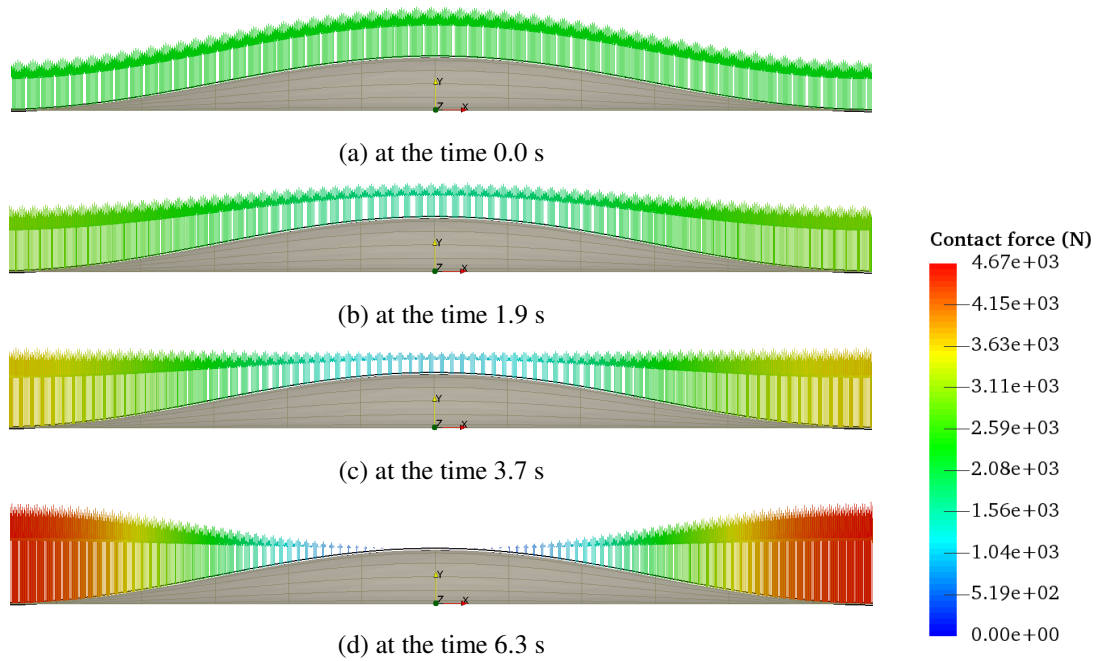
Source: prepared by the author.

Figure 100 to Figure 102, in their turn, show the evolution of the contact forces during the application of the dynamic load for the conformal imperfection case. It is possible to note that, with the increase of the load, the initial uniform distribution of the contact forces is modified: there is a decrease of the contact forces at the central region of the imperfection and an increase of the contact forces at the end regions of the imperfection. However, there is no inward movement, that is, there is no pre-upheaval flexure. Figure 101 and Figure 102 present details of the central region of the pipeline after the beginning of the upheaval. Since the central contact forces that appear after the upheaval are quite large when compared to the adjacent forces, the latter do not appear in the scale of Figure 101 and Figure 102.

The two types of imperfections commented in the present work do not represent the infinite types of imperfections that can happen in practice. Other types of imperfection can,

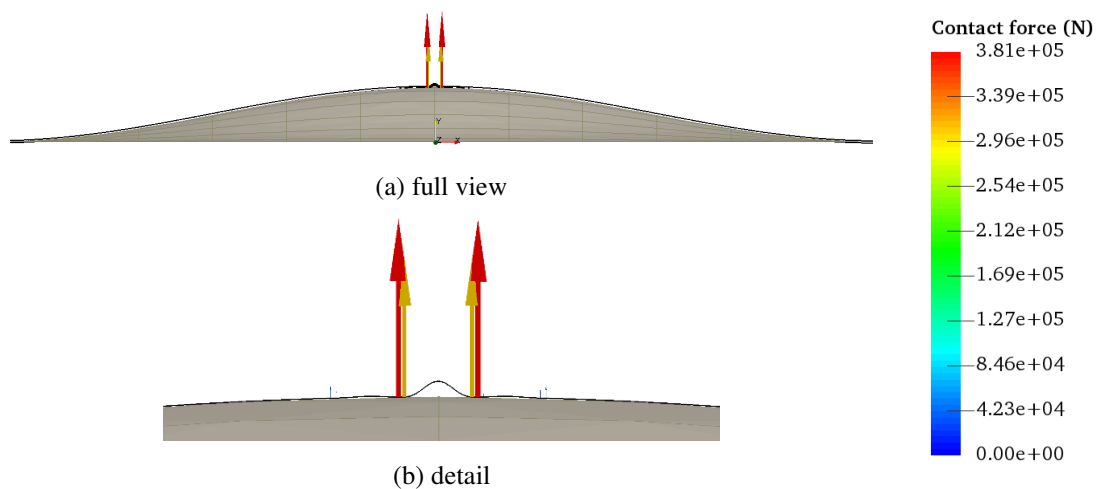
for example, increase or decrease the critical loads presented. Therefore, since the conformal imperfection analyzed is more favorable for safety, it will not be dealt with details in the present work (from an engineering point of view).

Figure 100 – Contact forces for the conformal imperfection case at the times 0.0 s, 1.9 s, 3.7 s and 6.3 s.



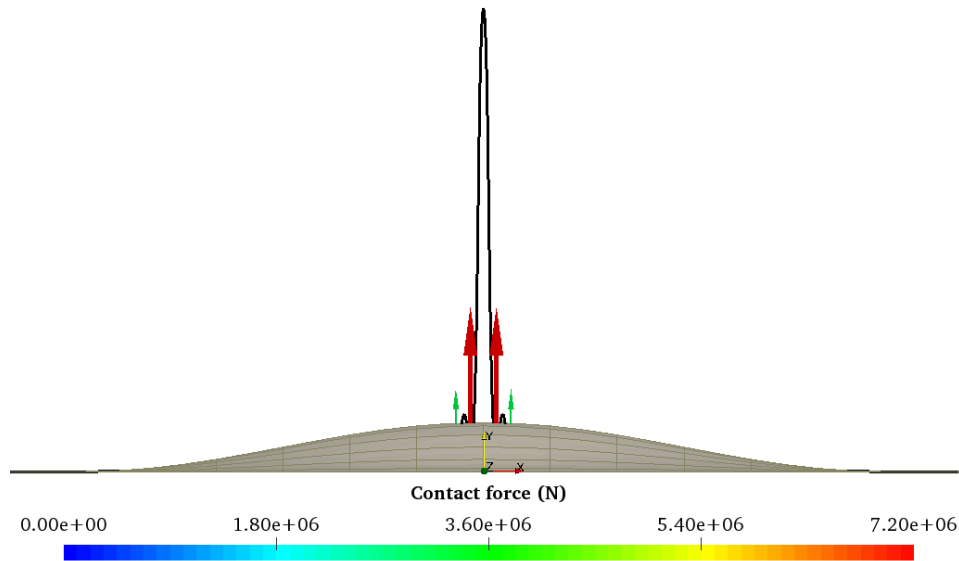
Source: prepared by the author.

Figure 101 – Contact forces for the conformal imperfection case at the time 6.5 s.



Source: prepared by the author.

Figure 102 – Contact forces for the conformal imperfection case at the time 6.6 s.



Source: prepared by the author.

### 5.3.2.3 Influence of the friction between the pipeline and the soil in upheaval buckling

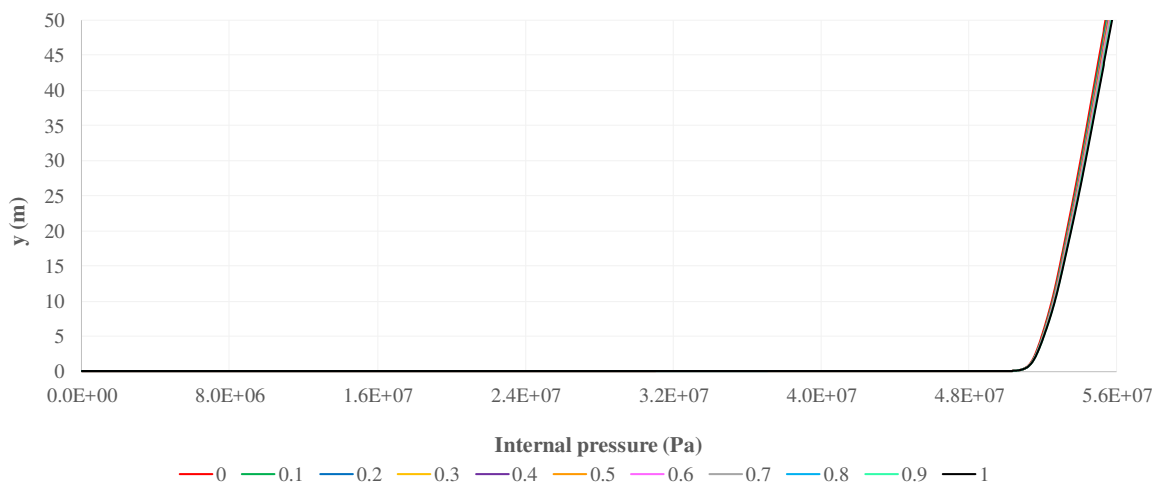
All previous simulations did not consider friction between the pipeline and the soil. Although this condition is not compatible with practical cases, it allowed to analyze independently the effects of the type of loading and of the imperfection amplitude in upheaval buckling. Once these effects have been analyzed, the friction can be included in the numerical model in order to verify its influence in the upheaval buckling of pipelines. For each of the four imperfections presented, ten different coefficients of friction are used to perform the simulations. These coefficients of friction range from 0.1 to 1.0 with a step of 0.1.

With respect to the approaches used for applying the internal pressure, only the application of the internal pressure with the aid of Eq. (190) can be used directly in the models with friction, in order to produce coherent results. This is because, since the friction can act over the entire length of the pipeline, only the distributed load of Eq. (190) provides realistic scenarios. If axial forces were applied in a concentrated way at the pipeline ends, they would have their effects diminished gradually by the friction over the pipeline length. So, depending on the pipeline length, the axial forces could be totally annulled by the friction, not allowing the buckling of the pipeline. To use axial forces for representing approximately the internal pressure effect, it is necessary to determine their magnitude from Eq. (188), incorporating the friction effect in the term  $T_{tw}$ . Such approach is commented in Bai and Bai (2014). However, in the present work, it was chosen to use only the application of the internal pressure by Eq.

(190) in the simulations with friction.

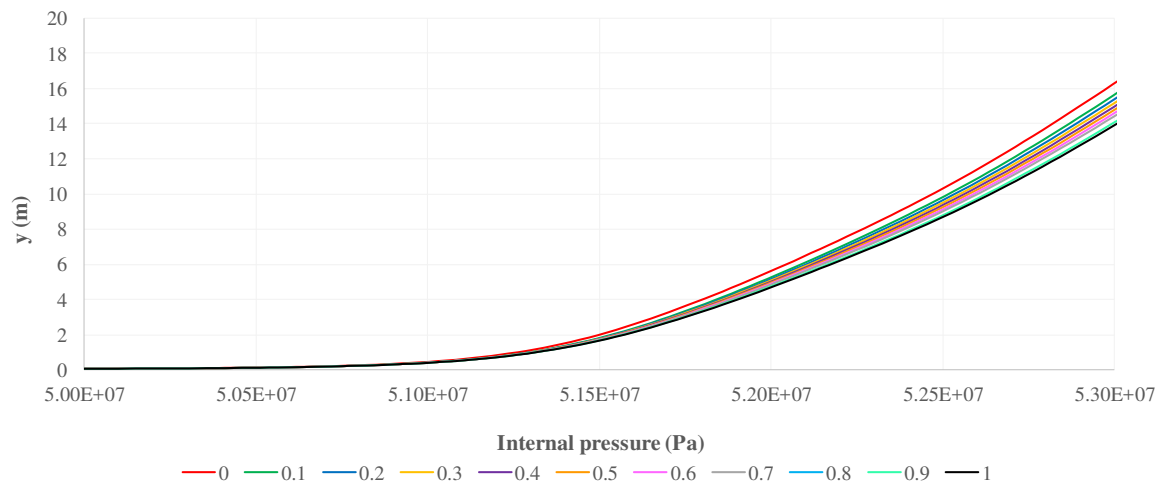
All stages of loading of the models without friction are maintained in the models with friction: the static laying process of the pipeline and the dynamic application of 82806942 Pa of internal pressure in 16 s. The graphs of the coordinate y of the central node of the pipeline versus the internal pressure are shown in Figure 103 to Figure 110 for the four imperfection amplitudes.

Figure 103 – Coordinate y of the central node versus the internal pressure for distinct friction coefficients – imperfection amplitude equal to 0.05 m.



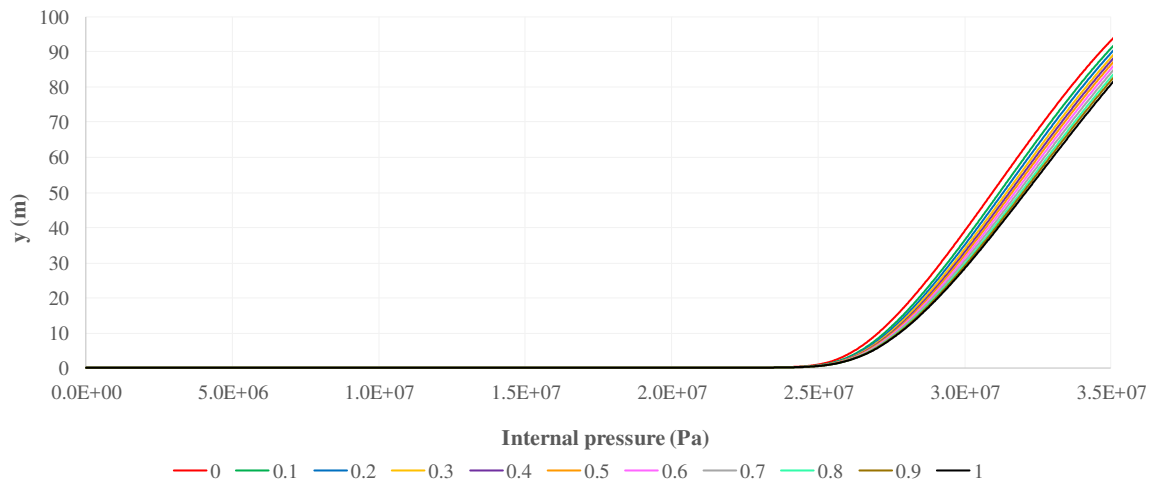
Source: prepared by the author.

Figure 104 – Coordinate y of the central node versus the internal pressure for distinct friction coefficients – imperfection amplitude equal to 0.05 m – detail.



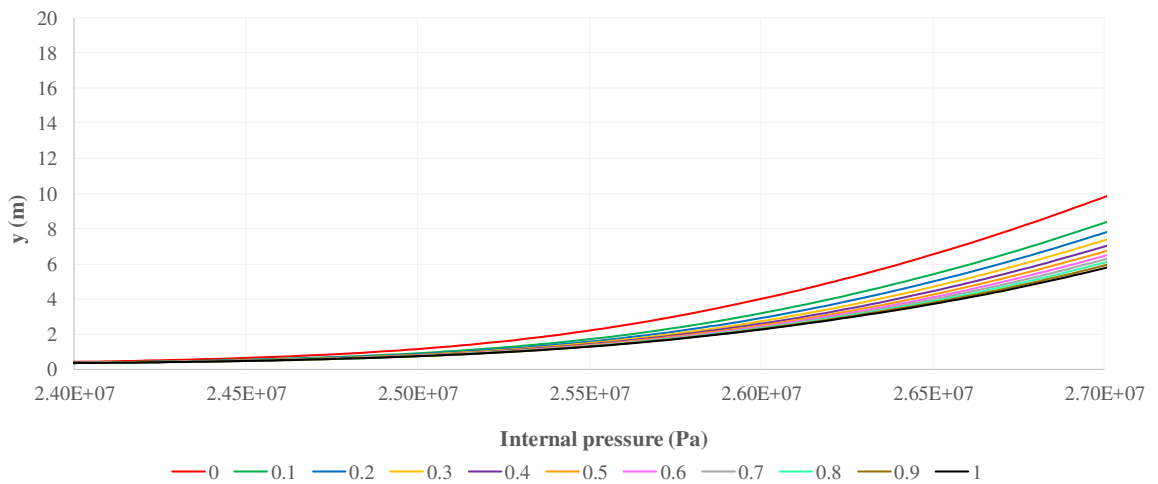
Source: prepared by the author.

Figure 105 – Coordinate y of the central node versus the internal pressure for distinct friction coefficients – imperfection amplitude equal to 0.25 m.



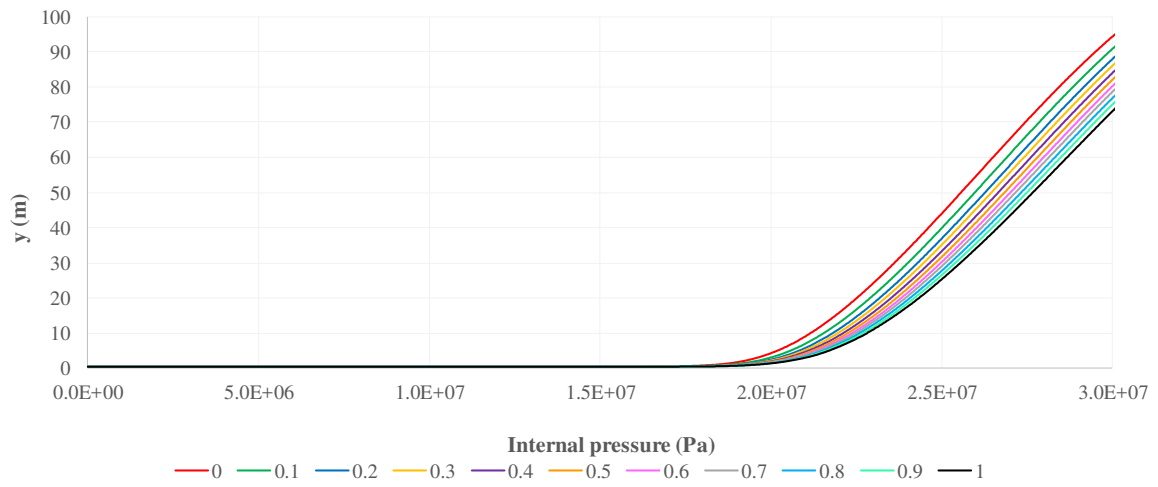
Source: prepared by the author.

Figure 106 – Coordinate y of the central node versus the internal pressure for distinct friction coefficients – imperfection amplitude equal to 0.25 m – detail.



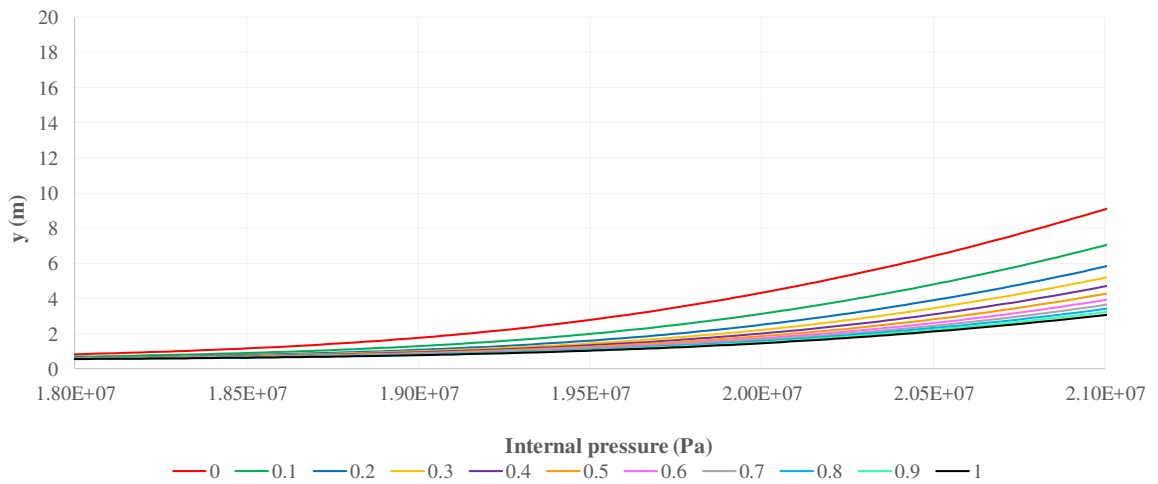
Source: prepared by the author.

Figure 107 – Coordinate y of the central node versus the internal pressure for distinct friction coefficients – imperfection amplitude equal to 0.50 m.



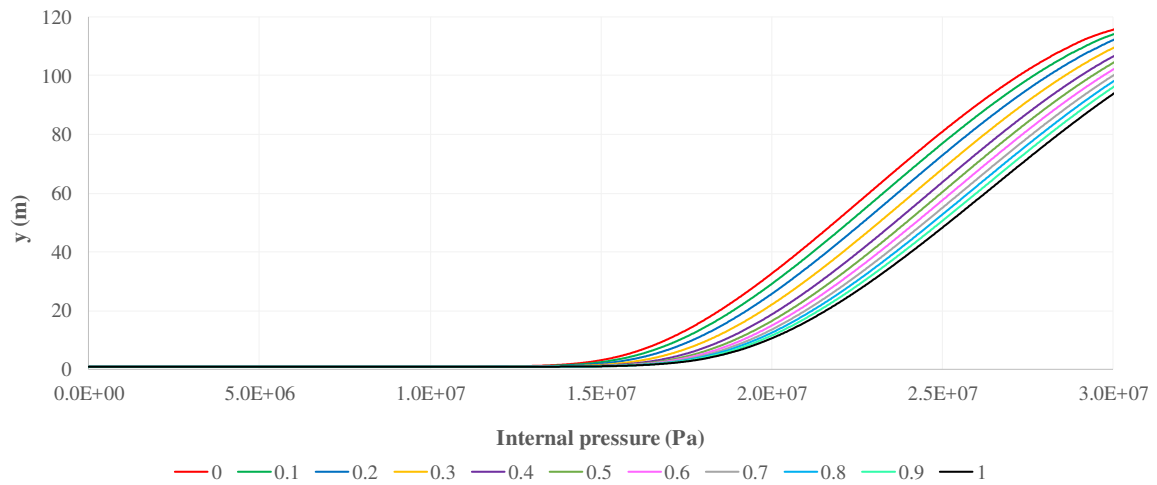
Source: prepared by the author.

Figure 108 – Coordinate y of the central node versus the internal pressure for distinct friction coefficients – imperfection amplitude equal to 0.50 m – detail.



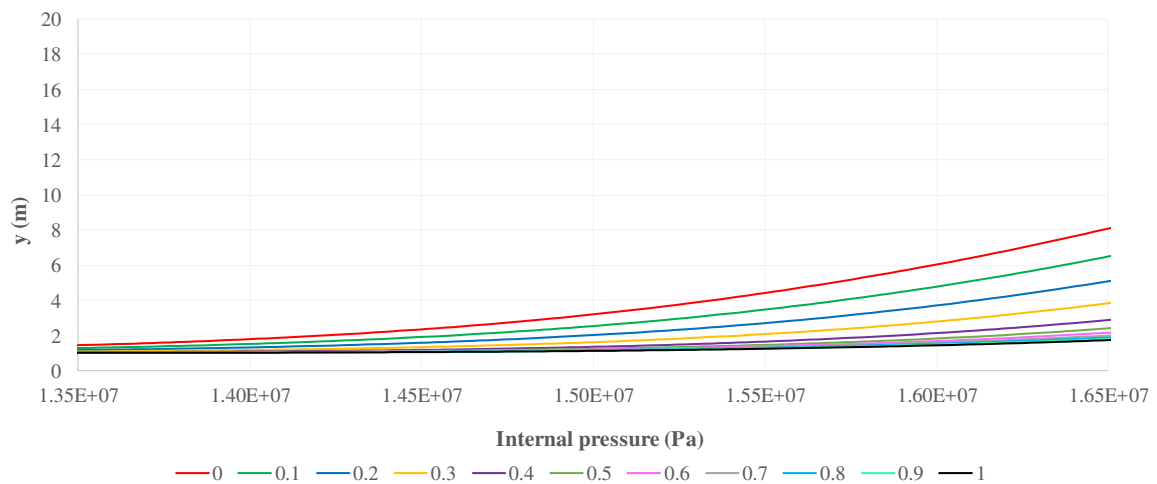
Source: prepared by the author.

Figure 109 – Coordinate  $y$  of the central node versus the internal pressure for distinct friction coefficients – imperfection amplitude equal to 1.00 m.



Source: prepared by the author.

Figure 110 – Coordinate  $y$  of the central node versus the internal pressure for distinct friction coefficients – imperfection amplitude equal to 1.00 m – detail.



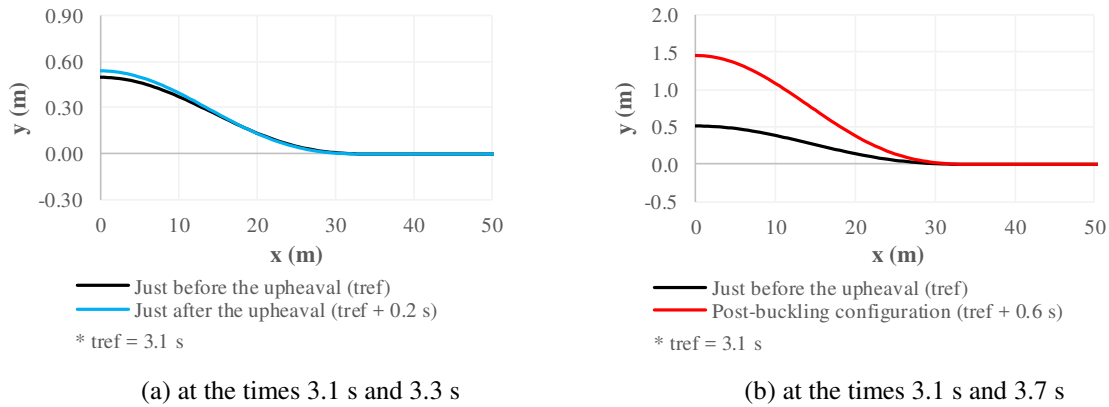
Source: prepared by the author.

From the previous graphs, it is possible to observe that larger coefficients of friction lead to larger buckling critical loads for all imperfections analyzed. Besides this, for the same imperfection amplitude, the influence of the friction in the buckling critical load is greater for smaller coefficients of friction and as this coefficient increases, the variations of critical load are smaller. It is also possible to observe from the details, comparing the results of different imperfection amplitudes, that, although the difference is small, the influence of the friction in the buckling critical load is greater for larger imperfection amplitudes.

In order to compare the post-buckling configurations for different coefficients of

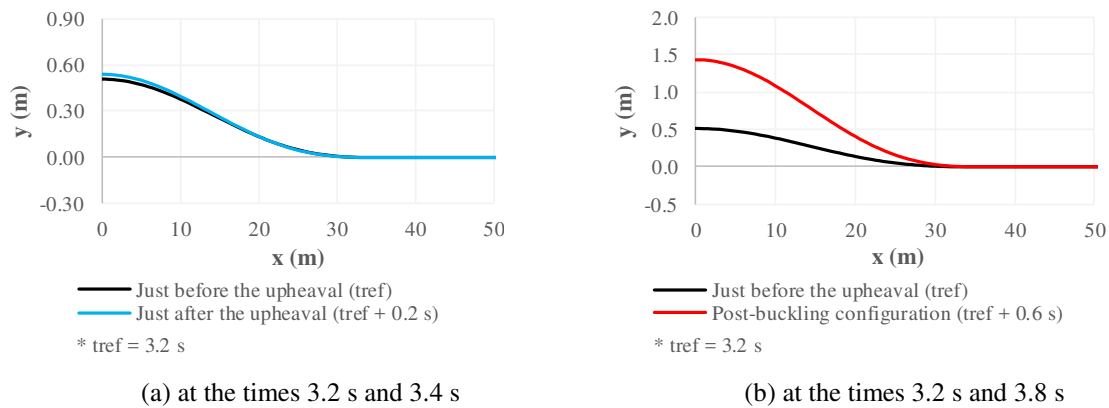
friction between the pipeline and the soil, some of them, based on the imperfection amplitude equal to 0.50 m, are presented from Figure 111 to Figure 114.

Figure 111 – Post-buckling configurations for the coefficient of friction equal to 0.1.



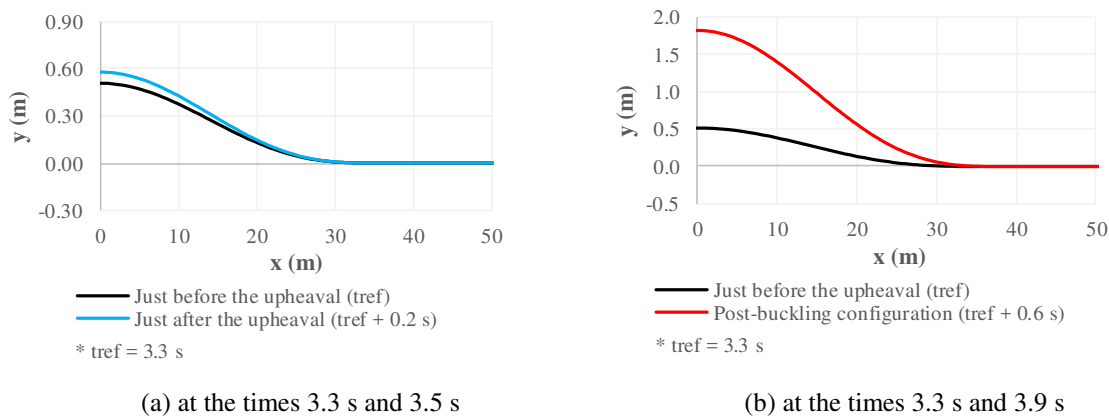
Source: prepared by the author.

Figure 112 – Post-buckling configurations for the coefficient of friction equal to 0.5.



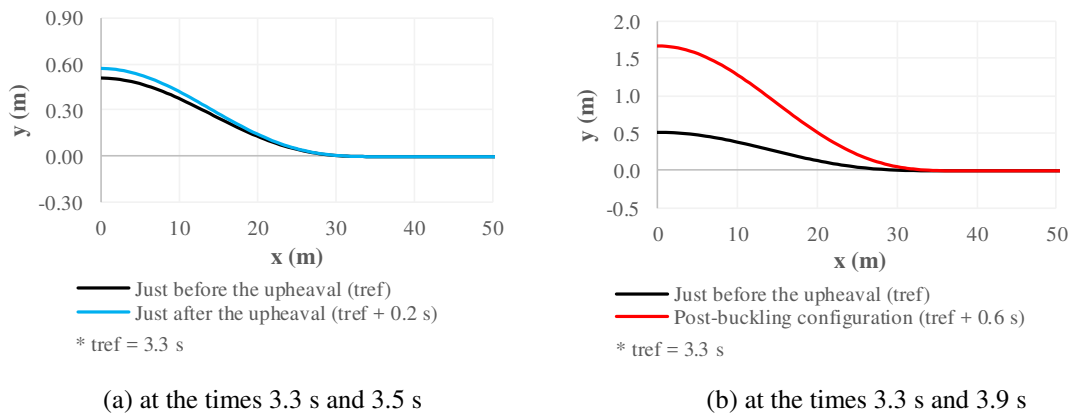
Source: prepared by the author.

Figure 113 – Post-buckling configurations for the coefficient of friction equal to 0.8.



Source: prepared by the author.

Figure 114 – Post-buckling configurations for the coefficient of friction equal to 1.0.



Source: prepared by the author.

It is possible to observe that, for the same load increase from the buckling critical loads, the post-buckling configurations are practically the same, with few variations. It means that the variation of friction influences only the buckling critical loads, not significantly influencing the evolution of the post-buckling configurations from the pipeline upheaval.

## 6 DISCUSSIONS

The literature review presented in Section 2 gathered the basic concepts and the main researches that have been developed in the area of buckling of pipelines as a whole. The concept of effective axial force was addressed with details, since it is, from a global point of view, the fundamental parameter to understand the effects of the pressure in pipelines and why they can buckle under the action of the pressure load. Analytical and numerical studies related to the buckling of pipelines itself were also presented in order to describe the mechanism of buckling and the parameters that can influence it, especially with regard to the buckling critical load. Such studies played a fundamental role in the elaboration and understanding of the numerical models developed by the present work. The study of Taylor and Tran (1996), for example, which addresses the buckling of pipelines laid on prop imperfections, was the basis of comparison for the numerical results.

Through the works analyzed, it was possible to verify that the buckling phenomenon that occurs in HPHT pipelines is quite complex and depends on many variables, such as: the pipeline geometry, the pipeline material, the process of laying the pipeline on the soil, the pipeline layout on the soil, the load that acts on the pipeline, the soil profile and its imperfections, the soil properties, the adoption of buckling mitigating measures, etc. So, with this initial contextualization of the subject, it was possible to delimit the scope of the present work, identifying the gaps that it sought to fill. Considering the small number of studies that deal exclusively with the internal pressure load in the context of buckling of pipelines, the general objective of the present work was to analyze the upheaval instability of pipelines triggered by the internal pressure, studying basically three parameters that can affect the phenomenon: the application of the internal pressure, the soil prop imperfections and the friction between the pipeline and the soil. The discussions promoted here were based on the results obtained from numerical models developed in *Giraffe*, having, as mentioned, the support of the analytical studies. The numerical models, unlike the analytical ones, considered large displacements and finite rotations. The assumptions of rigid soil (when it was modeled) and elastic-linear behavior of the pipeline material, in their turn, were maintained.

Being the focus of the work, the internal pressure was applied in two different ways in the numerical simulations. The first approach consisted in the application of an equivalent compressive axial force that produced the same effective axial force as that produced by the internal pressure. So, this axial force was not obtained by the integration of the stresses on the pipeline cross section, as could be done, for example, to determine the effect of the

temperature load. The consideration of the axial force was made from Eq. (188), based on Sparks (1984) and Fyrileiv and Collberg (2005). Besides this, both follower and non-follower behaviors of the axial force were addressed in the analyses. The second approach for applying the internal pressure was equivalent to the integration of the internal pressure on the internal area of the pipeline. It is worth mentioning, however, that Eq. (190) was used as a distributed load dependent on pipeline curvature and equivalent to internal pressure action, following the results obtained by Gay Neto, Pimenta and Martins (2017), which is especially advantageous for computation purposes.

Concerning the numerical simulations, they were divided into two groups, which were basically differentiated by their objectives and by the boundary conditions of the pipelines simulated in *Giraffe*. The first group, presented in Section 5.2, consisted in geometrically-simple models that represented only the pipeline, through Timoshenko beam elements, with different boundary conditions at the pipeline ends, but with no consideration of the interaction between the pipeline and the soil. The objective of such models was to discuss the mechanisms for modelling and analyzing the buckling phenomenon. In other words, the intention of the models of Section 5.2 was to verify and discuss the equivalence between the aforementioned approaches for considering the internal pressure, besides discussing two methods for obtaining the structural response to the internal pressure: static and dynamic analyses. It is clearly a numerical application of the theoretical discussions about stability of structures made in Section 3.

The effect of imperfections in the instability of pipelines subjected to internal pressure was also analyzed in Section 5.2 in terms of post-buckling configurations and equilibrium paths/time-series of displacement. In general, the conclusion, corroborating the results of the researches presented in Section 2, is that, for small imperfections, the critical internal pressures tend to the critical internal pressures obtained analytically for perfect pipelines. If the imperfections increase, the critical internal pressures decrease. With regard to the equivalence between the approaches of application of internal pressure, the conclusion is that, applying the internal pressure as internal pressure properly speaking or applying the internal pressure as an equivalent follower compressive axial force, the results generated are the same both for post-buckling configurations and equilibrium paths/time-series of displacement.

The conclusions presented for the analyses of Section 5.2 apply both for the results obtained from static and dynamic analyses, if such methods of analysis are employed properly, that is, if the methods of analysis are compatible with the physical systems analyzed.

It is possible to say that the system nature depends on the boundary conditions and the load approaches. So, in general, the static analysis can be employed for conservative systems while the dynamic analysis can also be employed for non-conservative systems as, for instance, circulatory systems (case 4 of Section 5.2).

The models described in Section 5.2 did not have the purpose of reproducing the operational conditions of real pipelines. This fact is clearly visible due to the boundary conditions imposed in the four cases analyzed, which restrain the movements only of the ends of the pipelines and ignore the restriction caused by the soil over their length. Thus, the simulations performed are not compatible, and cannot be compared in quantitative terms of forces and displacements, with the results shown in Section 2. The main idea of the geometrically-simple models, at such point of the research, was to understand and analyze the role of the internal pressure in the global behavior of the structure concerning buckling, not worrying about other more complex influences. The best way for reaching this objective was to use known problems (Euler's columns) and apply the internal pressure, comparing the results obtained from the action of this pressure with the results obtained from the action of an equivalent axial force. As commented, this procedure allowed to draw conclusions about the best way to apply the axial force with the objective of reproducing the global effects of the internal pressure concerning the critical load and the post-buckling configuration. The discussion about the nature of the axial force required, by the way, a greater knowledge about stability of structures since, depending on how the load is applied and depending on the boundary conditions, the choice by a static or a dynamic analysis to evaluate the buckling may lead to results completely different. The stability of the pipeline, by the way, was also discussed in terms of the Lyapunov's first method, differentiating two types of instability: the divergence and the flutter.

The second group of simulations, presented in Section 5.3, involved more realistic models, in which the interaction between the pipeline and the soil was addressed. The objective of these models was to analyze the influence of the prop imperfection amplitude and of the friction between the pipeline and the soil in the buckling critical load and in the post-buckling configuration of the pipeline, besides validating the formulation proposed by Gay Neto, Pimenta and Martins (2017), summarized by Eq. (190), in more complex models. This second group was divided into two subgroups of models. The first subgroup, which included a more simplified model with the imperfection represented by a vertical concentrated force, had the objective of verifying if the order of magnitude of the analytical results proposed by Taylor and Tran (1996) could be confirmed numerically in the model used. This verification proved

the compatibility of the results. In the second subgroup, in its turn, the imperfection is modeled together with the flat ground, being possible to detect it by the contact model described in Section 4.3. This subgroup allowed, in fact, to analyze the influence of the prop imperfection amplitude and of the friction between the pipeline and the soil in upheaval buckling. As an extra discussion, the work presented interesting comparisons between the buckling that occurs in the presence of pointwise imperfections and the buckling that occurs in the presence of conformal imperfections, concluding that the latter are more favorable from an engineering point of view.

Concerning the validation of the equivalence between the follower axial force and the internal pressure, the two load approaches produced compression in the pipeline and led to the buckling with the same critical loads, inducing even the same post-buckling configurations. Therefore, the equivalence between the two load approaches for the buckling analysis is clearly evident. Such equivalence can be very useful in simpler and quicker analysis such as, for example, in those without friction, in which the use of the axial force can be made directly. The axial force can also be used in cases with friction, provided its consideration is included in Eq. (188), as proposed by Bai and Bai (2014). However, as the intention was to take the advantage of the numerical analysis and to make the study of the buckling more general, once the equivalence between the two load approaches has been proved, it was decided to apply the internal pressure provided by Eq. (190) in the simulations with friction, which also represents more accurately the action of the load on the pipeline.

Through the numerical analysis, it was observed again, as expected, a dependence between the amplitude of the prop imperfection and the buckling critical load: larger amplitudes generate smaller critical loads than smaller amplitudes. It was shown, by the way, that this dependence is nonlinear (Figure 79). It is important to emphasize again that all numerical analyses were geometrically nonlinear, considering large displacements and finite rotations, unlike the existing analytical models. It allowed to study the post-buckling configurations in a more coherent way. It was verified that the imperfection amplitude interferes in such post-buckling configurations: the same increase of load from the critical load, for the cases analyzed, generated the largest vertical displacements for the smallest imperfection studied. With the increase of the imperfection amplitude, such displacements were smaller and varied little from imperfection to imperfection. With respect to the influence of the friction, it can be concluded that its increase delays the onset of the buckling and that its influence decreases with the increase of the coefficient of friction, for a given imperfection amplitude. Besides this, for the cases studied, the friction had little influence, comparing to the influence of the imperfection amplitude, in the post-buckling configurations, when the pressure was

increased from the critical load. It is worth mentioning that the assumption of elastic-linear behavior of the steel used in the pipeline was not confirmed for all cases, being necessary analyses involving the plastic range of the steel for verifying possible differences in the results.

In general, it was possible to confirm many results obtained by previous authors. This is because, whenever possible, the present work sought to compare its numerical results to the results obtained by Taylor and Tran (1996), making the necessary adaptations. A difference of the present work compared to the other works is the causative load of the buckling that, as mentioned, was the internal pressure. The isolated application of this load and the presenting of the results in terms of pressure, as well as the comparison between the different approaches for applying such load in the sphere of buckling, do not have much previous discussion. The use of an enhanced numerical model for this aim can also be counted as novelty. Such formulations, as, for example, that proposed by Gay Neto, Pimenta and Martins (2017), by the way, had their applicability and efficiency proved.

## 7 CONCLUSIONS

The present work discussed the upheaval buckling phenomenon that occurs in pipelines considering the internal pressure separately, as the only triggering for buckling. Through the research, some conclusions were obtained, which are summarized below:

a) there is an equivalence between applying the internal pressure as a distributed load that is dependent on pipeline curvature (GAY NETO; PIMENTA; MARTINS, 2017) and as a follower compressive axial force, both in terms of critical loads and post-buckling configurations;

b) the numerical models proved the applicability of the formulation proposed by Gay Neto, Pimenta and Martins (2017) in a real context, obtaining results coherent with previous analytical models;

c) the use of static or dynamic analysis to study buckling depends on the nature of the physical system;

d) as predicted by previous works, the critical load decreases with the increase of the prop imperfection amplitude and increases with the increase of the coefficient of friction between the pipeline and the soil;

e) the enhanced numerical model employed in the simulations allowed to predict suitably the post-buckling configurations, since large displacements and finite rotations were considered, which can be very important to study the failure modes resulting from buckling;

f) besides some results known in the literature, it is possible to say that the imperfection amplitudes analyzed played a more important role in the post-buckling configurations of the pipeline than the friction between the pipeline and the soil;

g) the prop imperfections induced smaller critical loads than the conformal imperfections analyzed.

The subject of the present work has a wide range of possible future researches. It is possible to replicate the study for the lateral buckling or even simulate numerically the choice of the type of buckling, that is, verify which type naturally occurs. Advanced considerations about the soil deformability, as well as the inclusion of multiple imperfections, are also worth of investigation. The assumption of plasticity for the constitutive equation of the steel used in the pipeline can be included in the models in order to verify if there are significant modifications in the results obtained herein for higher levels of loading. Finally, with respect

to the loads, the external and internal hydrostatic pressures can be included. Such consideration can be important in subsea pipelines.

## REFERENCES

- AMERICAN PETROLEUM INSTITUTE. **API SPEC 5L**: specification for line pipe. Washington, 2012.
- AMERICAN SOCIETY OF CIVIL ENGINEERS. **Guidelines for the design of buried steel pipe**, American Lifelines Alliance, 2001.
- BAI, Qiang; BAI, Yong. **Subsea pipeline design, analysis, and installation**. [s.l.]: Gulf Professional Publishing, 2014. 784 p.
- BALLET, J. P.; HOBBS, R. E. Asymmetric effects of prop imperfections on the upheaval buckling of pipelines. **Thin-walled Structures**, [s.l.], v. 13, n. 5, p.355-373, Jan. 1992. Elsevier BV.
- BANDEIRA, Alex A.; WRIGGERS, Peter; PIMENTA, Paulo de M. Numerical derivation of contact mechanics interface laws using a finite element approach for large 3D deformation. **International Journal for Numerical Methods in Engineering**, [s.l.], v. 59, n. 2, p.173-195, 20 Nov. 2003. Wiley-Blackwell.
- BATHE, Klaus-jurgen; CHAUDHARY, Anil. A solution method for planar and axisymmetric contact problems. **International Journal for Numerical Methods in Engineering**, [s.l.], v. 21, n. 1, p.65-88, Jan. 1985. Wiley-Blackwell.
- BAZANT, Zdenek P.; CEDOLIN, Luigi. **Stability of structures: elastic, inelastic, fracture and damage theories**. [s.l.]: World Scientific Publishing Company, 2010. 1040 p.
- BRAZILIAN ASSOCIATION OF TECHNICAL STANDARDS. **NBR 15280-1**: dutos terrestres: parte 1: projeto. Rio de Janeiro, 2009.
- CARDOSO, Carlos de O. **Metodologia para análise e projeto de dutos submarinos submetidos a altas pressões e temperaturas via aplicação do método dos elementos finitos**. 2005. 583 f. Tese (Doutorado) – Engenharia Civil, Universidade Federal do Rio de Janeiro, Rio de Janeiro, 2005.
- DET NORSKE VERITAS. **DNV-OS-F101**: Offshore standard: submarine pipeline systems. Hovik, 2013.
- DET NORSKE VERITAS. **DNV-RP-F110**: recommended practice: global buckling of submarine pipelines: structural design due to high temperature/high pressure. Hovik, 2007.
- DVORKIN, Eduardo N.; TOSCANO, Rita G. Effects of internal/external pressure on the global buckling of pipelines. In: FIRST MIT CONF. ON COMPUTATIONAL FLUID AND SOLID MECHANICS, 1, 2001, New York. **Computational Fluid and Solid Mechanics**. New York: Elsevier, 2001, p.159-164.
- E&P Magazine, 2015. Available at: <<http://www.epmag.com/archives/features/64.htm>>. Accessed in: 22 July 2016.

FAN, Shengsheng. **Upheaval buckling of offshore pipelines**. 2013. 112 f. Master's thesis – Norwegian University of Science and Technology, Trondheim, 2013.

FISCHER, K. A.; WRIGGERS, P. Frictionless 2D contact formulations for finite deformations based on the mortar method. **Computational Mechanics**, [s.l.], v. 36, n. 3, p.226-244, 14 Apr. 2005. Springer Nature.

FRANCAVILLA, A.; ZIENKIEWICZ, O. C. A note on numerical computation of elastic contact problems. **International Journal for Numerical Methods in Engineering**, [s.l.], v. 9, n. 4, p.913-924, 1975. Wiley-Blackwell.

FYRILEIV, Olav; COLLBERG, Leif. Influence of pressure in pipeline design: effective axial force. In: INTERNATIONAL CONFERENCE ON OFFSHORE MECHANICS AND ARCTIC ENGINEERING (OMAE 2005), 24., 2005, Halkidiki. **Proceedings...** Halkidiki: ASME, 2005, p.1-8.

GAY NETO, Alfredo. Dynamics of offshore risers using a geometrically-exact beam model with hydrodynamic loads and contact with the seabed. **Engineering Structures**, [s.l.], v. 125, p.438-454, Oct. 2016. Elsevier BV.

GAY NETO, Alfredo. **Generic interface readily accessible for finite elements (*Giraffe*) – User's manual**. 2017. Available at: <<http://sites.poli.usp.br/p/alfredo.gay/>>. Accessed in: 18 Apr. 2017.

GAY NETO, Alfredo; MARTINS, Clóvis de A. Structural stability of flexible lines in catenary configuration under torsion. **Marine Structures**, [s.l.], v. 34, p.16-40, Dec. 2013. Elsevier BV.

GAY NETO, Alfredo; MARTINS, Clóvis A.; PIMENTA, Paulo de M. Static analysis of offshore risers with a geometrically-exact 3D beam model subjected to unilateral contact. **Computational Mechanics**, [s.l.], v. 53, n. 1, p.125-145, 20 July 2013. Springer Nature.

GAY NETO, Alfredo; PIMENTA, Paulo de Mattos; MARTINS, Clóvis de Arruda. Hydrostatic pressure load in pipes modeled using beam finite elements: theoretical discussions and applications. **Journal of Engineering Mechanics**, [s.l.], v. 143, n. 4, p.1-12, Apr. 2017. American Society of Civil Engineers (ASCE).

GAY NETO, Alfredo; PIMENTA, Paulo M.; WRIGGERS, Peter. A master-surface to master-surface formulation for beam to beam contact. Part I: frictionless interaction. **Computer Methods in Applied Mechanics and Engineering**, [s.l.], v. 303, p.400-429, May 2016. Elsevier BV.

GAY NETO, Alfredo; PIMENTA, Paulo M.; WRIGGERS, Peter. Contact between rolling beams and flat surfaces. **International Journal for Numerical Methods in Engineering**, [s.l.], v. 97, n. 9, p.683-706, 17 Dec. 2013. Wiley-Blackwell.

GAY NETO, Alfredo; PIMENTA, Paulo de M.; WRIGGERS, Peter. Contact between spheres and general surfaces. Submitted to **Computer Methods in Applied Mechanics and Engineering**, 2017.

GAY NETO, Alfredo; PIMENTA, Paulo M.; WRIGGERS, Peter. Self-contact modeling on beams experiencing loop formation. **Computational Mechanics**, [s.l.], v. 55, n. 1, p.193-208, 12 Nov. 2014. Springer Nature.

GODOY, Luis A. **Theory of elastic stability: analysis and sensitivity**. [s.l.]: CRC Press, 1999. 450 p.

HOBBS, Roger E. In-Service buckling of heated pipelines. **Journal of Transportation Engineering**, [s.l.], v. 110, n. 2, p.175-189, Mar. 1984. American Society of Civil Engineers (ASCE).

HUNT, G. W.; BLACKMORE, A. Homoclinic and heteroclinic solutions of upheaval buckling. **Philosophical Transactions of the Royal Society A: Mathematical, Physical and Engineering Sciences**, [s.l.], v. 355, n. 1732, p.2185-2195, 15 Nov. 1997. The Royal Society.

ISAAC, Obele I. **Lateral buckling and axial walking of surface laid subsea pipeline**. 2013. 197 f. Master's thesis – Course of Offshore Technology/Subsea Technology, University of Stavanger, Stavanger, 2013.

KERR, A. D. Analysis of thermal track buckling in the lateral plane. **Acta Mechanica**, [s.l.], v. 30, n. 1-2, p.17-50, Mar. 1978. Springer Nature.

LIU, Run *et al.* Numerical studies on global buckling of subsea pipelines. **Ocean Engineering**, [s.l.], v. 78, p.62-72, Mar. 2014. Elsevier BV.

LIU, Run; WANG, Wu-gang; YAN, Shu-wang. Finite element analysis on thermal upheaval buckling of submarine burial pipelines with initial imperfection. **Journal of Central South**

MORAES, Marcello da C. **Estruturas de fundações**. São Paulo: McGraw Hill, 1976. 205 p.

NATIONAL AGENCY OF PETROLEUM, NATURAL GAS AND BIOFUELS (Brazil). **Anuário estatístico do petróleo, gás natural e biocombustíveis**, 2015. Available at: <<http://www.anp.gov.br/wwwanp/publicacoes/anuario-estatistico/2440-anuario-estatistico-2015>>. Accessed in: 15 June 2017.

NORDNES, 2015. Available at: <[http://www.nordnes.nl/rockinstallation/upheaval\\_buckling.jpg](http://www.nordnes.nl/rockinstallation/upheaval_buckling.jpg)>. Accessed in: 15 June 2017.

PEEK, R. Correction to the infinite mode for lateral buckling of pipelines. **Journal of Transportation Engineering**, [s.l.], v. 135, n. 9, p.668-669, Sept. 2009. American Society of Civil Engineers (ASCE).

PUSO, Michael A. A 3D mortar method for solid mechanics. **International Journal for Numerical Methods in Engineering**, [s.l.], v. 59, n. 3, p.315-336, 5 Dec. 2003. Wiley-Blackwell.

SPARKS, C. P. The influence of tension, pressure and weight on pipe and riser deformations and stresses. **Journal of Energy Resources Technology**, [s.l.], v. 106, n. 1, p.46-54, 1984. ASME International.

STADTER, J. T.; WEISS, R. O. Analysis of contact through finite element gaps. **Computers & Structures**, [s.l.], v. 10, n. 6, p.867-873, Dec. 1979. Elsevier BV.

TAYLOR, Neil; GAN, Aik B. Submarine pipeline buckling: imperfection studies. **Thin-walled Structures**, [s.l.], v. 4, n. 4, p.295-323, Jan. 1986. Elsevier BV.

TAYLOR, Neil; TRAN, Vinh. Experimental and theoretical studies in subsea pipeline buckling. **Marine Structures**, [s.l.], v. 9, n. 2, p.211-257, Jan. 1996. Elsevier BV.

THOMPSON, J. M. T. **Instabilities and catastrophes in science and engineering**. New York: John Wiley & Sons, 1982. 226 p.

TRANSPETRO. **Protocolo SIC Transpetro N° 00375/2017** [personal message]. Message received by <mari\_e\_mari@hotmail.com> on July 3, 2017.

WRIGGERS, Peter. **Computational contact mechanics**. New York: Springer Verlag, 2006. 530 p.

WRIGGERS, P.; ZAVARISE, G. On contact between three-dimensional beams undergoing large deflections. **Communications in Numerical Methods in Engineering**, [s.l.], v. 13, n. 6, p.429-438, June 1997. Wiley-Blackwell.

YOUNG, Warren C.; BUDYNAS, Richard G.; SADEGH, Ali M. **Roark's formulas for stress and strain**. [s.l.]: The McGraw-Hill Companies, 2011. 1072 p.

ZAVARISE, G.; WRIGGERS, P. Contact with friction between beams in 3-D space. **International Journal for Numerical Methods in Engineering**, [s.l.], v. 49, n. 8, p.977-1006, 2000. Wiley-Blackwell.

ZENG, Xianguang; DUAN, Menglan; CHE, Xiaoyu. Critical upheaval buckling forces of imperfect pipelines. **Applied Ocean Research**, [s.l.], v. 45, p.33-39, Mar. 2014. Elsevier BV.

ZHANG, Xihu; DUAN, Menglan. Prediction of the upheaval buckling critical force for imperfect submarine pipelines. **Ocean Engineering**, [s.l.], v. 109, p.330-343, Nov. 2015. Elsevier BV.

ZIEGLER, Hans. **Principles of structural stability**. [s.l.]: Birkhäuser, 1968. 150 p.